Directed Evolution Approaches for Improved Genetically Encoded Fluorescent Calcium Ion and Voltage Indicators

by

Yongxin Zhao

A thesis submitted in partial fulfillment of the requirements for the degree of

Doctor of Philosophy

Department of Chemistry
University of Alberta

Abstract

Fluorescent proteins (FP) have revolutionized our imaging technologies and facilitated visualization of biochemical and physiological processes occurring in complex biological systems, which has opened up a new and unprecedented era in cell biology. Although FPs mainly serve as passive fluorescent labels for reporting gene expression and protein localization, FP-based indicators also serve as indispensable tools for dynamic imaging of cellular signaling including neuronal activities. However, few FP-based indicators provide robust performance for *in vivo* imaging, and the development of reliable FP-based indicators remains a challenging engineering problem, mainly due to lack of structural information for rational design and effective methodologies of protein engineering.

The goal of this thesis work is to tackle the long-standing challenge of engineering FP-based indicators for improved performance. This thesis describes a variety of directed evolution strategies to develop FP-based indicators for neuronal activities. First, I developed a colony-based directed evolution method to screen for improved single FP-based calcium ion (Ca^{2+}) indicators. This novel strategy accelerated the engineering of single FP-based Ca^{2+} indicator and led to several variants with improved performance and various new colors. This palette

of new Ca^{2+} indicators enables simultaneous monitoring of Ca^{2+} transients in different cellular compartments or different types of cells, which opens up a new era of colorful Ca^{2+} imaging.

Next, by combining microfluidic technology and colony-based screening, I designed an automated cell sorting approach that enables screening variants of FP-based Ca^{2+} indicator with throughput up to 300 cells/s. This new approach saved considerable time and effort for evolving a new yellow FP-based Ca^{2+} indicator, Y-GECO. The end product, Y-GECO1, is a useful tool for Ca^{2+} imaging in cell cultures and brain slices.

Finally, I designed a hierarchical screening method to engineer Archaerhodopsin-based voltage indicators with a focus on improving fluorescent brightness. The latest generation of variants, designated QuasAr1 and QuasAr2, shows superior performance and brightness compared to their predecessors. Together with our collaborators, we demonstrated that QuasAr1 and QuasAr2 enable fully optical electrophysiological interrogation of neuronal circuits in intact brain tissues.

Preface

Chapter 2 of this thesis has been published as **Y. Zhao**, S. Araki, J. Wu, T. Teramoto, Y-F. Chang, M. Nakano, A. S. Abdelfattah, M. Fujiwara, T. Ishihara, T. Nagai, and R. E. Campbell*, "An Expanded Palette of Genetically Encoded Ca^{2+} Indicators". *Science*, 2011, **333**, 1888-1891. I was responsible for the experiment designs, screening and characterization of all the GECOs, data collection and analysis as well as the manuscript composition. S. Araki performed characterization of GECOs in HeLa cells. J. Wu contributed to screening R-GECO. T. Teramoto, Y-F. Chang, M. Nakano and M. Fujiwara contributed to applications of GECOs in culture hippocampal neurons and worms. A. S. Abdelfattah contributed to construction of protein models. T. Ishihara and T. Nagai were senior authors and supervised experiments done in their lab. R. E. Campbell perceived and oversaw the whole project and wrote the manuscript.

A version of Chapter 3 has been submitted for publication as **Y. Zhao**, A. S. Abdelfattah, A. Ruangkittisakul, K. Ballanyi, R. E. Campbell* and D. J. Harrison*, 'Microfluidic cell sorter-aided directed evolution of a protein-based calcium ion indicator with an inverted fluorescent response'. I was responsible for the concept formation, screening and characterization of Y-GECO, data collection and analysis as well as the manuscript composition. A. S. Abdelfattah and A. Ruangkittisakul contributed to brain slices experiments and involved manuscript composition. K. Ballanyi was a senior author and supervised aspects of the research. R. E. Campbell and D. J. Harrison perceived and oversaw the whole project, and wrote the manuscript.

A version of Chapter 4 has been submitted for publication as D. R. Hochbaum (equal contribution), **Y. Zhao** (equal contribution), S. L. Farhi, N. Klapoetke, C. A. Werley, V. Kapoor, P. Zou, J. M. Krajl, D. Maclaurin, N. Smedemark-Margulies, J. Saulnier, G. L. Bouting, Y. Cho, M. Melkonian, G. K. Wong, D. J. Harrison, V. Murthy, B. Sabatini, E. S. Boyden (equal contribution), R. E. Campbell (equal contribution; *correspondence related to directed evolution), A. E. Cohen*, 'All-optical electrophysiology in mammalian neurons using engineered microbial rhodopsins'. I was a co-first author in the manuscript, designed the screen strategy and engineered QuasArs, the key components of "Optopatch" system, and also contributed to manuscript composition. D. R. Hochbaum designed the Optopatch construct and system. D. R. Hochbaum contributed to engineering of the QuasArs. D. R. Hochbaum, N. Klapoetke, and Y. Cho engineered CheRiff. D. R. Hochbaum and S. Farhi acquired the optical electrophysiology data. C. A. Werley developed the low-magnification imaging system. V. Kapoor and J. Saulnier designed and prepared the slice experiments. D. Maclaurin conceived the SNAPT algorithm. P. Zou performed measurements of rhodopsin photophysics. J. M. Krajl screened ion-channel blockers on hiPSC-derived neurons. N. Smedemark-Margulies performed cell culture and sample preparation. G. L. Bouting performed immunostaining in hiPSC-derived neurons. M. Melkonian and G. K. Wong provided the transcriptomic data from which SdChR was mined and phenotyped. D. R. Hochbaum and A. E. Cohen wrote the paper with input from R. E. Campbell and myself. D. J. Harrison, V. Murthy, B. Sabatini, E. S. Boyden, and R. E. Campbell supervised aspects of the research. A. E. Cohen conceived and oversaw the project.

Acknowledgement

Foremost, I would like to express my sincere gratitude to my co-supervisors Professors Robert E. Campbell and D. Jed Harrison for their strong support and great guidance during my Ph.D. study and research, for their patience, intelligence, enthusiasm to Science, and immense knowledge. I feel very fortunate that I have two brilliant advisors and mentors for my Ph.D. career. My scientific journey in the past five years would not be so exciting and rewarding without their tremendous help. I would like to thank my thesis committee: Professor Liang Li, Professor Nils Petersen and Professor Michael Lin for their support, encouragement and brilliant comments on my Ph.D. work. In addition, I am very grateful for the support from my friends and my colleagues in Campbell lab and Harrison lab. Finally, I would like to thank the support from my parents throughout my career, and thank my fiancée Feifei for her unequivocal support, patience and great love at all times, as always, for which my mere expression of thanks likewise is not sufficient.

For the work of Chapter 2 that was performed in University of Alberta, we thank L. L. Looger for GCaMP3 cDNA (Addgene plasmid 22692) and H. Imamura for AT1.03 and mitAT1.03 plasmids. Technical advice or support was provided by J. H. Weiner, Q. Tran, K. Saito, T. Matsuda, N. Sato, N. Yonezawa, the Nikon Imaging Center at Hokkaido University, and the University of Alberta Molecular Biology Service Unit. Sequences have been deposited in GenBank (accession numbers JN258409 to JN258415). Plasmid requests will be handled through Addgene and covered under the Uniform Biological Material Transfer Agreement. This work was supported by Alberta Innovates (Y.Z.); Canadian Institutes of Health Research, and Natural Sciences and Engineering Research

Council of Canada (R.E.C.). R.E.C. holds a Tier II Canada Research Chair in Bioanalytical Chemistry.

For the work of Chapter 3, technical support and assistance was provided by the University of Alberta Nanofab, the Molecular Biology Service Unit, Hiofan Hoi, Christopher W. Cairo and Andy Holt. Plasmid pJMK004 was a generous gift from Adam E. Cohen. This work was supported by Natural Sciences and Engineering Research Council of Canada (Discovery grants to R.E.C. and D.J.H and a Vanier scholarship to A.S.A.), Canadian Institutes of Health Research (R.E.C.), MNT financial assistance for microfabrication, the University of Alberta (fellowship to Y.Z.), Canada Foundation of Innovation/ Alberta Advanced Education & Technology and Alberta Innovates (Scientist award to K.B. and scholarships to Y.Z. and A.S.A.). R.E.C. holds a Tier II Canada Research Chair. The University of Alberta has filed a provisional U.S. patent application on Y-GECO1.

For the work of Chapter 4 that was performed at the University of Alberta, we thank the Natural Sciences and Engineering Research Council of Canada (Discovery grants to R.E.C. and D.J.H), the Canadian Institutes of Health Research (R.E.C.), and graduate scholarships from the University of Alberta and Alberta Innovates (Y.Z.). R.E.C. holds a Tier II Canada Research Chair. The 1000 Plants (1KP) initiative, led by GKSW, is funded by the Alberta Ministry of Enterprise and Advanced Education, Alberta Innovates Technology Futures (AITF) Innovates Centre of Research Excellence (iCORE), Musea Ventures, and BGI-Shenzhen.

Table of Content

List of Tables

List of Figures

List of Abbreviations

2P	2-photon
Ach	Acetylcholine
ACSF	Artificial cerebrospinal fluid
AIS	Axon initial segment
AP	Action potential
Arch	Archaerhodopsin
avGFP	*Aequorea victoria* GFP
BFP	Blue fluorescent protein
BiFC	Bimolecular fluorescence complementation
BRET	Bioluminescence resonance energy transfer
CFP	Cyan fluorescent protein
ChR	Channelrhodopsin
cp	Circularly permutated
ddFP	Dimerization-dependent fluorescent protein
DMD	Digital micromirror device
EGFP	Enhanced green fluorescent protein
ER	Endoplasmic reticulum
ESPT	Excited state proton transfer
FACS	Fluorescence-activated cell sorting
FP	Fluorescent protein
FRET	Förster resonance energy transfer

GECI	Genetically encoded calcium ion indicator
GEVI	Genetically encoded voltage indicator
GFP	Green fluorescent protein
GPCR	G_q protein–coupled receptor
HDBI	4’- hydroxybenzilidene-2,3-dimethylimidazolinone
OFP	Orange fluorescent protein
RFP	Red fluorescent protein
SNAPT	Sub-Nyquist action potential timing
SNR	Signal-to-noise ratio
StEP	Staggered extension process
TTX	Tetrodotoxin
TS	Trafficking sequence
WPRE	Woodchuck hepatitis virus posttranscriptional regulatory element
wt	Wild type
YFP	Yellow fluorescent protein
μFACS	Micro fluorescence-activated cell sorting

Chapter 1. Introduction

Since a fluorescent protein (FP) was first discovered in *Aequorea victoria* in 1960s by Shimomura *et al.* (*1*), FPs have become one of the most thoroughly studied and exploited class of proteins in cell biology and have revolutionized the way we observe the biological world. *Aequorea victoria* green FP (avGFP) and its homologues have been well established as markers and indicators for monitoring protein localization, small molecule dynamics, enzyme activities, the interactions between biomolecules and physiological changes in living tissues. Extensive efforts to engineer FP and FP-based indicators for improved or new properties have been made and the list of FP and FP-based indicators continues to grow so rapidly that it is impractical to track every new report of an engineered FP or FP-based indicator. In this chapter, I will provide an overview of current FP technology with focus on the development of FP-based indicators and the breakthroughs in engineering improved Ca^{2+} and voltage indicators for neuroimaging.

1.1 FPs: the chassis of genetically encoded fluorescent probes

1.1.1 FP structure

All FPs possess a β-barrel structure consisted of 11 β-strands, with an α -helix through the central axis of the cylinder (**Figure 1.2**, PDB ID 1EMA (*2*)). The α -helix contains the chromophore and is buried almost perfectly in the center of the β-barrel, which is conventionally called a β-can. Although naturally

occurring FPs are discovered in a wide variety of marine animal species, the β-can structure is highly conserved. Once the β-can is folded properly, the chromophore can be autonomously formed from a specific tripeptide sequence and exhibits visible wavelength fluorescence (*3*). This feature makes FPs fascinating genetically encoded markers, as introducing an appropriate DNA fragment encoding a FP into almost any organism will result in the appearance of fluorescence (*4, 5*). More importantly, the FP gene can be conveniently manipulated using standard molecular biology tools, which facilitates the creation of recombinant fusion proteins or FPs with modified properties. These FP-containing constructs have proven to be non-toxic to living organisms, allowing the creation of transgenic fluorescent animals to become a standard endeavor. In this way, fluorescent labeling of almost any protein of interest in living organisms can be achieved, including a variety of mammals that could not otherwise be labeled using traditional synthetic fluorophores.

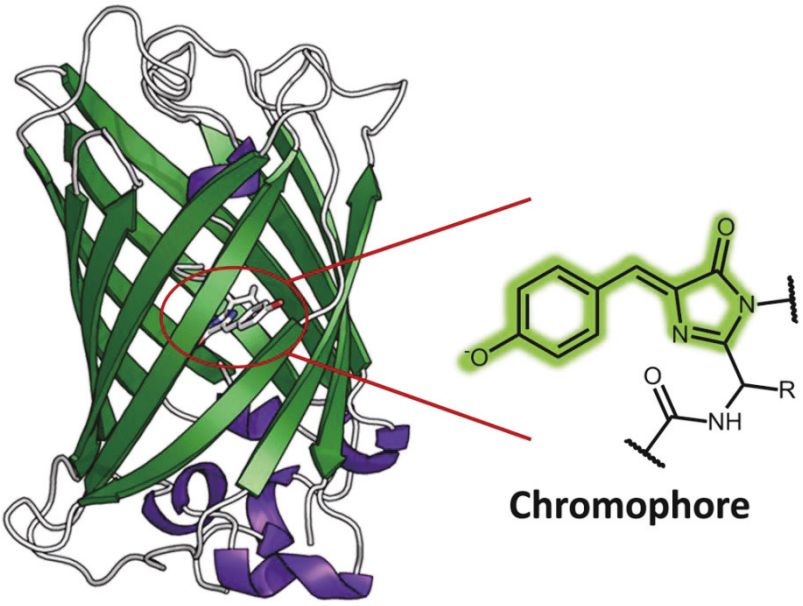

Figure 1.1 Structure of GFP and its chromophore. PDB ID:1EMA (*2*).

1.1.2 Chromophore and color variations

1.1.2.1 Chromophore structures of FPs

The chromophore structure of the naturally occurring GFP was first determined over three decades ago (*6*) (**Figure 1.2**). The mechanism of the GFP chromophore maturation has been extensively studied and is reasonably well-understood (**Figure 1.2**). First, the GFP folds into a nearly native conformation. Residue 65-67 will then form the chromophore by the following sequential reactions: nucleophilic attack of the Gly67 amide nitrogen on the carbonyl carbon of Ser65 results in the formation of imidazolinone, followed by oxidation by molecular oxygen, and finally dehydration (*3, 7-13*) (**Figure 1.2**). Although some exceptions exist, the majority of FPs have a chromophore in the Z conformation (*14*). The oxidation is the rate-limiting step (*11*), and oxygen is the only reagent that is required by the chromophore formation. Depending on the FP, this process generally takes minutes to hours to complete.

In contrast, the formation of other types of FP chromophores is less understood, and particularly there is some debate regarding the mechanism of formation of red FP (RFP) chromophore (*10, 15, 16*). All known RFP chromophores possess a GFP-like chromophore with extra double bonds that extend the conjugated system (**Figure 1.2**). The chemistry of RFP chromophore formation is complex, and several competing mechanisms have been proposed (*10, 15, 17-19*). It is believed that most RFPs mature via a common DsRed-like pathway. Previous studies suggested that the matured DsRed chromophore forms via a green fluorescent intermediate (*20*), but there is increasing evidence suggesting that the maturation occurs via an unusual blue intermediate for DsRed

while other RFPs do mature via a green chromophore intermediate (*10*). The blue-to-red chromophore conversion can be disrupted with certain mutations, resulting in a blue FP (*21*). The maturation of red fluorescence is often incomplete, and a significant fraction of proteins fail to achieve red fluorescence and become trapped in, e.g., a green-emissive state via a competing pathway (**Figure 1.2**). The presence of this green "contamination" for many RFPs can leading to significant experimental complications (*22*).

Various different chromophore structures have been discovered (**Figure 1.2**), though the GFP-like green chromophore and DsRed-like red chromophore are the most common. Other chromophore structures have been artificially created by substituting the chromophore-forming tripeptide. For example, introduction of different aromatic amino acids to replace the central tyrosine in the GFP chromophore results in violet-, cyan-, and blue-emitting FPs (*3*).

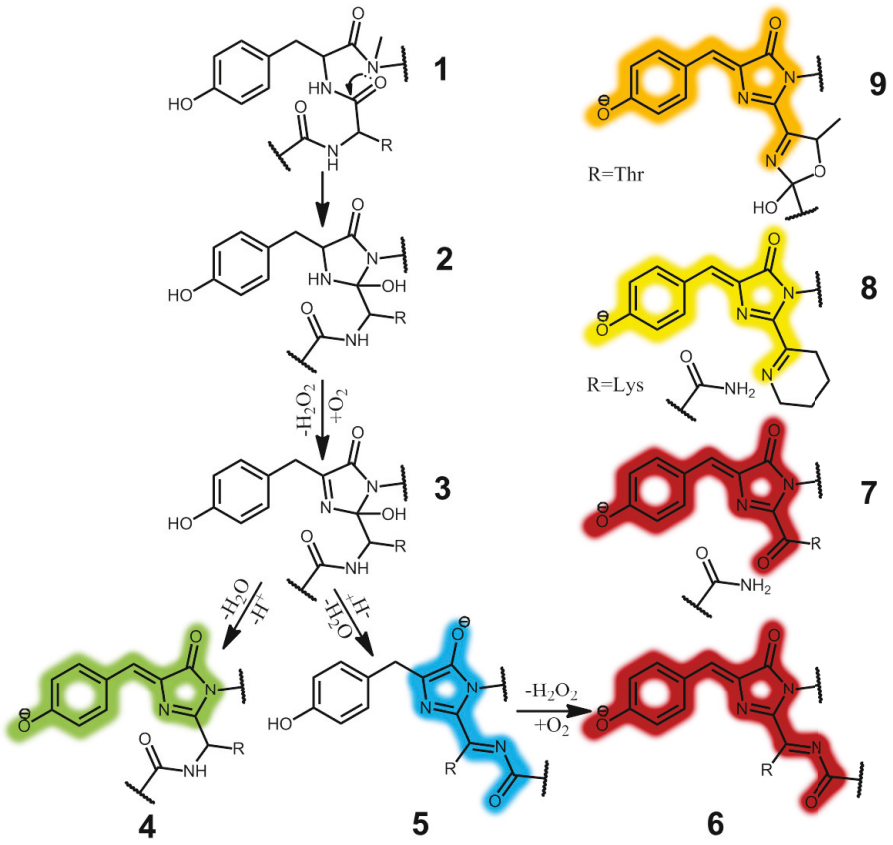

Figure 1.2 Proposed maturation mechanisms for a range of chromophores. Starting from the chromophore tripeptide (1), the abundantly occurring green chromophore (4) is formed via step 1 - 3. In other cases the chromophore matures via the blue-emitting intermediate (5) to the DsRed-like chromophore (6). Through chromophore and environment modification, a range of different chromophores can be generated (7-9). Modified from Dedecker *et al* 2013 (*23*).

1.1.2.2 The effect of the chromophore environment on the fluorescence emission

Fascinatingly, the structure of FP chromophores determines only part of the spectroscopic properties. The chromophore interacts with surrounding amino acid residues and possibly highly ordered water molecules inside the barrel, forming a

complex interaction network that determines the spectroscopic properties. Single mutations in the FP barrel can significantly influence the spectroscopic properties of the protein or even render it nonfluorescent (*3*). Owing to the protection of the coupled network provided by the barrel, FPs are remarkably resistant to chemically or heat-induced denaturation, and even proteolysis (*24*).

Synthetic analogues of the FP chromophore and short digestion fragments have been extensively used for studying the effect of the chromophore environment on the fluorescence emission (*25, 26*). One typical example is 4'-hydroxybenzilidene-2,3-dimethylimidazolinone (HBDI, **Figure 1.3**). HBDI is very weakly fluorescent (fluorescent quantum yield 10^{-4}) in aqueous solution at room temperature, compared to avGFP (quantum yield about 0.8) (*27*). Ultrafast spectroscopy of HBDI reveals that highly efficient internal conversion occurs in a wide range of solvents leading to deactivation of the excited state on sub-picosecond time scale, which is too short for fluorescence to be competitive (*28-30*). In contrast, avGFP displays excited-state lifetimes of about 3 ns. HDBI does become fluorescent at very low temperatures that are below the glass transition temperature of the solvent (*27, 29, 31*). Although there is still debate on the mechanism associated with this fast internal conversion, the current consensus attributes it to rotation or flexibility along one of the bonds associated with the methylene bridge (*25, 26*). The chromophore environment in FPs has evolved to prevent this internal conversion from occurring and thus lead to high fluorescence quantum yields.

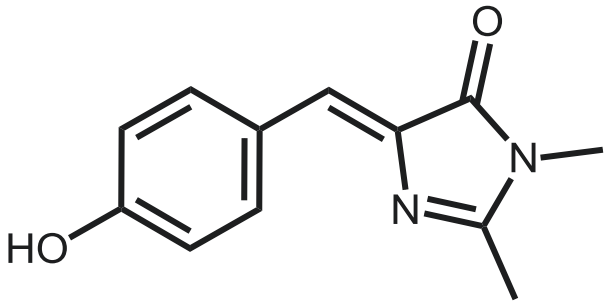

Figure 1.3 Structure of 4'- hydroxybenzilidene-2,3-dimethylimidazolinone (HBDI).

The chromophore in FPs can be either protonated or deprotonated depending on the pH of the solution (*3, 32*). Many spectroscopic properties of the protein can be explained in terms of the protonation state of the chromophore. For instance, the deprotonated anionic state absorbs at about 470 nm in avGFP, and a protonated neutral state absorbs at about 390 nm (*27*). Analogous observations can be made for almost all known FPs (although the wavelengths may be different) as long as there is a titratable group in the chromophore, with few exceptions (*33*). In avGFP, excitation of the anionic state results in green fluorescence with a maximum at about 505 nm. Excitation of the neutral form at 395 nm in avGFP is unusual because it also emits bright green fluorescence emission that is similar to that of the anionic state. The mechanism behind this phenomenon was discovered to be fast excited-state proton transfer (ESPT) (*34*) via an internal proton wire (*35*). ESPT is not common among FPs, but it can be exploited for engineering FPs that display very large apparent Stokes shifts (*36-38*).

Although the surrounding chromophore environment has the strongest effects on FP photophysics and photochemistry, the spectroscopic properties can also depend on mutations far from the chromophore. For example, 12 mutations were

found necessary to fully generate a red fluorescent phenotype from the ancestral Kaede-like green FP. Strikingly, some mutations were not in proximity of the chromophore and only affected the overall fold stability of the protein (*39*). A FP Dronpa is found possessing a light-induced change in the protonation state and configuration of the chromophore, which leads to significant localized changes in the conformation of the protein (*40*).

1.1.3 Practical issues of FPs

Genetically encoded fluorescence is a very powerful tool for imaging of biology activities. However, naturally occurred FPs from marine animal species evolved to possess properties that are optimal for the survival of those animals. Therefore in practice the FPs are not necessarily optimal for the biological contexts that we are most interested in. Accordingly, researchers expend a tremendous amount of effort to optimize FPs for experimental applications. Fortunately, because FPs are genetically encoded, their structure and properties can be readily manipulated using the standard tools of molecular biology. Furthermore, their relatively good expression in *E. coli* facilitates screening for a desired fluorescence phenotype in high throughput. In this section, we will discuss several practical aspects of FPs and efforts to engineer improved variants.

1.1.3.1 Colors

Improved versions of GFP with better brightness and folding efficiency were developed soon after the first demonstration of its heterogeneous expression in a model organism (*41-43*). It was found that the fluorescent color of GFP could be altered dramatically to blue or yellow by introducing only one or a few mutations

(*3*). This shows the fluorescent color of FPs heavily depends on the chromophore structure and its environment. Despite the tremendous success in engineering avGFP for improved photophysical properties and altered hues, some developments have remained elusive. Despite extensive efforts, the emission wavelength of avGFP has not been extended above 530 nm effectively. Only one engineered avGFP variant was reported with partial red emission at 585 nm (*44*). Fortunately, this engineering problem has been solved by Nature. FPs with red-shifted fluorescent excitation and emission wavelengths have been discovered in reef corals and anemones (*45, 46*).

Red shifted fluorescence wavelengths provide a major advantage in imaging, because red wavelength fluorescence minimizes the autofluorescence and scattering problems of biological tissue, which is more significant with the blue/green/yellowish fluorescence of avGFP homologues. At shorter wavelengths light is strongly absorbed by pigment proteins, such as melanin or hemoglobin, and the optical scattering and phototoxicity are more severe. Accordingly more red shifted FPs are generally preferable relative to more blue-shifted FPs (*47*). This trend remains true through to wavelengths of about 1000 nm, beyond which the absorbance of water becomes the limiting factor. For these reasons, the optimal wavelength range for exciting and observing the emission of fluorescent probes (often referred to as the "optical window") runs from approximately 650 nm to 1000 nm in biological tissues (*47-49*). To better use the optical window for fluorescence imaging *in vivo*, much effort has been invested in engineering FPs with ever more red-shifted wavelengths and pushing both their excitation and emission wavelengths into the near-infrared (*50-53*). An alternative approach is to

use near-infrared 2-photon (2P) excitation to excite FPs that fluoresce at visible wavelengths (*54, 55*).

1.1.3.2 Oligomerization

Most natural FPs have been found to exhibit a strong to moderate tendency to form quaternary structure (*56*). For instance, avGFP and its derivatives tend to dimerize at high concentrations, FPs isolated from *Renilla* sea pansies form dimers, and all the native yellow, orange, and red FPs isolated from reef corals and anemones are tetramers (*57, 58*). Oligomerization of FPs can be problematic for many applications in cell imaging. In particular, when FPs are fused to a host protein for targeting to specific organelles or studying the protein-protein interactions of the host protein (*59-61*), the oligomeric structure can contribute to mislocalization of the fusion protein.

In addition to oligomerization, some FPs can also undergo higher order aggregation leading to undesired mislocalized FP aggregates inside the cells and increased cytotoxicity. To date, little is known about the mechanism of FP aggregation. One hypothesis is that aggregation may be due to non-specific oligomerization triggered by electrostatic or hydrophobic interactions between FP copies. A study on DsRed supports the role of electrostatic interaction in aggregation. Yanushevich *et al.* analyzed the crystal structure of DsRed and speculated that DsRed tetramers possess a negatively charged protein surface while each DsRed copy contains four positively charged residues in its N-terminus. The positively charged N-terminus can serve as salt bridges with adjacent DsRed tetramers which eventually form a stable net-like 'polymeric' structure (*i.e.*, the aggregates). Based on this rationale, Yanushevich *et al.*

substituted Lys and Arg residues close to the N-terminus with negatively charged or neutral residues to produce the non-aggregating DsRed2 mutant (*62*).

To address the problem of oligomerization, Campbell *et al.* successfully engineered a monomeric RFP (mRFP1) from DsRed, by sequential introduction of repulsive residue interactions (*63*). This mRFP1 forms less aggregates and has enabled red fluorescence labeling experiments that were otherwise impossible with DsRed. The strategy to engineer monomeric FPs has been adapted in many other works to reduce the oligomerization tendency of FPs (*63, 64*).

1.1.3.3 Photophysics

Good photostability of a FP is critical for a successful imaging experiment as it determines how much illumination dose can be tolerated by the FP before it irreversibly photobleaches. Accordingly, photostability influences how much fluorescent output can be detected in practice. Photostability is particularly important for long term imaging, for imaging of weak fluorescent signals from proteins expressed at low levels, and for quantitative measurements. Some wild-type FPs possess high photostability presumably because of the importance of photostability for wild-type FPs to function properly in the marine animals. However, no natural FPs have evolved to endure the very high light power levels used in typical microscopy experiments. Some engineered FP variants do preserve the good photostability of their corresponding wild-type FP, such as EGFP which is derived from avGFP (*3, 65*). However, it is more typical for an engineered FP to have worse photostability than its corresponding wild-type FP, following optimization for improved brightness, development of different colors, or monomerization.

Only a few research efforts dedicated to improving the photostability of FPs have been reported to date (*66, 67*), owing to a poor general understanding of the photodestruction mechanism and the lack of appropriate methods that are capable of evaluating the complex photostability of FPs comprehensively. In literature reports, the photostability of FPs is generally defined as the time required to reach 50% of the initial emission rate of 1,000 photons/s for each FP (*67-69*). However, the photostability of any given FP depends on many experimental parameters. Light source, illumination intensity and frequency, as well as excitation wavelengths have great influence on the photophysics of FPs. For example, TagRFP-T was engineered for improved photostability using colony-based screening (*67*), but is actually less photostable than its predecessor TagRFP under laser illuminations (*70*). Similarly, mPlum is more photostable than mRaspberry in wide-field imaging but it is the opposite in confocal imaging (*71*). In addition, the phenomenon of FP photobleaching is often confused with reversible photochromism (*72, 73*) or irreversible photoconversion that causes a shift in fluorescent spectra (*74-77*).

Based on the discussion above, it would be wise to consider the complex nature of FP photostability when choosing a photostable FPs for a particular experimental design. The numbers provided in the literature can only provide a general guide and may not be applicable to the particular experimental conditions of interest. Parallel experiments with more than one photostable FP and careful evaluation under the actual experiment setup is recommended.

1.1.4 Methods of FP engineering

In the previous section, we discussed some practical issues regarding the use of FPs for live cell imaging, which are emblematic for the challenges faced in FP development. In the past two decades, extensive efforts in engineering of improved FPs using both rational design and high throughput screening led to a dramatic expansion of the inventory of useful FPs for fluorescent imaging. In this section, I will briefly overview the current methods and challenges in the development of FPs, which are also applicable to FP-based indicators.

In a typical process of developing FPs with improved properties, the first step is often rational or semi-rational design that guides the introduction of mutations at specific positions based on the knowledge of FP of interest (*78*). A successful rational design requires an insightful analysis of the structure of a FP. For example, such analysis could be based on knowledge of the interacting residues at the interfaces between two FP copies in a native FP oligomer. Based on this analysis, the experimenter could rationally introduce mutations that are designed to disrupt the key interactions and decrease the oligomeric state of the FP (*63, 79, 80*). Rational design approach is fairly successful for addressing some design challenges such as as FP monomerization (*63, 79, 80*) and chromophore modification for different hues (*3, 33, 69*), in which the target residues are typically well known. The challenge of rational design is to modify FP for a specific improvement without affecting other properties. With the current technologies, it is difficult to predict all the potential interactions of targeted mutation with adjacent residues and other parts of FPs. Therefore, even in the

cases where only one mutation is introduced, other important parameters of the resultant FP are likely to deteriorate if no further engineering effort is taken.

Prototype FPs generated by rational designs often require further optimization by a process called directed evolution. Directed evolution relies on a specifically designed methodology to iteratively select variants with improved properties of interest from a library containing hundreds to thousands of randomly mutated FP variants. An advantage of directed evolution approaches is that a comprehensive understanding of the function-structure relation of the FP is not required. As long as the screening method can effectively identify and collect mutants with improved properties, such as folding efficiency (*81*), fluorescence brightness (*41*), or other photophysical properties (*67, 82, 83*).

There are several platforms for directed evolution of FPs. Colony on-plate screening selects FP variants based on the digital fluorescent images of *E. coli* colonies on a nutrient agar plate. Currently, colony on-plate screening (*63, 76, 80, 84*) has been the most successful approach for development of FPs due to its robustness, flexibility for customization, and low cost. Fluorescence-activated cell sorting (FACS) provides much higher throughput to screen FP-expressing cells for brightness (*41*) and different colors (*69*). The higher throughput of FACS significantly reduces the labor and time to find improved variants compared to colony on-plate screening. However, FACS requires expensive instrument and maintenance and has limited customization in terms of screening parameters. The recent advance of microfluidic technologies enables new platforms that potentially can combine the merits of both colony on-plate screen and FACS. Unlike FACS, microfluidic chips are cost effective and amenable to customization for screening specific properties of FP. They are also capable of automatic high

throughput screening that saves much time and effort compared to a colony on-plate screen. For example, droplet-based microfluidic chips have been used for directed evolution of enzymes with improved catalytic rate (*85, 86*). Recently, Jimenez and coworkers reported a microfluidic platform that is capable of screening FP variants for improved photostability (*87, 88*).

1.2 FP-based indicators and their design principles

Living cells are highly dynamic and highly complex systems where many thousands of biochemical processes could be taking place at any one time. Fluorescent indicators based on engineered FPs for visualizing dynamics of biological processes would be very powerful tools for understanding complex cellular mechanisms. Unmodified FPs are difficult to use for this purpose. Although the relatively inert chromophores of FPs provide advantages as a passive marker of protein expression, localization and organelle structure (which are still the most common applications of FP), the inertness of the chromophore is also a disadvantage in applications where probing dynamic changes of biological properties is the goal. Thus, specialized FPs that are engineered to be fluorescent indicators are required. In the last two decades, FPs have proven their versatility to be engineered as genetically encoded indicators for probing numerous biochemical and physiological changes in cells, such as the concentration of secondary messengers, membrane potential, protein-protein interactions, cellular signaling, and many others (*89*). Generally speaking, FP-based indicators are multi-domain fusion proteins consisting of a sensor domain (a protein that can respond to a biological parameter of interest) and a reporter domain (usually consisting of one or two FPs). The sensing domain responds to a change in the

environment and induces a molecular conformational change that, in turn, modulates the photophysical properties of the reporter domain (*89*). These changes in photophysical properties could include either a change in the fluorescent brightness at one wavelength, or a ratiometric change where the fluorescence increases at one wavelength but decreases at another.

The key challenge of developing FP-based indicators is how to transduce a molecular conformation change of the sensor domain into a change of a fluorescent property of the reporter domain. Several transduction mechanisms have been developed for converting a wide variety of biophysical or biochemical changes into either intensometric or ratiometric changes in FP fluorescence. Traditional mechanisms include Förster resonance energy transfer (FRET) between two FPs, bimolecular fluorescence complementation (BiFC) (*90-92*) and modulation of FP chromophore environment (single FP-based indicators) (*92-95*). More recently, three new mechanisms have been developed for designing FP-based indicator. They are bioluminescence resonance energy transfer (BRET) (*96*) from a luciferase to a FP, dimerization-dependent FPs (ddFPs) (*97, 98*). We can group them into three categories: indicators based on energy transfer (FRET and BRET), indicators based on complementation (BiFC and ddFPs) and single FP-based indicators.

1.2.1 Indicators based on energy transfer

FRET is a phenomenon that involves radiationless energy transfer between two chromophores. When a donor chromophore possesses a fluorescent emission that overlaps with the absorption of acceptor chromophore, the excited state of the donor chromophore may transfer the energy to an acceptor chromophore via

non-radiative dipole-dipole coupling. The efficiency of FRET is inversely proportional to the sixth power of the distance between the donor and acceptor, thus very sensitive to small changes in distance.

FRET is one of the most common mechanisms used for designing FP-based indicators. In most cases, a standard pair of donor and acceptor FPs is chosen without requirement for further engineering, and this pair is then strategically fused to the termini of the sensing protein. This fusion is done is such a way that the expected conformational change, associated with the biological process of interest, will modulate the FRET efficiency between the donor FP and acceptor FP. There are many design strategies available for constructing FRET-based FP indicators (**Figure 1.4**). The most important advantage of FRET technology is that the ratio of the fluorescence intensities in the donor and acceptor channels allows internal calibration for quantitative microscopic imaging. Generally speaking, ratiometric imaging cancels out many sources of measurement variability such as various expression levels of proteins in different cells, uneven illumination, out of focus, and motion artifact, which minimize the imaging artifacts and permits quantification of intracellular Ca^{2+} concentration (*99*).

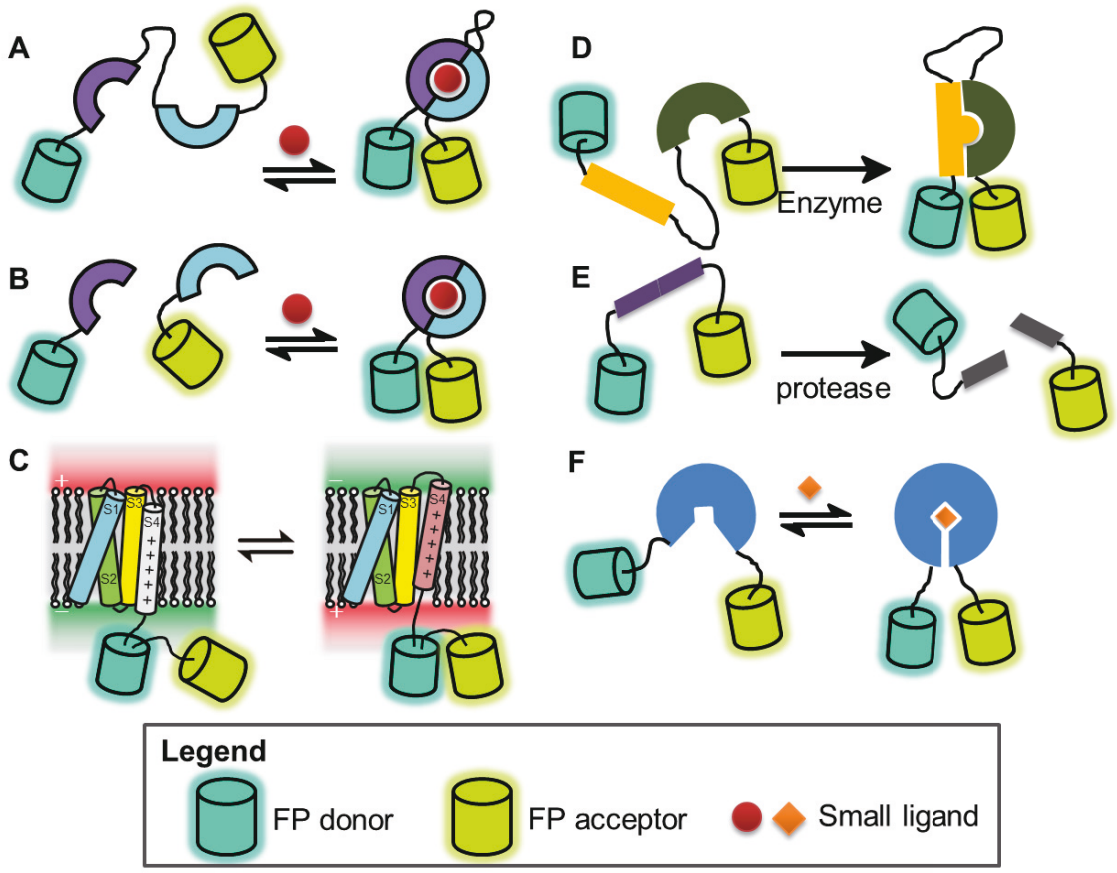

Figure 1.4 Examples of design strategies of FP-based FRET reporter.

(A) Intramolecular reporters of small molecules. (B) Intermolecular reporters of small molecules. (C) Reporters of voltage-dependent intramolecular rearrangements. (D) Reporters of enzymatic activity. (E) Protease reporters. (F) Allosteric 'clam-shell' reporters. (This figure has been modified based on Alford *et al* 2013 (*89*).)

One of the major disadvantages of FRET-based FP indicators is that they require two color channels, which requires multiparameter imaging (*89*). One way to circumvent this problem is to substitute the donor FP with a self-illuminating protein reporter (e.g. *Renilla* luciferase) and exploit BRET, which is similar to FRET except that the bioluminescent donors get excited via chemical reactions

instead of by absorbance of light. This approach does not require the excitation of the donor FP and therefore frees up one of the color channels. The major drawback of BRET-based indicators is that they are generally dimmer than regular FRET-based indicator due to the lower photon flux, as the brightest luciferase only emits around one hundredth as many photons as a typical FP (*100*).

1.2.2 Indicators based on complementation

1.2.2.1 Bimolecular fluorescence complementation

FPs can be genetically split into two non-fluorescent fragments that can assemble into the native fluorescent structure when they are brought sufficiently close to each other (*91, 101*) (**Figure 1.5**A). This phenomenon can be used as a design strategy to construct indicators for visualizing protein-protein interactions in living cells. Potentially interacting protein partners can be genetically fused to each of the split FP fragments. When the partners interact, the two split FP fragments are brought into close proximity and combine to form an intact FP. Because there is essentially no fluorescence prior to protein-protein interaction, this approach generates higher fluorescent contrast compared to other types of FP-based indicators. Bimolecular fluorescence complementation (BiFC) can be applied with FPs with different hues ranging from blue to far red (*102-106*), and it can also be used to identify potential interacting protein partners of interest (*107*). The disadvantages of BiFC includes slow kinetics and the irreversible reconstitution process due to very high affinity between the two complement split fragments, which limits its applications for probing fast or reversible biological events (*101*).

1.2.2.2 Dimerization-dependent FPs

To overcome the limitations of BiFC-based designs, Alford *et al.* reported a novel design strategy for engineering FP-based indicators, which shares similar concepts with split-FP design and FRET-based design (*97, 98*). In this strategy, Alford *et al.* engineered a palette of FPs that are dimly fluorescent in the monomeric state but exhibit significantly brighter fluorescence upon dimerization (**Figure 1.5**B). Because intact FPs are used in dimerization-dependent FPs (ddFP) (rather than split FP fragments in BiFC), the complementation occurs much faster than split-FP indicators and is fully reversible. Arguably, the ddFP approach is similar to the FRET-based approach as the fluorescence signal depends on the distance between the two FP partners. However, the critical difference is that the two FP partners of ddFPs have moderate affinity for each other and will spontaneously dimerize in high concentration while spontaneous dimerization is less of a concern for monomeric FP FRET pairs.

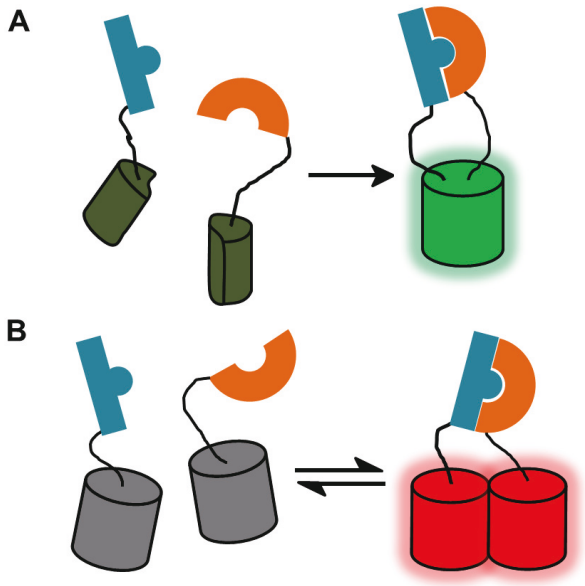

Figure 1.5 Complementation-based strategies.

(A) Bimolecular fluorescence complementation. (B) Dimerization-dependent FPs.

1.2.3 Single FP-based indicators

Single FP-based indicators only utilize a single engineered FP, in which the chromophore environment has been engineered to be sensitive to the analyte of interest. Although most of the single FP-based indicators generate an intensiometric signal (*i.e.* single color), there are examples of single FP-based indicators engineered as a ratiometric sensor (*92, 108*). In general, single FP based indicators generate larger fluorescent signals than other types of reversible indicators. On the other hand, it is often difficult to engineer a practically useful single FP-based indicator since it requires intensive modification on the FP β-barrel, which is likely detrimental to the brightness and folding of the targeted FP.

Single FP-based indicators can be divided into two sub-classes based on whether a foreign sensing domain is adapted. In the first sub-class, the FP serves as both sensor and fluorescent reporter units. This is usually achieved by utilizing either an intrinsic or engineered molecule recognition site that is part of the FP β-barrel. Generally speaking, the intrinsic molecule recognition sites only bind to small analytes such as H^+ (pH sensors (*109*)), Cl^- (chloride indicators (*110*)) or some metal ions (*111*) as they can penetrate into the β-barrel and influence the chromophore environment. A broader range of sensor specificities can be achieved by introducing additional molecule recognition sites on the surface of β-barrel such as disulfide bonds for redox sensing (*112-114*), the EF hand motif for Ca^{2+} sensing (*115*), and modifying the chromophore sequence with unnatural

amino acids (*116, 117*). The major limitation of this design is that the scope of analytes that are amenable to detection by this approach is relatively small. In addition, FP-based indicators utilizing unnatural amino acids require extracellular supplement of unnatural amino acid components.

The second sub-class overcomes the major limitations of the FP-only approach by introducing a second protein "sensor" domain that is the basis for the analyte or biochemical activity specificity. This second domain undergoes a conformational change that results in modulation of the fluorescence of the host FP when responding to a specific biological event. In this way the potential applications of the single FP-based design are greatly expanded. In most cases, this design requires partial exposure of the FP chromophore to the environment to maximize the transduction efficiency of the sensor domain, by either directly inserting the sensor domain at positions near the chromophore, or by using a technique called circular permutation, in which the original N- and C- termini are fused together with a polypeptide linker and a new N- and C- termini is created at a site on the β-barrel near the phenolate group of the chromophore (*94, 118*). The classic example of this design is the single FP-based Ca^{2+} indicator. Baird *et al.* engineered a low affinity Ca^{2+} indicator (called camgaroo) (*94, 119*) by inserting the Ca^{2+}-sensing domain calmodulin (CaM) at position 145 of the yellow FP EYFP. However, the most popular design for single FP-based Ca^{2+} indicator was pioneered in parallel by Nakai and coworkers and Nagai and coworkers (*92, 120*). In this design, the new N- and C- termini of a circularly permutated FP (cpFP) were fused to the CaM-binding domain M13 and CaM itself, respectively (see **Figure 1.6**B). Structural analysis has revealed that Ca^{2+} induces a substantial conformational change of M13 and CaM, which in turn modulates the

environment of chromophore and alters the fluorescence output of the FP domain (*121, 122*). We discussed this type of FP-based Ca^{2+} indicator in more detail in the following sections.

1.3 Genetically encoded indicators for neuroimaging

Monitoring spatiotemporal activity patterns in neural circuits is a critical technique for understanding complex brain functions. Fluorescent live cell imaging is one of most powerful neuroimaging techniques for interrogation of neural microcircuits with high spatial and temporal resolution. The continuing advance of various fluorescent microscopy technologies and genetic labeling techniques heralds a growing prominence for these techniques for neuronal circuit analysis in complex tissue samples (*123-125*). Development of genetically encoded indicators contributes to this field by providing fluorescent probes capable of reporting key biochemical and physiological events in neuronal circuits. Compared to traditional synthetic organic dyes, genetically encoded indicators can be introduced into neural cells in much less invasive manners, such as by viral infection and the creation of transgenic animals. In addition, they can be expressed in specific cell types and sub-cellular compartments over long period of time. These features enable monitoring neural activities from a specific subset of neurons in intact tissues as well as chronic imaging of neural circuit dynamics.

Genetically encoded indicators of neuronal activity require the conversion of a relevant biochemical or physiological change into a fluorescence change. Some physiological changes relevant to neuronal activity are summarized in Table 1.1. Among these changes, membrane potential, ions and various neurotransmitters are valuable and feasible targets for interrogation of neuronal activities. Proteins that

sense those targets are available in nature and can be engineered in such a way that the conformation change of the sensor protein can modulate the fluorescence change of genetically encoded fluorophores.

Table 1.1 Biochemical changes associated with neuronal activities

Neuronal event	**Biochemical change**	**Example**
Action potential	Intracellular ion concentration	Na^+, K^+, Cl^-, Ca^{2+}
	Membrane potential	depolarization, hypolarization
Synaptic transmission	Release of neurotransmitters	glutamate, gamma-Aminobutyric acid (GABA), dopamine, endorphins, histamine, noradrenaline serotonin, somatostatin, substance P, cocaine and amphetamine regulated transcript, opioid peptides, acetylcholine (Ach), adenosine, anandamide, nitric oxide, among others.
	Vesicle fusion and release	SNAP (Soluble NSF Attachment Protein) Receptor (SNARE)
	Postsynaptic signaling	G_q protein–coupled receptor (GPCR), Ca^{2+}, Inositol trisphosphate (IP3), diacylglycerol (DAG), calmodulin-dependent protein kinase II (CaMKII), among others.

Genetically encoded fluorescent indicators that can detect change in Ca^{2+}, membrane potential, glutamate (a neurotransmitter) and pH have been developed with advanced protein engineering techniques (*92-95, 108, 109, 126-134*). Ca^{2+} indicators have been so far the most successful category owing to their large signal changes and high signal-to-noise ratio (SNR) (*108, 133, 135*). Furthermore, the

diverse roles of Ca^{2+} in cell signaling and neuronal activities have meant that the indicators are useful to a broad range of researchers. Indicators for probing neurotransmitters and pH are also important tools for monitoring synaptic transmission (*109, 128*). Although the overall performance of voltage indicators is relatively poor compared to Ca^{2+} indicators, development of voltage indicators has been accelerated recently due to the demands of the neuroscience community. Membrane potential is a direct measure of neural activity and can provide neuronal information with temporal resolution in the millisecond range, whereas Ca^{2+} signals are usually a hundred times slower.

1.3.1 Genetically encoded Ca^{2+} indicators for imaging of neuronal activities

In the past two decades, tools for imaging of free intracellular Ca^{2+} concentration have attracted much attention in neuroscience. Ca^{2+} is a ubiquitous intracellular signal and plays critical roles in various neuronal functions, such as synaptic transmission, neuron development and neuronal plasticity. Detecting spikes in the cytosolic Ca^{2+} concentration in a neuron is an indirect measure of neuron action potentials. When a neuron fires action potentials, its voltage-gated Ca^{2+} channels open up due to cell membrane depolarization. The resulting influx of the extracellular Ca^{2+} leads to an increase of intracellular Ca^{2+} concentration within a few milliseconds (*136-138*).

Traditionally, optical recordings of intracellular Ca^{2+} fluctuation have been done using synthetic organic dyes that exhibit Ca^{2+}-dependent fluorescence changes. Three decades ago, this field was revolutionized by the work of Roger Y. Tsien and coworkers who developed a series of synthetic Ca^{2+} indicator dyes with nearly ideal fluorescence properties (*99*). Tsien and coworkers also invented a

non-invasive way to load synthetic dyes into the cells using acetoxymethyl ester. Since then, synthetic dye-based Ca^{2+} indicators have remained indispensable tools used by neuroscientists to optically record the neuronal activities in *ex vivo* tissues or within the brain of a living animal (*139-141*).

Unfortunately, a number of limitations exist for the use of synthetic dyes for neuroimaging in intact brain tissues. In some cases, it is difficult to load the cells with acetoxymethyl ester modified synthetic Ca^{2+} indicators. Loading of synthetic Ca^{2+} indicators does not work in some model organisms such as *Caenorhabditis elegans* or the fruit fly *Drosophila melanogaster (141).* In addition, there is essentially no cell type specificity for loading of synthetic dyes, therefore subcellular labeling in individual pre- or post-synaptic sites is impossible. Although the specificity of synthetic Ca^{2+} indicators can be improved using genetic methods, this has not been successfully demonstrated *in vivo (142)*. In addition, the dyes tend to leak out of the cells during long term imaging, which makes it impossible for chronic imaging of neuronal activities.

To address the shortcomings of synthetic dyes in neuroimaging, the Tsien lab developed the first GECI based on FP and FRET. This work, published in 1997, is a very important milestone in the field of bioimaging (*143*). GECIs offer a number of advantages for bioimaging compared to synthetic Ca^{2+} indicators. GECIs are proteins that can be encoded in the form of DNA and introduced to the genome of model organisms by various molecular biology approaches that make invasive microinjection approaches unnecessary. GECIs can be conveniently targeted to subcellular compartment as well as to specific cell types. In addition, GECIs exhibit low cytotoxicity and permit Ca^{2+} imaging over longer time periods compared to synthetic Ca^{2+} indicators. Because they are genetically encoded,

GECI properties such as binding affinity, response dynamic range and kinetics can be readily modified by protein engineering to improve or customize the performance for specific applications.

Although a variety of design strategies have been reported for GECIs (*92, 94, 95, 97, 143, 144*), only two sensing mechanisms have been widely used. These strategies are FRET (*i.e.*, Cameleons (*143*) and TN-XXL (*145*).) and Ca^{2+}-dependent modulation of chromophore pK_a of a single FP (*i.e.*, GCaMP (*95*), pericam (*92*), and GECOs (*108*)). Development and application of GECIs based on these two design mechanisms were discussed in the following sections.

1.3.1.1 FRET-based GECIs

Cameleons, the first generation of GECIs (*143*), are chimeric proteins consisting of a blue or cyan FP as a FRET donor and a green or yellow FP as a FRET acceptor. The two FPs are connected by CaM and its binding partner M13 (the CaM-binding domain of myosin light chain kinase) (**Figure 1.6**A). A similar design with only the CaM-binding domain was also reported in 1997, the same year as cameleon, but has not been widely used (*144*). When bound to Ca^{2+}, CaM changes its conformation and sequentially binds to M13, which results in a more compact conformation that decreases the distance between the FRET donor and acceptor. This decrease distance causes an increase in FRET efficiency that manifests itself as a decrease in donor intensity and an increase in acceptor intensity. A drawback of the first generation cameleon (cameleon-1) is that it only exhibited a 70% change in emission ratio upon binding to Ca^{2+}, which limited the signal-to-noise ratio and fidelity for detecting Ca^{2+} dynamics. In 1999, Miyawaki *et al.* developed an improved version of cameleon with larger Ca^{2+} response and

less pH sensitivity compared to cameleon-1. These improved cameleons could be used to image Ca^{2+} dynamics in hippocampal neurons (*146*). In 2004, Nagai *et al.* further improved the Ca^{2+} response of cameleon by optimizing the relative orientation of the two chromophores in the Ca^{2+} indicator using circularly permuted YFPs (cpYFPs). The best variant, termed yellow-cameleon 3.6 (YC3.6), is more efficient at accepting the excited state energy from CFP in the Ca^{2+}-bound state, thereby increasing the ratiometric Ca^{2+}-dependent fluorescent response to nearly 600% (*147*). In the same work, they also generated a transgenic mouse line expressing YC3.6, in which YC3.6 could be used to detect stimulated neural activities, although with reduced dynamic range relative to *in vitro* experiments. To date, YC3.6 remains one of the most popular GECIs for neural imaging. In 2010, Nagai and coworker engineered a high Ca^{2+} affinity version of cameleon called YC-nano with K_d values ranging from 15 nM to 140 nM and up to 1,450% Ca^{2+} dependent change in the ratio of YFP/CFP. Compared to traditional GECIs with lower Ca^{2+} affinities, YC-nano variants perform better in cells where the resting intracellular Ca^{2+} concentration is low and are capable of detecting subtle Ca^{2+} transients associated with intercellular signaling dynamics and neuronal activity (*148*).

Interference from intracellular proteins is a potential problem for GECIs based on CaM, because CaM is a ubiquitous signal protein that interacts with many kinases, phosphatases, and ion channels. The presence of intracellular proteins that can interact with calmodulin may interfere with the function of GECIs and lead to reduced or diminished dynamic range (*141*). In 2004, Griesbeck and coworkers engineered a new type of FRET-based GECI, called TN-L15, by replacing calmodulin with troponin C (TnC) that interact with fewer

endogenous proteins (*149*). In 2006, Mank *et al.* reported further improvements in the dynamic range and kinetics of TnC-based Ca^{2+} indicators by engineering the magnesium- and calcium-binding properties within the C-terminal lobe. The best variant to arise from that work, TN-XL, exhibits a highly reproducible fluorescence signal with fast rise and decay times, as demonstrated in the presynaptic motor neurons of transgenic flies (*150*). By deletion of low affinity N-terminal lobes, the same group obtained a further improved version of TnC-based GECIs, designated TN-XXL, with higher affinity to Ca^{2+}. They demonstrated the usefulness of TN-XXL for the chronic imaging in mouse brain *in vivo* (*145*). Very recently, Thestrup *et al.* developed a new FRET-based indicator 'Twitch', based on *Opsanus* troponin C, with reduced number of Ca^{2+}-binding sites compared to TN-XXL (*134*). They optimized the 'Twitch' indicator by combining a large functional screen in bacteria colonies with a secondary screen in rat hippocampus neuron culture. The optimized 'Twitch' indicator has performance comparable to a commonly used synthetic organic Ca^{2+} indicator dye Oregon Green Bapta-1-AM and enables detection of action potential in neurons and functional tracking of highly mobile T lymphocytes (*134*).

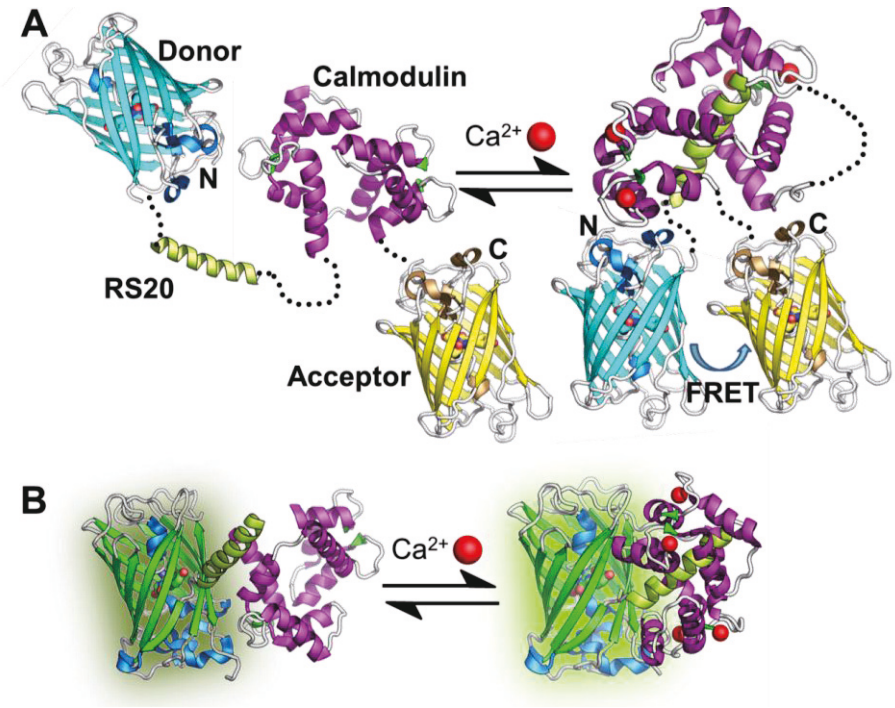

Figure 1.6 Schematic demonstration of genetically encoded Ca^{2+} indicators. (A) Models of FRET-based Ca^{2+} indicators based on Ca^{2+}-binding domains M13 and calmodulin. (B) Models of Single FP-based Ca^{2+} indicators. The models are based on crystal structure of GCaMP2 (PDB ID 3EK8 and 3EKU) (*122*).

1.3.1.2 Single FP-based indicators

In 1999, Baird *et al.* reported an interesting new approach for generating GECIs (*94*). In this work, they inserted calmodulin at the residue position 145 of an enhanced version of yellow FP (EYFP) and found that the EYFP-calmodulin insertion, dubbed 'camgaroo1', is a viable Ca^{2+} indicator for use in live cells. Camgaroo1 contains only a single FP and is the first example of single FP-based GECIs. Two years later, Griesbeck *et al.* engineered camgaroo2 based on an improved YFP (Citrine) with improved folding and reduced chloride and pH sensitivities (*119*).

Camgaroos are not useful for neural imaging since their Ca^{2+} affinity is 7 μM which is outside the normal physiologically range (50 to 5,000 nM (*137*)). However, the idea of converting a conformational change of a Ca^{2+} binding domain into a change in the environment of the FP chromophore was an important one that has served as the basis for many additional Ca^{2+} indicators with appropriate affinities and high dynamic range. In 2001, two research groups in Japan independently reported a variation on the camgaroo design that consisted of a FP, circularly permutated at position 148, with CaM and M13 fused at the C- and N-termini, respectively (**Figure 1.6**B). The resulting constructs, designated pericam (created by Nagai *et al* (*92*)) and GCaMP1 (created by Nakai *et al* (*95*)), both exhibit larger dynamic range and higher affinity to Ca^{2+} compared to camgaroos.

Compared to FRET-based cameleons, it is generally more difficult to engineer single FP-based GECIs. The difficulty stems from the fact that the sensing mechanism of single FP-based GECIs is not as conceptually obvious as FRET-based GECIs, in which the dynamic range and affinity can be tuned by replacing new FPs, adjusting the length of linkers and introducing mutations in CaM. In 2005, Reiff *et al.* briefly mentioned GCaMP1.3 and GCaMP1.6 in their comparative study on *in vivo* performance of available GECIs for probing neural activities in flies (*151*). They found the response characteristics of all tested indicators considerably differed from each other. GCaMP1.6 reported high rates of neural activity with the largest and fastest fluorescence changes, but suffered from photobleaching. On the other hand, an expanded range of neural activity evoked fairly linear fluorescence changes and a corresponding linear increase in the SNR of GCaMP1.3. In the same year, the second generation of GCaMP,

termed GCaMP2, was reported to be functional in a transgenic line of mice (*152*). To gain insight into the mechanism of GCaMP2, Wang *et al.* determined the X-ray crystal structure of GCaMP2 and found a sophisticated Ca^{2+} sensing mechanism (*121, 122*). Briefly, in the Ca^{2+}-bound state of GCaMP2, a key residue R377 in CaM is positioned near the fluorophore and stabilizes it in a deprotonated state similar to that observed in EGFP. The insight provided by this structure, and those of related variants, has greatly assisted the engineering of improved GCaMPs. In 2009, guided by the crystal structure of GCaMP2, Lin *et al.* engineered the third generation of GCaMP, GCaMP3 (*153*). Compared to other GECIs of that time, GCaMP3 exhibited several fold better Ca^{2+} response for imaging of neural activities in worms, flies and mice (*153*).

Although GECIs provide multiple advantages in imaging, the sensitivity and speed of available GECIs had not yet surpassed those of most commonly used synthetic Ca^{2+} indicators, such as Oregon Green Bapta-1-AM and fluo-4 (*154*). This situation has started to change. In 2013, GCaMP6, the latest version of GCaMP with further improvements in signal magnitude and SNR in neuronal cells (*133*), was reported by Chen *et al.*. The authors present evidence that GCaMP6 is the first GECI to surpass the performance of synthetic Ca^{2+} indicator for *in vivo* imaging.

Synthetic Ca^{2+} indicators generally have fluorescence change with response time constant less than 1 millisecond, which is much faster than GECIs. The slow kinetic response of GECIs limits their capacity for resolving high-frequency neuronal Ca^{2+} oscillation. To address this shortcoming, Sun *et al.* developed fast versions of GCaMPs, based on GCaMP3, which possess up to 20-fold accelerated off-responses (*155*). Fast GCaMPs have better performance for tracking Ca^{2+}

spikes in *Drosophila* auditory neurons responding to natural courtship songs and observing rapid Ca^{2+} responses in mammalian neurons compared to GCaMP3 and GCaMP5G (*155*).

1.3.1.3 Applications of Ca^{2+} imaging for neuronal activities using GECIs

Transgenic animals expressing GECIs

GECIs have unique advantages for loading populations of neurons in behaving animals. GECIs could be loaded by minimally invasive approaches, such as virus injection and in utero electroporation. In addition, transgenic animals expressing GECIs could be readily generated. The first Ca^{2+} imaging in behaving animals was done in 2000 by Kerr *et al.* using *C. elegans* (*138*) expressing a cameleon construct. The cameleons responded to electrically evoked Ca^{2+} transients in individual *C. elegans* neurons. In 2002, Fiala *et al.* reported the use of cameleon2.1 (*146*) in the *Drosophila* brain (*156*). They successfully visualized odorant-evoked intracellular Ca^{2+} concentration changes in selectively labeled olfactory projection neurons both postsynaptically in the antennal lobe (in the primary olfactory neuropil) and presynaptically in the mushroom body calyx (a structure involved in olfactory learning and memory) (*156*). In 2003, Yu *et al.* expressed two versions of camgaroo (*94*) in *Drosophila* mushroom bodies (*94, 157*). Wang *et al.* developed a sensitive imaging system for the *Drosophila* brain that couples two-photon microscopy with the specific expression of GCaMP (*158*). Liu *et al.* studied the function of thermosensory neurons in *Drosophila* larvae using a yellow cameleon YC2.1 (*159*).

In 2003, the first example of using GECIs in neural imaging in vertebrates was done in a stable transgenic line of zebrafish expressing cameleon YC2.1

(*160*). Up to that point, GECIs had been used for Ca^{2+} imaging only in worms and flies, and no one had yet demonstrated whether GECIs could detect Ca^{2+} transients in normally behaving vertebrates. In 2004, Hasan and Denk *et al* reported the production of stable transgenic mouse lines expressing camgaroo-2 and inverted pericam and both GECIs were functional for detecting neural activities in mouse brains (*161*). Later, mouse lines expressing GCaMP2 (*152*) and YC3.6 (*147*) were also reported. Transgenic animal lines expressing GECIs are now available to the research community. There are several public resources for interested users, including the Jackson laboratory (http://www.jax.org/index.html) and the Janelia farm GENIE project (http://research.janelia.org/genie/).

Neuronal circuit mapping and dynamics monitoring in defined cell classes

Fluorescence imaging using GECIs is a powerful approach for mapping neural connections and monitoring circuit dynamics in anatomical space. Using specific promoters, GECIs can be genetically targeted to a subset of the neuronal population, which allows researchers to identify sub-populations of neurons with specific functions and define their organization. For example, an improved transgenic mouse line expressing GCaMP2 in specific cell population was reported in 2007 by Díez-García and Knöpfel *et al.* (*162*) Using this mouse line, they characterized the function of synapses generated by parallel fibers in the cerebellum (*163, 164*). In a more recent study, a zebrafish line expressing GCaMP3 specifically in the spinal motor neurons was used to study the development of central pattern generators (*165*).

Genetically encoded indicators that are targeted to specific cell types can also help to reveal the maps in overlaid or intermingled neural circuits. For example,

Flecther *et al.* used GCaMP2 to image macroscopic pre- and post-synaptic sensory maps of the mouse olfactory bulb (*166, 167*). In the studies, they used synaptopHluorin (*127*), a genetically encoded indicator of synaptic release, to generate odor maps that represent the presynaptic activity of olfactory nerve terminals. Simultaneous fluorescence imaging of GCaMP2-expressing neurons that are synaptically excited by olfactory nerves provided postsynaptic odor maps of the olfactory bulb (*166, 167*).

GECIs also enable monitoring neural circuit dynamics. Recently, Harvey *et al.* used GCaMP3 and imaging at single-cell resolution which revealed that neurons in the posterior parietal cortex were sequentially activated when a mouse decided to take either the left or right path in a virtual environment while being cued as to which path will lead to a water reward (*168*).

Previous techniques only enable interrogation of neural circuits in a very small region of the brain, which are unlikely to reveal correlation of populations of neurons in distant regions. To properly understand the brain functions and behaviors, we need to examine neural activities in the intermediate or higher level of organization. Recording neuronal activities in the whole brain with single-cell resolution has been one of the most challenging objectives of modern neuroscience. Early in 2013, Ahrens *et al.* moved a big step toward this goal with the advance of light sheet microscopy technology (*169*). Using a Ca^{2+} indicator known as GCaMP5G (*170*), they successfully recorded neural activities from the whole brain of the larval zebrafish *in vivo*, and identified two populations of neurons in distant regions with correlated activity patterns and likely have important roles in swimming (*169*).

Chronic imaging of neuronal activities

Unlike synthetic dyes that leak out of cells over time after injection, the expression of GECIs can be stable for weeks to months or can even sustain for the complete life time of a transgenic animals, which make GECIs suitable for chronic imaging *in vivo*. For FRET-based GECIs, TN-XXL has been used for long-term *in vivo* imaging of Ca^{2+} response from visually stimulated layer 2/3 cortical neurons in mice (*145*). Virally expressed YC3.6 in mice was reported to successfully detect visual response from the same neurons during behavior response over one month (*171*). Similarly, YC3.6 was also used for mapping sensory response in mouse somatosensory cortex over several weeks (*172*). Studies have demonstrated the usefulness of single FP-based GECIs for long term *in vivo* imaging of neuronal activities in mouse brain such as mouse motor cortex[17] and CA1 neurons from the hippocampus (*173*) using GCaMP3. Long-term imaging of GCaMP3 has revealed learning-related circuit changes *(174)*. GCaMP6, the most state-of-art GECI to date, was used for long term imaging to monitor the organization and dynamic of neural circuit in mouse visual cortex (*133*).

1.3.2 Genetically encoded voltage indicators for imaging of neuronal activities

Compared to GECIs, genetically encoded voltage indicators (GEVIs) directly measure the most fundamental neuron signal, action potential, while GECIs probe slow Ca^{2+} signals that lag behind action potentials. In addition, GEVIs can measure subthreshold membrane potential fluctuation as well as hyperpolarization of neurons, which cannot lead to Ca^{2+} concentration change. However, in practice,

GECIs are more widely used for imaging of neuronal activities, whereas GEVIs are rarely used. Interestingly, synthetic organic Ca^{2+} indicators are also more widely used compared to synthetic organic voltage indicators. The challenge of using GEVIs for neuroimaging is two fold. From the perspective of probe, the currently available GECIs are generally more sensitive and brighter than GEVIs. In addition, since plasma membrane has much smaller volume than cytosol and therefore limits total amount of fluorophores, GEVIs are generally less sensitive and dimmer. The membrane tethered nature of GEVIs also makes them notoriously difficult to engineer. From an instrumental point of view, voltage imaging requires a very restricted integration time as membrane potentials generally rise within milliseconds, which significantly limits the available photons for each frame of acquisition and requires a much more expensive microscope system and camera compared to Ca^{2+} imaging. In the following section, we discussed the engineering of GEVIs and applications thereof as well as future directions.

The first GEVI, FlaSh (*93*), was reported in 1997, the same year as the first GECI cameleon. In the next five years, SPARC (*175*), VSFP (*176*) and improved FlaSh (*177*) were developed. They all belong to the first class of GEVIs, which utilize FPs as the fluorescence reporter. The early versions of this class utilize either the intact K^+ or Na^+ channels or their voltage sensing domains as the voltage sensing unit and couple the voltage-dependent conformation change into the modulation of fluorescence of FPs. However, they did not lead to wide usage because of the issues of poor membrane trafficking and cytotoxicity in neurons (*178*).

Advanced versions of VSFP were not available until the report of VSFP2s by Knöpfel and coworkers in 2007 (*130*). VSFP2 uses the voltage sensing domain of the sea squirt *Ciona intestinalis* voltage sensor-containing phosphatase to modulate FRET between donor and acceptor FPs and displays excellent membrane trafficking in mammalian cells. Although the dynamic range for voltage sensing is fairly small, VSFP2s are capable of monitoring electrical events of neurons, a milestone in the field of GEVIs. Improved versions of FRET-based VSFP and single FP-based VSFPs were developed (*131, 179-182*) throughout the following years, though without much success on improving the signal magnitude and SNR.

The small signal magnitudes and slow kinetics of VSFP-type GEVIs has limited their applications for monitoring neuronal electrical activity. In 2012, Pieribone and coworkers reported an advanced version of VSFP-type GEVI, ArcLight, and its derivatives which exhibit large changes in fluorescence intensity in response to voltage changes (*183*). ArcLight uses super ecliptic pHluorin as the fluorescent reporter. Strikingly, a single point mutation A227D dramatically improves the dynamic range for voltage sensing by 5 times. Although Arclight is still a slow probe, its large signal magnitude allows reliable detection of single action potentials and excitatory potentials in individual neurons and dendrites, thus becomes currently the most promising GEVIs for *in vivo* imaging.

The second class of GEVIs is hybrid 'hVOS' indicators (*184*) consisting of a membrane targeted GFP and a fluorescence quencher dipicrylamine (DPA). The fluorescence of membrane targeted GFP is modulated by the FRET between the FP and the DPA that migrates through the membrane bilayer depending on voltage. However, strictly speaking, hVOS is not completely genetically encoded

and requires a supplement of DPA, which is toxic to cells in high dosage. In addition, the distribution of DPA in tissue is difficult to control. Hence, the applications of the hVOS type GEVIs are limited.

Recently, a new class of GEVIs based on microbial rhodopsins has been developed by Cohen and coworkers (*129, 185*). Microbial rhodopsin-based GEVIs including proteorhodopsin and Archaerhodopsin-3, are integral membrane proteins consist of seven transmembrane alpha helixes. A retinal molecule binds to the apoprotein by forming a Schiff base carbon-nitrogen double bond with a lysine residue at the core of the protein, which constitutes the fluorescent chromophore. This new class of GEVIs exhibits different mechanism for voltage sensing from VSFP and hVOS type GEVIs. The pKa of the Schiff base is modulated by the electric field cross the membrane and thus leads to a change of the fluorescence. Arch-based fluorescent voltage indicators can express functionally in the plasma membrane of mammalian cells and are capable of resolving neuronal action potentials with high sensitivity and high SNR (*129*).

However, currently available Arch-based voltage indicators have a few disadvantages. First, illumination of the wild-type protein generated a hyperpolarizing photocurrent, as the wild-type protein is a light-driven proton pump. On the other hand, the fluorescent response of the mutant Arch D95N that does not generate photocurrent had a substantial slow component. Yet other drawbacks were that both Arch and Arch D95N were dim, with the brightness of Arch increasing as a nonlinear function of illumination intensity (*186*), and neither protein was trafficked efficiently to the plasma membrane. Although Gong *et al.* recently reported non-pumping mutants Arch EEN and Arch EEQ with improved voltage sensitivity, the issues of dim fluorescence and slow kinetics are still

unsolved and therefore the applications of Arch-based voltage indicators in intact brain tissues remain elusive.

Voltage imaging using GEVIs has been considered a promising approach to study neuronal activities at high spatial and temporal resolution in the era of light-based electrophysiology (*187*). However, few applications have been demonstrated to date, owing to the lack of GEVIs with desirable properties. Knöpfel and coworkers first demonstrated the feasibility of using GEVIs in the brain of mice *in vivo* (*132*). VSFP-based imaging successfully resolved synaptic potentials and action potentials from individual cells in cortical brain slices in single trials, with low SNRs (*132*). In the follow-up work, they developed VSFP-butterfly with maximum voltage sensitivity tuned around the resting potential of neurons. Using VSFP-butterfly, they were able to detect synaptic potentials from individual cells *in vivo* with higher SNR compared to previous generations of VSFP. Soon after the development of Arclight, Cao *et al.* (*188*) has reported a landmark work in optical *in vivo* voltage recordings. Using ArcLight^2, they successfully imaged the electrical activity of single neurons, subcellular compartments and populations of genetically targeted neurons in the intact brain of a living *Drosophila* fruit fly (*188*). Arclight provides a robust signal with sufficient SNR to decipher *in vivo* single electrical events, such as action potentials and hyperpolarization events in neurons, which are critical to understand neural computation processes.

1.3.3 Other genetically encoded indicators for imaging of neuronal activities

Synaptic transmission is essential for neurons to communicate with each other and process information flow in a neural network, and it is widely believed

that synapses play an important role in formation of memory (*189*). Therefore, probing synaptic transmission is as important as probing changes of the Ca^{2+} concentration and membrane potential in neurons. With appropriately chosen sensor domain, engineered genetically encoded fluorescent indicators could convert the processes of synaptic transmission into changes of fluorescent signal, and thus have drawn a lot of attention recently. There are different strategies to generate neurotransmission indicators. The most straightforward strategy aims to directly probe the concentration change of neurotransmitters during neurotransmission. Other strategies include coupling neurotransmitter binding events to other optical readouts and detection of pH changes in synaptic clefts due to the events of synaptic vehicle fusion.

Neurotransmitters are endogenous chemical compounds that transmit neural signals from one neuron to the other neural cells. Many neurotransmitters are amino acids, such as glutamate, glycine and GABA, or biogenic amines, such as dopamine and serotonin, or even peptides and proteins, such as somatostatin and substance P (*190*). Binding of neurotransmitters may either inhibit or excite the postsynaptic neurons. Among numerous neurotransmitters, glutamate is the major excitatory amino acid neurotransmitter in mammalian neural systems (*191*). The first genetically encoded neurotransmitter indicator was made in 2005 and could probe glutamate (*192*). Upon binding to glutamate, the indicator converts the allosteric change of a bacterial glutamate binding protein ybeJ (also known as GltI) into change of FRET signal (*192*). In the same year, a glutamate indicator GluSnFR with similar design was also reported by Tsien and coworkers (*193*). In 2008, Hire *et al.* optimized the performance of GluSnFR by systematic optimization of linker designs and glutamate affinities. The end product,

SuperGluSnFR, was demonstrated capable of quantitative optical measurements of the time course of synaptic glutamate release, spillover, and reuptake in cultured hippocampal neurons with centisecond temporal and spine-sized spatial resolution (*128*). In 2013, Marvin *et al.* reported the first single FP-based glutamate indicator iGluSnFR (*194*). iGluSnFR was engineered *in vitro* for maximized fluorescence response, and it could robustly detect glutamate releasing events with appropriate signal-to-noise ratio and kinetics for *in vivo* imaging in worms, zebrafishs and mice (*194*). Bacteria express a variety of periplasmic binding proteins for GABA, Ach, glycine and other small molecules that serve as neurotransmitter in the brain. A design principle similar to iGluSnFR may be promising to produce a series of genetically encoded indicators for probing various neurotransmitters in spine-sized spatial resolution.

Instead of probing the neurotransmitters directly, one could probe the neurotransmitter binding events by coupling it to a different optical observable using a multi-component system. Nguyen *et al.* described a multi-component system, called cell-based neurotransmitter fluorescent engineered reporters (CNiFERs), to monitor *in situ* neurotransmitter receptor activation (*195*). CNiFERs are engineered cultured cells that stably express an M1 Ach receptor and a GECI TN-XXL. The system utilizes the GPCR cascade to convert receptor activity into a rise in cytosolic Ca^{2+} which is reported by TN-XXL. Nguyen *et al.* injected CNiFERs in the frontal cortex of the adult rat and used CNiFERs to probe the change of cholinergic signaling induced by an atypical neuroleptic drug (*195*). Substitution of the M1 receptor with other Cys-loop receptors produced various versions of CNiFERs for serotonin and other neurotransmitters (*196*). The advantages of this system include modular design and signal amplification

through coupling to Ca^{2+}, but this system is not able to detect neurotransmission in spine-size spatial resolution and is too slow due to the nature of multi-component signaling cascade.

Another strategy to construct FP-based indicators for neurotransmission is to exploit the acidic pH inside secretory vesicles to visualize vesicle exocytosis and recycling in the synaptic clefts (*197*). In 1998, Miesenböck *et al.* generated a pH-sensitive mutant of GFP ('pHluorins') by structure-guided combinatorial mutagenesis. The authors fused pHluorins to a vesicle membrane protein (synaptophysin) and targeted pHluorins to secretory and synaptic vehicles. The targeted pHluorins, termed synapto-pHluorin, successfully reported transmission events at individual synaptic boutons, as well as secretion and fusion of single secretory granules (*109*). In 2002, Miesenböck and coworkers targeted synapto-pHluorin in the fly antennal lobe, where synapto-pHluorin enables functional imaging of olfactory circuits in *Drosophila (198)*. In 2004, Bozza *et al.* generated transgenic mice expressing synapto-pHluorin, which reports synaptic vesicle fusion in olfactory sensory neurons in mice. Furthermore, synapto-pHluorin selectively labeled presynaptic terminals of sensory neurons in glomeruli of the olfactory bulb and enables the analysis of previously inaccessible neuronal populations and chronic imaging from genetically identified neurons *in vivo* (*127*). Very recently, Li *et al.* developed a red version of genetically encoded indicators ('sypHTomato') for neurotransmission by fusing a red pH-sensitive FP ('pHTomato') to the vesicular membrane protein synaptophysin (*199*). Combined with green GECI GCaMP3, sypHTomato permits simultaneous imaging of Ca^{2+} and neurotransmitter release in neural networks (*199*).

Chloride ions (Cl^-) regulate multiple physiological functions, including regulation of cell volume, intracellular pH, fluid secretion, and maintenance of the resting membrane potential. For the perspective of neurotransmission, Cl^- is essential for inhibitory transmission as presynaptic release of GABA activates postsynaptic GABA receptors, leading to Cl^- fluxes that underlie synaptic inhibition. In 2000, Kuner *et al.* developed the first generation of genetically encoded chloride indicator, Clomeleon (*110*). Clomeleon is a fusion protein consisting of a Cl^--sensitive YFP and Cl^--insensitive CFP. YFP contains a Cl^- binding site close to the chromophore and has decreased fluorescent intensity upon binding to Cl^-. Therefore, Cl^- binding to YFP alters the FRET between CFP donor and YFP acceptor, which enables ratiometric imaging of intracellular Cl^- in neurons (*110*) and brain tissues (*200*). However, it is challenging to use Clomeleon to image GABA-induced Cl^- fluxes, as the affinity of Clomeleon (~100 mM) is far beyond the typical physiological range of intracellular Cl^- (5~6 mM) and its change (as large as 4 mM) for postsynaptic inhibitory transmission (*200*). To solve this issue, Grimley *et al.* tuned the halide affinity and fluorephore characteristic of YFP and developed the second generation of Cl^- indicator, SuperClomeleon (*201*). SuperClomeleon has a Cl^- affinity of 8.1 mM and can robustly detect inhibitory synaptic activity in single, cultured mouse neurons produced by exogenous GABA or inhibitory synaptic activity (*201*).

1.3.4 The challenges and perspective of genetically encoded indicators for imaging of neuronal activities

Optical interrogation of neuronal activities *in vivo* using genetically encoded indicators has been a highly promising methodology for neuroscientists who are

interested in studying neural circuits. However, practical issues have caused delay in acceptance of this methodology for neuroscientists. One hurdle is the requirement of combined knowledge and skills from multidiscipline, including electrophysiology, genetics and imaging technology. Fortunately, this issue is being overcome by the rapidly growing choices of transgenic animal lines expressing various genetically encoded indicators, as well as by commercial virus production services, which release researchers from the tedious and time-consuming processes for making their own transgenic animal lines or the virus for gene delivery.

Despite the rapid progress of this field, it is clear that the overall performance of genetically encoded indicators is still far below the standard required as practical tools for neuroscientists. It requires significant improvement of the properties of genetically encoded indicators, including brightness, response kinetics and magnitude, photostability and selectivity, to surpass the performance of established synthetic organic indicators. The performance gap between GECIs and GEVIs also needs to be eliminated by developing GEVIs based on novel mechanisms that are fundamentally fast and sensitive to better probe membrane potential changes.

In addition, light scattering imposes severe constrains for imaging of neuronal activities in deep tissues. Since near-infrared light can penetrate deeper in scattering medium, the scattering problems could be alleviated by developing indicators with further red-shifted wavelength toward near-infrared regime.

It is also challenging to develop imaging systems that are capable of imaging of neuronal activities in a large volume of brain tissue with single-cell level of

spatial resolution and millisecond acquisition speed. Hopefully, this goal can be achieved by improvement of imaging modalities, such as digital light sheet microscopy (*202*), rapid automated modular microscope, aberration-corrected multifocus microscopy (*203*), Spatial Light Modulator microscopy (*204*), as well as advances making faster and more sensitive cameras, new excitation sources and improved imaging software. While light scattering severely limits optical imaging of neuronal activities in deep brain tissue, instrumental strategies which could potentially sidestep the scattering problems (*205*) are available. These include miniaturized optical devices embedded near the brain region of interest (*206-208*), multiphoton imaging (*55*), and online inversion of the scattering matrix (*209*). We believe that, with the advance of genetically encoded indicators and imaging technologies, neuroscience can be enlightened in the era of light.

1.4 Scope of my thesis

The objectives of my thesis focus on developing protein-engineering methodologies that could lead to improved FP-based Ca^{2+} indicators and voltage indicators. Among various protein engineering approaches, directed evolution approaches would be preferable, since rational designs are difficult due to the generally limited information on the structural-function relationships for FP-based indicators. To date, only a few crystal structures of genetically encoded indicators have been reported (*122, 170, 210*), and they are almost exclusively for single FP-based Ca^{2+} indicators. Directed evolution introduces random mutations in the protein sequence and mimics the iterative natural selection of proteins for specific properties. This procedure does not require detail knowledge about the protein of

interest. The general workflow of directed evolution used in my thesis work is summarized in Figure 1.7.

In Chapter 2, I describe the development of a novel directed evolution strategy for improved single FP-based Ca^{2+} indicators with various hues. This work led to an expanded palette of genetically encoded calcium indicators and opened the door for multi-color calcium imaging, which was previously impractical. In Chapter 3, I apply microfluidic technology to accelerate our directed evolution approach and develop a new screening strategy with higher throughput compared to the traditional approach. With this strategy, I successfully developed a yellow FP-based calcium indicator that adds a new color in the current palette of FP-based calcium indicators. In Chapter 4, the focus switches from genetically encoded calcium indicators to the state-of-the-art microbial rhodopsin-based voltage indicator Arch. I designed a new strategy for directed evolution of Arch variants with improved properties. The best Arch variants from the directed evolution exhibit superior performance in neural cells compared to the original version.

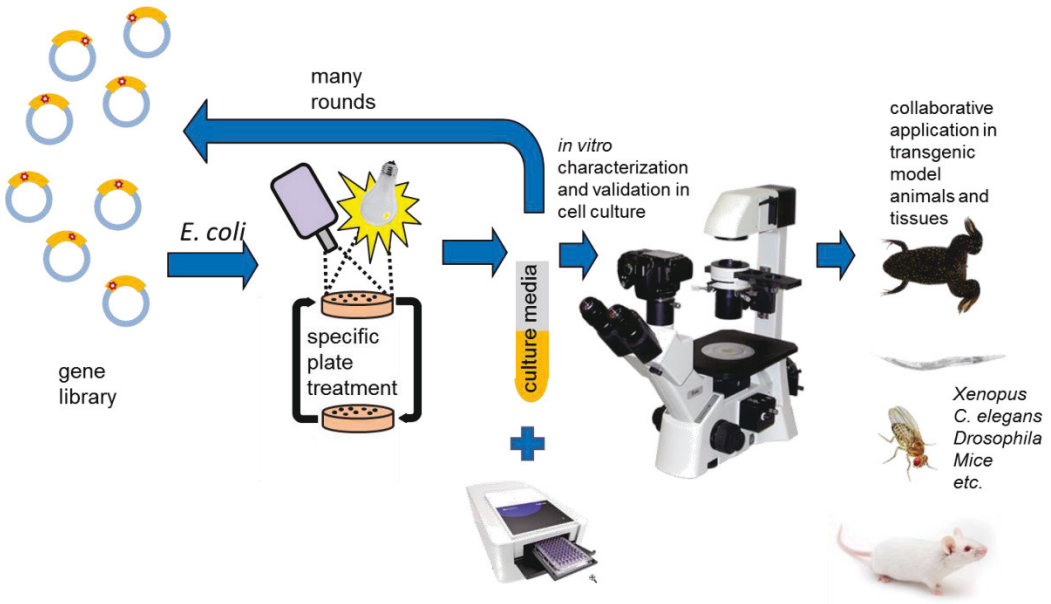

Figure 1.7 General scheme of directed evolution for evolving improved genetically encoded fluorescent indicators.

1.5 References

1. O. Shimomura, F. H. Johnson, Y. Saiga, Extraction, Purification and Properties of Aequorin, a Bioluminescent Protein from the Luminous Hydromedusan, Aequorea. *Journal of Cellular and Comparative Physiology* **59**, 223 (1962).
2. M. Ormö *et al.*, Crystal structure of the Aequorea victoria green fluorescent protein. *Science* **273**, 1392 (1996).
3. R. Y. Tsien, The green fluorescent protein. *Annual Review of Biochemistry* **67**, 509 (1998).
4. M. Chalfie, Y. Tu, G. Euskirchen, W. W. Ward, D. C. Prasher, Green Fluorescent Protein as a Marker for Gene-Expression. *Science* **263**, 802 (1994).

5. S. Inouye, F. I. Tsuji, Aequorea green fluorescent protein: Expression of the gene and fluorescence characteristics of the recombinant protein. *FEBS Letters* **341**, 277 (1994).

6. O. Shimomura, Structure of the chromophore of Aequorea green fluorescent protein. *FEBS Letters* **104**, 220 (1979).

7. N. P. Lemay *et al.*, The Role of the Tight-Turn, Broken Hydrogen Bonding, Glu222 and Arg96 in the Post-translational Green Fluorescent Protein Chromophore Formation. *Chemical physics* **348**, 152 (2008).

8. R. Heim, D. C. Prasher, R. Y. Tsien, Wavelength mutations and posttranslational autoxidation of green fluorescent protein. *Proceedings of the National Academy of Sciences of the United States of America* **91**, 12501 (1994).

9. A. B. Cubitt *et al.*, Understanding, improving and using green fluorescent proteins. *Trends in Biochemical Sciences* **20**, 448 (1995).

10. R. M. Wachter, J. L. Watkins, H. Kim, Mechanistic Diversity of Red Fluorescence Acquisition by GFP-like Proteins. *Biochemistry* **49**, 7417 (2010).

11. B. G. Reid, G. C. Flynn, Chromophore Formation in Green Fluorescent Protein. *Biochemistry* **36**, 6786 (1997).

12. D. P. Barondeau, C. D. Putnam, C. J. Kassmann, J. A. Tainer, E. D. Getzoff, Mechanism and energetics of green fluorescent protein chromophore synthesis revealed by trapped intermediate structures. *Proceedings of the National Academy of Sciences of the United States of America* **100**, 12111 (2003).

13. M. A. Rosenow, H. A. Huffman, M. E. Phail, R. M. Wachter, The Crystal Structure of the Y66L Variant of Green Fluorescent Protein Supports a Cyclization−Oxidation−Dehydration Mechanism for Chromophore Maturation†,‡. *Biochemistry* **43**, 4464 (2004).

14. J. Petersen *et al.*, The 2.0-Å Crystal Structure of eqFP611, a Far Red Fluorescent Protein from the Sea Anemone Entacmaea quadricolor. *Journal of Biological Chemistry* **278**, 44626 (2003).

15. F. V. Subach, V. V. Verkhusha, Chromophore Transformations in Red Fluorescent Proteins. *Chemical Reviews* **112**, 4308 (2012).

16. A. Miyawaki, D. M. Shcherbakova, V. V. Verkhusha, Red fluorescent proteins: chromophore formation and cellular applications. *Current Opinion in Structural Biology* **22**, 679 (2012).

17. V. V. Verkhusha, D. M. Chudakov, N. G. Gurskaya, S. Lukyanov, K. A. Lukyanov, Common Pathway for the Red Chromophore Formation in Fluorescent Proteins and Chromoproteins. *Chemistry & Biology* **11**, 845 (2004).

18. R. L. Strack, D. E. Strongin, L. Mets, B. S. Glick, R. J. Keenan, Chromophore Formation in DsRed Occurs by a Branched Pathway. *Journal of the American Chemical Society* **132**, 8496 (2010).

19. S. Pletnev, F. V. Subach, Z. Dauter, A. Wlodawer, V. V. Verkhusha, Understanding Blue-to-Red Conversion in Monomeric Fluorescent Timers and Hydrolytic Degradation of Their Chromophores. *Journal of the American Chemical Society* **132**, 2243 (2010).

20. L. A. Gross, G. S. Baird, R. C. Hoffman, K. K. Baldridge, R. Y. Tsien, The structure of the chromophore within DsRed, a red fluorescent protein

from coral. *Proceedings of the National Academy of Sciences of the United States of America* **97**, 11990 (2000).

21. O. M. Subach, P. J. Cranfill, M. W. Davidson, V. V. Verkhusha, An Enhanced Monomeric Blue Fluorescent Protein with the High Chemical Stability of the Chromophore. *PLoS ONE* **6**, e28674 (2011).

22. M. Cotlet *et al.*, Identification of different emitting species in the red fluorescent protein DsRed by means of ensemble and single-molecule spectroscopy. *Proceedings of the National Academy of Sciences of the United States of America* **98**, 14398 (2001).

23. P. Dedecker, F. C. De Schryver, J. Hofkens, Fluorescent Proteins: Shine on, You Crazy Diamond. *Journal of the American Chemical Society* **135**, 2387 (2013).

24. S. H. Bokman, W. W. Ward, Renaturation of Aequorea green-fluorescent protein. *Biochemical and Biophysical Research Communications* **101**, 1372 (1981).

25. S. R. Meech, Excited state reactions in fluorescent proteins. *Chemical Society Reviews* **38**, 2922 (2009).

26. L. M. Tolbert, A. Baldridge, J. Kowalik, K. M. Solntsev, Collapse and Recovery of Green Fluorescent Protein Chromophore Emission through Topological Effects. *Accounts of Chemical Research* **45**, 171 (2011).

27. H. Niwa *et al.*, Chemical nature of the light emitter of the Aequorea green fluorescent protein. *Proceedings of the National Academy of Sciences of the United States of America* **93**, 13617 (1996).

28. K. L. Litvinenko, N. M. Webber, S. R. Meech, An ultrafast polarisation spectroscopy study of internal conversion and orientational relaxation of

the chromophore of the green fluorescent protein. *Chemical Physics Letters* **346**, 47 (2001).

29. N. M. Webber, K. L. Litvinenko, S. R. Meech, Radiationless Relaxation in a Synthetic Analogue of the Green Fluorescent Protein Chromophore. *The Journal of Physical Chemistry B* **105**, 8036 (2001).

30. M. Vengris *et al.*, Ultrafast Excited and Ground-State Dynamics of the Green Fluorescent Protein Chromophore in Solution. *The Journal of Physical Chemistry A* **108**, 4587 (2004).

31. S. S. Stavrov, K. M. Solntsev, L. M. Tolbert, D. Huppert, Probing the Decay Coordinate of the Green Fluorescent Protein: Arrest of Cis−Trans Isomerization by the Protein Significantly Narrows the Fluorescence Spectra. *Journal of the American Chemical Society* **128**, 1540 (2006).

32. W. W. Ward, H. J. Prentice, A. F. Roth, C. W. Cody, S. C. Reeves, Spectral perturbations of the aequorea green-fluorescent protein. *Photochemistry and Photobiology* **35**, 803 (1982).

33. H.-w. Ai, N. C. Shaner, Z. Cheng, R. Y. Tsien, R. E. Campbell, Exploration of New Chromophore Structures Leads to the Identification of Improved Blue Fluorescent Proteins†. *Biochemistry* **46**, 5904 (2007).

34. M. Chattoraj, B. A. King, G. U. Bublitz, S. G. Boxer, Ultra-fast excited state dynamics in green fluorescent protein: multiple states and proton transfer. *Proceedings of the National Academy of Sciences of the United States of America* **93**, 8362 (1996).

35. K. Brejc *et al.*, Structural basis for dual excitation and photoisomerization of the Aequorea victoria green fluorescent protein. *Proceedings of the*

National Academy of Sciences of the United States of America **94**, 2306 (1997).

36. T. Kogure, H. Kawano, Y. Abe, A. Miyawaki, Fluorescence imaging using a fluorescent protein with a large Stokes shift. *Methods* **45**, 223 (2008).

37. K. D. Piatkevich *et al.*, Monomeric red fluorescent proteins with a large Stokes shift. *Proceedings of the National Academy of Sciences of the United States of America* **107**, 5369 (2010).

38. D. M. Shcherbakova, M. A. Hink, L. Joosen, T. W. J. Gadella, V. V. Verkhusha, An Orange Fluorescent Protein with a Large Stokes Shift for Single-Excitation Multicolor FCCS and FRET Imaging. *Journal of the American Chemical Society* **134**, 7913 (2012).

39. S. F. Field, M. V. Matz, Retracing evolution of red fluorescence in GFP-like proteins from Faviina corals. *Molecular Biology and Evolution* **27**, 225 (2010).

40. H. Mizuno *et al.*, Light-dependent regulation of structural flexibility in a photochromic fluorescent protein. *Proceedings of the National Academy of Sciences of the United States of America* **105**, 9227 (2008).

41. B. P. Cormack, R. H. Valdivia, S. Falkow, FACS-optimized mutants of the green fluorescent protein (GFP). *Gene* **173**, 33 (1996).

42. A. Crameri, E. A. Whitehorn, E. Tate, W. P. C. Stemmer, Improved Green Fluorescent Protein by Molecular Evolution Using DNA Shuffling. *Nature Biotechnology* **14**, 315 (1996).

43. R. Heim, A. B. Cubitt, R. Y. Tsien, Improved green fluorescence. *Nature* **373**, 663 (1995).

44. A. S. Mishin *et al.*, The First Mutant of the Aequorea victoria Green Fluorescent Protein That Forms a Red Chromophore†. *Biochemistry* **47**, 4666 (2008).

45. M. V. Matz *et al.*, Fluorescent proteins from nonbioluminescent Anthozoa species. *Nature Biotechnology* **17**, 969 (1999).

46. J. Wiedenmann *et al.*, A far-red fluorescent protein with fast maturation and reduced oligomerization tendency from Entacmaea quadricolor (Anthozoa, Actinaria). *Proceedings of the National Academy of Sciences of the United States of America* **99**, 11646 (2002).

47. N. C. Deliolanis *et al.*, Performance of the red-shifted fluorescent proteins in deep-tissue molecular imaging applications. *Journal of Biomedical Optics* **13**, 044008 (2008).

48. R. Weissleder, A clearer vision for *in vivo* imaging. *Nature Biotechnology* **19**, 316 (2001).

49. V. Ntziachristos, Fluorescence Molecular Imaging. *Annual Review of Biomedical Engineering* **8**, 1 (2006).

50. M. W. Davidson, R. E. Campbell, Engineered fluorescent proteins: innovations and applications. *Nature Methods* **6**, 713 (2009).

51. D. M. Shcherbakova, O. M. Subach, V. V. Verkhusha, Red Fluorescent Proteins: Advanced Imaging Applications and Future Design. *Angewandte Chemie International Edition* **51**, 10724 (2012).

52. D. Shcherbo *et al.*, Near-infrared fluorescent proteins. *Nature Methods* **7**, 827 (2010).

53. D. M. Shcherbakova, V. V. Verkhusha, Near-infrared fluorescent proteins for multicolor *in vivo* imaging. *Nature Methods* **10**, 751 (2013).

54. M. Drobizhev, N. S. Makarov, S. E. Tillo, T. E. Hughes, A. Rebane, Two-photon absorption properties of fluorescent proteins. *Nature Methods* **8**, 393 (2011).

55. P. T. C. So, C. Y. Dong, B. R. Masters, K. M. Berland, Two-photon excitation fluorescence microscopy. *Annual Review of Biomedical Engineering* **2**, 399 (2000).

56. D. A. Shagin *et al.*, GFP-like proteins as ubiquitous metazoan superfamily: evolution of functional features and structural complexity. *Molecular biology and evolution* **21**, 841 (2004).

57. M. V. Matz *et al.*, Fluorescent proteins from nonbioluminescent Anthozoa species. *Nature biotechnology* **17**, 969 (1999).

58. D. Yarbrough, R. M. Wachter, K. Kallio, M. V. Matz, S. J. Remington, Refined crystal structure of DsRed, a red fluorescent protein from coral, at 2.0-angstrom resolution. *Proceedings of the National Academy of Sciences of the United States of America* **98**, 462 (2001).

59. U. Lauf, P. Lopez, M. M. Falk, Expression of fluorescently tagged connexins: a novel approach to rescue function of oligomeric DsRed-tagged proteins. *FEBS letters* **498**, 11 (2001).

60. P. Gavin, R. J. Devenish, M. Prescott, An approach for reducing unwanted oligomerisation of DsRed fusion proteins. *Biochemical and biophysical research communications* **298**, 707 (2002).

61. A. Soling, A. Simm, N. Rainov, Intracellular localization of Herpes simplex virus type 1 thymidine kinase fused to different fluorescent proteins depends on choice of fluorescent tag. *FEBS letters* **527**, 153 (2002).

62. Y. G. Yanushevich *et al.*, A strategy for the generation of non-aggregating mutants of Anthozoa fluorescent proteins. *FEBS Letters* **511**, 11 (2002).

63. R. E. Campbell *et al.*, A monomeric red fluorescent protein. *Proceedings of the National Academy of Sciences of the United States of America* **99**, 7877 (2002).

64. H. W. Ai, J. N. Henderson, S. J. Remington, R. E. Campbell, Directed evolution of a monomeric, bright and photostable version of Clavularia cyan fluorescent protein: structural characterization and applications in fluorescence imaging. *The Biochemical journal* **400**, 531 (2006).

65. G. H. Patterson, J. Lippincott-Schwartz, A photoactivatable GFP for selective photolabeling of proteins and cells. *Science* **297**, 1873 (2002).

66. N. C. Shaner *et al.* Evaluating and improving the photostability of fluorescent proteins, *Proceedings of the SPIE* (2009), vol. 7191, pp. 719105-719105-11.

67. N. C. Shaner *et al.*, Improving the photostability of bright monomeric orange and red fluorescent proteins. *Nature Methods* **5**, 545 (2008).

68. N. C. Shaner, G. H. Patterson, M. W. Davidson, Advances in fluorescent protein technology. *Journal of Cell Science* **120**, 4247 (2007).

69. N. C. Shaner *et al.*, Improved monomeric red, orange and yellow fluorescent proteins derived from Discosoma sp. red fluorescent protein. *Nature Biotechnology* **22**, 1567 (2004).

70. J. L. Lubbeck, K. M. Dean, H. Ma, A. E. Palmer, R. Jimenez, Microfluidic flow cytometer for quantifying photobleaching of fluorescent proteins in cells. *Analytical Chemistry* **84**, 3929 (2012).

71. D. Shcherbo *et al.*, Far-red fluorescent tags for protein imaging in living tissues. *Biochem. J* **418**, 567 (2009).

72. R. Ando, H. Mizuno, A. Miyawaki, Regulated fast nucleocytoplasmic shuttling observed by reversible protein highlighting. *Science* **306**, 1370 (2004).

73. C. C. David *et al.*, Spectroscopic characterization of Venus at the single molecule level. *Photochemical & Photobiological Sciences* **11**, 358 (2012).

74. J. S. Marchant, G. E. Stutzmann, M. A. Leissring, F. M. LaFerla, I. Parker, Multiphoton-evoked color change of DsRed as an optical highlighter for cellular and subcellular labeling. *Nature Biotechnology* **19**, 645 (2001).

75. A. M. Bogdanov *et al.*, Green fluorescent proteins are light-induced electron donors. *Nature Chemical Biology* **5**, 459 (2009).

76. H. Hoi *et al.*, A monomeric photoconvertible fluorescent protein for imaging of dynamic protein localization. *Journal of Molecular Biology* **401**, 776 (2010).

77. G.-J. Kremers, K. L. Hazelwood, C. S. Murphy, M. W. Davidson, D. W. Piston, Photoconversion in orange and red fluorescent proteins. *Nature Methods* **6**, 355 (2009).

78. F. V. Subach, K. D. Piatkevich, V. V. Verkhusha, Directed molecular evolution to design advanced red fluorescent proteins. *Nature Methods* **8**, 1019 (2011).

79. H. Hoi *et al.*, An Engineered Monomeric Zoanthus sp. Yellow Fluorescent Protein. *Chemistry & Biology* **20**, 1296 (2013).

80. H.-w. Ai, S. Olenych, P. Wong, M. Davidson, R. Campbell, Hue-shifted monomeric variants of Clavularia cyan fluorescent protein: identification of the molecular determinants of color and applications in fluorescence imaging. *BMC Biology* **6**, 13 (2008).

81. J.-D. Pédelacq, S. Cabantous, T. Tran, T. C. Terwilliger, G. S. Waldo, Engineering and characterization of a superfolder green fluorescent protein. *Nature Biotechnology* **24**, 79 (2005).

82. J. Goedhart *et al.*, Bright cyan fluorescent protein variants identified by fluorescence lifetime screening. *Nature Methods* **7**, 137 (2010).

83. T. Grotjohann *et al.*, Diffraction-unlimited all-optical imaging and writing with a photochromic GFP. *Nature* **478**, 204 (2011).

84. H. Hoi *et al.*, An Engineered Monomeric Zoanthus sp. Yellow Fluorescent Protein. *Chemistry and Biology*.

85. K. M. Esvelt, J. C. Carlson, D. R. Liu, A system for the continuous directed evolution of biomolecules. *Nature* **472**, 499 (2011).

86. J. J. Agresti *et al.*, Ultrahigh-throughput screening in drop-based microfluidics for directed evolution. *Proceedings of the National Academy of Sciences of the United States of America* **107**, 4004 (2010).

87. J. L. Lubbeck, K. M. Dean, L. M. Davis, A. E. Palmer, R. Jimenez, A Microfluidic Cell Sorter for Directed Evolution of Fluorescent Proteins Based on Dark-State Conversion and Photobleaching. *Biophysical Journal* **100**, 175a (2011).

88. L. M. Davis, J. L. Lubbeck, K. M. Dean, A. E. Palmer, R. Jimenez, Microfluidic cell sorter for use in developing red fluorescent proteins with improved photostability. *Lab on a Chip* **13**, 2320 (2013).

89. S. C. Alford, J. Wu, Y. Zhao, R. E. Campbell, T. Knöpfel, Optogenetic reporters. *Biology of the Cell* **105**, 14 (2013).

90. T. K. Kerppola, Bimolecular fluorescence complementation (BiFC) analysis as a probe of protein interactions in living cells. *Annual review of biophysics* **37**, 465 (2008).

91. I. Ghosh, A. D. Hamilton, L. Regan, Antiparallel leucine zipper-directed protein reassembly: application to the green fluorescent protein. *Journal of the American Chemical Society* **122**, 5658 (2000).

92. T. Nagai, A. Sawano, E. S. Park, A. Miyawaki, Circularly permuted green fluorescent proteins engineered to sense Ca^{2+}. *Proceedings of the National Academy of Sciences of the United States of America* **98**, 3197 (2001).

93. M. S. Siegel, E. Y. Isacoff, A Genetically Encoded Optical Probe of Membrane Voltage. *Neuron* **19**, 735 (1997).

94. G. S. Baird, D. A. Zacharias, R. Y. Tsien, Circular permutation and receptor insertion within green fluorescent proteins. *Proceedings of the National Academy of Sciences of the United States of America* **96**, 11241 (1999).

95. J. Nakai, M. Ohkura, K. Imoto, A high signal-to-noise Ca^{2+} probe composed of a single green fluorescent protein. *Nature Biotechnology* **19**, 137 (2001).

96. K. Saito *et al.*, Luminescent proteins for high-speed single-cell and whole-body imaging. *Nature Communication* **3**, 1262 (2012).

97. Spencer C. Alford, Ahmed S. Abdelfattah, Y. Ding, Robert E. Campbell, A Fluorogenic Red Fluorescent Protein Heterodimer. *Chemistry & Biology* **19**, 353 (2012).

98. S. C. Alford, Y. Ding, T. Simmen, R. E. Campbell, Dimerization-Dependent Green and Yellow Fluorescent Proteins. *ACS Synthetic Biology* **1**, 569 (2012).

99. G. Grynkiewicz, M. Poenie, R. Y. Tsien, A new generation of Ca^{2+} indicators with greatly improved fluorescence properties. *Journal of Biological Chemistry* **260**, 3440 (1985).

100. C. Wu *et al.*, *In vivo* far-red luminescence imaging of a biomarker based on BRET from Cypridina bioluminescence to an organic dye. *Proceedings of the National Academy of Sciences of the United States of America* **106**, 15599 (2009).

101. T. K. Kerppola, Bimolecular fluorescence complementation (BiFC) analysis as a probe of protein interactions in living cells. *Annual review of biophysics* **37**, 465 (2008).

102. J. Chu *et al.*, A novel far-red bimolecular fluorescence complementation system that allows for efficient visualization of protein interactions under physiological conditions. *Biosensors and Bioelectronics* **25**, 234 (2009).

103. J.-Y. Fan *et al.*, Split mCherry as a new red bimolecular fluorescence complementation system for visualizing protein–protein interactions in living cells. *Biochemical and Biophysical Research Communications* **367**, 47 (2008).

104. G. Jach, M. Pesch, K. Richter, S. Frings, J. F. Uhrig, An improved mRFP1 adds red to bimolecular fluorescence complementation. *Nature Methods* **3**, 597 (2006).

105. K. Ohashi, T. Kiuchi, K. Shoji, K. Sampei, K. Mizuno, Visualization of cofilin-actin and Ras-Raf interactions by bimolecular fluorescence

complementation assays using a new pair of split Venus fragments. *BioTechniques* **52**, 45 (2012).

106. Y. J. Shyu, H. Liu, X. Deng, C. Hu, Identification of new fluorescent protein fragments for biomolecular fluorescence complementation analysis under physiological conditions. *BioTechniques* **40**, 61 (2006).

107. C.-D. Hu, Y. Chinenov, T. K. Kerppola, Visualization of Interactions among bZIP and Rel Family Proteins in Living Cells Using Bimolecular Fluorescence Complementation. *Molecular Cell* **9**, 789 (2002).

108. Y. Zhao *et al.*, An Expanded Palette of Genetically Encoded Ca^{2+} Indicators. *Science* **333**, 1888 (2011).

109. G. Miesenbock, D. A. De Angelis, J. E. Rothman, Visualizing secretion and synaptic transmission with pH-sensitive green fluorescent proteins. *Nature* **394**, 192 (1998).

110. T. Kuner, G. J. Augustine, A Genetically Encoded Ratiometric Indicator for Chloride: Capturing Chloride Transients in Cultured Hippocampal Neurons. *Neuron* **27**, 447 (2000).

111. P. Eli, A. Chakrabartty, Variants of DsRed fluorescent protein: Development of a copper sensor. *Protein Science* **15**, 2442 (2006).

112. G. T. Hanson *et al.*, Investigating mitochondrial redox potential with redox-sensitive green fluorescent protein indicators. *Journal of Biological Chemistry* **279**, 13044 (2004).

113. C. T. Dooley *et al.*, Imaging dynamic redox changes in mammalian cells with green fluorescent protein indicators. *Journal of Biological Chemistry* **279**, 22284 (2004).

114. H. Østergaard, A. Henriksen, F. G. Hansen, J. R. Winther, Shedding light on disulfide bond formation: engineering a redox switch in green fluorescent protein. *The EMBO Journal* **20**, 5853 (2001).

115. S. Tang *et al.*, Design and application of a class of sensors to monitor Ca^{2+} dynamics in high Ca^{2+} concentration cellular compartments. *Proceedings of the National Academy of Sciences of the United States of America* **108**, 16265 (2011).

116. S. Chen, Z.-j. Chen, W. Ren, H.-w. Ai, Reaction-Based Genetically Encoded Fluorescent Hydrogen Sulfide Sensors. *Journal of the American Chemical Society* **134**, 9589 (2012).

117. Z.-j. Chen, W. Ren, Q. E. Wright, H.-w. Ai, Genetically Encoded Fluorescent Probe for the Selective Detection of Peroxynitrite. *Journal of the American Chemical Society* **135**, 14940 (2013).

118. S. Topell, J. Hennecke, R. Glockshuber, Circularly permuted variants of the green fluorescent protein. *FEBS Letters* **457**, 283 (1999).

119. O. Griesbeck, G. S. Baird, R. E. Campbell, D. A. Zacharias, R. Y. Tsien, Reducing the Environmental Sensitivity of Yellow Fluorescent Protein: MECHANISM AND APPLICATIONS. *Journal of Biological Chemistry* **276**, 29188 (2001).

120. J. Nakai, M. Ohkura, K. Imoto, A high signal-to-noise Ca^{2+} probe composed of a single green fluorescent protein. *Nat Biotech* **19**, 137 (2001).

121. Q. Wang, B. Shui, M. I. Kotlikoff, H. Sondermann, Structural Basis for Calcium Sensing by GCaMP2. *Structure* **16**, 1817 (2008).

122. J. Akerboom *et al.*, Crystal Structures of the GCaMP Calcium Sensor Reveal the Mechanism of Fluorescence Signal Change and Aid Rational Design. *Journal of Biological Chemistry* **284**, 6455 (2009).

123. F. Helmchen, W. Denk, Deep tissue two-photon microscopy. *Nature Methods* **2**, 932 (2005).

124. G. Miesenböck, I. G. Kevrekidis, Optical imaging and control of genetically designated neurons in functioning circuits. *Annual Review of Neuroscience* **28**, 533 (2005).

125. K. Svoboda, R. Yasuda, Principles of Two-Photon Excitation Microscopy and Its Applications to Neuroscience. *Neuron* **50**, 823 (2006).

126. P. Marcaggi, H. Mutoh, D. Dimitrov, M. Beato, T. Knöpfel, Optical measurement of mGluR1 conformational changes reveals fast activation, slow deactivation, and sensitization. *Proceedings of the National Academy of Sciences* **106**, 11388 (2009).

127. T. Bozza, J. P. McGann, P. Mombaerts, M. Wachowiak, *In vivo* Imaging of Neuronal Activity by Targeted Expression of a Genetically Encoded Probe in the Mouse. *Neuron* **42**, 9 (2004).

128. S. A. Hires, Y. Zhu, R. Y. Tsien, Optical measurement of synaptic glutamate spillover and reuptake by linker optimized glutamate-sensitive fluorescent reporters. *Proceedings of the National Academy of Sciences* **105**, 4411 (2008).

129. J. M. Kralj, A. D. Douglass, D. R. Hochbaum, D. Maclaurin, A. E. Cohen, Optical recording of action potentials in mammalian neurons using a microbial rhodopsin. *Nature Methods* **9**, 90 (2012).

130. D. Dimitrov *et al.*, Engineering and Characterization of an Enhanced Fluorescent Protein Voltage Sensor. *PLoS ONE* **2**, e440 (2007).

131. H. Tsutsui, S. Karasawa, Y. Okamura, A. Miyawaki, Improving membrane voltage measurements using FRET with new fluorescent proteins. *Nat Meth* **5**, 683 (2008).

132. W. Akemann, H. Mutoh, A. Perron, J. Rossier, T. Knopfel, Imaging brain electric signals with genetically targeted voltage-sensitive fluorescent proteins. *Nature Methods* **7**, 643 (2010).

133. T.-W. Chen *et al.*, Ultrasensitive fluorescent proteins for imaging neuronal activity. *Nature* **499**, 295 (2013).

134. T. Thestrup *et al.*, Optimized ratiometric calcium sensors for functional *in vivo* imaging of neurons and T lymphocytes. *Nature Methods* **advance online publication**, (2014).

135. J. Wu *et al.*, Improved Orange and Red Ca^{2+} Indicators and Photophysical Considerations for Optogenetic Applications. *ACS Chemical Neuroscience* **4**, 963 (2013).

136. M. J. Berridge, Neuronal calcium signaling. *Neuron* **21**, 13 (1998).

137. M. J. Berridge, P. Lipp, M. D. Bootman, The versatility and universality of calcium signalling. *Nature Reviews Molecular Cell Biology* **1**, 11 (2000).

138. R. Kerr *et al.*, Optical Imaging of Calcium Transients in Neurons and Pharyngeal Muscle of C. elegans. *Neuron* **26**, 583 (2000).

139. O. Garaschuk *et al.*, Optical monitoring of brain function *in vivo*: from neurons to networks. *Pflügers Archiv* **453**, 385 (2006).

140. W. Göbel, F. Helmchen, *In vivo* calcium imaging of neural network function. *Physiology* **22**, 358 (2007).

141. M. Mank, O. Griesbeck, Genetically Encoded Calcium Indicators. *Chemical Reviews* **108**, 1550 (2008).

142. D. W. Domaille, E. L. Que, C. J. Chang, Synthetic fluorescent sensors for studying the cell biology of metals. *Nature Chemical Biology* **4**, 168 (2008).

143. A. Miyawaki *et al.*, Fluorescent indicators for Ca^{2+} based on green fluorescent proteins and calmodulin. *Nature* **388**, 882 (1997).

144. V. A. Romoser, P. M. Hinkle, A. Persechini, Detection in living cells of ca^{2+}-dependent changes in the fluorescence emission of an indicator composed of two green fluorescent protein variants linked by a calmodulin-binding sequence: a new class of fluorescence indicators. *Journal of Biological Chemistry* **272**, 13270 (1997).

145. M. Mank *et al.*, A genetically encoded calcium indicator for chronic *in vivo* two-photon imaging. *Nature Methods* **5**, 805 (2008).

146. A. Miyawaki, O. Griesbeck, R. Heim, R. Y. Tsien, Dynamic and quantitative Ca^{2+} measurements using improved cameleons. *Proceedings of the National Academy of Sciences of the United States of America* **96**, 2135 (1999).

147. T. Nagai, S. Yamada, T. Tominaga, M. Ichikawa, A. Miyawaki, Expanded dynamic range of fluorescent indicators for Ca^{2+} by circularly permuted yellow fluorescent proteins. *Proceedings of the National Academy of Sciences of the United States of America* **101**, 10554 (2004).

148. K. Horikawa *et al.*, Spontaneous network activity visualized by ultrasensitive Ca^{2+} indicators, yellow Cameleon-Nano. *Nature Methods* **7**, 729 (2010).

149. N. Heim, O. Griesbeck, Genetically Encoded Indicators of Cellular Calcium Dynamics Based on Troponin C and Green Fluorescent Protein. *Journal of Biological Chemistry* **279**, 14280 (2004).

150. M. Mank *et al.*, A FRET-Based Calcium Biosensor with Fast Signal Kinetics and High Fluorescence Change. *Biophysical Journal* **90**, 1790 (2006).

151. D. F. Reiff *et al.*, *In vivo* Performance of Genetically Encoded Indicators of Neural Activity in Flies. *The Journal of Neuroscience* **25**, 4766 (2005).

152. J. Díez-García *et al.*, Activation of cerebellar parallel fibers monitored in transgenic mice expressing a fluorescent Ca^{2+} indicator protein. *European Journal of Neuroscience* **22**, 627 (2005).

153. L. Tian *et al.*, Imaging neural activity in worms, flies and mice with improved GCaMP calcium indicators. *Nature Methods* **6**, 875 (2009).

154. K. R. Gee *et al.*, Chemical and physiological characterization of fluo-4 Ca^{2+}-indicator dyes. *Cell Calcium* **27**, 97 (2000).

155. X. R. Sun *et al.*, Fast GCaMPs for improved tracking of neuronal activity. *Nature Communication* **4**, (2013).

156. A. Fiala *et al.*, Genetically Expressed Cameleon in Drosophila melanogaster Is Used to Visualize Olfactory Information in Projection Neurons. *Current Biology* **12**, 1877 (2002).

157. D. Yu, G. S. Baird, R. Y. Tsien, R. L. Davis, Detection of Calcium Transients in DrosophilaMushroom Body Neurons with Camgaroo Reporters. *The Journal of Neuroscience* **23**, 64 (2003).

158. J. W. Wang, A. M. Wong, J. Flores, L. B. Vosshall, R. Axel, Two-Photon Calcium Imaging Reveals an Odor-Evoked Map of Activity in the Fly Brain. *Cell* **112**, 271 (2003).

159. L. Liu, O. Yermolaieva, W. A. Johnson, F. M. Abboud, M. J. Welsh, Identification and function of thermosensory neurons in Drosophila larvae. *Nature Neuroscience* **6**, 267 (2003).

160. S.-i. Higashijima, M. A. Masino, G. Mandel, J. R. Fetcho, Imaging Neuronal Activity During Zebrafish Behavior With a Genetically Encoded Calcium Indicator. *Journal of Neurophysiology* **90**, 3986 (2003).

161. M. T. Hasan *et al.*, Functional Fluorescent Ca^{2+} Indicator Proteins in Transgenic Mice under TET Control. *PLoS Biology* **2**, e163 (2004).

162. J. Díez-García, W. Akemann, T. Knöpfel, *In vivo* calcium imaging from genetically specified target cells in mouse cerebellum. *NeuroImage* **34**, 859 (2007).

163. D.-l. Qiu, T. Knöpfel, An NMDA Receptor/Nitric Oxide Cascade in Presynaptic Parallel Fiber–Purkinje Neuron Long-Term Potentiation. *The Journal of Neuroscience* **27**, 3408 (2007).

164. D.-l. Qiu, T. Knöpfel, Presynaptically expressed long-term depression at cerebellar parallel fiber synapses. *Pflügers Archiv - European Journal of Physiology* **457**, 865 (2009).

165. E. Warp *et al.*, Emergence of Patterned Activity in the Developing Zebrafish Spinal Cord. *Current Biology* **22**, 93 (2012).

166. M. L. Fletcher *et al.*, Optical Imaging of Postsynaptic Odor Representation in the Glomerular Layer of the Mouse Olfactory Bulb. *Journal of Neurophysiology* **102**, 817 (2009).

167. M. L. Fletcher, Analytical Processing of Binary Mixture Information by Olfactory Bulb Glomeruli. *PLoS ONE* **6**, e29360 (2011).

168. C. D. Harvey, P. Coen, D. W. Tank, Choice-specific sequences in parietal cortex during a virtual-navigation decision task. *Nature* **484**, 62 (2012).

169. M. B. Ahrens, M. B. Orger, D. N. Robson, J. M. Li, P. J. Keller, Whole-brain functional imaging at cellular resolution using light-sheet microscopy. *Nature Methods* **10**, 413 (2013).

170. J. Akerboom *et al.*, Optimization of a GCaMP Calcium Indicator for Neural Activity Imaging. *The Journal of Neuroscience* **32**, 13819 (2012).

171. M. L. Andermann, A. M. Kerlin, C. Reid, Chronic cellular imaging of mouse visual cortex during operant behavior and passive viewing. *Frontiers in Cellular Neuroscience* **4**, (2010).

172. M. Minderer *et al.*, Chronic imaging of cortical sensory map dynamics using a genetically encoded calcium indicator. *The Journal of Physiology* **590**, 99 (2012).

173. D. A. Dombeck, C. D. Harvey, L. Tian, L. L. Looger, D. W. Tank, Functional imaging of hippocampal place cells at cellular resolution during virtual navigation. *Nature Neuroscience* **13**, 1433 (2010).

174. D. Huber *et al.*, Multiple dynamic representations in the motor cortex during sensorimotor learning. *Nature* **484**, 473 (2012).

175. K. Ataka, V. A. Pieribone, A Genetically Targetable Fluorescent Probe of Channel Gating with Rapid Kinetics. *Biophysical Journal* **82**, 509 (2002).

176. R. Sakai, V. Repunte-Canonigo, C. D. Raj, T. Knöpfel, Design and characterization of a DNA-encoded, voltage-sensitive fluorescent protein. *European Journal of Neuroscience* **13**, 2314 (2001).

177. G. Guerrero, M. S. Siegel, B. Roska, E. Loots, E. Y. Isacoff, Tuning FlaSh: Redesign of the Dynamics, Voltage Range, and Color of the Genetically Encoded Optical Sensor of Membrane Potential. *Biophysical Journal* **83**, 3607 (2002).

178. B. J. Baker *et al.*, Three fluorescent protein voltage sensors exhibit low plasma membrane expression in mammalian cells. *Journal of Neuroscience Methods* **161**, 32 (2007).

179. A. Lundby, H. Mutoh, D. Dimitrov, W. Akemann, T. Knöpfel, Engineering of a Genetically Encodable Fluorescent Voltage Sensor Exploiting Fast Ci-VSP Voltage-Sensing Movements. *PLoS ONE* **3**, e2514 (2008).

180. L. Jin *et al.*, Random insertion of split-cans of the fluorescent protein venus into Shaker channels yields voltage sensitive probes with improved membrane localization in mammalian cells. *Journal of Neuroscience Methods* **199**, 1 (2011).

181. L. Barnett, J. Platisa, M. Popovic, V. A. Pieribone, T. Hughes, A Fluorescent, Genetically-Encoded Voltage Probe Capable of Resolving Action Potentials. *PLoS ONE* **7**, e43454 (2012).

182. W. Akemann *et al.*, Imaging neural circuit dynamics with a voltage-sensitive fluorescent protein. *Journal of Neurophysiology* **108**, 2323 (2012).

183. L. Jin *et al.*, Single Action Potentials and Subthreshold Electrical Events Imaged in Neurons with a Fluorescent Protein Voltage Probe. *Neuron* **75**, 779 (2012).

184. B. Chanda *et al.*, A hybrid approach to measuring electrical activity in genetically specified neurons. *Nature Neuroscience* **8**, 1619 (2005).

185. J. M. Kralj, D. R. Hochbaum, A. D. Douglass, A. E. Cohen, Electrical Spiking in Escherichia coli Probed with a Fluorescent Voltage-Indicating Protein. *Science* **333**, 345 (2011).

186. D. Maclaurin, V. Venkatachalam, H. Lee, A. E. Cohen, Mechanism of voltage-sensitive fluorescence in a microbial rhodopsin. *Proceedings of the National Academy of Sciences of the United States of America* **110**, 5939 (2013).

187. E. Pastrana, Light-based electrophysiology. *Nature Methods* **9**, 38 (2011).

188. G. Cao *et al.*, Genetically Targeted Optical Electrophysiology in Intact Neural Circuits. *Cell* **154**, 904 (2013).

189. M. A. LYNCH, Long-Term Potentiation and Memory. *Physiological Reviews* **84**, 87 (2004).

190. S. H. Snyder, R. B. Innis, Peptide Neurotransmitters. *Annual Review of Biochemistry* **48**, 755 (1979).

191. C. W. Cotman, D. T. Monaghan, in *Excitatory Amino Acids and Epilepsy,* R. Schwarcz, Y. Ben-Ari, Eds. (Springer US, 1986), vol. 203, pp. 237-252.

192. S. Okumoto *et al.*, Detection of glutamate release from neurons by genetically encoded surface-displayed FRET nanosensors. *Proceedings of*

the National Academy of Sciences of the United States of America **102**, 8740 (2005).

193. R. Y. Tsien, Building and breeding molecules to spy on cells and tumors. *FEBS Letters* **579**, 927 (2005).

194. J. S. Marvin *et al.*, An optimized fluorescent probe for visualizing glutamate neurotransmission. *Nature Methods* **10**, 162 (2013).

195. Q.-T. Nguyen *et al.*, An *in vivo* biosensor for neurotransmitter release and in situ receptor activity. *Nature Neuroscience* **13**, 127 (2010).

196. J. G. Yamauchi *et al.*, Characterizing Ligand-Gated Ion Channel Receptors with Genetically Encoded Ca^{2+} Sensors. *PLoS ONE* **6**, e16519 (2011).

197. T. C. Sudhof, The synaptic vesicle cycle: a cascade of protein–protein interactions. *Nature* **375**, 645 (1995).

198. M. Ng *et al.*, Transmission of Olfactory Information between Three Populations of Neurons in the Antennal Lobe of the Fly. *Neuron* **36**, 463 (2002).

199. Y. Li, R. W. Tsien, pHTomato, a red, genetically encoded indicator that enables multiplex interrogation of synaptic activity. *Nature Neuroscience* **15**, 1047 (2012).

200. K. Berglund *et al.*, Imaging synaptic inhibition in transgenic mice expressing the chloride indicator, Clomeleon. *Brain Cell Biology* **35**, 207 (2006).

201. J. S. Grimley *et al.*, Visualization of Synaptic Inhibition with an Optogenetic Sensor Developed by Cell-Free Protein Engineering Automation. *The Journal of Neuroscience* **33**, 16297 (2013).

202. P. J. Keller, A. D. Schmidt, J. Wittbrodt, E. H. Stelzer, Reconstruction of zebrafish early embryonic development by scanned light sheet microscopy. *Science* **322**, 1065 (2008).

203. S. Abrahamsson *et al.*, Fast multicolor 3D imaging using aberration-corrected multifocus microscopy. *Nature Methods* **10**, 60 (2012).

204. S. Quirin, D. S. Peterka, R. Yuste, Instantaneous three-dimensional sensing using spatial light modulator illumination with extended depth of field imaging. *Optics Exp* **21**, 16007 (2013).

205. A. H. Marblestone* *et al.*, Physical Principles for Scalable Neural Recording. *Frontiers in Computational Neuroscience* **7**, (2013).

206. A. M. Caravaca-Aguirre, E. Niv, D. B. Conkey, R. Piestun, Real-time resilient focusing through a bending multimode fiber. *Optics Express* **21**, 12881 (2013).

207. A. N. Zorzos, E. S. Boyden, C. G. Fonstad, Multiwaveguide implantable probe for light delivery to sets of distributed brain targets. *Optics Letters* **35**, 4133 (2010).

208. A. N. Zorzos, J. Scholvin, E. S. Boyden, C. G. Fonstad, Three-dimensional multiwaveguide probe array for light delivery to distributed brain circuits. *Optics Letters* **37**, 4841 (2012).

209. D. B. Conkey, A. M. Caravaca-Aguirre, R. Piestun, High-speed scattering medium characterization with application to focusing light through turbid media. *Optics express* **20**, 1733 (2012).

210. J. Akerboom *et al.*, Genetically encoded calcium indicators for multi-color neural activity imaging and combination with optogenetics. *Frontiers in Molecular Neuroscience* **6**, (2013).

Chapter 2. An expanded palette of genetically encoded Ca^{2+} indicators

2.1 Abstract

Engineered FP chimeras that modulate their fluorescence in response to changes in calcium ion (Ca^{2+}) concentration are powerful tools for visualizing intracellular signaling activity. However, despite a decade of availability, the palette of single FP-based Ca^{2+} indicators has remained limited to a single green hue. We have expanded this palette by developing blue, improved green, and red intensiometric indicators, as well as an emission ratiometric indicator with an 11,000% ratio change. This series enables improved single color Ca^{2+} imaging in neurons and transgenic *Caenorhabditis elegans*. In HeLa cells, Ca^{2+} was imaged in three subcellular compartments; and, in conjunction with a CFP-YFP-based indicator, Ca^{2+} and ATP were simultaneously imaged. This palette of indicators paints the way to a colorful new era of Ca^{2+} imaging.

2.2 Introduction

Fluorescent indicators for the quantification of intracellular Ca^{2+} have been indispensable tools of cell biology for three decades (*211*); yet the need for new indicators has continued to grow as advances in molecular biology and microscopy instrumentation reveal the limitations of each previous generation. Accordingly, there has been a push towards Ca^{2+} indicators that are longer wavelength, ratiometric, higher signal-to-noise, and, since the advent of green FP

A version of this chapter has been published in journal *Science*: Zhao, Y.; Araki, S.; Wu, J.; Teramoto, T.; Chang, Y.-F.; Nakano, M.; Abdelfattah, A. S.; Fujiwara, M.; Ishihara, T.; Nagai, T.; Campbell, R. E. *Science* **2011**, *333*, 1888.

(GFP), genetically encodable. A ratiometric indicator excites or emits at distinct wavelengths in the Ca^{2+}-free and Ca^{2+}-bound states, and provides the advantages of being quantitative and less susceptible to imaging artifacts. Two important classes of genetically encoded Ca^{2+} indicators are the Förster resonance energy transfer (FRET)-based cameleon-type (*143*), and the single GFP-type, such as GCaMP3 (*95*) and flash-pericam (*92*), that are dim in the absence of Ca^{2+} and bright when bound to Ca^{2+}. GCaMPs are composed of a circularly permuted (cp) GFP fused to the CaM-binding region of chicken myosin light chain kinase (M13) at its N-terminus and a vertebrate calmodulin (CaM) at its C-terminus. Binding of Ca^{2+} causes the M13 and CaM domains to interact and the interface between CaM and the FP to reorganize, leading to an increase in fluorescence due to water-mediated interactions between the chromophore and R377 (*212*) of CaM (*121, 122*).

Although directed protein evolution has provided many improved FPs, it has not proven particularly effective for the production of improved GCaMPs. Directed evolution of FPs is typically guided by digital fluorescence imaging of large libraries of gene variants expressed in *Escherichia coli* colonies. In this manner, rare clones that harbor a mutation that confers a desirable trait, such as improved brightness or altered hue, can be identified in libraries of $>10^5$ variants. Lacking an analogous screen for GCaMP Ca^{2+} response, researchers have identified improved variants by manual testing (*122, 213*) and a medium-throughput cell-based assay (*153*).

2.3 Results and Discussion

To accelerate the development of improved and hue-shifted GCaMP-type indicators, we developed a colony-based screen for Ca^{2+}-dependent fluorescent changes (Figure 2.1 and SOM text). The premise of this screening system is that Ca^{2+} indicators targeted to the *E. coli* periplasm can be shifted towards the Ca^{2+}-free or Ca^{2+}-bound states by experimental manipulation of the environmental Ca^{2+} concentration. Accordingly, screening of large libraries of genetic variants of GCaMP-type indicators can be achieved by digital fluorescence imaging, at both high and low Ca^{2+} conditions, of plates containing hundreds of *E. coli* colonies each. We used this screening system to undertake a process of directed evolution that explored the sequence space accessible from the most optimized single FP Ca^{2+} indicator, GCaMP3 (*153*). Initially, we created a large library by error-prone PCR and screened ~2×10^5 colonies to identify the offspring with the largest Ca^{2+}-dependent changes in green fluorescence (*214*). Following this and subsequent iterative rounds of library creation and screening (Figure 2.5), we arrived at a set of 3 improved variants (Figures 2.7, 2.8 and Table 2.1). We designated these green fluorescent genetically encoded Ca^{2+}-indicators for optical imaging as G-GECO1 (Figure 2.2ABC), G-GECO1.1, and G-GECO1.2. Parallel efforts to evolve flash-pericam (*92*) did not produce variants with properties that rivaled the G-GECOs. The G-GECOs share a Ca^{2+}-dependent increase in fluorescence (2,300-2,600%) that is approximately double that of GCaMP3 (Table 2.2), demonstrating the effectiveness of the molecular evolution strategy. The primary differences between the three variants are the apparent dissociation constants (K_d') for Ca^{2+} (750 nM, 620 nM, and 1150 nM, respectively; 540 nM for GCaMP3) and the fact that G-GECO1 exhibits the least fluorescence when

excited at ~400 nm and may be preferred when used in conjunction with violet-excitable probes.

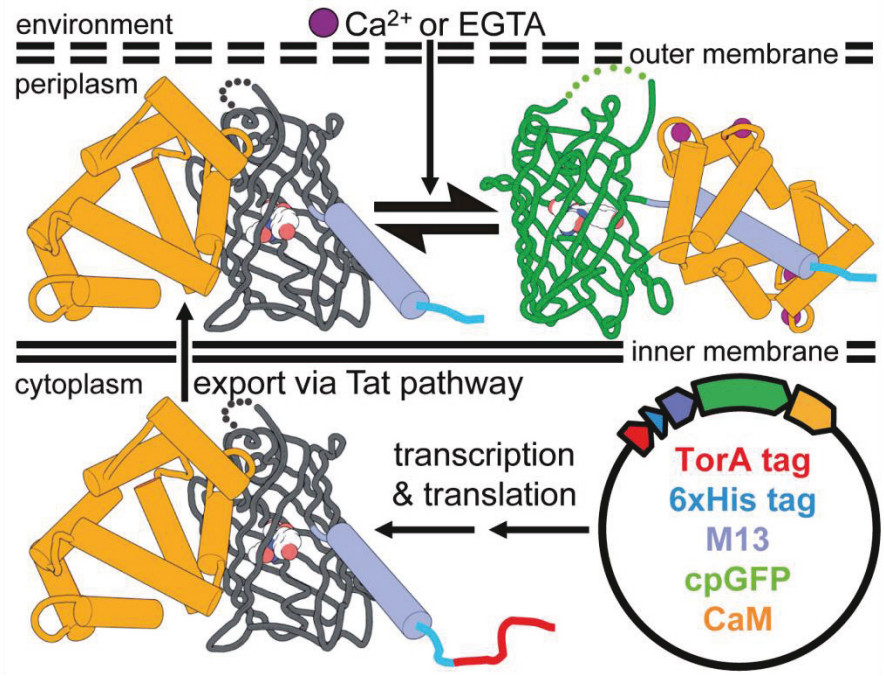

Figure 2.1 Schematic of the system for image-based screening of *E. coli* colonies.

The GCaMP variant, as represented by GCaMP2 (PDB ID 3EVU and 3EVR) (*121*), has a TorA periplasmic export tag (*215*).

Our success in developing the G-GECOs led us to explore the evolution of GECOs with altered fluorescent hues. We attempted to construct a blue fluorescent GECO (B-GECO) by introducing the GFP Y66H substitution to produce the histidine-derived chromophore of blue FP (BFP), into G-GECO1.1. To create an initial library of variants, we randomized 3 amino acids (V63, R377, K380) with side chains in close proximity to the chromophore (*121*). Screening of this >18,000-member library led to the identification of a first generation

B-GECO with 400% signal change. Additional rounds of evolution ultimately produced B-GECO1 (Table 2.1, Figures 2.6, 2.9A, and 2.10A) which has a 700% signal change (Figure 2.2BC), a K_d' of 480 nM (Table 2.2), and is relatively pH-insensitive compared to G-GECO1 (22% vs. 92% quenched at pH 6) (Figure 2.S6).

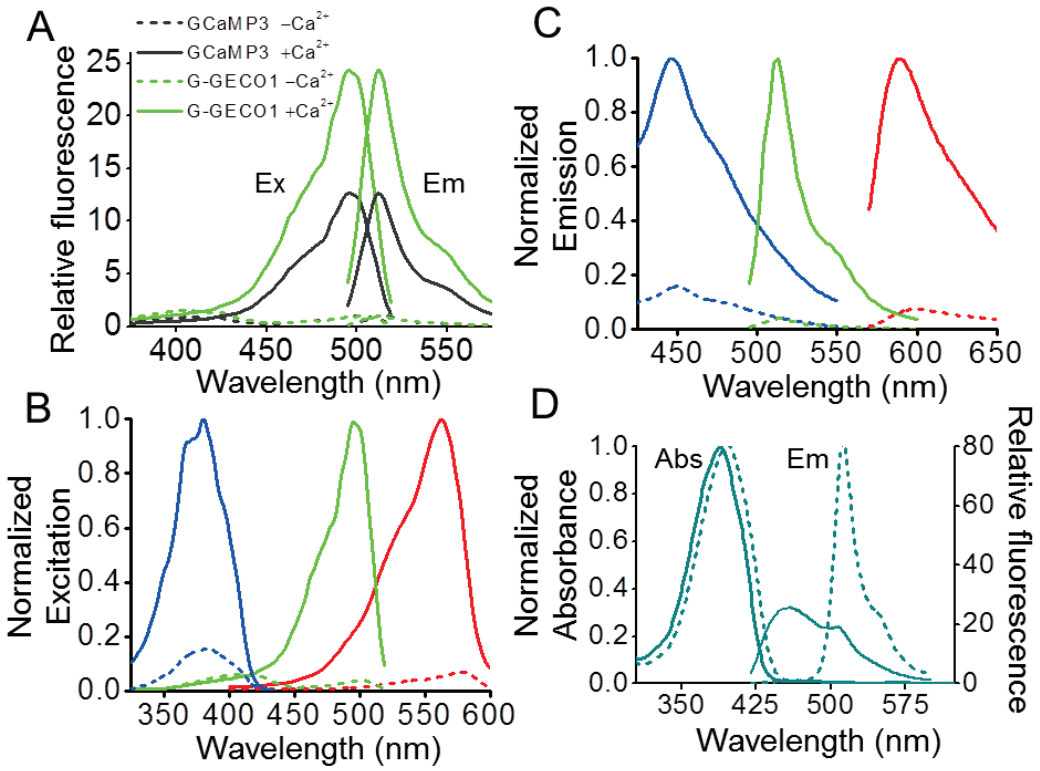

Figure 2.2 Spectral profiles of GECOs.

(**A**) Fluorescence excitation (Ex) and emission spectra (Em) normalized to the Ca^{2+}-free state. (**B**) Normalized excitation spectra of Ca^{2+}-free (dashed line) and Ca^{2+}-bound (solid line) B-GECO1 (blue), G-GECO1 (green), and R-GECO1 (red). (**C**) Emission spectra represented as in (**B**). (**D**) Absorbance (Abs) and emission spectra for Ca^{2+}-free (dashed line) and Ca^{2+}-bound (solid line) GEM-GECO1.

Red-shifted fluorescent indicators are preferable to blue-shifted ones due to the lower phototoxicity and greater tissue penetration associated with longer wavelength light. To construct a potential red fluorescent GECO (R-GECO), we first replaced the cpGFP of G-GECO1.1 with an analogous cp version (N_{term}-146 to 231-GGTGGS-1 to 145-C_{term}) of the mApple red FP (*67*). The first generation library was created by error-prone PCR and randomization of the first and last residues of cpmApple (63 and 302 by GECO numbering, Figure 2.6). From this library we identified R-GECO0.1, which exhibited a modest response to Ca^{2+} (60% increase). Additional rounds of directed evolution afforded major improvements and resulted in the production of R-GECO1 (Table 2.1, Figures 2.7, 2.9B, and 3.0B) which exceeds GCaMP3 in terms of its Ca^{2+} response. R-GECO1 has a 1,600% intensity change (Figure 2.2BC), a K_d' of 480 nM, and absorption and emission maxima that are ~80 nm red-shifted relative to the G-GECO series (Table 2.2).

Late in the directed evolution process we used a PCR-based method (*216*) to recombine the mutations of advanced intermediates and final products of the B-GECO, G-GECO, and flash-pericam series. This recombination produced our most improved B- and G-GECOs, but also yielded some unexpected variants. For example, some of the brightest blue fluorescent variants had a tyrosine-derived chromophore and exhibited a Ca^{2+}-dependent change in the ratio of blue (~450 nm) to green (~510 nm) fluorescence when excited at ~400 nm (Figure 2.2D). We speculate that, in the Ca^{2+}-free state, the chromophore of this blue-green emission ratiometric GECO (GEM-GECO) undergoes excited state proton transfer (ESPT) and emits from the lower energy (green fluorescent) anionic form. In the Ca^{2+}-bound state, ESPT is blocked and the chromophore emits from the higher

energy (blue fluorescent) neutral form. Additional library creation and screening led to GEM-GECO1 (Table 2.1, Figures 2.7 and 2.9C) which exhibits an 11,000% ratio change and a K_d' of 340 nM (Table 2.2).

Yet another unexpected discovery in the recombination library was a green excitation ratiometric-GECO (GEX-GECO) which exhibits a large Ca^{2+}-dependent change in the ratio between 400 nm and 488 nm excitation (Figure 2.9C). This indicator is analogous to the previously reported ratiometric-pericam that undergoes a ~1,000% ratio change (*92*). Further directed evolution produced GEX-GECO1 (Table 2.1, Figure 2.7 and 2.9D), which exhibits a 2,600% change in excitation ratio, a K_d' of 318 nM, and the most rapid approach to equilibrium (k_{obs}) of any of the GECOs (Table 2.3, Figure 2.11).

To explore the utility of our best GECOs, we performed a series of imaging experiments to investigate their performance relative to previously reported indicators and to determine if they could be used for multicolor Ca^{2+} imaging in single cells. Initially, we expressed individual GECOs in HeLa cells and imaged their intensity (or ratio) during treatment with histamine and *in situ* dynamic range calibration (Table 2.4, Figure 2.3A-H). The performance of the GECOs in cells closely paralleled their performance *in vitro*. We next explored the use of the G- and R-GECO1 in dissociated rat hippocampal neurons (Figure 2.3IJ). Consistent with our HeLa experiments, G-GECO1 proved superior to, and R-GECO1 comparable to, GCaMP3 for imaging of spontaneous Ca^{2+} oscillations. To achieve imaging of neuronal activity in a whole animal, we turned to GEM-GECO1 due to its large ratiometric change. Exposure of a transgenic *C. elegans*, with GEM-GECO1 expressed in the AWA sensory neuron, to a perfused solution of diacetyl produced a 44% ratio change (Figure 2.3KL); a substantial improvement

over the 18% ratio change obtained with YC3.60 under similar conditions (*217*). This improvement was obtained with a CFP/YFP filter set that provided diminished autofluorescence signal, but is not ideally matched to the GEM-GECO1 spectrum.

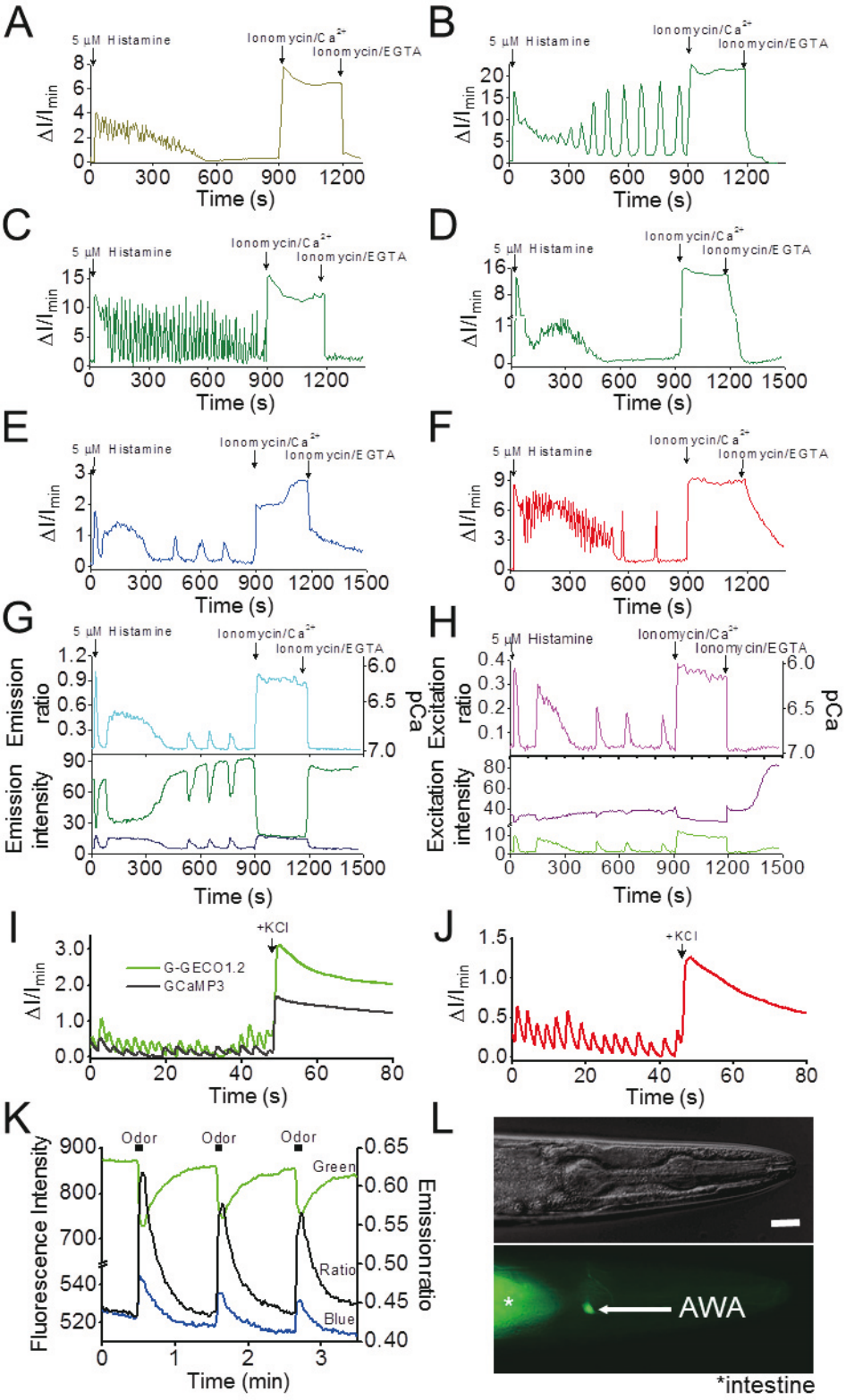
A
5 μM Histamine
Ionomycin/Ca2+
Ionomycin/EGTA
ΔI/Imin
Time (s)
B
C
D
E
F
G
Emission ratio
Emission intensity
pCa
H
Excitation ratio
Excitation intensity
I
+KCl
G-GECO1.2
GCaMP3
J
K
Odor
Green
Ratio
Blue
Fluorescence Intensity
Emission ratio
Time (min)
L
AWA
*intestine

Figure 2.3 Single color imaging with GECOs.

(**A-H**) Intensity vs. time traces for transfected HeLa cells. (**A**) GCaMP3; (**B**) G-GECO1; (**C**) G-GECO1.1; (**D**) G-GECO1.2; (**E**) B-GECO1; (**F**) R-GECO1; (**G**) GEM-GECO1; and (**H**) GEX-GECO1. Ionomycin/Ca^{2+}, ionomycin/EGTA, and the initial histamine-induced spike are generally consistent for a given variant (Table 2.4), but the histamine-induced oscillations are highly variable between cells. Accordingly, lower amplitude oscillations (e.g., **A** and **D**) do not necessarily indicate poorer indicator performance. (**I**) Imaging of spontaneous Ca^{2+} oscillations in neurons. (**J**) R-GECO1 imaged under conditions similar to (**I**). (**K**) Ratiometric imaging of *C. elegans* with GEM-GECO1 expressed in the AWA neuron. (**L**) Bright field and fluorescence images of the worm imaged in (**K**). Scale bar indicates 10 μm. Filter specifications are in Table 2.5.

The palette of GECOs transforms Ca^{2+} imaging from a monochromatic to a multichromatic endeavor. With appropriate targeting and selection of GECO hues, it should be possible to visualize correlated changes in Ca^{2+} in different organelles of a single cell. To explore this possibility, we imaged HeLa cells co-transfected with plasmids encoding targeted versions of R-GECO1, G-GECO1, and either B-GECO1 or GEM-GECO1 (Figure 2.4A-E). As mitochondrial autofluorescence interferes with the emission of B-GECO1, but not with the ratiometric emission of GEM-GECO1, we prefer the latter 3-color combination. To determine if R-GECO1 could be used to image Ca^{2+} dynamics in conjunction with a CFP-YFP FRET-based indicator, we co-expressed R-GECO1 and ATeam1.03, a FRET-based ATP indicator (*218*), in HeLa cells. As recently observed with a synthetic Ca^{2+} indicator (*219*), histamine treatment resulted in transient

increases in cytoplasmic (Figure 2.4F) and mitochondrial (Figure 2.4G) ATP concentrations, albeit with a lag relative to cytoplasmic Ca^{2+}.

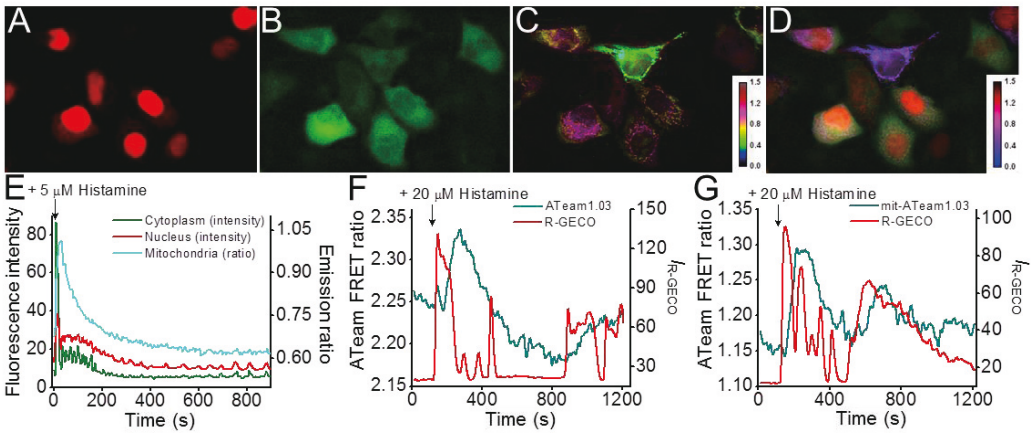

Figure 2.4 Multicolor imaging with GECOs.

(**A-C**) HeLa cells transfected with nucleus-localized R-GECO1, cytoplasmic G-GECO1, and mitochondria-localized GEM-GECO1. (**A**) Red fluorescence. (**B**) Green fluorescence with cyan (~470 nm) excitation. (**C**) Pseudocolored ratio of blue to green fluorescence with UV (~380 nm) excitation (**C**). (**D**) Merge of images **A-C**, with GEM-GECO1 ratio in magenta. Images are from Movie S1. (**E**) Intensity or ratio vs. time traces for each channel represented in **A-C**. Filter specifications are in Table 2.5. (**F**) Imaging of cytoplasmic Ca^{2+} and ATP. (**G**) Imaging of cytoplasmic Ca^{2+} and mitochondrial ATP.

2.4 Conclusion

In summary, we have engineered a palette of GECOs and demonstrated that they open the door to Ca^{2+} imaging experiments that were previously impractical. Specifically, these new indicators enable imaging of multiple Ca^{2+} indicators in single cells, imaging of neuronal activity in *C. elegans* with improved sensitivity,

and, in the case of R-GECO1, multi-parameter imaging with CFP/YFP FRET-based biosensors. In addition, GEM-GECO1 and R-GECO1 should facilitate imaging of neuronal activity following optogenetic channel activation since they are excited at wavelengths spectrally distinct from the action spectra of certain channels (*220*).

2.5 Experimental procedures

2.5.1 General

Synthetic DNA oligonucleotides used for cloning and library construction were purchased from Integrated DNA Technologies or Hokkaido System Science. The sequences of all oligonucleotides used in this work are provided in Table 2.6. Pfu polymerase (Fermentas) or KOD+ (Toyobo Life Science) were used for non-mutagenic PCR amplifications in the buffer supplied by the respective manufacturer. Taq polymerase (New England Biolabs) in the presence of $MnCl_2$ (0.1 mM) was used for error-prone PCR amplifications. PCR products and products of restriction digests were routinely purified using preparative agarose gel electrophoresis followed by DNA isolation using the GeneJET gel extraction kit (Fermentas) or QIAEX II gel extraction kit (Qiagen). Restriction endonucleases were purchased from Fermentas or Takara Biosciences and used according to the manufacturer's recommended protocol. Ligations were performed using T4 ligase in Rapid Ligation Buffer (Promega). Small-scale isolation of plasmid DNA was performed by GeneJET miniprep kit (Fermentas) or by alkaline lysis of bacteria (a pellet derived from 1.5-3 mL of liquid culture)

followed by ethanol precipitation of the DNA. Large-scale plasmid DNA purifications were performed by alkaline lysis of bacteria (a pellet derived from 150-200 mL of liquid culture) followed by successive steps of isopropanol precipitation, PEG 8000 precipitation, and 2 rounds of phenol/chloroform extraction. The cDNA sequences for all GECOs and fusion constructs were confirmed by dye terminator cycle sequencing using the BigDye Terminator Cycle Sequencing kit (Applied Biosystems). The source and detailed specifications for all filters used for fluorescence screening and imaging are provided in Table 2.5. To determine the Ca^{2+} concentration in growth media, LB liquid medium was prepared according to manufacturer's instruction (Broth Lennox, Fisher Scientific, catalog number BP1427-2) and purified GEM-GECO was used to determine the concentration of free Ca^{2+} using a standard addition method to account for matrix effects.

2.5.2 Construction of the TorA protein export plasmid for GCaMP3

The TorA protein export plasmid (pTorPE) was constructed by inserting a digested DNA fragment encoding TorA-6×His-GCaMP3-SsrA into the NcoI/HindII sites of pBAD/His B (Invitrogen). The insert region was assembled by a 2-part overlap extension PCR. The 5' piece used in the overlap extension contained the DNA encoding the TorA signal peptide and was prepared by PCR amplification of *E. coli* strain DH10B (Invitrogen) genomic DNA with primers FW_TorA and RV_TorA. Primer FW_TorA contains a NcoI site and primer RV_TorA contains a XbaI site and a region that overlaps with primer FW_XbaI-6His1. The 3' piece used in the overlap extension was prepared by PCR amplification of the gene encoding 6×His-GCaMP3 (in vector backbone

pEGFP-N1, Addgene plasmid 22692) with primers FW_XbaI_6His1 and RV_SsrA-GCaMP3. Primer RV_SsrA-GCaMP3 contains an XmaI site followed by the coding sequence for the SsrA tag and a HindIII site. Prior to PCR amplification, a NcoI site in GCaMP3 domain was removed using the Quikchange method with primer FW_GCaMP3_c105a. The PCR fragments were purified by agarose gel electrophoresis. The full length TorA-6×His-GCaMP3-SsrA chimera was assembled by overlap extension PCR using primers FW_TorA and RV_SsrA-GCaMP3 and a template composed of a mixture of the 5' and 3' PCR fragments (1 μL each). The full-length product (approximately 1400 bp) was purified by agarose gel electrophoresis and the doubly digested product was ligated into the NcoI and HindIII sites of pBAD/His B (Invitrogen) to yield pTorPE-GCaMP3 with NcoI-TorA-XbaI-6×His-GCaMP3-XmaI-SsrA–HindIII in the multiple cloning site.

2.5.3 Construction of GECO gene libraries

Error-prone PCR amplifications for construction of libraries of randomly mutated genes was performed as described above. In the first two rounds of G-GECO library construction, primers FW_XbaI-6His2 and RV_GCaMP-XmaI (in which an XmaI site follows the last residue of the CaM portion of the GECO construct) were used for error-prone PCR. The resulting PCR products were digested with Xba1 and Xma1 and ligated with similarly digested pTorPE-GCaMP3. Subsequent to our observation that the SsrA tag was truncated in some of our most favorable variants, we switched to using reverse primer YY in which a stop codon and a HindIII site immediately follow the last residue of the CaM. In this case, the PCR products were digested with Xba1 and HindIII and ligated into the

similarly digested pTorPE vector backbone. For site-directed mutagenesis or library construction by full or partial randomization of one or more codons, either the QuikChange Multi kit (Agilent Technologies) or overlap extension PCR was employed. Following ligation, electrocompetent *E. coli* strain DH10B cells was transformed with the library of gene variants and cultured overnight at 37 ℃ on 10-cm Petri dishes of LB-agar supplemented with 50 μg/mL ampicillin (Sigma) and 0.0002% to 0.0008% (wt/vol) L-arabinose (Alfa Aesar). The initial B-GECO library was constructed using the QuikChange Multi kit with G-GECO1.1 as template and primers G-B_V63VILM, G-B_T223ST_Y224H and G-B_R377X_N380X.

The initial cpmApple gene library was assembled by a two-part overlap extension PCR. The 5' piece used in the overlap extension was prepared by PCR amplification with a mixture of two different forward primers (FW_XhoI-X-147mc, FW_XhoI-X-148mc) and a single reverse primer (RV_GGTGGS-mCherry). Primers FW_XhoI-X-147mc and FW_XhoI-X-148mc contains a XhoI site and primer RV_GGTGGS-mCherry contains a cp linker GGTGGS and an overlap region with primer FW_GGTGGS-mCherry. The 3' piece for use in the overlap extension was prepared by PCR amplification with using a single forward primer (FW_GGTGGS-mCherry) and a mixture of two different revers primers (RV_MluI-X 143mc and RV_MluI-X 144mc). Primer RV_MluI-X 143mc and RV_MluI-X 144mc contains an MluI site. The PCR fragments were confirmed by agarose gel electrophoresis and purified. The full-length cpmApple gene library was assembled by overlap extension PCR using an equimolar mixture of primers FW_XhoI-X-147mc, FW_XhoI-X-148mc, RV_MluI-X 143mc and RV_MluI-X 144mc together with a mixture of the 5' and

3’ PCR fragments (1 μL each) as the template. The full-length product (approximately 1400 bp) was purified by agarose gel electrophoresis and the doubly digested product was ligated into the XhoI and MluI sites of a modified pTorPE-G-GECO1.1 in which a second MluI site had been first removed by QuikChange Multi procedure with primer Destroy_MluI.

2.5.4 Screening of GECO gene libraries

The imaging system used for library screening has previously been described in detail (*221*). For libraries generated by random mutagenesis, we screened 10,000–20,000 colonies (10–20 plates of bacterial colonies) per round, typically stopping screening when a number of substantially improved variants had been identified. For libraries generated by randomization of one or more codons, we screened approximately 3-fold more colonies than the expected library diversity (e.g., 12,000 colonies for a 4,000-member library). During library screening we picked colonies that exhibited the top 0.01% to 0.1% change of fluorescence intensity (or ratio) upon application of an EGTA solution (2 mM EGTA, 30 mM Tris-HCl, pH 7.4; applied using a spray bottle that produced a fine mist). In later rounds of screening, we also picked the top 0.01% to 0.1% of colonies based only on their brightness (or ratio) prior to application of EGTA. Picked clones were individually cultured in 4 mL liquid LB medium (0.0016% L-arabinose, 200 μg/ml ampicillin) that was then shaken (250 rpm) for either 36 h at 30 °C (in earlier generations) or 22 h at 37 °C (in later generations).

Proteins extracted from the liquid cultures of the picked clones were subjected to a second stage of screening in a Safire2 fluorescence microplate reader (Tecan). Extraction of periplasmic protein from *E. coli* cultures was

performed by a cold osmotic shock procedure. Briefly, bacterial cells were harvested by centrifugation at 13,000 g for 2 min at 4 °C and gently resuspended in 500 μL of ice-cold pH 8.0 buffer containing 30 mM Tris·Cl, 1 mM EDTA and 20% sucrose. After 5 min of gentle agitation on ice, the bacteria were again pelleted by centrifugation (9,000 g for 5 min at 4°C), resuspended in 400 μL of ice-cold 5 mM $MgSO_4$, and gently agitated for 10 min on ice. Following centrifugation to pellet the intact bacteria (9,000 g for 5 min at 4°C), the supernatant (the osmotic shock fluid containing the periplasmic protein fraction) was collected. In cases where the periplasmic export efficiency was particularly low, cytoplasmic protein was extracted by suspension of the osmotic shock cell fraction in B-PER (Pierce) followed by centrifugation to pellet the cell debris.

2.5.5 Protein purification and *in vitro* spectroscopy

To purify GECOs for *in vitro* spectroscopic characterization, the pTorPE plasmid harboring the variant of interest was first used to transform electrocompetent *E. coli* DH10B cells. Following selection on LB/ampicillin (200 μg/ml), single colonies were picked and used to inoculate 4 mL LB medium (200 μg/ml ampicillin, 0.0016% L-arabinose). Bacterial cultures were shaken at 250 rpm and allowed to grow for 40 h at 30 °C. Bacteria were harvested by centrifugation (10,000 g for 5 min), resuspended in 30 mM Tris-HCl buffer (pH 7.4), lysed by French press, and clarified by centrifugation at 13,000 g for 45 mins at 4°C. Proteins were purified from the cell-free extract by Ni-NTA affinity chromatography (Agarose Bead Technologies). Purified proteins were dialyzed into either 30 mM Tris, 150 mM NaCl, pH 7.4 or 10 mM MOPS, 100 mM KCl, pH 7.2. Absorption spectra were recorded on a DU-800 UV-visible

spectrophotometer (Beckman) and fluorescence spectra were recorded on either a Safire2 platereader (Tecan) or a QuantaMaster spectrofluorometer (Photon Technology International). For ratiometric GECOs, the response to Ca^{2+} is expressed as 100 * (R_{max}-R_{min})/R_{min}. For GEM-GECO, R = (I at 455 nm)/ (I at 511 nm), where I = fluorescence intensity when excited at 400 nm. For GEX-GECO R = (I with 400 nm excitation)/ (I with 488 nm excitation), where I = fluorescence intensity at 510 nm.

Standards for quantum yield determination were quinine (for B-GECO, GEX-GECO, and GEM-GECO), fluorescein (for G-GECO), and mCherry (for R-GECO). Briefly, the concentration of protein in a buffered solution (30 mM MOPS, pH 7.2, with either 10 mM EGTA or 10 mM Ca-EGTA) was adjusted such that the absorbance at the excitation wavelength was between 0.2 and 0.6. A series of dilutions of each protein solution and standard, with absorbance values ranging from 0.01 to 0.05, was prepared. The fluorescence spectra of each dilution of each standard and protein solution were recorded and the total fluorescence intensities obtained by integration. Integrated fluorescence intensity vs. absorbance was plotted for each protein and each standard. Quantum yields were determined from the slopes (S) of each line using the equation: $\Phi_{protein} = \Phi_{standard} \times (S_{protein}/S_{standard})$.

Extinction coefficients were determined by first measuring the absorption spectrum of each GECO in Ca^{2+}-free buffer (30 mM MOPs, 100 mM KCl and 10 mM EGTA at pH 7.2) and Ca^{2+}-buffer (30 mM MOPS, 100 mM KCl and 10 mM Ca-EGTA at pH 7.2). The concentrations of G-GECO, GEM-GECO and GEX-GECO were determined by measuring the absorbance following alkaline denaturation and assuming ε = 44,000 $M^{-1}cm^{-1}$ at 446 nm. For R-GECO, the

protein concentration was determined by comparing the absorption peak for denatured R-GECO to that of denatured mCherry (determined to have ε = 38,000 $M^{-1}cm^{-1}$ at 455 nm) following alkaline denaturation of both proteins. The concentration of B-GECO was determined by BCA assay (Pierce). Extinction coefficients of each protein were calculated by dividing the peak absorbance maximum by the concentration of protein.

To determine the apparent pK_a for each GECO, a series of phosphate-free buffers was prepared as follows. A solution containing 30 mM trisodium citrate and 30 mM borax was adjusted to pH 11.5 and HCl (12 M and 1M) was then added dropwise to provide solutions with pH values ranging from 11.5 to 3 in 0.5 pH unit intervals. The pH titration of Ca^{2+}-free protein were performed by adding 1 L of concentrated protein in Ca^{2+}-free buffer (30 mM MOPS, 100 mM KCl, 10 mM EGTA, at pH 7.2) into 100 L of each of the buffers described above. The pH titration of the Ca^{2+}-bound protein was performed by adding 1 L of protein in Ca^{2+} containing buffer (30 mM MOPS, 100 mM KCl and 10 mM $CaCl_2$, pH 7.2) into 100 L of the pH buffers. The fluorescence of each GECO in each buffer condition was recorded using a Safire2 multiwell fluorescence platereader (Tecan).

2.5.6 Determination of Ca^{2+} K_d' and Ca^{2+}-association kinetics

Ca^{2+} titrations were performed by dilution (1:100) of a concentrated protein solution into a series of buffers which were prepared by mixing Ca^{2+}-saturated and Ca^{2+}-free buffers (30 mM MOPS, 100 mM KCl, 10 mM EGTA, pH 7.2, either with or without 10 mM Ca^{2+}) to provide a series of solutions with free Ca^{2+} concentration ranges from 0 nM to 3,900 nM at 25 °C (*99*). The fluorescence

intensity of protein in each solution was determined and plotted as a function of Ca^{2+} concentration. Experiments were performed in triplicate and the averaged data from the three independent measurements was fit to the Hill equation.

Ca^{2+}-association kinetics were determined by stopped-flow photometry on a SX20 stopped-flow spectrometer (Applied Photophysics). The GECO indicator (in 30 mM MOPs, 1 mM EGTA and 100 mM KCl) was rapidly mixed (1:1) with a series of Ca^{2+} buffers that were prepared by mixing of a buffered solution (30 mM MOPs, 100 mM KCl) with different ratios of 10 mM EGTA and 10 mM Ca-EGTA. The change in the fluorescence or absorbance signal during rapid mixing provided the relaxation rate constants (k_{obs}) for the Ca^{2+} association reaction at various Ca^{2+} concentrations (from 300 nM to 1500 nM). By fitting the observed data to the equation $k_{obs} = k_{on} \times [Ca^{2+}]^n + k_{off}$, the kinetic constants of Ca^{2+} association k_{on} and dissociation k_{off} were determined.

2.6.7 Construction of mammalian expression plasmids.

To construct the plasmids for validation and testing of Ca^{2+} indicators in HeLa cells, the gene in the pBAD vector was first PCR amplified using primers GCaMP_FW_BamH1 and GCaMP_RV_EcoR1. For B-GECOs that contained the Ser5Pro substitution, primer Cpd_S5P_FW_BamH1 was used in place of GCaMP_FW_BamH1. PCR products were subjected to phenol/chloroform extraction followed by ethanol precipitation, then redissolved in 16 μL of deionized water. The DNA was digested with BamH1 and EcoR1 in a total volume of 20 μL and then purified by electrophoresis on a 1% agarose gel (Agarose S, Nippon Gene Co.) followed by gel extraction. Purified DNA fragments were ligated into the polylinker region of a modified pcDNA3 plasmid

digested with BamH1 and EcoR1 and similarly purified. The modified pcDNA3 plasmid had been made by deleting 2224 nucleotides (including the SV40 promoter, the SV40 origin of replication, the Neomycin ORF, and the SV40 poly A region) from the original 5.4 kb pcDNA3. The ligation reaction was used for transformation of chemically competent *E. coli* XL10-Gold (Agilent Technologies) by heat shock at 42 ℃ for 45 s. Cells were plated on LB/agar supplemented with ampicillin and individual colonies were picked into 3 mL of LB/ampicillin following overnight incubation at 37 ℃. Liquid cultures were shaken at 155 rpm and 37 ℃ for 12-15 h and then a small scale isolation of plasmid DNA was performed. Each gene was fully sequenced using T7_FW, F-EGFP-C, and BGH_RV primers. Once the sequence had been confirmed, *E. coli* XL10-Gold was again transformed with each plasmid, plated, and an individual colony was used to inoculate 150-200 mL of LB/ampicillin. Following shaking at either 37 ℃ for 12-15 h or 23 ℃ for 48 h, a large-scale plasmid purification was performed on the culture. Plasmids from large-scale purifications were stored in TE buffer and used for transfection as described below.

To construct the nucleus-targeting expression plasmids for use in multicolor imaging, a similar procedure to that described above was used. Briefly, a two-step PCR protocol was used. In the first PCR step, the GECO of interest was PCR amplified with GCaMP_RV_EcoR1 and either

GCaMP_2NLS_FW1 or Cpd_2NLS_FW1 (for B-GECO). The resulting PCR product is used as the template in a second PCR amplification with GCaMP_RV_EcoR1 and Cpd_2NLS_FW2. The full-length PCR product, which contains the gene encoding the GECO of interest, with 2 copies of the NLS

sequence (DPKKKRKV) at the N-terminal end, was ligated into the BamH1 and EcoR1 sites of the modified pcDNA3 plasmid as described above.

To construct the mitochondria-targeting expression plasmid, pcDNA3-mitAT1.03 (*218*) was digested with BamHI and EcoRI and the plasmid backbone purified by gel electrophoresis. To prepare the insert for ligation with the cut plasmid, the GECO of interest was PCR amplified using GCaMP_RV_EcoR1 and either GCaMP_FW_BamH1_mito or Cpd_S5P_FW_BamH1_mito (for B-GECO). Digestion and purification of the insert DNA, followed by ligation with the digested plasmid afforded an expression vector encoding the vector of interest fused to 2 copies of the mitochondria targeting sequence of cytochrome c oxidase subunit VIII at the N-terminal end.

2.5.7 HeLa cell culture imaging

HeLa cells (40-60% confluent) on collagen-coated 35 mm glass bottom dishes (Mastumami) were transfected with 1 μg of plasmid DNA and 4 μL lipofectamine 2000 (Invitrogen) according to the manufacturers instructions. After 2 h incubation the media was exchanged to DMEM with 10% fetal bovine serum and the cells were incubated for an additional 24 h at 37 ℃ in a CO_2 incubator. For flash-pericam variants, cells were incubated at 28 ℃. Immediately prior to imaging, cells were washed twice with Hanks balanced salt solution (HBSS) and then 1 mL of 20 mM HEPES buffered HBSS was added.

Cell imaging was performed with an inverted Eclipse Ti-E (Nikon) equipped with an Orca-R2 digital CCD camera (Hamamatsu Photonics K.K.), a Micro

scanning stage MSS-BT110 (Chuo Precision Industrial Co. Ltd.), and a Chamlide IC incubator system (Live Cell instrument). The AquaCosmos software package (Hamamatsu Photonics K.K.) was used for automated microscope and camera control. For determination of dynamic ranges in live cells, cells were imaged with a 40× oil objective lens (NA 1.3), excitation light intensity was decreased to 1% with a neutral density filter (ND100), and a 0.6× lens was placed between the microscope and the CCD camera. All imaging, with the exception of cells expressing flash-pericam variants, was performed at 37 ℃. Flash-pericam variants were imaged at room temperature. For 3-color GECO imaging, an objective lens with excellent chromatic aberration correction through the visible range is strongly recommended.

For imaging of histamine-induced Ca^{2+} dynamics, cells were imaged with a 500 ms exposure (2×2 binning) acquired every 5 s for a duration of 15 min. Approximately 30 s after the start of the experiment, histamine (10 μL) was added to a final concentration of 5 μM. Once the experiment had ended, cells were washed 2× with HBSS, and then incubated for 10 min in 1 mL HHBSS to allow histamine-induced oscillations to subside. Cells are then imaged as described above, with exposures every 10 s for a duration of 5 min. Approximately 30 s after imaging is started, 1 mL of 2 mM $CaCl_2$, 10 μM ionomycin in Ca^{2+}- and Mg^{2+}-free HHBSS (HHBSS (-)) is added to the dish via peristaltic pump. At the end of the experiment, cells are washed 3× with HHBSS (-). Following addition of 1 mL of 1 mM EGTA, 5 μM ionomycin in HHBSS (-), cells were imaged again with exposures every 5 s for a total of 5 min.

For co-imaging of GECOs and fura-2, HeLa cells were transfected and cultured 24 h at 37 ℃ as described above. Cells were then incubated for 15 min

at room temperature with 1 μM fura-2 AM and 0.5× PowerLoad concentrate (Invitrogen) in HHBSS. Cells were washed twice with HHBSS and then imaged in HHBSS with microscope settings identical to those described above. Filters are provided in Table 2.5.

In Figure 2.3GH, GEM-GECO1 and GEX-GECO1 ratios are expressed on the right hand axis as pCa = $-\log_{10}[Ca^{2+}]$. Ratios were converted to Ca^{2+} concentrations using the equation $[Ca^{2+}] = (K_d{'}^{n} \times (R-R_{min})/ (R_{max}-R))^{1/n}$; where K_d' is the apparent dissociation constant (Table 2.2); n is the Hill coefficient (Table 2.2); R is the experimental ratio; R_{min} is the experimental ratio obtained during ionomycin/EGTA treatment; and R_{max} is the ratio during ionomycin/Ca^{2+} treatment (*222*).

2.5.8 Preparation and imaging of rat hippocampal neuron culture

All experimental procedures were performed in accordance with the guidelines of the Animal Experiment Committee of Hokkaido University. Pregnant Wister rats were decapitated following ether anesthesia. Dissociated hippocampal neurons were prepared at embryonic day 18, and were grown on a homemade 35-mm glass bottom dish containing MEM with 2% B27 Supplement (GIBCO), 2 mM glutamine, 1 mM sodium pyruvate (GIBCO), penicillin-G potassium salt (50 units/mL), and streptomycin sulfate (50 g/mL). On the 4th day *in vitro* (DIV-4), half of the culture medium was replaced with MEM containing 2% FBS, 1×N_2 Supplement (Invitrogen), and penicillin-streptomycin. Neuronal cells were transfected at DIV-7 with pcDNA3-GCaMP3, pcDNA3-G-GECO1 or pcDNA3-R-GECO1 by using calcium phosphate precipitation. Cells were imaged 2-4 days after transfection on a wide-field

epifluorescence inverted microscope (Eclipse Ti-E, Nikon) equipped with a 60× oil objective lens (Plan Apo NA1.4). For excitation of G-GECO1 and GCaMP3, the samples were illuminated with light from a 100 W mercury arc lamp that was passed through 25% and 12.5% neutral density filters and a 480/40 nm bandpass filter. For excitation of R-GECO1, the light was passed through 25% and 50% neutral density filters and 562/40 bandpass filter. The emission filter for G-GECO1 and GCaMP3 was 535/40 nm and for R-GECO1 it was 624/40 nm. Digital images were acquired every 100 ms using an EM-CCD camera (Evolve, Roper) in a 2×2 binning mode.

2.5.9 Preparation and imaging of transgenic C. elegans

To construct the GEM-GECO1 expression plasmid, the GEM-GECO1 coding region (starting from Met36, as numbered in Figure 2.6), was amplified using primers GCaMP_FW_Ce_BamH1 and GCaMP_RV_Ce EcoRI and used to construct a destination vector using the Gateway system (Invitrogen). This was used to make an expression plasmid fragment by LR reaction with an entry vector containing an odr-10 promoter. Transgenic animals were constructed by microinjection of the DNA mixture (100 ng/μL podr-10::GEM-GECO1 plasmid with 100 ng/μL pbLH98, a rescuing lin-15 construct) (*217*).

Imaging in C. elegans was carried out as previously described (*217*), with a slight modification. A worm expressing GEM-GECO1 in the AWA neurons was put into a PDMS microfluidic chip for Ca^{2+} imaging. For imaging of Ca^{2+} response of AWA to odorant, diacetyl (0.02%) was diluted with the imaging buffer (50 mM NaCl, 1 mM $CaCl_2$, 1 mM $MgCl_2$, 0.01% gelatin, and 25 mM HEPES, pH 6.0) and perfused at the top of the worm head. Optical recordings

were performed on an OLYMPUS BX53 upright compound microscope fitted with an ORCA D2 CCD camera (Hamamatsu Photonics K.K.) and an optical block containing the filters as listed in Table 2.5. Fluorescence images were acquired by using HCimage software (Hamamatsu Photonics K.K.) at 1~2 frames/second with a 2×2 binning mode.

2.5.10 Co-imaging of R-GECO1 and a FRET-based ATP indicator

For co-imaging of Ca^{2+} and ATP dynamics, HeLa cells were transfected with pcDNA3-R-GECO1 and either pcDNA3-AT1.03 or pcDNA3-mitAT1.03 (mitochondrial targeting). Cell imaging was performed with an inverted microscope (Eclipse Ti-E, Nikon) equipped with an Orca-R2 digital CCD camera (Hamamatsu Photonics K.K.), a micro-scanning stage MSS-BT110 (Chuo Precision Industrial Co. Ltd.), and a Chamlide IC incubator system (Live Cell Instrument). The MetaMorph software package (Molecular Devices) was used for automated microscope and camera control. Cells were imaged with a 40× oil objective lens (Plan Fluor NA 1.3) and illuminated using a mercury arc lamp thorough 1% and 12.5% ND filters with a 500 ms exposure acquired every 10 s with a 2×2 binning mode for a duration of 20 min. Imaging was performed at 37 °C using a heated chamber on the microscope stage (INUG2-ONI, Tokai Hit). Interference filters used for imaging of R-GECO1 and CFP-YFP are provided in Table 2.5. Prior to imaging of histamine-induced Ca^{2+} and ATP dynamics, HeLa cells were washed twice with DMEM supplemented with 20 mM HEPES, 5.5 mM galactose, and 1 mM pyruvate adjusted to pH 7.3.

2.5.11 Construction of structural models of GECOs

Models of G-, B-, GEM-, and GEX-GECOs (Figures 2.8 and 2.9) were constructed with initial coordinates taken from the atomic structure of Ca^{2+}-bound GCaMP2 (PDB ID 3EVR) (*121*). In the case of B-GECO, PyMOL (www.pymol.org) was used to substitute the GCaMP2 chromophore with the blue FP chromophore (PDB ID 1BFP) through alignment of the α -carbon atoms. The Rosetta fixed backbone design protocol was used to introduce substitutions and repack amino acid side chains for each GECO (*223*). For each substitution, the residue was repacked and minimized on the fixed backbone coordinates of GCaMP2. The energy was then evaluated using Rosetta all-atom energy function.

The R-GECO1 model was constructed with initial coordinates taken from the atomic structures of mCherry (PDB ID 2H5Q) and GCaMP2. The model of the hybrid protein was generated in PyMOL by alignment of the α -carbon atoms of mCherry and the FP portion of GCaMP2. Rosetta molecular modeling software was then used to link both domains using the kinematic closure loop modeling protocol (*224*). Loop residues P60 to V63 (linking M13 and the FP domain) and M300 to T303 (linking FP and calmodulin) were given full backbone and sidechain-rotamer flexibility to link both domains. The lowest energy construct was then selected as the initial input for fixed backbone design where the substitutions unique to R-GECO were made as described for the other GECOs. Output from fixed backbone design for all GECOs was used for generation of Figures 2.8 and 2.9 using PyMOL.

2.6 Supplemental text

2.6.1 A colony based screen for Ca^{2+}-dependent fluorescence changes

To facilitate the discovery and optimization of improved GCaMP variants, we developed a system that enables us to perform an image-based screen for Ca^{2+}-dependent changes of GCaMP fluorescence in colonies of *E. coli*. The key to this system is that the GCaMP is targeted to the *E. coli* periplasm (17), where the initially high concentration Ca^{2+} can be experimentally depleted by treatment with a solution of the high affinity Ca^{2+}-chelator, EGTA. It should be noted that screening libraries of cytoplasmic GCaMPs expressed in colonies of *E. coli* has two major drawbacks. The first is that the Ca^{2+} concentration cannot be readily manipulated. The second is that the intracellular Ca^{2+} concentration is approximately 100 nM (*225*), well below the 542 nM K_d' of GCaMP3 (*153*). Accordingly, GCaMP-type indicators in the *E. coli* cytoplasm will exist almost entirely in the Ca^{2+}-free state and performing directed evolution by picking the brightest colonies of *E. coli* would be counterproductive, as it would favor variants with increased Ca^{2+}-free state brightness and correspondingly decreased dynamic range. Picking the dimmest colonies is also counterproductive, since it is much more likely that dim fluorescence will arise due to poor expression or poor folding (an outcome that could result from many possible mutations), rather than diminished brightness of the Ca^{2+}-free state relative to the Ca^{2+}-bound state (the outcome of only a few rare mutations).

In designing our TorA protein export plasmid (pTorPE), we choose to start from the pBAD/His B (Invitrogen) backbone since the araB promotor provides

tightly regulated L-arabinose-dependent protein expression in *E. coli*. GCaMP3, the most recent addition to the GCaMP-lineage (*153*), was used for validation experiments and as the initial template for directed evolution. The signal peptide of TMAO reductase (TorA) was chosen as the export sequence since it has previously been shown to mediate the export of GFP to the periplasm (17). In an effort to minimize the contribution of residual cytoplasmic protein to the overall fluorescence of each colony, we introduced a C-terminal SsrA sequence (AANDENYALAA) that could induce degradation of cytoplasmic proteins by ClpXP and ClpAP (*226*). During G-GECO evolution we discovered several variants that exhibited more efficient export to the periplasm but contained no mutations in the GECO domain. Some of these clones contained substitutions in the TorA sequence and others had a truncation of the C-terminal SsrA sequence. For all subsequent rounds of screening, we used a version of the pTorPE plasmid that contained an enhanced TorA sequence and no SsrA sequence. The sequence of the enhanced TorA export sequence is MNNNDLFQASRRRFLAQLG[G to S]LT[V to D]AG[M to T]LGPSLLTPRRATAAQAATDAS. Substitutions relative to the original sequence are in brackets.

Our first proof-of-principle experiment was to spray a fine mist of a pH buffered solution of EGTA (2 mM EGTA, 30 mM Tris-HCl, pH 7.4) on a plate of *E. coli* colonies that had been previously transformed with pTorPE-GCaMP3 and grown on 0.0004% L-arabinose (weight/volume). Rewardingly, we observed that the fluorescence intensity of the colonies decreased by about 30% upon application of the EGTA solution. Further investigation revealed that the concentration of free Ca^{2+} in our LB media was 156 μM and that application of the EGTA spray was sufficient to diminish free Ca^{2+} to a concentration (~300 nM)

that was below the GCaMP3 K_d' and thus shift it primarily to the Ca^{2+}-free state. Having demonstrated that it was possible to experimentally-induce Ca^{2+}-dependent changes in GCaMP3 fluorescence in colonies of *E. coli*, we set out to systematically optimize the concentration of L-arabinose present in the growth media. A series of agar plates with concentrations of L-arabinose ranging from 0.0002% to 0.0128% were prepared. E coli was transformed with pTorPE-GCaMP3 and grown on plates for 20 h at 37 °C, followed by 24 h at room temperature. A digital fluorescence image (filters information provided in Table 2.5) of each plate was acquired and then each plate was evenly and identically sprayed with an EGTA solution using a conventional fine mist sprayer. The EGTA solution was allowed to soak into the media until no drops were visible and this procedure of spraying and drying was repeated two additional times. A second digital fluorescence image was acquired and then the two images (before and after spraying) were digitally aligned and processed using Image-Pro Plus (Media Cybernetics) macros. The processing macro calculated the average fluorescence intensities of every colony in both the first (I_{Ca}) and the second image (I_{EGTA}) and exported the values to an spreadsheet where the fluorescence change ($\Delta I = (I_{Ca} - I_{EGTA})/ I_{Ca}$) was calculated for each colony. As shown in Figure 2.12A, I_{Ca} reached a maximum around 0.0032% L-arabinose while ΔI decreased substantially at concentrations of L-arabinose greater than 0.0016%. In addition, we observed morphological changes in some colonies at concentrations of L-arabinose greater than 0.0032%. Based on these results we used 0.0002% to 0.0008% L-arabinose for all subsequent experiments.

To ensure that the export system was working as it had had been designed to do, we performed control experiments in which either buffered solution lacking

EGTA was sprayed on the plate or in which GCaMP3 was confined to the cytoplasm (Figure 2.12B). These control experiments revealed that both export to the periplasm and the application of EGTA were necessary in order to achieve a robust Ca^{2+}-dependent change in fluorescence intensity. Specifically, when using the export system we obtained of ΔI values of 0.24 ± 0.044. The value ΔI was reduced to close to the level of the noise if buffer lacking EGTA was sprayed on identically treated colonies (0.019 ± 0.017) or if GCaMP3 was expressed without the TorA tag (0.038 ± 0.024).

To augment our primary colony-based screen, we sought to add a secondary screening step in which the Ca^{2+}-dependent change in fluorescence of each of the top variants was assessed using protein extracted from the periplasmic fraction of *E. coli* that had been grown in liquid culture overnight. To test the effectiveness of this procedure, the dynamic ranges of GCaMP3 in both the periplasmic fraction (osmotic shock fluid) and the cytoplasmic fraction (B-PER (Pierce) extraction) were tested using a fluorescence microplate reader. This test revealed that the dynamic range of GCaMP3 was about 330% in osmotic shock fluid and about 180% in B-PER (Figure 2.12C). We attribute the increased dynamic range in the osmotic shock fluid to the decreased autofluorescence relative to B-PER. It should be noted that the osmotic shock fluid contains 5 mM Mg^{2+} so variants with poor selectivity for Ca^{2+} relative to Mg^{2+} could be identified and discarded at this step. Accordingly, testing of the osmotic shock fluid was used as our secondary assay during all library screening.

In principle, our screening strategy could be adapted to screening of genetically encoded fluorescent indicators for other analyte, such as pH, small molecules and other metal ions.

2.6.2 Comparing the properties of GECO variants to small molecule indicators

Despite the widespread availability of genetically encoded protein-based Ca^{2+} indicators, synthetic organic dye-based Ca^{2+} indicators remain popular tools in live cell imaging applications (1, 19). The ongoing popularity of dye-based Ca^{2+} indicators is attributable to several factors which include: the wide selection of fluorescent hues; their high intensiometric and ratiometric signal changes; and a simple loading procedure that involves incubating tissue with a membrane-permeant form of the indicator. Disadvantages of dye-based indicators, relative to protein-based indicators, include: the lack of a straightforward method for targeting to specific subcellular localizations or specific subset of cells; a more invasive loading procedure (*i.e.*, loading of membrane permeable dyes vs. transfection and virus infection); impossible to use for chronic imaging; and, obviously, the inability to create stable cell lines or transgenic animals that permanently express the indicator.

The GECO series of Ca^{2+} indicators has effectively narrowed the gap, at least in terms of color selection and the signal changes, between the synthetic dye-based indicators and the genetically encoded indicators. Indeed, several of the new GECO variants have spectral properties (Table 2.2) that, ostensibly, resemble those of popular dye-based indicators. Specifically, parallels can be drawn between: the G-GECOs and fluo-3; GEX-GECO1 and fura-2; GEM-GECO1 and indo-1; and R-GECO1 and rhod-2. Fluo-3, like the G-GECOs, is a green intensiometric indicator, with a ~100× signal change (G-GECOs, ~25×) and a K_d' of ~400 nM (G-GECOs, ~600-1000 nM). One important advantage of fluor-3

relative to the G-GECOs is its relatively low pK_a of ~5 (G-GECOs, ~7.2-7.6) that renders it insensitive to physiologically relevant changes in pH. Rhod-2, like R-GECO1, is a red intensiometric indicator with a ~200× signal change (R-GECO1, ~16×) and a K_d' of ~600 nM (R-GECO1, ~500 nM). Fura-2, like GEX-GECO1, exhibits excitation ratiometric green fluorescence and binds Ca^{2+} with a K_d' of ~100-200 nM (GEX-GECO1, ~300 nM). One disadvantage of fura-2 relative to GEX-GECO1 is that fura-2 is excited at UV wavelengths (~340 nm and ~380 nm) whereas GEX-GEXO1 is excited in the visible range (~400 nm and ~480 nm). Of the examples provided here, the greatest similarity in terms of spectral properties is between indo-1 and GEM-GECO1. Indo-1 is an emission ratiometric indicator that emits at ~400 nm and ~480 nm (GEM-GECO1, 460 nm and 510 nm) when excited at ~350 nm (GEM-GECO1, ~400 nm), and that has a K_d' of ~250 nM (GEM-GECO1, ~340 nM).Values for synthetic dye indicators are from obtained from published literature (1, 19) and the Molecular Probes Handbook (available online at www.invitrogen.com).

Based on the comparisons provided above, it is apparent that, in terms of the range of hues and Ca^{2+} affinities available, genetically encoded indicators may one day surpass synthetic indicators. One aspect that was not mentioned above were the kinetics of Ca^{2+} binding and dissociation. The synthetic indicators discussed above have dissociation rate constants (k_{off}) that are typically 10^2-10^4× times faster (*211*) than the k_{off} values for the GECOs (Table 2.3). While modest improvements in the kinetics of protein-based indicators are certain to be realized, it is unlikely that they could ever rival dye-based indicators in this respect. However, the slower kinetics of genetically encoded indicators do not hamper

their usefulness in many typical experiments, as we have demonstrated with co-imaging of fura-2 with either G-GECO1.2 or R-GECO1 (Figure 2.13).

2.6.3 Ca^{2+} dissociation constants and dynamic range of GECO variants

To realize maximum sensitivity, a Ca^{2+} indicator should have a K_d' that is between the lowest and highest physiological Ca^{2+} concentrations that are expected in a given experiment, and so the K_d' of a particular Ca^{2+} indicator will dictate the type of experiments that it is best suited for (*222*). The concentration of the Ca^{2+} in the cytoplasm of a resting cell is typically below 100 nM and, following pharmacological stimulation, can rise to values of 1-10 μM. Accordingly, the GECOs, with their K_d' values of ~200 nM (B-GECO1), ~300 nM (GEX- and GEM-GECO1), ~500 nM (R-GECO1), ~600 mM (G-GECO1.1), ~700 (G-GECO1), and ~ 1.1 μM (G-GECO1.2), are generally well positioned for imaging of these changes. More specifically, the indicators with sub μM K_d' values, such as B-GECO1, GEX-GECO1, GEM-GECO1, R-GECO1, G-GECO1, and G-GECO1.1, are most sensitive to changes in the 100 nM to 1 μM range, but are less sensitive to changes in the 1-10 μM range (where G-GECO1.2 would be preferred), and insensitive to changes above 10 μM. Spontaneous Ca^{2+} oscillations (e.g., in neuronal culture) or evoked responses in whole animals (e.g., odor evoked response in C. elegans) will not generate such high transient Ca^{2+} concentrations, and so indicators with K_d' values of 100 nM or less would be ideal. However, for indicators with exceptionally high ratiometric changes, such as GEM-GECO1, their useful range is broadened to both higher and lower Ca^{2+} concentrations. Accordingly, we expect that GEM-GECO1 will be useful for imaging of spontaneous Ca^{2+} in a wide variety of contexts and cell types. Future

work on optimizing of GECO variants may provide variants with K_d' values of 50 nM or less, which should provide improved signal change during spontaneous and evoked changes in Ca^{2+} concentration. For imaging of Ca^{2+} dynamics in the ER, it will be necessary to engineer GECO variants with K_d' values in the 10s of μM (*222*).

2.7 Supporting Figures

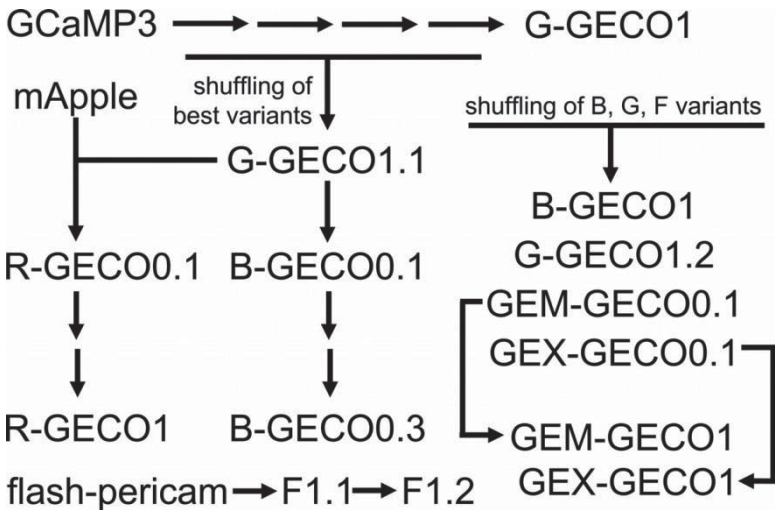

Figure 2.5 GECO genealogy.

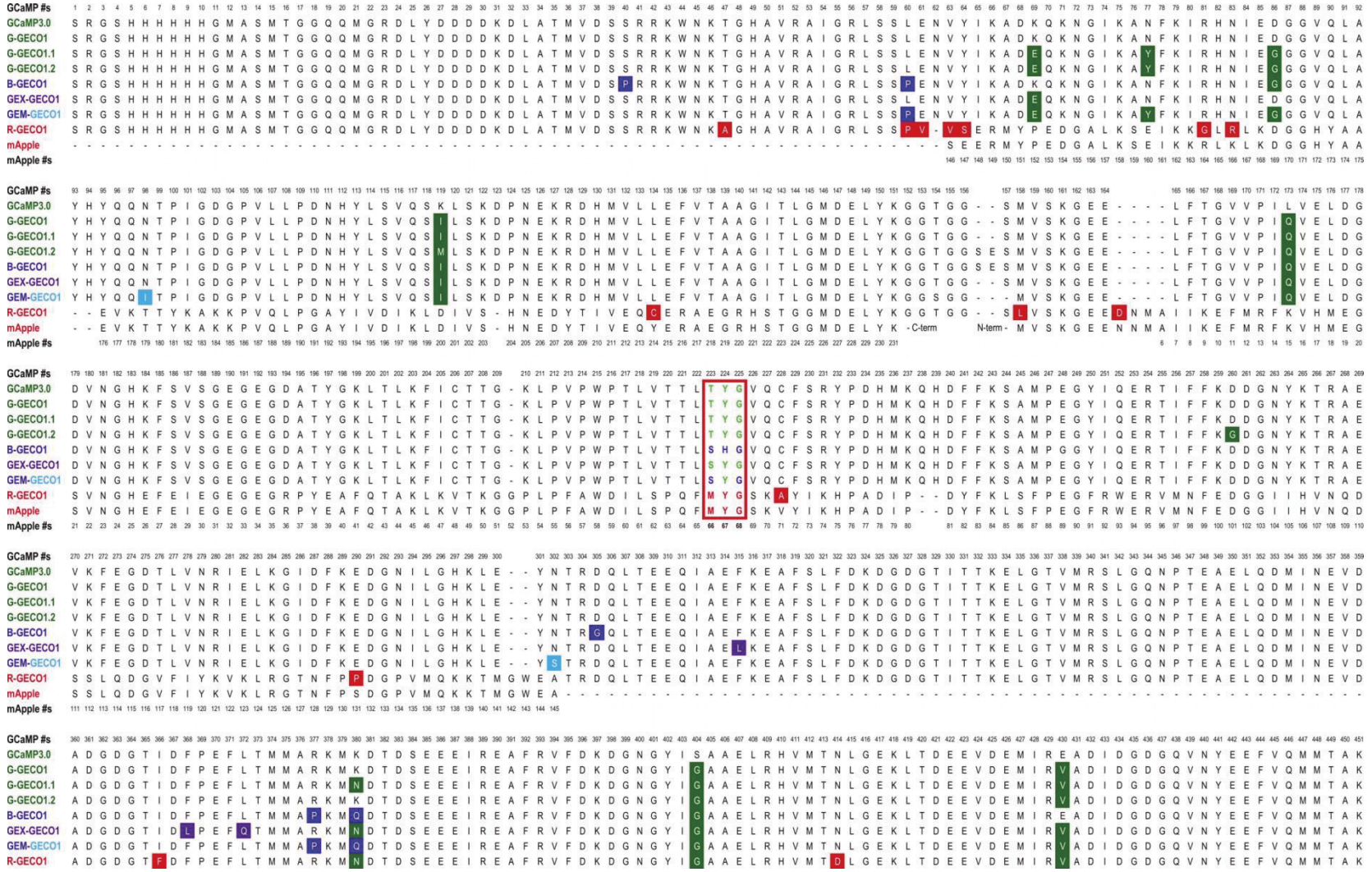
GCaMP #s
GCaMP3.0
G-GECO1
G-GECO1.1
G-GECO1.2
B-GECO1
GEX-GECO1
GEM-GECO1
R-GECO1
mApple
mApple #s
C-term
N-term

Figure 2.6 Sequence alignment of new variants described in this work.

Substitutions are summarized in Table 2.1. The numbering is consistent with that previously used for GCaMP variants that included the His-tag-containing leader sequence (*153*). In the current work the leader sequence was included only for bacterial expression. For expression in cell culture and *C. elegans*, the leader sequence was removed such that M36 was the first residue of the protein.

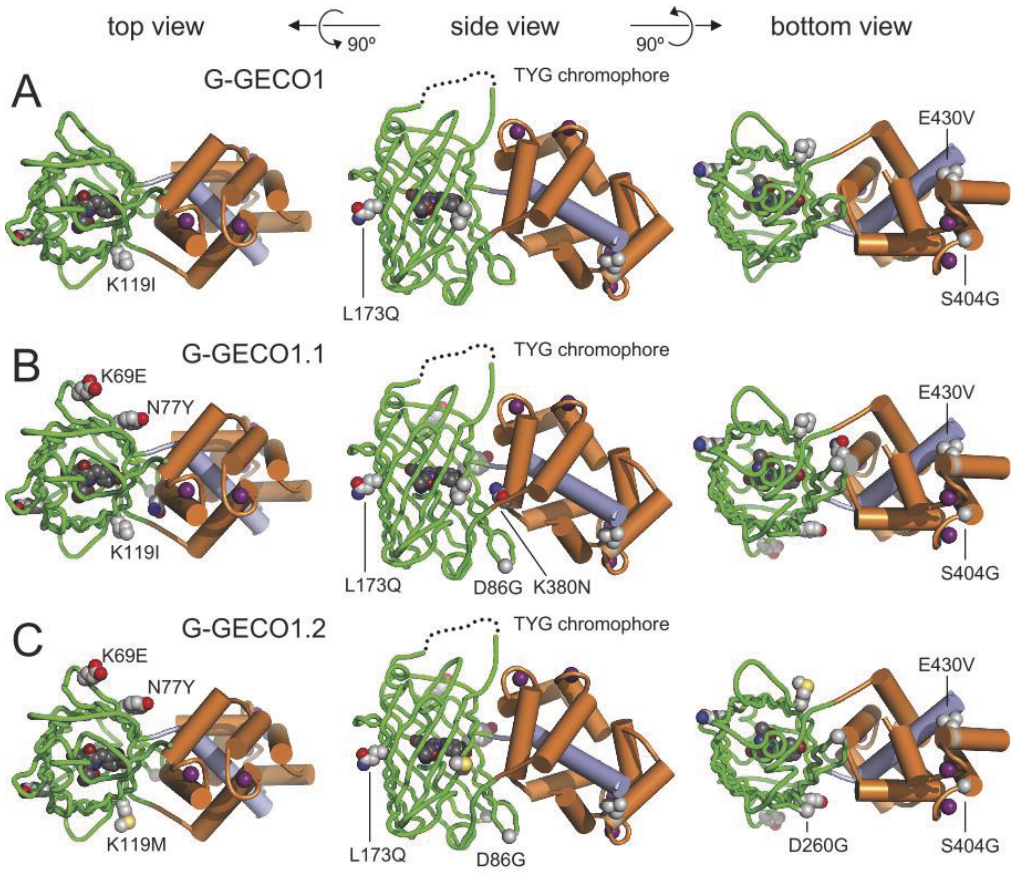

Figure 2.7 Location of substitutions in modeled structures of (A) G-GECO1; (B) G-GECO1.1; and (C) G-GECO1.2.

All substitutions are relative to GCaMP3 (*153*). Three views of each protein are provided, with substituted residues represented only once within each set of three views. The dotted line represents the linker that connects the former N- and C-terminus in the cpFP. Note that all three G-GECOs have substitutions at a residue of CaM that interacts with M13 (E430V) and a residue within the FP that interacts with the FP to CaM linker (K119I or M). G-GECO1.1 and 1.2 have a third substitution in close proximity to the M13 to FP linker (N77Y). We speculate that these substitutions conspire to subtly change the orientation of both M13 and CaM

relative to the FP domain, which in turn modulates the chromophore environment such that its pK_a is increased in both the Ca^{2+}-free and Ca^{2+}-bound states (Table 2.2). This increase in the pK_a diminishes the fluorescence of the chromophore in the Ca^{2+}-free state by shifting it further toward the neutral (non-fluorescent) form and away from the anionic (green fluorescent) form.

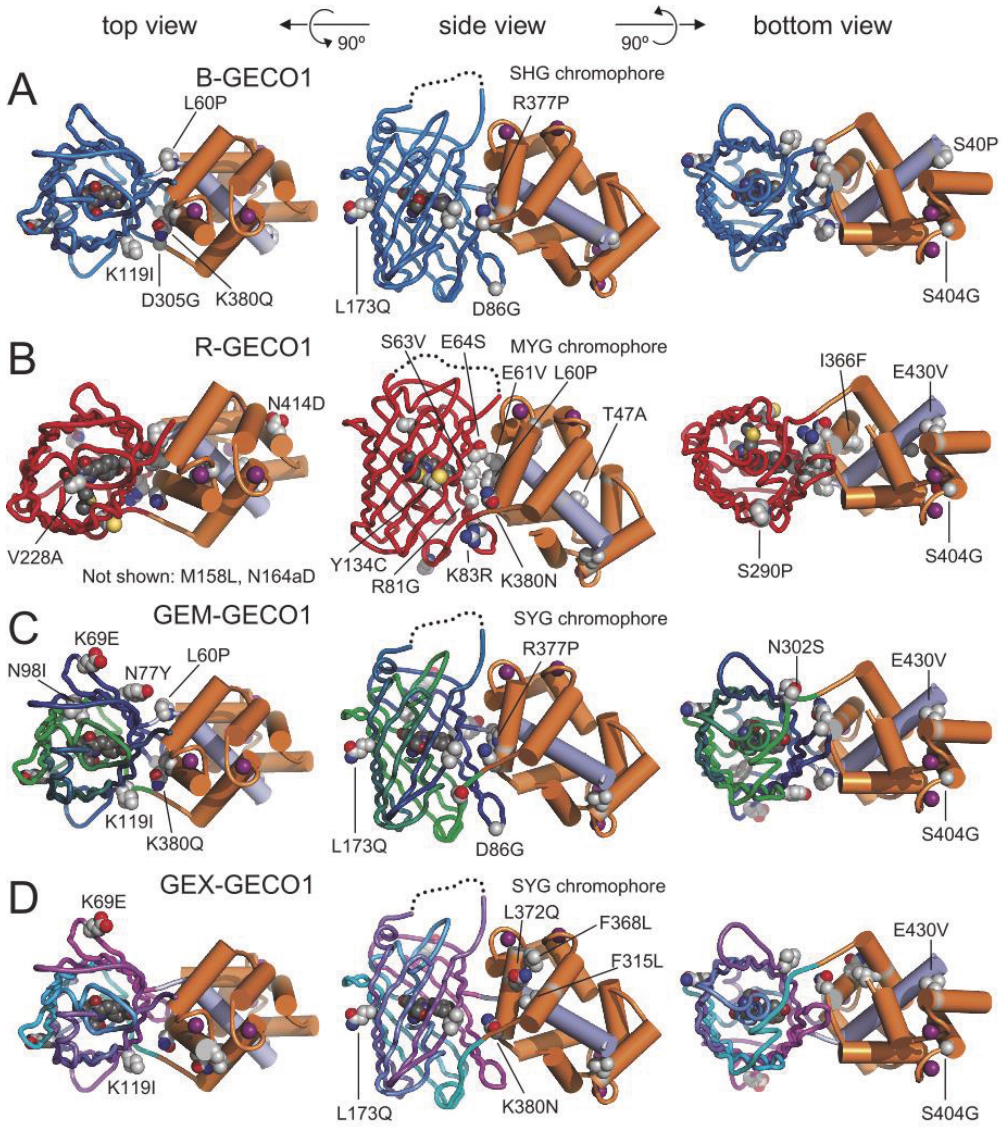

Figure 2.8 Location of substitutions in modeled structures of (A) B-GECO1; (B) R-GECO1; (C) GEM-GECO1; and (D) GEX-GECO1.

All substitutions are relative to GCaMP3 (*153*), except those within the mApple-derived portion of R-GECO1, which are relative to mApple (*67*). The R377P substitution present in both B-GECO1 and GEM-GECO1 occurs in an α -helical region of CaM. In the modeled structure, the proline is in an unrealistic high-energy conformation that clashes with the adjacent residues in the α -helix. We have chosen to keep the backbone fixed for the models represented here, although it is apparent that a substantial reorganization of this region of CaM must accompany this substitution. Detailed structural characterization by X-ray crystallography will be necessary in order to fully elucidate the effect of R377P and all other substitutions on the structure and mechanism of these Ca^{2+} indicators.

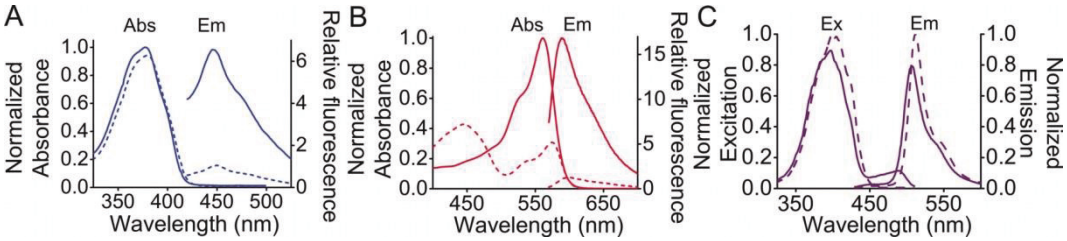

Figure 2.9 Additional spectral characterization of GECOs described in this work.

For all panels, the Ca^{2+}-free state is represented with a dotted line and Ca^{2+}-bound state is represented with a solid line. (**A**) Absorbance (Abs) and emission spectra (Em) of B-GECO1; (**B**) Absorbance and emission spectra of R-GECO1; and (**C**) Excitation (Ex) and emission spectra of GEX-GECO1.

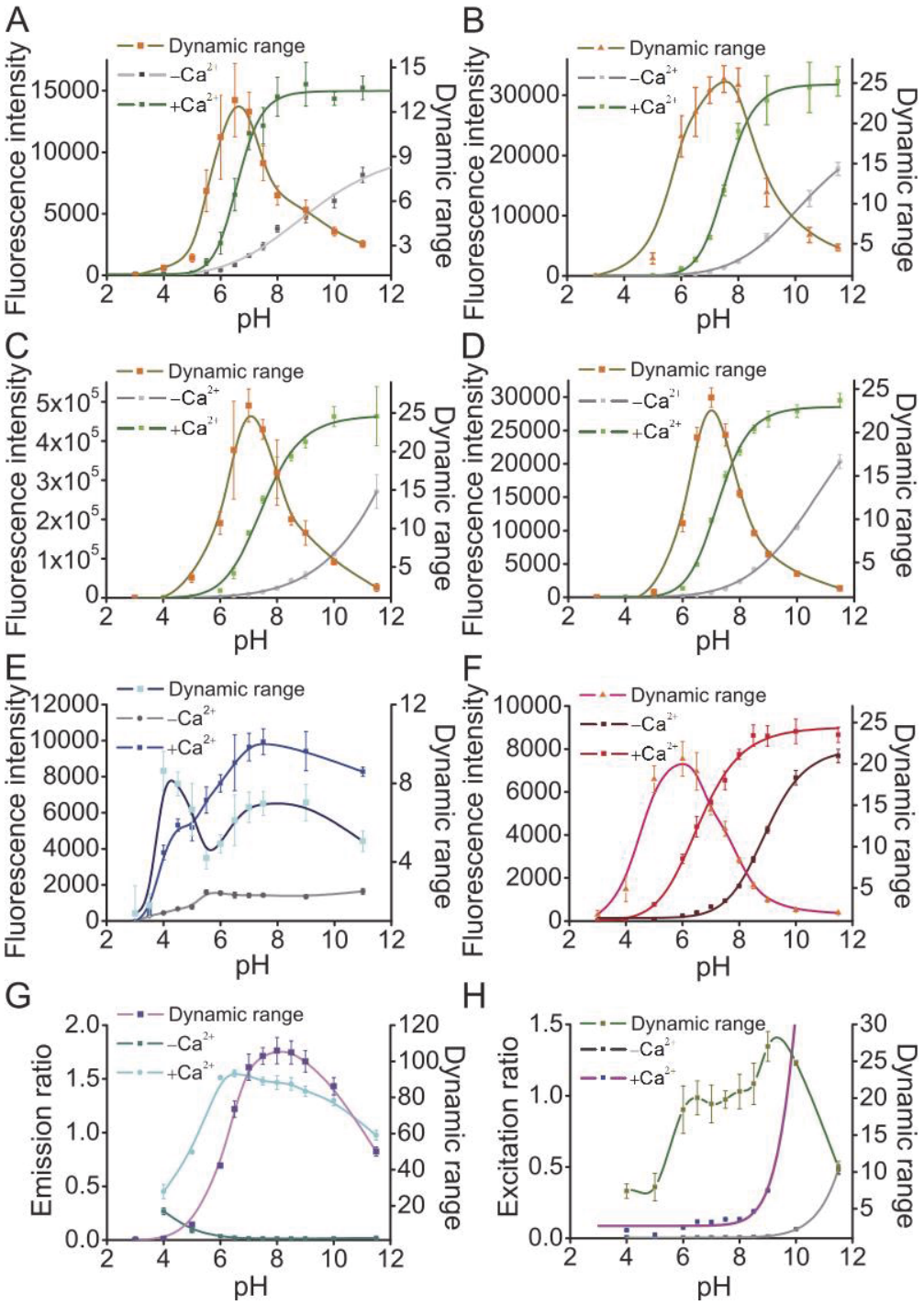

Figure 2.10 Intensity (or ratio) and dynamic range of GECOs as a function of pH.

The dynamic range is calculated by dividing the intensity (or ratio) of the Ca^{2+}-bound state by the intensity (or ratio) of the Ca^{2+}-free state. Experimental pK_a values are summarized in Table 2.2. (**A**) GCaMP3; (**B**) G-GECO1; (**C**) G-GECO1.1; (**D**) G-GECO1.2; (**E**) B-GECO1; (**F**) R-GECO1; (**G**) GEM-GECO1; and (**H**) GEX-GECO1.

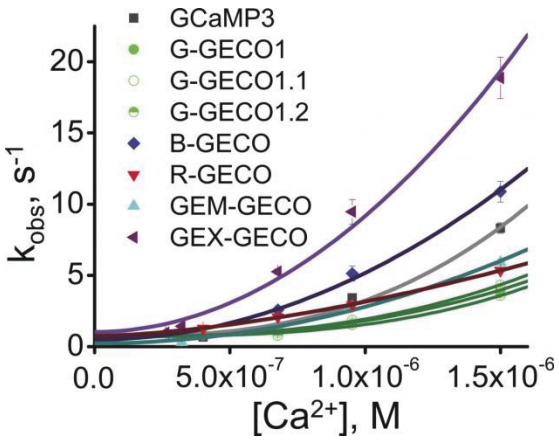

Figure 2.11 Stopped flow kinetic characterization of GECOs.

Observed relaxation rate constants (k_{obs}) are plotted as a function of Ca^{2+} for each of the GECOs described in this work. Association and dissociation rate constants (k_{on} and k_{off}, respectively) were determined by fitting to the equation $k_{obs} = k_{on}[Ca^{2+}]^n + k_{off}$. Values are tabulated in Table 2.3.

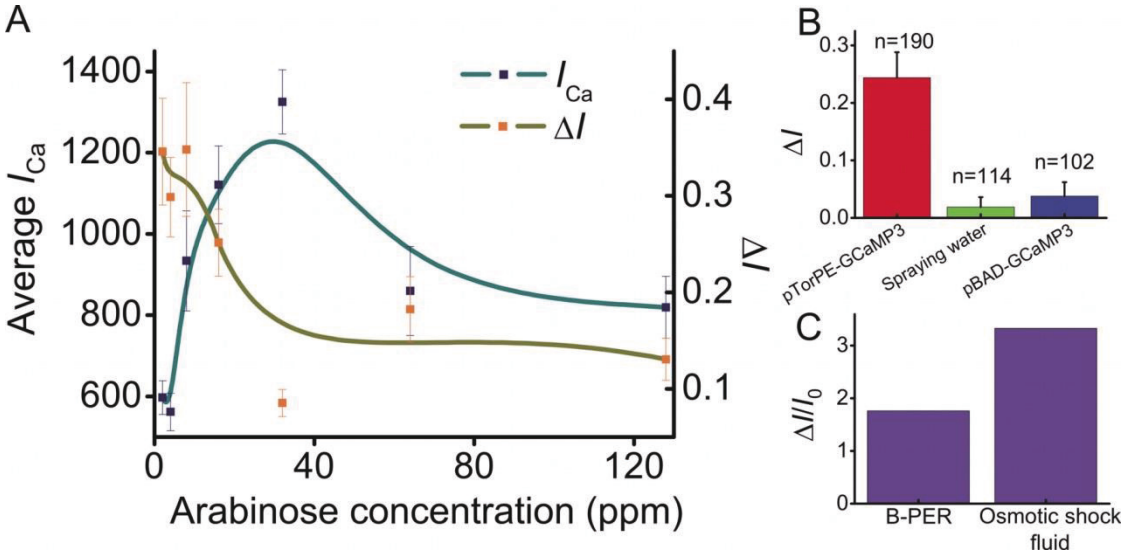

Figure 2.12 Validation and optimization of the colony based screen for Ca^{2+}-dependent fluorescence changes.

(**A**) Brightness and dynamic range as a function of L-arabinose concentration in the growth media. The smoothed lines are shown to emphasize the trend in each data set. (**B**) Control experiments to determine if both export to the periplasm and the application of EGTA are necessary in order to achieve Ca^{2+}-dependent fluorescent changes in fluorescence intensity. (**C**) Comparison of the dynamic range of GCaMP3 extracted from bacteria in osmotic shock fluid and in B-PER.

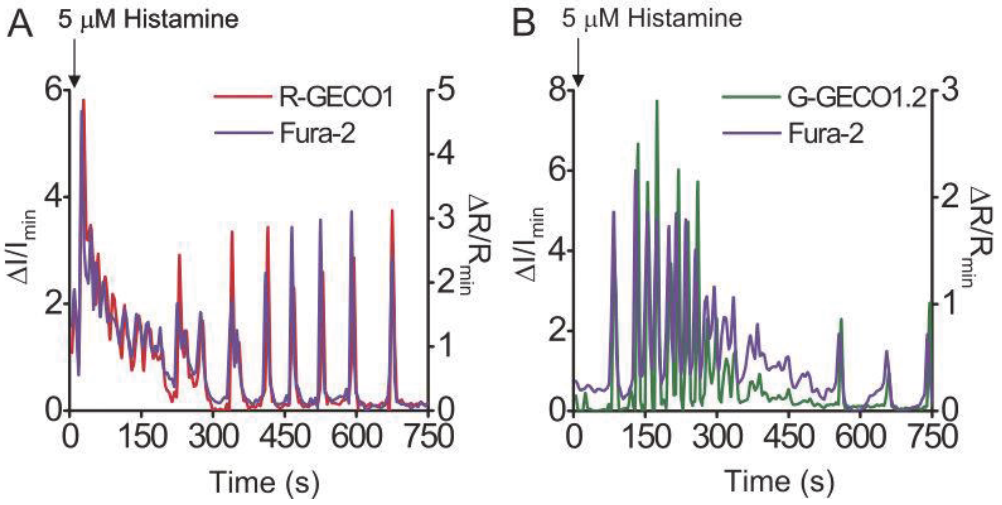

Figure 2.13 Co-imaging of fura-2 and either R-GECO1 (A) or G-GECO1.2 (B).

The slight offset between peaks for the two indicators arises from the sequential acquisition of images at each time point.

2.8 Supporting Tables

Table 2.1 List of all substitutions for GECOs described in this work

Protein	Substitutions relative to GCaMP3 unless otherwise noted

G-GECO0.5	K119I/L173Q/S404G
G-GECO1	K119I/L173Q/S404G/E430V
G-GECO1.1	K69E/N77Y/D86G/K119I/L173Q/K380N/S404G/E430V
G-GECO1.2	K69E/N77Y/D86G/K119I/L173Q/D260G/S404G/E430V
B-GECO0.1	K69E/N77Y/D86G/K119I/L173Q/T223S/Y224H/ R377P/K380Q/ S404G/E430V
B-GECO1	S40P/L60P/D86G/K119I/L173Q/T223S/Y224H/D305G/R377P/K380Q/ S404G
R-GECO1	Substitutions relative to the mApple-derived analogue of GCaMP3: T47A/L60P/E61V/S63V/E64S/R81G/K83R/Y134C/M158L/N164aD/V228A/ S290P/I366F/K380N/S404G/N414D/E430V
GEM-GECO1	L60P/K69E/N77Y/D86G/N98I/K119I/L173Q/T223S/N302S/R377P/K380Q/S 404G/E430V
GEX-GECO1	K69E/K119I/L173Q/T223S/F315L/F368L/L372Q/K380N/S404G/E430V
flash-pericam1.1	Substitutions relative to flash-pericam: Q70L/M246L/H304L
flash-pericam1.2	Substitutions relative to flash-pericam: Q70L/D86G/M246L/H304L

Table 2.2 Properties of final GECOs and selected intermediates.

Protein	Ca^{2+}	λ_{abs} (nm) with ε ($mM^{-1}·cm^{-1}$) in parenthesis	λ_{em} with Φ in parenthesis	Brightness [1] ($mM^{-1}·cm^{-1}$)	pK_a	Intensity or ratio change[2] ± Ca^{2+}	K_d' for Ca^{2+} (nM) with Hill coefficient in parenthesis
GCaMP3	-	399 (36); 496 (11)	513 (0.20)	2	8.73	12×	542 (2.73)
	+	399 (20); 496 (50)	513 (0.44)	22	6.6		
G-GECO0.5	-	398 (41); 496 (3.4)	512 (0.23)	0.78	10.07	20×	957 (1.98)
	+	398 (16); 496 (44)	512 (0.40)	17.6	7.19		
G-GECO1	-	398 (42); 496 (3)	512 (0.22)	0.66	10.05	25×	749 (2.97)
	+	398 (25); 496 (41)	512 (0.42)	17.2	7.57		
G-GECO1.1	-	398 (42); 496 (3)	512 (0.20)	0.6	10.19	26×	618 (2.05)
	+	398 (28); 496 (34)	512 (0.46)	15.6	7.5		
G-GECO1.2	-	402 (37); 498 (2)	513 (0.25)	0.5	10.44	23×	1150 (2.11)
	+	402 (22); 498 (33)	513 (0.36)	11.9	7.24		
B-GECO0.1	-	380 (14)	446 (0.028)	0.39	5.03	4.3×	260 (2.28)
	+	380 (14)	446 (0.12)	1.7			

B-GECO1	-	378 (22)	446 (0.02)	0.44	5.04	7×	164 (2.64)
	+	378 (23)	446 (0.18)	4.1	5.60		
R-GECO1	-	445 (22); 577 (15)	600 (0.06)	0.72	8.9	16×	482 (2.06)
	+	445 (9); 561 (51)	589 (0.20)	10.2	6.59		
GEM-GECO1	-	397 (34)	511 (0.31)	10.2	6.16[5]	110×	340 (2.94)
	+	390 (36)	455 (0.18)	6.5			
GEX-GECO1	-	397 (32), 482 (0)	512 (0.21)	6.7	~6[5]	26×	318 (2.78)
	+	390 (32), 482 (2.5)	506 (0.19, 0.39)[3]	6.1, 1[4]			

[1]Brightness is defined as the product of ε and Φ. [2]Defined as the ratio of emission intensities for intensiometric GECOs, the ratio of emission ratios for GEM-GECO1, and the ratio of excitation ratios for GEX-GECO1, where the Ca^{2+}-bound state is the numerator and the Ca^{2+}-free state is the denominator. For R-GECO1, which undergoes an 11 nm blue shift when it binds Ca^{2+}, the intensity at 589 nm is used for both states. The emission ratio for GEM-GECO1 is defined as (fluorescence intensity for excitation at 390 nm and emission at 455 nm)/ (fluorescence intensity for excitation at 390 nm and emission at 511 nm). The excitation ratio for GEX-GECO1 is defined as (fluorescence intensity for excitation at 395 nm and emission at 512 nm)/ (fluorescence intensity for excitation at 450 nm and emission at 512 nm). [3]Quantum yield of GEX-GECO1 in the Ca^{2+}-bound state was measured for excitation at both 390 nm and 482 nm. [4]The brightness of GEX-GECO1 in the Ca^{2+}-bound state for excitation at both 390 nm and 482 nm is provided. [5]The pK_a of GEM-GECO1 and GEX-GECO1 is the pH at which the dynamic range is 50% of maximum.

Table 2.3 Kinetic characterization of final GECOs.

Protein	k_{on} ($M^{-n}s^{-1}$)	k_{off} (s^{-1})	n	K_d', kinetic (nM) [1]	K_d', static (nM) [2]
GCaMP3	6.26×10^{16}	0.700	2.7	618	542
G-GECO1	9.08×10^{15}	0.700	2.7	831	749
G-GECO1.1	8.17×10^{15}	0.675	2.6	809	618
G-GECO1.2	8.55×10^{17}	0.700	3.0	936	1150
B-GECO1	4.68×10^{12}	0.490	2.0	324	164
R-GECO1	9.52×10^{9}	0.752	1.6	484	482
GEX-GECO1	8.14×10^{12}	1.030	2.0	356	318
GEM-GECO1	2.58×10^{12}	0.224	2.0	295	340

[1] $K_d'_{, kinetic} = (k_{off}/k_{on})^{1/n}$. [2] From **Table 2.2**

Table 2.4 Systematic characterization of the Ca^{2+}-dependent fluorescence of GECOs in HeLa cells.

Cells were treated first with histamine (abb. His), then with Ca^{2+}/ionomycin (abb. Ca^{2+}), and finally with EGTA/ionomycin (abb. EGTA).

Protein	n[1]	Maximum Ca^{2+} to minimum EGTA ratio	Maximum His to minimum His ratio	Maximum His to maximum Ca ratio
GCaMP3	38	5.3±2.3	4.6±0.9	0.71±0.14
G-GECO1	31	9.4±2.6	8.2±4.0	0.64±0.22
G-GECO1.1	38	11.6±2.9	11.7±3.4	0.69±0.22
G-GECO1.2	42	19.0±7.4	10.2±4.7	0.72±0.43
B-GECO1	38	4.2±1.6	3.5±0.9	0.83±0.26
R-GECO1	22	4.9±1.9	9.2±1.3	0.98±0.15
GEM-GECO1	29	28.5±11.7	28.2±14.7	0.86±0.19
GEX-GECO1	50	10.6±4.1	9.7±3.5	1.04±0.40

[1]Number of individual transfected cells on which systematic calibration experiments were performed.

Table 2.5 Filters[1] for screening and live cell imaging.

Protein	Colony-based screening	HeLa cell culture	Rat hippocampal neuron culture	*C. elegans*
GCaMP3, flash-pericam, G-GECO series	Ex: 470/40 nm Dichroic: none Em: 525/50 nm	Ex: 470/40 nm Dichroic: 505 nm Em: 510 nm long pass or 520/35 nm	Ex: 480/40 nm Dichroic: 505 nm Em: 535/40 nm	N/A[2]
B-GECO1	Ex: 395/40 nm Dichroic: none Em: 460/40 nm	Ex: 370/36 nm Dichroic: 409 nm Em: 400 nm long pass or 447/60 nm	N/A	N/A
R-GECO1	Ex: 535/50 nm Dichroic: none Em: 610/75 nm	Ex: 562/40 nm Dichroic: 593 nm Em: 624/40 nm	Ex: 562/40 nm Dichroic: 593 nm Em: 624/40 nm	N/A
GEM-GECO1	Ex: 395/40 nm Dichroic: none Em1: 460/40 nm Em2: 525/50 nm	Ex: 377/50 nm Dichroic: 409 nm Em1: 447/40 nm Em2: 520/35 nm	N/A	Ex: 414/46 nm Dichroic: 450 nm Em1: 483/32 nm Em2: 542/27 nm
GEX-GECO1	Ex1: 395/40 nm Ex2: 470/40 nm Dichroic: none Em: 535/30 nm	Ex1: 365/50 nm Ex2: 475/40 nm Dichroic: 495 nm Em: 520/35 nm	N/A	N/A

Protein	Colony-based screening	HeLa cell culture	Rat hippocampal neuron culture	*C. elegans*
CFP-YFP FRET pair	N/A	Ex: 438/24 nm Dichroic: 458 nm Em1: 483/32 nm Em2: 534/30 nm	N/A	N/A
Fura-2	N/A	Ex1: 340/26 nm Ex2: 387/11 nm Dichroic: 409 nm Em: 510/84 nm	N/A	N/A

[1]Bandpass filters are defined using the convention of center wavelength/full bandwidth in nm unless otherwise noted. Filters were purchased from Semrock and Chroma. [2]Not applicable.

Table 2.6 Oligonucleotides used in this work

Name	Sequence (5' to 3')
FW_TorA	GCGATGCCATGGGTTTAAAGAGGAGAAAGGTCATGAACA ATAACGATCTCTTTCAG
RV_TorA	ATGATGAGAACCTCTAGAAGCGTCAGTCGCCGCTTG
FW_6His	GACGCTTCTAGAGGTTCTCATCATCATCATCATCATGG
RV_SsrA-GCaMP3	GCGATGAAGCTTCTAAGCTGCTAAAGCGTAGTTTTCGTC GTTTGCTGCCCCGGGACCACCCTTCGCTGTCATCATTTG TACAAACTCTTCGTAGTTT
FW_XbaI-6His	GCGATGTCTAGAGGTTCTCATCATCATCATCATCATGGT ATGGCTAGC
RV_GCaMP-XmaI	GCGATGCCCGGGACCACCCTTCGCTGTCATCATTTGTAC AAACTCTTCGTAGTTT
RV_GCaMP-Stop-HindIII	GCGATGAAGCTTCTACTTCGCTGTCATCATTTGTACAAA CTCTTCGTAGTTT
FW_GCaMP3_c105a	GATAAGGATCTCGCCACAATGGTCGACTCATCACG
G-B_V63VILM	AGGTCGGCTGAGCTCACTAGAGAACVTVTATATCAAGGC CGACAAG
G-B_T223ST_Y224H	CTCGTGACCACCCTGWCNCACGGCGTGCAGTGCT
G-B_R377X_N380X	GACTTCCCTGAGTTCCTGACAATGATGGCANNKAAAATG NNKGACACAGACAGTGAAGAAGAAATTAGAGAA
FW_XhoI-X-148mc	GCGATGCTCGAGKBYGAGCGGATGTACCCCGAGGAC
FW_XhoI-X-147mc	GCGATCCTCGAGKBYTCCGAGCGGATGTACCCCG
RV_GGTGGS-mCherry	ACTCCCGCCTGTACCTCCCTTGTACAGCTCGTCCATGCC GC
RV_MluI-X 144mc	GGCATGACGCGTRVMCTCCCAGCCCATGGTCTTCTTCTG
RV_MluI-X 143mc	GGCATGACGCGTRVMCCAGCCCATGGTCTTCTTCTGCAT

FW_GGTGGS-mCherry	GGGAGGTACAGGCGGGAGTATGGTGAGCAAGGGCGAGGAGGATAA
Destroy_MluI	CAAAGCCATGACAAAAACGCGAAACAAAAGTGTCTATAATCAC
GCaMP_FW_BamH1	GAGGATCCACCATGGTCGACTCATCACGTC
GCaMP_RV_EcoR1	CGCGAATTCTTACTTCGCTGTCATCATTTGTAC
Cpd_S5P_FW_BamH1	GAGGATCCACCATGGTCGACTCA**C**CACGTC
T7_FW	TAATACGACTCACTATAGG
F-EGFP-C	CATGGTCCTGCTGGAGTTCGTG
BGH_RV	TAGAAGGCACAGTCGAGG
GCaMP_2NLS_FW1	GAAGGTCGATCCTAAGAAGAAACGCAAGGTGATGGTCGACTCATCACGTC
Cpd_2NLS_FW1	GAAGGTCGATCCTAAGAAGAAACGCAAGGTGATGGTCGACTCACCACGTC
Cpd_2NLS_FW2	GAGGATCCACCATGGACCCAAAAAAGAAGCGGAAGGTCGATCCTAAGAAG
GCaMP_FW_BamH1_mito	GAGGATCCAACCATGGTCGACTCATCACGTC
Cpd_S5P_FW_BamH1_mito	GAGGATCCAACCATGGTCGACTCA**C**CACGTC
GCaMP_FW_Ce_BamH1	CGACGGATCCAAAAAATGGTCGACTCATCACGTCG
GCaMP_RV_Ce EcoR1	CGACGAATTCTTACTTCGCTGTCATCATTTGTAC

2.9 References and Notes

67. N. C. Shaner *et al.*, Improving the photostability of bright monomeric orange and red fluorescent proteins. *Nature Methods* **5**, 545 (2008).

92. T. Nagai, A. Sawano, E. S. Park, A. Miyawaki, Circularly permuted green fluorescent proteins engineered to sense Ca^{2+}. *Proceedings of the National Academy of Sciences of the United States of America* **98**, 3197 (2001).

95. J. Nakai, M. Ohkura, K. Imoto, A high signal-to-noise Ca^{2+} probe composed of a single green fluorescent protein. *Nature Biotechnology* **19**, 137 (2001).

99. G. Grynkiewicz, M. Poenie, R. Y. Tsien, A new generation of Ca^{2+} indicators with greatly improved fluorescence properties. *Journal of Biological Chemistry* **260**, 3440 (1985).

121. Q. Wang, B. Shui, M. I. Kotlikoff, H. Sondermann, Structural Basis for Calcium Sensing by GCaMP2. *Structure* **16**, 1817 (2008).

122. J. Akerboom *et al.*, Crystal Structures of the GCaMP Calcium Sensor Reveal the Mechanism of Fluorescence Signal Change and Aid Rational Design. *Journal of Biological Chemistry* **284**, 6455 (2009).

143. A. Miyawaki *et al.*, Fluorescent indicators for Ca^{2+} based on green fluorescent proteins and calmodulin. *Nature* **388**, 882 (1997).

153. L. Tian *et al.*, Imaging neural activity in worms, flies and mice with improved GCaMP calcium indicators. *Nature Methods* **6**, 875 (2009).

211. R. Y. Tsien, *Monitoring cell calcium*. Calcium as a cellular regulator (Oxford University Press, Oxford, UK, New York, 1999), pp. 28-54.

212. Single-letter abbreviations for amino acid residues are: A, Ala; C, Cys; D, Asp; E, Glu; F, Phe; G, Gly; H, His; I, Ile; K, Lys; L, Leu; M, Met; N, Asn; P, Pro; Q, Gln; R, Arg; S, Ser; T, Thr; V, Val; W, Trp; and Y, Tyr.

213. Y. N. Tallini *et al.*, Imaging cellular signals in the heart *in vivo*: Cardiac expression of the high-signal Ca^{2+} indicator GCaMP2. *Proceedings of the National Academy of Sciences of the United States of America* **103**, 4753 (2006).

214. Materials and methods are available as supporting material at *Science* Online.

215. C. M. Barrett, N. Ray, J. D. Thomas, C. Robinson, A. Bolhuis, Quantitative export of a reporter protein, GFP, by the twin-arginine translocation pathway in *Escherichia coli*. *Biochemical and Biophysical Research Communications* **304**, 279 (2003).

216. H. Zhao, W. Zha, *In vitro*'sexual'evolution through the PCR-based staggered extension process (StEP). *Nature Protocols* **1**, 1865 (2006).

217. Y. Shinkai *et al.*, Behavioral choice between conflicting alternatives is regulated by a receptor guanylyl cyclase, GCY-28, and a receptor tyrosine kinase, SCD-2, in AIA interneurons of Caenorhabditis elegans. *The Journal of Neuroscience* **31**, 3007 (2011).

218. H. Imamura *et al.*, Visualization of ATP levels inside single living cells with fluorescence resonance energy transfer-based genetically encoded indicators. *Proceedings of the National Academy of Sciences of the United States of America* **106**, 15651 (2009).

219. M. Nakano, H. Imamura, T. Nagai, H. Noji, Ca^{2+} regulation of mitochondrial ATP synthesis visualized at the single cell level. *ACS Chemical Biology* **6**, 709 (2011).

220. F. Zhang *et al.*, Optogenetic interrogation of neural circuits: technology for probing mammalian brain structures. *Nature Protocols* **5**, 439 (2010).

221. Z. Cheng, R. E. Campbell, Assessing the Structural Stability of Designed β - Hairpin Peptides in the Cytoplasm of Live Cells. *ChemBioChem* **7**, 1147 (2006).

222. A. E. Palmer, R. Y. Tsien, Measuring calcium signaling using genetically targetable fluorescent indicators. *Nature Protocols* **1**, 1057 (2006).

223. R. Das, D. Baker, Macromolecular modeling with rosetta. *Annual Review of Biochemistry* **77**, 363 (2008).

224. D. J. Mandell, E. A. Coutsias, T. Kortemme, Sub-angstrom accuracy in protein loop reconstruction by robotics-inspired conformational sampling. *Nature Methods* **6**, 551 (2009).

225. P. Gangola, B. Rosen, Maintenance of intracellular calcium in Escherichia coli. *Journal of Biological Chemistry* **262**, 12570 (1987).

226. A. W. Karzai, E. D. Roche, R. T. Sauer, The SsrA–SmpB system for protein tagging, directed degradation and ribosome rescue. *Nature Structural & Molecular Biology* **7**, 449 (2000).

Chapter 3. Microfluidic cell sorter-aided directed evolution of a protein-based calcium ion indicator with an inverted fluorescent response

3.1 Abstract

We demonstrate a simple and low cost microfluidic fluorescence activated cell sorting system (μFACS) for directed evolution of fluorescent proteins (FP) and FP-based calcium ion (Ca^{2+}) indicators. The system was employed to pre-screen libraries of up to 10^6 variants of a yellow FP-based Ca^{2+} indicator (Y-GECO) with throughput up to 300 cells/s. Compared to traditional manual screening of FP libraries, this system accelerated the discovery of improved variants and saved considerable time and effort during the directed evolution of Y-GECO. Y-GECO1, the final product of the μFACS-aided directed evolution, has a unique fluorescence hue that places it in the middle of the spectral gap that separates the currently available green and orange FP-based Ca^{2+} indicators, exhibits bright fluorescence in the resting (Ca^{2+} free) state, and gives a large response to intracellular Ca^{2+} fluctuations in live cells.

3.2 Introduction

The calcium ion (Ca^{2+}) has a pivotal role in cell signaling, serving as the critical second messenger for numerous signaling pathways and processes in essentially all cell types. The Ca^{2+}-signaling system is highly versatile and operates with a diverse array of spatial and temporal patterns in different tissues

A version of this chapter has been submitted for publication. I was responsible for the concept formation, screening and characterization of all the produced protein indicators, data collection and analysis as well as the manuscript composition.

(*137, 227*). To interrogate Ca^{2+} dynamics, it is essential to develop technologies that enable visualization and quantitative measurement of intracellular Ca^{2+} signals. Compared to synthetic dye-based Ca^{2+} indicators, FP-based Ca^{2+} indicators offer a number of advantages for Ca^{2+} imaging in live cells and tissues. Specifically, FP-based Ca^{2+} indicators are genetically encoded and can therefore be delivered to cells transiently in the minimally invasive form of the corresponding gene or constitutively expressed in transgenic animals (*228*). Furthermore, with appropriate gene promoters and trafficking signals, FP-based Ca^{2+} indicators can be expressed only in specific cell types or targeted to specific subcellular compartments.

Extensive protein engineering efforts have led to an expansion of the toolbox of FP-based Ca^{2+} indicators and introduced new members with improved or novel properties (*108, 133, 135, 155, 229*). One effective approach for developing improved FP-based Ca^{2+} indicators is the manual one-by-one testing of a small selection of variants rationally designed on the basis of structure-based hypotheses regarding the mechanism (*133, 148, 153, 170*). Arguably, a more effective approach for discovering improved FP-based Ca^{2+} indicators is the use of directed evolution, where large libraries of randomly generated variants are subjected to a high-throughput screen to identify improved variants (*108, 135, 229*). Such directed evolution efforts have typically relied on manual on-plate screening of bacterial colony fluorescence with moderate throughput of up to 10^4 variants every few days. In this way rare clones with improved or unanticipated novel properties, that would be unlikely to be identified by rational approaches, can be discovered

A promising approach for increasing the size of FP-based libraries that can be screened, and thereby increasing the odds of finding improved variants, is to exploit the ability of fluorescence activated cell sorting (FACS) to rapidly evaluate and sort very large numbers of fluorescently labeled cells. Relative to the labor-intensive and time-consuming process of on-plate screening, the throughput of FACS is 3 orders of magnitude higher (*41*). Unfortunately, FACS equipment is expensive, requires a high level of technical skill to operate, and is typically ineffective for screening properties other than brightness, such as analyte-dependent fluorescence changes or photoconversion. Microfluidic FACS (μFACS) devices are a promising alternative to traditional FACS for screening FP and FP-based Ca^{2+} indicators, as they are inexpensive and much more amenable to customization. Recently, a number of μFACS devices have been reported to screen fluorescently-labeled cells (*86, 88, 230*), which could potentially be customized for screening libraries of FP-based Ca^{2+} indicators. In this work we have built a similar, cost-effective high-throughput μFACS device (*230, 231*) and used it for the directed evolution of a single FP-based Ca^{2+} indicator derived from the yellow FP mPapaya1 (*79*).

The design of the single FP-based Ca^{2+} indicator engineered in this work is similar to that of Pericam and GCaMP (*92, 95*). In this design, the C- and N-termini of a circularly permutated FP (cpFP) are fused to calmodulin (CaM) and a peptide binding partner (smooth muscle myosin light-chain kinase peptide M13), respectively. The large conformational change associated with binding of CaM to Ca^{2+} followed by binding of M13 to Ca^{2+}-bound CaM, results in a change in the FP chromophore environment that modulates its fluorescent properties (*92, 95, 108, 229*). Single FP reporters have been developed from engineered versions of

Aequorea GFP (*92, 95*), *Clavularia sp.* FP (*229*), *Discosoma* RFP (*108*) and *Entacmea quadricolor* RFP (*210*). In this work, we have chosen to use a cp version of the monomeric *Zoanthus sp*. yellow FP-derived variant known as mPapaya0.4 (*79*), the best mPapaya available at the beginning of this work, which has a unique emission wavelength around 540 nm. We reason that a Ca^{2+} indicator that retained the fluorescence hue of mPapaya would fill the spectral gap between GCaMP (*95*) and O-GECO1 (*135*) in the visible wavelength palette of available FP-based Ca^{2+} indicators and provide new opportunities for multicolor Ca^{2+} imaging.

3.3 Experimental Procedures

3.3.1 Reagents

Synthetic DNA oligonucleotides used for cloning and library construction were purchased from Integrated DNA Technologies. The sequences of all oligonucleotides used in this work are provided in Table 3.3. *Pfu* polymerase (Fermentas) or AccuPrime™ *Pfx* SuperMix (Invitrogen) were used for non-mutagenic PCR amplifications in the buffer supplied by the respective manufacturer. *Taq* polymerase (New England Biolabs) in the presence of $MnCl_2$ (0.1 mM) was used for error-prone PCR amplifications. PCR products and products of restriction digests were routinely purified using preparative agarose gel electrophoresis followed by DNA isolation using the GeneJET gel extraction kit (Fermentas). Restriction endonucleases were purchased from Fermentas and used according to the manufacturer's recommended protocol. Ligations were performed using T4 ligase (Invitrogen). In some cases, Gibson Assembly (New

England Biolabs) was used. Small-scale isolation of plasmid DNA was performed by GeneJET miniprep kit (Fermentas). The cDNA sequences for all Y-GECO variants and fusion constructs were confirmed by dye terminator cycle sequencing using the BigDye Terminator Cycle Sequencing kit (Applied Biosystems).

3.3.2 Microfluidic device fabrication

The design of the microfluidic cell sorter was based on the work of Chen *et al.* (*230*). Briefly, the device was fabricated using the conventional microreplica molding technique (*232*) in which device features were photolithographically defined by SU-8 photoresist mold and then transferred to a PDMS substrate (Sylgard 184, Dow Corning). The actuation chamber of the PDMS substrate was created by manual cutting using a surgery knife, and the inlets and outlets were created using 2 mm punch. For device assembly, the PDMS substrate and glass were surface treated using a plasma generator (Electro-Technic Products Inc.). The PDMS substrate and the glass surface were placed into physical contact and the device was incubated at 65 °C for 20 min to allow the surfaces to bond. The stainless steel surface of the piezoelectric actuator (APC international) was aligned to the PDMS actuation chamber and put in contact with the PDMS substrate and sealed with commercially available syringe epoxy steel adhesive (Gorilla Glue). Finally, Teflon tubing was inserted into the inlets and outlets of the device for fluid flow introduction.

3.3.3 Construction of Y-GECO gene libraries

The design of Y-GECO is based on well-established designs described by our group and others (*92, 95, 108, 210, 233*). The initial cpmPapaya gene library

was assembled by a two-part overlap extension PCR. The 5' piece used in the overlap extension was prepared by PCR amplification with a mixture of two different forward primers (FW_XhoI_X_148mPapaya, FW_XhoI_XX_148mPapaya) and a single reverse primer (RV_GGTGGS_mPapaya). Primers FW_XhoI_X_148mPapaya and FW_XhoI_XX_148mPapaya contains an XhoI site and primer RV_GGTGGS_mPapaya encodes a cp linker (amino acid sequence GGTGGS) and an overlap region with primer FW_GGTGGS-mPapaya. The 3' piece for use in the overlap extension was prepared by PCR amplification with a single forward primer (FW_GGTGGS-mPapaya) and a different reverse primer (RV_MluI_X_147mPapaya). Primer RV_MluI_X_147mPapaya contains a MluI site. The PCR fragments were confirmed by agarose gel electrophoresis and purified. The full-length cpmPapaya gene library was assembled by overlap extension PCR using an equimolar mixture of primers FW_XhoI_X_148mPapaya, FW_XhoI_XX_148mPapaya and RV_MluI_X_147mPapaya together with a mixture of the 5' and 3' PCR fragments (1 μL each) as the template. The full-length product (approximately 700 bps) was purified by agarose gel electrophoresis and the doubly digested product was ligated into the XhoI and MluI sites of a modified pTorPE-G-GECO1.1 from which a second MluI site had been removed (*108*).

Error-prone PCR amplifications for construction of libraries of randomly mutated genes were performed using primers FW_XbaI_6His and RV_CaM_stop_HindIII. The PCR products were digested with XbaI and HindIII and ligated into the similarly digested pTorPE vector backbone. For site-directed mutagenesis or library construction by full or partial randomization of one or

more codons, either the QuikChange Lightning Single or Multi kit (Agilent Technologies) was used. Following ligation, electrocompetent *E. coli* strain DH10B cells was transformed with the library of gene variants and cultured overnight at 37 °C on 10-cm Petri dishes of LB-agar supplemented with 200 μg/mL ampicillin (Sigma) and 0.0020% (wt/vol) L-arabinose (Alfa Aesar).

3.3.4 Screening of GECO gene libraries

The library screening of genetically encoded Ca^{2+} indicators using traditional colony-based manual screening method has been previously described in detail (*108*). For μFACS-aided screening, the screening protocol was modified accordingly. Briefly, a library of Y-GECO was used to transform competent *E. coli* and the transformed cells were plated on agar plates with roughly 30~100 times higher number of cells. It is critical that the freshly transformed cells should not be grown in liquid culture directly as many mutants that do not express protein will be enriched in culture due to faster growth times. This resulted in a high density of colonies (~10^5 cells per plate) on the agar plate after overnight incubation at 37 °C. Cells were then collected by washing the colonies with M9 buffer supplemented with 100 μg/mL ampicillin, 0.1% glycerol, 0.002% L-arabinose and 1 mM EGTA. The cell density was measured by BD Accuri C6 flow cytometer (BD bioscience) and adjusted to 10^4 cells/μL accordingly.

The cell suspension was loaded into a μFACS system via the middle input channel using a syringe pump (Harvard Apparatus). The sample flow was confined by the sheath flows (consisting of the same M9 buffer) on both sides. The Y-GECO mutants that were flowing through the laser illumination point were excited by 488-nm argon ion laser beam, and the fluorescent emission was

collected by a homemade confocal epifluorescence microscope using a 25× objective (numerical aperture (NA): 0.35, Leitz Wetzlar). A customized LabVIEW program was design for signal processing and chip control. PMT signals were acquired at a sampling frequency of 100 kHz. The noise level was calculated based on the variation of baseline PMT signals sampled every 0.5 ms. The SNR of the fluorescence signal of variants was calculated in real time. The pieozoelectric actuation was triggered when the SNR signal of Y-GECO variants was larger than a pre-defined threshold, determined based on statistical analysis of cell fluorescence signals in the samples prior to cell sorting. The sorted bright variants were collected via collection channels and grown on agar-plate overnight at 37 °C, picked the next day and cultured in liquid LB medium at 37 °C overnight.

Proteins extracted from the overnight liquid cultures of the picked clones by either the traditional method or the μFACS-aided screening method were subjected to an additional screening in a Safire2 fluorescence microplate reader (Tecan). Briefly, cells were harvested by centrifugation at 13,000 g for 2 min at 4 °C. Y-GECO variants along with other cytoplasmic proteins were extracted by suspension of cells using surfactant B-PER (Pierce) followed by centrifugation to pellet unwanted cell debris. The performance of each selected variant was evaluated in a fluorescence microplate reader. Their brightness and Ca^{2+}-dependent response was compared to the best variant from the previous round. Finally, the brightest functional variants were used as the library template for the next round of directed evolution.

3.3.5 Protein purification and *in vitro* spectroscopy

To purify Y-GECOs for *in vitro* spectroscopic characterization, the pTorPE plasmid harboring the variant of interest was first used to transform electrocompetent *E. coli* DH10B cells. Following selection on LB/ampicillin (200 μg/mL), single colonies were picked and used to inoculate 4 mL LB medium (200 μg/mL ampicillin only). Bacterial subcultures were shaken at 250 rpm and allowed to grow overnight at 37 °C. The next day, 1 mL of bacterial subculture was added into a modified TB rich medium (1L sterilized medium contains 20 g LB mix, 14 g tryptone, 7 g yeast extract, 9.2 g K_2HPO_4, 2.2 g KH_2PO_4 and 8 mL glycerol, pH was adjusted to 7.4). The cultures were shaken at 250 rpm and inoculated at room temperature for two days. Bacteria were harvested by centrifugation (10,000 g for 5 min), resuspended in 30 mM Tris-HCl buffer (pH 7.4), lysed by French press, and clarified by centrifugation at 13,000 g for 30 mins at 4 °C. Proteins were purified from the cell-free extract by Ni-NTA affinity chromatography (Agarose Bead Technologies). The buffer of purified proteins was exchanged into 10 mM MOPS, 100 mM KCl, pH 7.2. Absorption spectra were recorded on a DU-800 UV-visible spectrophotometer (Beckman) and fluorescence spectra were recorded on a Safire2 platereader. The response to Ca^{2+} is expressed as $(R_{max}\text{-}R_{min})/R_{min}$. For Y-GECO, R = (*I* with 416 nm excitation)/ (*I* with 527 nm excitation), where *I* = fluorescence intensity at 560 nm.

Standards for quantum yield determination were FP mT-Sapphire (*234*) for the emission of Y-GECOs with 414 nm excitation and Citrine (*119*) for the emission of Y-GECOs with 524 nm excitation. The detailed procedure has been described previously (*108*). The fluorescence emission spectra of each dilution

of each standard and protein solution were recorded at excitation either 414 nm or 524 nm and the total fluorescence intensities obtained by integration. Integrated fluorescence intensity vs. absorbance was plotted for each protein and each standard. Quantum yields were determined from the slopes (*S*) of each line using the equation: $\Phi_{protein} = \Phi_{standard} \times (S_{protein}/S_{standard})$.

Extinction coefficients were determined by first measuring the absorption spectrum of each GECO in Ca^{2+}-free buffer (30 mM MOPs, 100 mM KCl and 10 mM EGTA at pH 7.20) and Ca^{2+}-buffer (30 mM MOPS, 100 mM KCl and 10 mM Ca-EGTA at pH 7.20). The concentrations of GCaMP6f were determined by measuring the absorbance following alkaline denaturation and assuming = 44,000 $M^{-1}cm^{-1}$ at 446 nm. For Y-GECOs, the protein concentration was determined by comparing the absorption peak for denatured Y-GECO to that of denatured mPapaya following alkaline denaturation of both proteins. Extinction coefficients of each protein were calculated by dividing the peak absorbance maximum by the concentration of protein.

pH titrations were carried out by diluting concentrated purified proteins into pH buffers containing 50 mM citrate, 50 mM Tris, 50 mM glycine, 100 mM NaCl, and either 5 mM $CaCl_2$ or 5 mM EGTA that were pre-adjusted to 14 different pH values between 4.50 and 11.50 pK_a values were determined from the inflection point of a sigmoid fit to fluorescence ratio versus pH.

Determination of Ca^{2+} K_d' was done according to the protocol described previously (*108*). Briefly concentrated protein solution was diluted into a series of buffers which were prepared by mixing Ca^{2+}-saturated and Ca^{2+}-free buffers (30 mM MOPS, 100 mM KCl, 10 mM EGTA, pH 7.2, either with or without 10 mM Ca^{2+}) with free Ca^{2+} concentration ranges from 0 nM to 3,900 nM at 25 °C.

The fluorescence ratio of Y-GECO in each solution was determined and plotted as a function of Ca^{2+} concentration. Experiments were performed in triplicate and the averaged data from the three independent measurements was fit to the Hill equation.

Ca^{2+}-dissociation kinetics was determined by stopped-flow photometry on an SX20 stopped-flow reaction analyzer (Applied Photophysics, Ltd., Leatherhead, UK). Excitation slit widths were set to 3 mm (equivalent to a wavelength bandwidth of 13.95 nm) and emission slit widths were set to 8 mm (equivalent to a wavelength bandwidth of 37 nm). Data were acquired using ProData SX software (Applied Photophysics, Ltd., Leatherhead, UK). The GECO indicator (in 30 mM MOPs, 0.2 mM $CaCl_2$ and 100 mM KCl) was rapidly mixed (1:1) with a buffered solution (30 mM MOPs, 10 mM EGTA and 100 mM KCl). The change in the fluorescence signal during rapid mixing provided the dissociation k_{off}. All measurements were made at ambient temperature, 20 °C.

3.3.6 Construction of mammalian expression plasmids

In this work, three types of mammalian expression plasmids were used. All genes were fully sequence verified before transfection. To construct the plasmids for validation and testing of Ca^{2+} indicators in HeLa cells, we cloned Y-GECO variants into a modified pcDNA vector that has been described previously (*108*). The gene in the pBAD vector was first PCR amplified using primers Fw_BamHI_Kozak_6His and RV_CaM_stop_EcoRI. PCR products were gel purified and digested with BamHI and EcoRI. Purified DNA fragments were ligated into the modified pcDNA3 plasmid digested with BamHI and EcoRI and similarly purified. The ligation reaction was used for transformation of

electrocompetent *E. coli* DH10B cells. Cells were plated on LB/agar supplemented with ampicillin and individual colonies were picked into 4 mL of LB/ampicillin following overnight incubation at 37 °C. Liquid cultures were shaken at 250 rpm and 37 °C for 12-15 h and then a small scale isolation of plasmid DNA was performed.

For expression in neurons, we cloned our Y-GECO variants into the BamHI/EcoRI sites of a lentivirus vector pJMK004 (FCK-ArchD95N-GFP, Addgene: 34616) or the BamHI/HindIII sites of an adeno-associated virus vector pAAV2-hSyn-R-GECO1. All the viral vectors were used directly for transfection without performing virus production. The FCK-ArchD95N-GFP vector contains a CaMKII promoter and a Woodchuck Hepatitis Virus Posttranscriptional Regulatory Element (WPRE) after the 3' end of the open reading frame, and the pAAV2-hSyn-R-GECO1 vector contains a human synapsin I promoter and a WPRE after the 3' end of the open reading frame. For construction of FCK-Y-GECO plasmids, the Y-GECO DNA for ligation was first generated by PCR using forward primer Fw_FCK_Gib_6His_YGECO and reverse primer RV_FCK_Gib_YGECO_stop, purified as described before. The ligation was done by a Gibson Assembly reaction with the lentivirus vector digested by BamHI and EcoRI following the manufacturer's instruction. For construction of pAAV2-hSyn-Y-GECO plasmids, the Y-GECO DNA fragment was generated by PCR using forward primer Fw_FCK_Gib_6His_YGECO and reverse primer RV_CaM_stop_HindIII. In case of preparing pAAV2-hSyn-Lyn-Y-GECO plasmids, Forward primers Fw_BamHI_Lyn and Fw_Lyn_GECOs and reverse primer RV_CaM_stop_HindIII were used to generate DNA fragment via two

steps of PCR. The DNA fragments were then purified, digested and ligated into the cut adeno-associated virus vector digested by BamHI and HindIII.

3.3.7 HeLa cell culture imaging

HeLa cells (40-60% confluent) on home-made 35 mm glass bottom dishes were transfected with 1 μg of plasmid DNA and 2 μL Turbofect (Thermo Scientific) or 3 μL lipofectamine 2000 (Invitrogen) according to the instruction of respective manufacturers. After 3 h incubation the media was exchanged to DMEM with 10% fetal bovine serum (FBS) and the cells were incubated for an additional 24 h at 37 °C in a CO_2 incubator. Immediately prior to imaging, cells were washed twice with Hanks balanced salt solution (HBSS) and then 1 mL of 20 mM HEPES buffered HBSS was added.

Wide-field imaging was done on a wide-field epifluorescence inverted microscope (Eclipse Ti-E, Nikon) equipped with a Photometrics QuantEM 512SC camera. The NIS-Elements Advanced Research (Nikon) was used for automated microscope and camera control. For determination of dynamic ranges in live cells, cells were imaged with a 20× air objective lens (NA 0.8). All imaging was performed at room temperature. For excitation of GCaMP6 and one channel of Y-GECO, the samples were illuminated with light from a 100 W mercury arc lamp that was passed through a 480/40 nm bandpass filter. The long pass dichroic mirror was 505 nm. The emission filter was 535/40 nm. For recording the long Stoke shift fluorescence of Y-GECO, 438/24 nm excitation filter, 458 long pass dichroic and 542/27 nm emission filter were used. 25% neutral density filter was used to decrease the strength of illumination for both indicators.

For imaging of histamine-induced Ca^{2+} dynamics, cells were imaged acquired with appropriate exposure every 4 s. Approximately 30 s after the start of the experiment, 100 μM histamine (10×) was added to a final concentration of 10 μM. Approximately 10 min after addition of histamine, 10 mM EGTA, 40 μM ionomycin in Ca^{2+}- and Mg^{2+}-free HHBSS (10×) is added to the dish to a final concentration 1 mM EGTA, 4 μM ionomycin. At the end of the experiment, 20 mM $CaCl_2$, 40 μM ionomycin in HHBSS (10×) is added to a final concentration 2 mM $CaCl_2$, 4 μM ionomycin.

3.3.8 Imaging of rat hippocampal neuron culture

Dissociated hippocampal cells from Sprague-Dwaley rats of embryonic day 18 (E18) stored in Hibernate® EB Complete Media were purchased from BrainBits LLC. The cells were grown on a homemade 35-mm glass bottom dish containing NbActiv4 (BrainBits LLC) supplemented with 2% FBS, penicillin-G potassium salt (50 units/mL), and streptomycin sulfate (50 μg/mL). On the 4th day *in vitro* (DIV-4), half of the culture medium was replaced with fresh media. Neuronal cells were transfected at DIV-7 with chosen plasmids using Lipofectamine 2000 or GenJet (SignaGen Laboratories) according to the manufacturer's instruction. Cells were imaged 2-4 days after transfection.

The system setup for wide-field imaging was similar to that for HeLa experiment except of the following. A 60× oil objective lens (CFI Plan Apo NA: 1.4), or a 40× air objective lens (CFI Plan Apo NA: 0.9) was used for neuron imaging. For GCaMP6, 25% neutral density filter was used. For Y-GECO1, 12.5% neutral density filter was used. The exposure time for both indicators was 10 ms. For excitation of R-GECO1, the excitation filter was 545/30 nm, the long pass

dichroic was 565 nm and the emission was collected through 620/60 nm filter. Neurons were imaged in the culture medium at room temperature 20 °C.

For confocal imaging, Fluorescence signals were measured using a confocal microscope and software (20× XLUMPlanF1, NA: 1.00, water immersion objective; Olympus FV1000; Carsen group, Markham, Ontario, Canada). Similarly, Olympus FV1000 connected with a Ti:Sa laser (10 W Mira/Verdi; Coherent, Santa Clara, CA) was used for two-photon imaging. With reduced resolution and 2 - 4 μs/pixel scanning rate, the image acquisition was adjusted to be 1-3 frames/s to effectively detect Ca^{2+} oscillation of neurons expressing Y-GECO1.

3.3.9 Preparation and transfection of rat hippocampal organotypic brain slices

All procedures for brain slice experiments were carried out in compliance with the guidelines of the Canadian Council for Animal Care and with the approval of the University of Alberta Animal Care and Use Committee for Health Sciences.

Brains were dissected from 0-day-old (P0) Sprague Dawley rat in ice-cold HBSS containing 1.3 mM $CaCl_2$ and 1 mM $MgSO_4$. Horizontal 250 um thick brain slices were generated using a vibrating microtome (Leica VT1000S, Leica Microsystems) as described previously (Panaitescu *et al.*, 2013) and were placed on a sterile 0.4 μm pore membrane cell culture insert (Millipore PICMORG50). The insert and slice were then placed in a Petri dish containing 1.5 mL of NbActiv4 (BrainBits) supplemented with 5% fetal bovine serum (FBS) and penicillin-G potassium salt (50 units/mL), and streptomycin sulfate (50 μg/mL).

Slices were cultured at 37 °C and 5% CO_2 for 24 h prior to transfection by electroporation. The insert and slice were then placed directly above a Platinum Plate Petri dish electrode (CUY700-P2E, Nepa Gene), and the gap between the electrode and the membrane was filled with electroporation buffer (EB) (HBSS + 1.5 mM $MgCl_2$ + 10 mM glucose). Plasmids (pcDNA3.1, Life Technologies) for expression of the gene of interest were dissolved in EB at a concentration of 1 µg/µl and sufficient volume was added to just cover the slice. A square platinum electrode (CUY700-P2L, Nepa Gene) was then placed directly above the hippocampus slice and a power supply was used to apply five 20 V pulses (5 ms each, 1 Hz). The direction of electrical field was reversed and a second set of five pulses with the same settings was applied. The EB buffer was carefully removed from the slices and they were then put back and incubated at 37 °C and 5% CO_2.

3.3.10 Confocal imaging of theophylline-induced Ca^{2+} elevations in rat organotypic hippocampal slices.

A modified version of protocol for Ca^{2+} imaging in brain slices (*235, 236*) has been used in this work. Immediately prior to imaging, the slices were perfused with superfusate containing (in mM): 120 NaCl, 3 KCl, 1 $CaCl_2$, 2 $MgSO_4$, 26 $NaHCO_3$, 1.25 NaH_2PO_4 and 10 D-glucose (pH adjusted to 7.4 by gassing with 95% O_2, 5% CO_2), at 5 mL/min using a peristaltic pump (Watson-Marlow Alitea-AB) and kept at room temperature. Imaging was started within 10 min following activation of the perfusion system. Fluorescence signals were measured using a confocal microscope and software (20× XLUMPlanF1, NA: 1.00, water immersion objective; Olympus FV1000; Olympus). The cells were excited with

488nm laser (Olympus) and emission was collected from 500 nm – 600 nm using a variable secondary dichroic mirror.

Images were acquired at 2 - 3× digital zoom at a reduced frame resolution (256 × 256) and with 4 μs/pixel scanning rate, This allowed image acquisition to be 1 - 2 frames/s to effectively detect cytosolic Ca^{2+} oscillations of neurons and glial cells expressing Y-GECO1. For imaging of theophylline-induced Ca^{2+} dynamics, images were acquired every 0.5 s. Theophylline (10 mM, Sigma Aldrich, Canada) was dissolved in superfusate and bath applied via peristaltic pump approximately 30 s after the start of the experiment. The drug was washed approximately 10 mins later by switching back to control superfusate.

3.4 Results and Discussion

3.4.1 Construction of the Y-GECO prototype and initial screening for improved variants

To construct a potential yellow FP-based Ca^{2+} indicator, we replaced the cpGFP domain of G-GECO1.1 (*108*) with the analogous cp version (N-term-148 to 238-GGTGGS-1 to 147-C-term) of mPapaya0.4 (*79*). We designed 2 libraries in which one or two residues at the new N-terminus (residues 27 and 28 by Y-GECO numbering, Figure 3.2) and one residue at the C- terminus of cpmPapaya (residue 272, Figure 3.2) were randomized (Figure 3.1A and B). The first version of the library had just residue 28 randomized at the N- terminus, while the second library had both 27 and 28 randomized. These two libraries were cloned into a customized vector that targets variants to the periplasmic space of *E. coli* cells (*108*). After plasmid transformation by electroporation, *E. coli* cells

were plated on agar plates and formed individual colonies. Traditional on-plate manual screening of both libraries led to the identification of a variant (Y-GECO0.1) from the second library with an 88% decrease in fluorescence upon binding Ca^{2+} (Figure 3.1C). However, Y-GECO0.1 exhibited dim fluorescence and poor folding efficiency relative to mPapaya0.4. Two rounds of directed evolution for improved folding efficiency using manual screening led to the identification of Y-GECO0.5a and b (Figure 3.2) which were still dim but had better folding efficiency and similar dynamic range to Y-GECO0.1. At this point it was apparent that many more rounds of directed evolution would be necessary to improve Y-GECO to the point where it would be useful for live cell imaging. We reasoned that a μFACS-aided approach would accelerate this process and so we designed and applied a chip based on the work of Chen *et al.* (*230, 231, 237*)

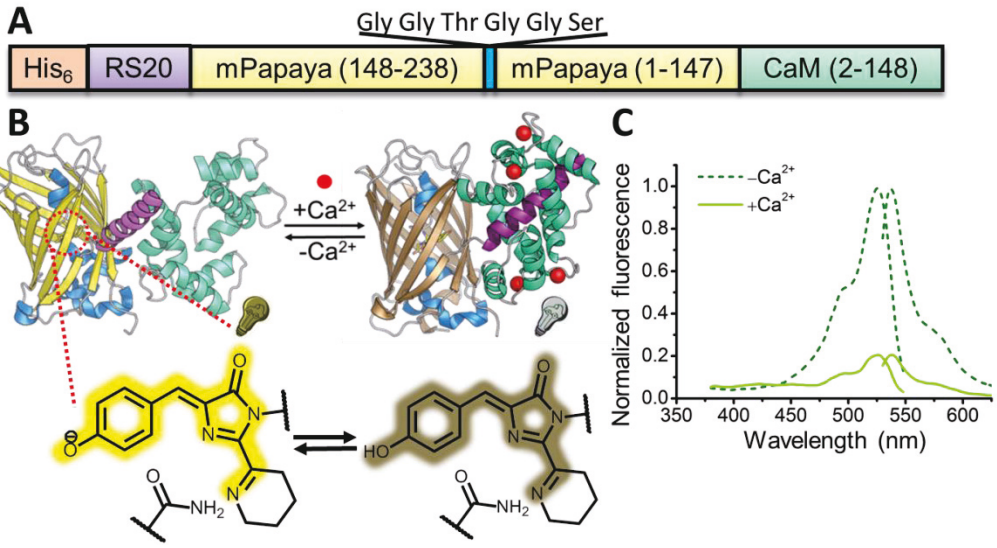

Figure 3.1 Construction of the Y-GECO prototype, Y-GECO0.1.

(A) Schematic representation of the sequence of the first generation Y-GECO Ca^{2+} indicator based on the recently reported yellow FP mPapaya0.4 (*79*). (B) Schematic representation of the tertiary structure and Ca^{2+}-sensing mechanism of

Y-GECO. The FP chromophore protonation state (*i.e.*, the pK_a) is modulated due to the conformation change associated with binding of M13 by Ca^{2+}-bound calmodulin (CaM), leading to the change in fluorescence. (C) Excitation and emission spectra of Y-GECO0.1, recorded at emission 560 nm and excitation 510 nm respectively.

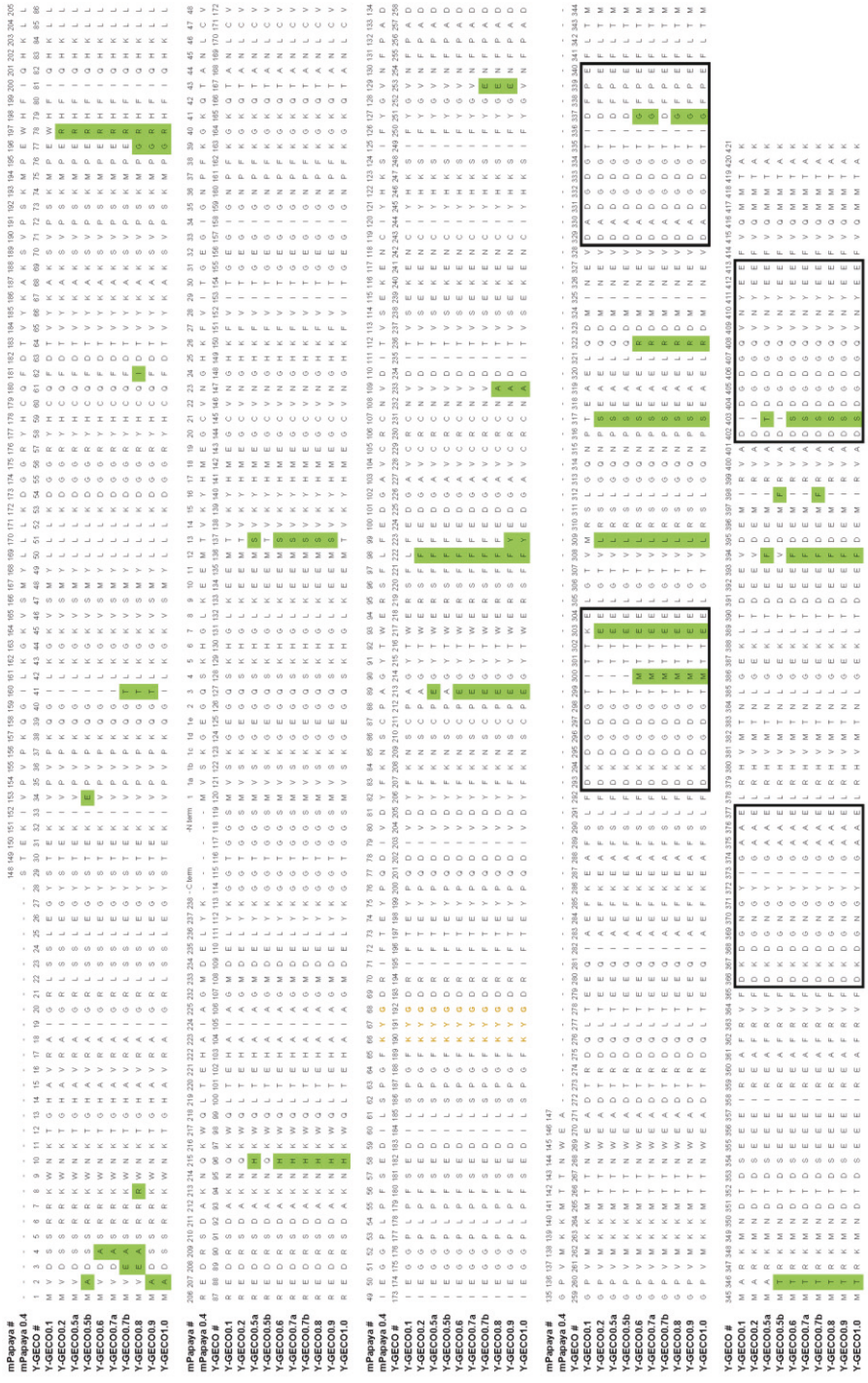

Figure 3.2 Sequence alignment of Y-GECO1 and select Y-GECO variants.

The KYG chromophore is highlighted in orange text. Positions of EF hands in CaM are boxed.

3.4.2 Design and fabrication of μFACS platform

A simple, low cost μFACS platform is ideal for the directed evolution of FP-based Ca^{2+} indicators as it greatly decreases the cost of fabrication and maintenance and can be readily adapted to the screen at hand compared to FACS. We elected to build a μFACS platform based on a polydimethylsiloxane (PDMS) microfluidic cell sorter chip with an integrated piezoelectric actuator (*230, 231, 237*). PDMS microchips containing 3 input channels and 3 output channels, connected with a 5-cm channel for buffer mixing were fabricated using standard soft lithography techniques. For operation of this chip, cell samples were continuously flowed through the middle input channel and were confined to single stream by sheath flow from the two side input channels. For a typical cell sample ($\sim 1\times10^7$ cells/mL), the chip could operate for more than 2 hours without obvious clogging. High signal-to-noise fluorescence detection of single bacterial cells expressing Y-GECO variants was achieved using laser excitation at 488 nm with confocal detection using a photomultiplier tube (PMT) (Figure 3.3D). The piezoelectric actuator integrated into the PDMS chip could be triggered for manipulation of fluid flow to achieve sorting into one of the side collection channels (Figure 3.3A).

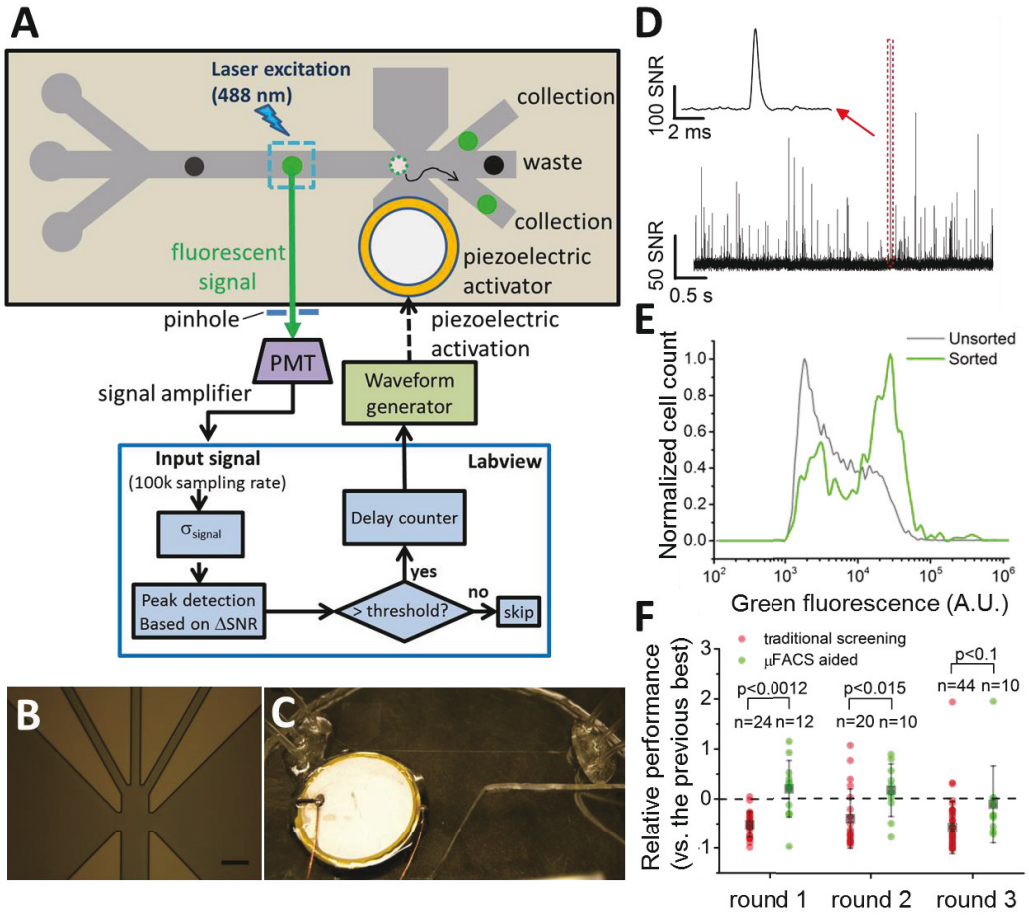

Figure 3.3 A simple and low cost μFACS platform for high throughput enrichment of libraries of FP and FP-based indicators.

(A) μFACS platform using on chip laser illumination and piezoelectric actuator, off chip confocal epifluorescence detection, PMT signal amplification and acquisition system, and electronic control system. The actuator mechanism is based on literature precedent (*230, 231*). (B) Microscopic image of channels at the sorting junction (scale bar: 150 μm). (C) View of whole microfluidic cell sorter. (D-F) Summary of screening results. (D) Signals of *E. coli* cells expressing Y-GECO libraries flowing on chip acquired by PMT detector. The SNR was defined as the ratio of the signal magnitude of cell fluorescence and the background noise level of PMT signals. Inset shows a bright variant. (E)

Cytometric histogram for a library of Y-GECO before and after sorting using μFACS system. (F) Screening results of selected variants from round 1 to round 3 with and without aid of μFACS system. Best variants were combined from both methods between each round. Each point represents the performance (brightness × maximum Ca^{2+} response) of each variant relative to the best from the previous round. Gray boxes show the average of relative performance; n is the number of tested variants, larger n indicates more time and effort invested; p values were obtained from two-tailed t-test, showing μFACS gave much better performance in the first two rounds and similar performance with much less effort (n is smaller) in the third round.

To facilitate semi-automated cell sorting on chip, we designed a custom LabVIEW program for signal processing and sorting control. The SNR of cell fluorescence was calculated in real time based on the magnitude and background noise level of PMT signals. Fluorescent signals with SNR higher than a pre-defined threshold triggered sorting based on piezoelectric actuation. The delay between detection at the PMT and piezoelectric pump actuation (*i.e.*, the response time of the system) was 2.2±0.6 ms (25 trials). The time for an individual cell to travel to the sorting junction was matched to this response time by adjusting the position of the detection point within the channel. Response time was primarily limited by communication between the computer and the chip. An embedded field programmable gate array chip for a close-loop sorting control could significantly improve the response time (*230*).

The major limiting factor that determines the throughput of the μFACS for library enrichment is the requirement that only one bacterial cell can be in the

sorting junction at a single moment. As the dimension of sorting junction was about 150 μm × 150 μm × 50 μm, the time for a bacterial cell to flow through the sorting junction was between 3 ms and 6 ms when the flow rate was between 10.5 μL/min and 21 μL/min. Given this sorting time range to avoid co-sorting of cells, the throughput of the system was between 150 cells/s and 300 cells/s. With this throughput, roughly 10^6 Y-GECO variants could be screened within 2 hours.

3.4.3 μFACS-aided directed evolution of Y-GECO

We designed a μFACS-aided directed evolution strategy for improving Y-GECO variants with the focus on improving brightness (Figure 3.4). Briefly, 10^6 *E. coli* cells expressing periplasm-localized Y-GECO variants were suspended in a Ca^{2+}-free buffer and loaded into the chip. The fluorescence signal of hundreds of cells was measured and analyzed to determine the threshold, which was the trigger to activate the sorting to collect the top 0.1% brightest clones. Cells collected during the μFACS pre-screen were grown as colonies on agar plates and then manually screened in a manner identical to the traditional on-plate screen. Flow cytometric analysis of the initial and enriched libraries by μFACS (Figure 3.3E) shows that our μFACS system could enrich bright variants and increase the fluorescence intensity of the dominant peak by a factor of 16. Unlike other GECOs, the fluorescence of Y-GECO variants is dim in the presence of Ca^{2+} and is bright in the absence of Ca^{2+}. Therefore, Y-GECO variants targeted to the *E. coli* periplasm using the pTorPE expression plasmid should be in the bright fluorescent state in cells suspended in Ca^{2+}-free buffer. Sorting of *E. coli*

expressing a library of variants on the basis of fluorescence brightness alone, should enrich for variants that are brighter in the Ca^{2+}-free state. This increased brightness could be attributable to either improved protein folding efficiency, or an increase in the intrinsic brightness of the indicator, both of which are desirable traits. Of course, improvements in these desirable traits could come at the expense of indicator dynamic range. To overcome this problem, it is necessary to perform a secondary *in vitro* screen for Ca^{2+} response. Briefly, colonies were picked based on the colony brightness and grown in liquid culture. Proteins were extracted from overnight cultures and tested for Ca^{2+} response in microplate reader.

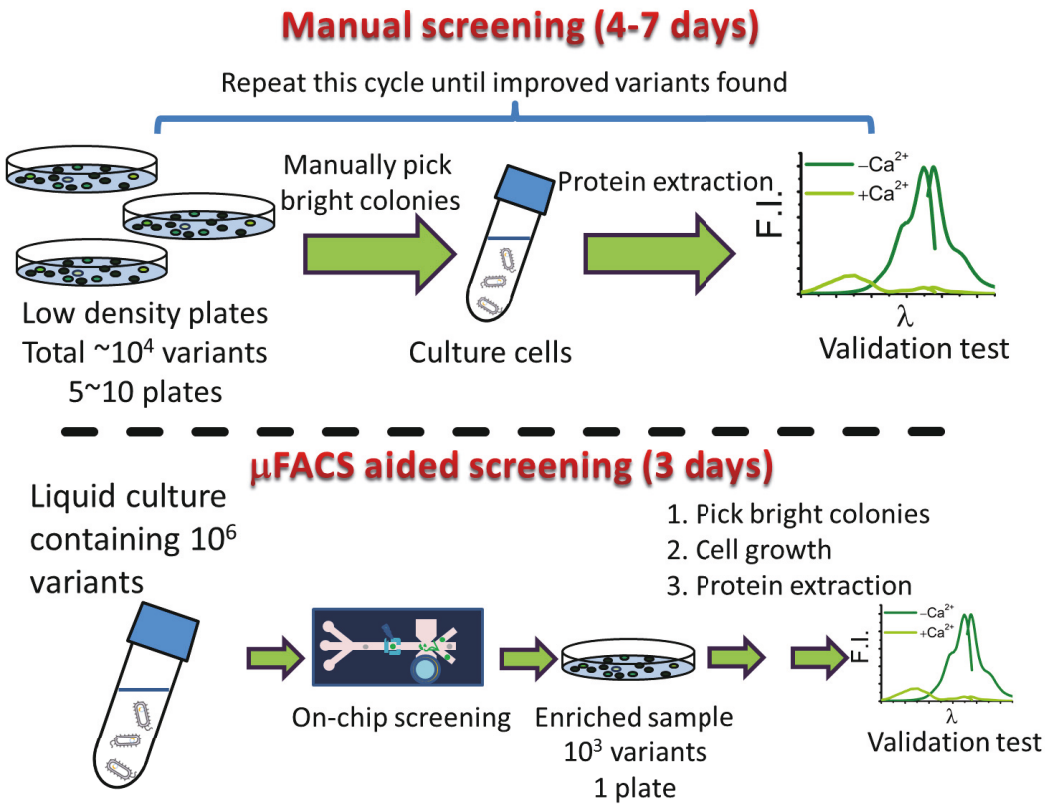

Figure 3.4 Schematic representation of screening procedures.

Starting from Y-GECO0.5a and b, which was prepared from the initial two rounds of directed evolution for improved folding, we performed three rounds of parallel screening using both manual on-plate screening and the μFACS-aided approach (Figure 3.4). To enable unbiased comparison of the two screening methods, after each round we combined the pool of the most superior variants found from both methods. The combined gene pool served as a template to generate a new library that was constructed by mixing gene variants generated by error-prone PCR with gene variants generated by DNA shuffling. The resulting library was then screened using both the traditional method and the μFACS-aided approach in parallel.

Compared to the traditional manual on-plate screen, the μFACS-aided approach identified improved Y-GECO variants using substantially less effort (Figure 3.3F), owing to the 100 times higher throughput of μFACS. In each of the first two rounds, the overall brightness and Ca^{2+} response of Y-GECO variants selected by the μFACS-aided approach was significantly higher than variants selected by the traditional on-plate screen. For round 3 it was apparent that beneficial mutations had become exceedingly rare within our library, presumably as the template had already acquired the most highly represented beneficial mutations. For this round, both screening methods produced effectively equivalent results, however, we had to pick 44 variants to find one superior variant using the traditional approach, while μFACS enrichment approach required only 10 variants

After completion of the third round of directed evolution using both on-plate screen and the μFACS-aided approach, each method led to identification of one best variant that showed seemingly satisfactory brightness and Ca^{2+} response. Fluorescence measurement of the purified proteins revealed that the variant identified in the third round of μFACS platform-aided directed evolution was superior, relative to the variant identified in the third round of traditional screening, in terms of brightness and Ca^{2+} response (Table 3.1). This variant, designated as Y-GECO1, has 17 mutations distributed throughout the protein sequence relative to Y-GECO0.1 (Figure 3.2 and Table 3.1), significant improvement on folding and brightness, a large ratiometric change, and an affinity to Ca^{2+} within the physiologically relevant range (see following section).

These results demonstrate that a μFACS-aided screen is more efficient for identifying improved FP-based Ca^{2+} indicators than the manual on-plate method. However, we believe that the full potential of this approach has not yet been fully utilized. The efficacy of directed evolution of FP-based Ca^{2+} indicators could be significantly increased by high throughput screening for both Ca^{2+} response and brightness simultaneously using a μFACS system. To achieve this, at least two detection points on both ends of the 5-cm main channel are required to facilitate detection of fluorescence changes of periplasm-targeted mutants before and after binding to Ca^{2+}. In this new detection scheme, further optimization of experiment parameters, such as flow rate, cell density, buffer composition and optics, will be critical for the performance of the μFACS. Related work is currently in progress.

3.4.4 *In vitro* characterization of Y-GECO1

Spectroscopic characterization of the purified proteins reveals that the Ca^{2+} binding of Y-GECO1 leads to 95% decrease in fluorescence emission when using 525 nm excitation. Notably, a new fluorescence excitation peak around 413 nm appears upon binding to Ca^{2+} and fluorescence intensity increases 10-fold when exciting at this wavelength. Thus, Y-GECO1 is a ratiometric Ca^{2+} indicator with a 200-fold peak-to-peak ratiometric change (Figure 3.5A) in fluorescence excitation. In this way, Y-GECO1 is analogous to the previously reported ratiometric-pericam (*92*) and GEX-GECO1 (*108*), but has a much larger dynamic range of Ca^{2+} response. In contrast to most previously reported GECO variants (*108, 135, 229*), in which the pK_a of chromophore shifts toward a lower value when bound to Ca^{2+}, the pK_a of Y-GECO1 chromophore shifts from 6.3 to 8.9 upon binding to Ca^{2+} and results in loss of overall fluorescence intensity (Figure 3.6B). *In vitro* titration with Ca^{2+} indicates the value of K_d' for Y-GECO1 is 190 nM (Figure 3.6A and Table 3.1).

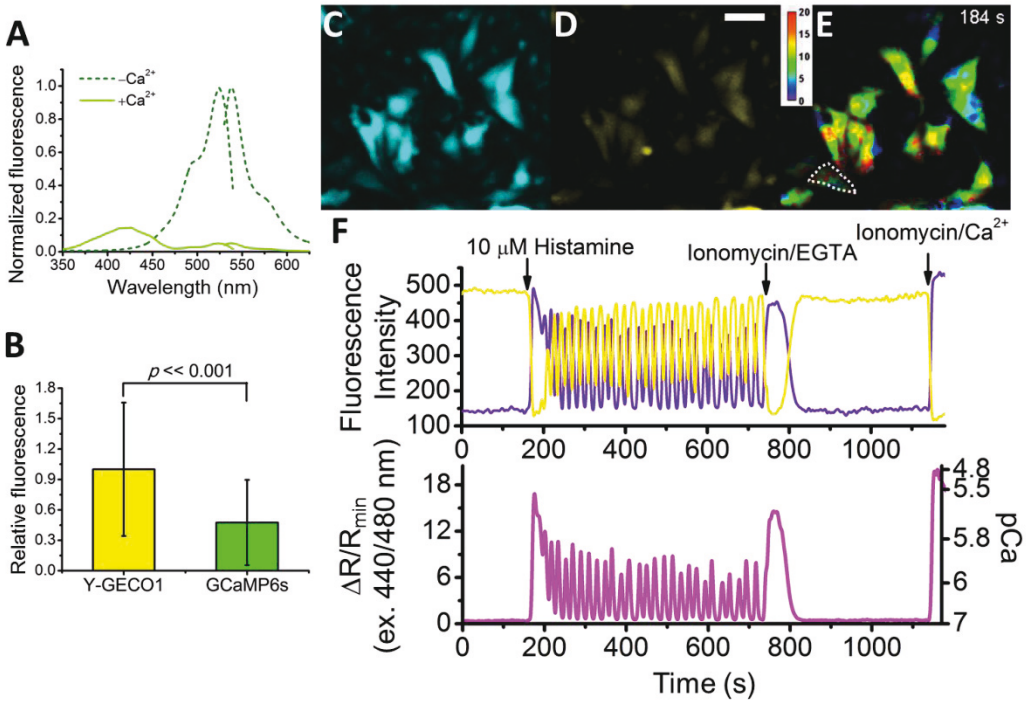

Figure 3.5 Characterization and application of Y-GECO1.

(A) Excitation and emission spectra of Y-GECO1, recorded with emission at 560 nm and excitation at 510 nm, respectively. (B) Comparison of brightness in the free resting cytosolic Ca^{2+} concentration ($[Ca^{2+}]_i$) of HeLa cells between Y-GECO1 (141 cells) and GCaMP6s (209 cells) using a common filter set for GFP. (C-E) Fluorescence images of HeLa cells expressing Y-GECO1 captured the moment of 10 μM histamine-induced intracellular Ca^{2+} rise. (C) Image acquired under 440 nm excitation. (D) Image acquired 480 nm excitation. Scale bar: 50 μm. (E) The ratiometric change $\Delta R/R_{min}$ image (ratio R was calculated from dividing image C by image D; R_{min} was the minimum ratio of 440 nm/ 480 nm after adding ionomysin/EGTA. $\Delta R/R_{min} = R/R_{min} - 1$). (F) Typical $[Ca^{2+}]_i$ transients and oscillations of a select cell (enclosed by a dotted line in E) induced by histamine stimulations. The sampling interval was 3 s. (F, upper) A typical cell trace acquired

under 480 nm (yellow line) and 440 nm (violet line) excitations. (F, lower) Excitation ratios, 440 to 480 nm. The right-hand ordinate calibrates $[Ca^{2+}]_i$ in *pCa*.

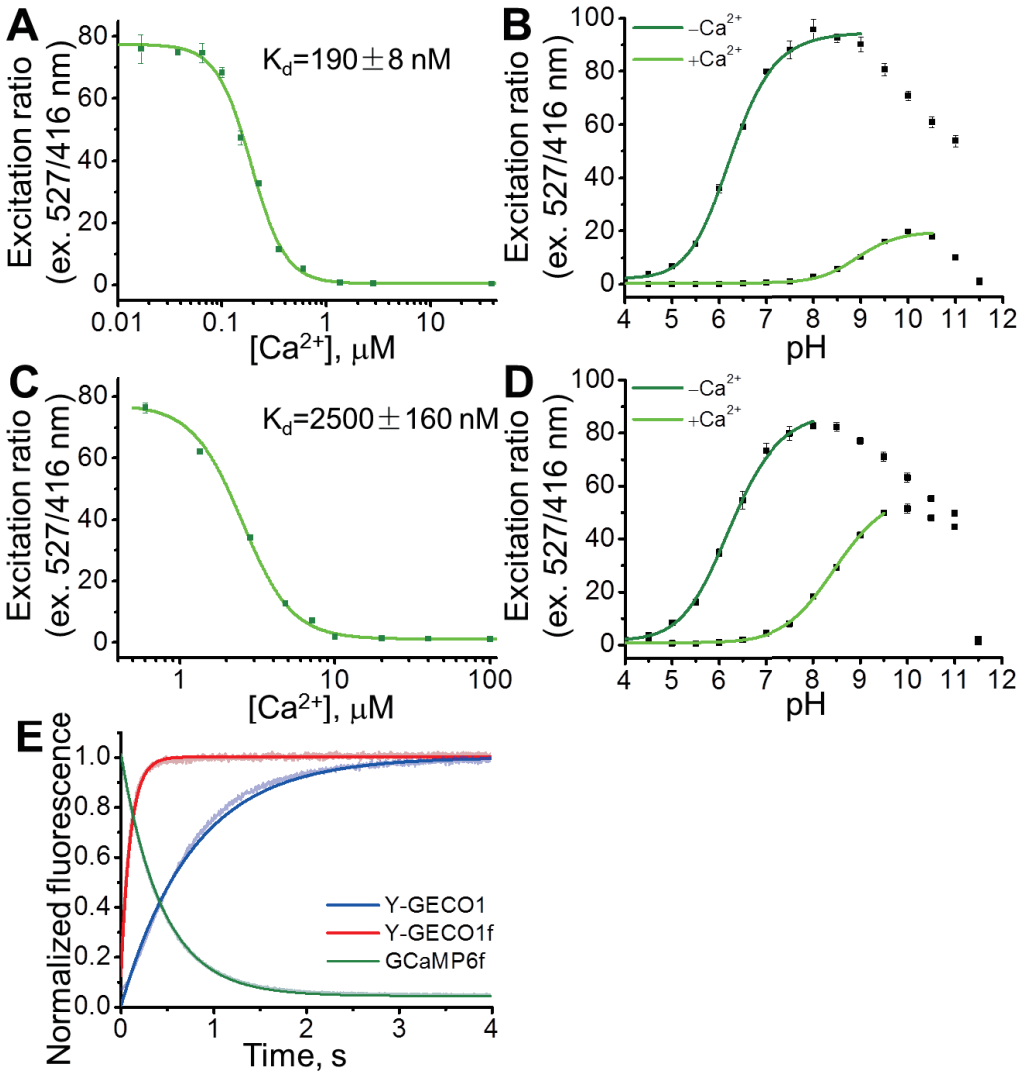

Figure 3.6 Characterization of K_d, *pKa* and kinetic of Y-GECO variants.

(A,C) Ca^{2+} titration of (A) Y-GECO1 and (C) Y-GECO1f. (B,D) pH titration of (B) Y-GECO1 and (D) Y-GECO1f with and without binding to Ca^{2+}. (E) Comparison of the off kinetic of Y-GECO1, Y-GECO1f and GCaMP6f.

Since mPapaya1 is superior to mPapaya0.4 in terms of brightness, photostability and maturation, we attempted to introduce some beneficial mutations of mPapaya1 relative to mPapaya0.4 (*79*) into Y-GECO1, but none of them led to further improved variants (data not shown), which suggests Y-GECO1 and mPapaya1 evolved via different evolution paths. Interestingly, Y-GECO1 shares one mutation F223Y (F99Y by mPapaya numbering) with mPapaya1 (Figure 3.2), which is reported to dramatically improve the photostability of mPapaya0.6. According to the crystal structure of zFP538 (PDB ID 2OGR) (*238*), F223Y could enhance interaction with the internal α-helix of the FP and influence the chromophore environment, which may result in improved photostability. In the case of Y-GECO1, F223Y might also improve the brightness and Ca^{2+} response since it was the only new mutation found in the last round of screening (Figure 3.2).

Y-GECO1 is an excitation ratiometric Ca^{2+} indicator because, unlike Y-GECO0.1, the Ca^{2+} bound form exhibits long Stokes shift fluorescence due to its ability to efficiently undergo excited-state proton transfer (ESPT). That is, the protonated form of the fluorophore, which exhibits maximal absorbance at 413 nm and predominates in the presence of Ca^{2+}, can become deprotonated in the excited state and emit fluorescence from the anionic form. ESPT has been observed in a number of other FPs and FP-based indicators including *Aequorea victoria* GFP (*34*), mKeima (*36*), ratiometric pericam (*92*), GEX-GECO1, and GEM-GECO1 (*108*).

We characterized the kinetics of the Ca^{2+} response by stopped-flow fluorescence spectroscopy. The k_{off} rate of Y-GECO1 was around 1.40 s^{-1} at 20 °C,

which was slightly slower than the fastest version of GCaMP6, known as GCaMP6f, which has a k_{off} of 2.32 s^{-1} at 20 °C) (Figure 3.6E). Although the kinetic response of Y-GECO1 should be sufficient for most of the applications, it has limited capability for resolving Ca^{2+} spikes and firing frequency variations in neurons (*155*) and in some subcellular locations, such as the cytoplasm of dendrites and dendritic spines, where physiological Ca^{2+} can rise within milliseconds (*239, 240*). Sun *et al.* has reported mutations that disrupt the CaM-M13 interaction and increase the k_{off} of GCaMP3 (*155*). Preliminary results indicate that analogous mutations improve the k_{off} of Y-GECO1. Specifically, Y-GECO1 ΔG13 (analogous to GCaMP3 ΔG47) has a k_{off} = 9.75 s^{-1} at 20 °C (Figure 3.6E), but a 60% decrease in dynamic range (Table 3.1). Efforts to further optimize this fast Y-GECO1 variant are ongoing.

3.4.5 Performance of Y-GECO1 in mammalian cell and tissue culture

To determine how Y-GECO1 performs in typical live cell imaging experiments, we recorded the response of Y-GECO1 to changes of the free cytoplasmic Ca^{2+} concentration ($[Ca^{2+}]_i$) in HeLa cells using established protocols (*222*). We used a CFP/YFP FRET filter set (438/24 nm excitation and 542/27 nm emission) for long Stokes shift yellow fluorescence and a FITC filter set (480/40 nm excitation and 535/50 emission) for observing short Stokes shift yellow fluorescence and GCaMP6s green fluorescence (*133*). While these filter combination are not perfectly matched to the fluorescence spectra of Y-GECO1, these sets are widely available and commonly used in cell imaging experiments. As expected, we observed opposing oscillations in the fluorescence intensities of both emission channels when cells were treated with 30 μM histamine (Figure

3.5F). Using this filter combination, the maximum intensity change of Y-GECO1 in HeLa cells was determined to be 6±1-fold and the maximum ratio change was 13 ± 3-fold (Table 3.2). In comparison, the maximum intensity change of GCaMP6s was 20±7-fold intensiometric change (Table 3.2). The ratiometric nature of Y-GECO1 facilitates quantitative measurement of Ca^{2+} concentration in the targeted cellular compartment (Figure 3.5F) relative to intensiometric indicators such as GCaMP6 and R-GECO1 (*108*). Although the FITC filter set did not match well with the excitation and emission of Y-GECO1, Y-GECO1 in resting state was about 220% as bright as GCaMP6s (Figure 3.5B). Presumably, the performance and brightness of Y-GECO1 could be further improved using a custom filter set with 425/40 nm and 500/40 nm excitation filters, and a 560/50 nm emission filter.

Y-GECO1 is capable of detecting Ca^{2+} transients in dissociated hippocampus neurons in wide-field fluorescence imaging with performance comparable to the current popular FP-based Ca^{2+} indicators GCaMP6s and R-GECO1. As shown in Figure 3.7, Y-GECO1 successfully detected spontaneous cytosolic Ca^{2+} ($[Ca^{2+}]_i$) oscillations in both soma and processes with large ratio change and excellent SNR. Y-GECO1 was able to reveal different $[Ca^{2+}]_i$ waveforms in the soma and processes (Figure 3.7A and B). In order to estimate the maximum signal change in neurons, KCl was added to a final concentration 50 mM to depolarize neurons and induce a large Ca^{2+} influx via voltage-activated Ca^{2+} channels (*139, 241, 242*). Using the filter set described above, the maximum change of Y-GECO1 was 8± 2-fold in ratio and 2.6±0.5-fold in intensity of the FITC channel. In comparison, the maximum change of intensiometric indicator GCaMP6s was 8±5-fold and R-GECO1 was 3±1 fold (Figure 3.8). While the intensity change is smaller for

Y-GECO1 than GCaMP6s, the ability to give ratiometric sensing is a major advantage.

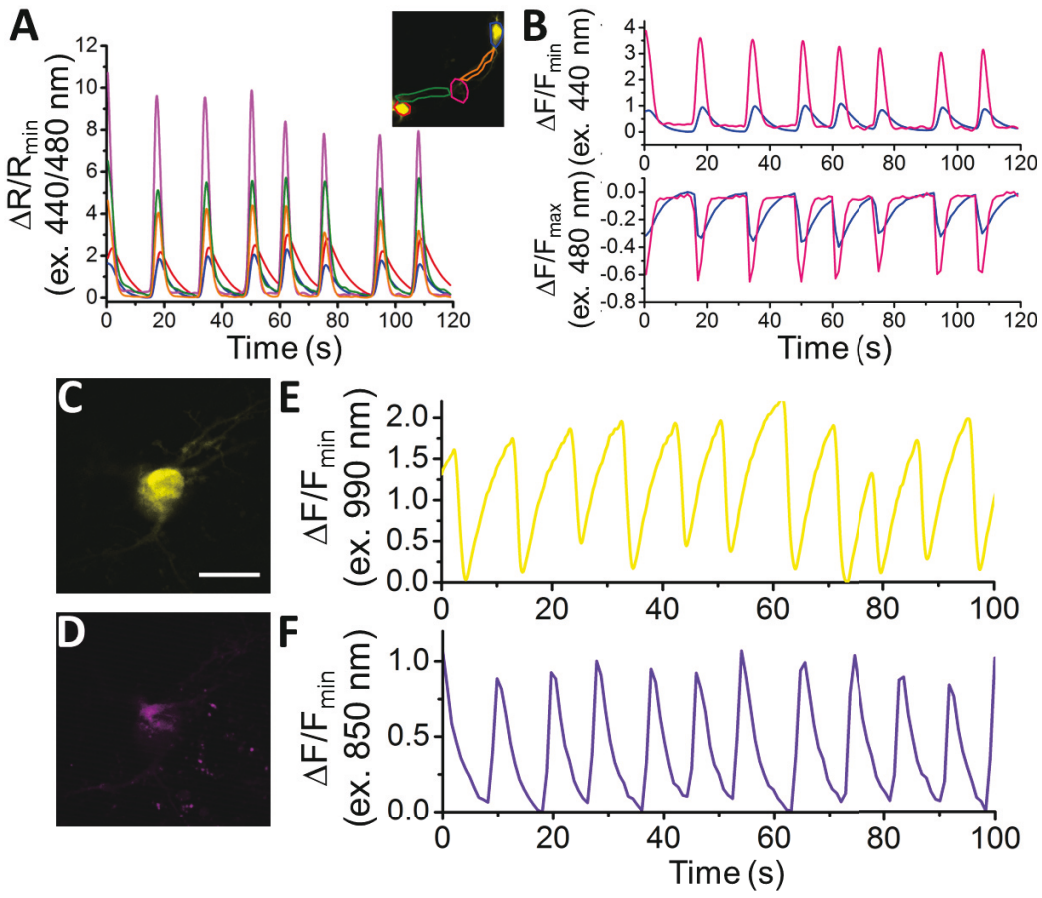

Figure 3.7 Wide-field and two photon imaging of Y-GECO1 in dissociated rat hippocampal neurons.

(A-B) Results of wide-field imaging. (A) The time course changes in the ratio of 440 nm excitation to 480 nm excitation channel indicate spontaneous $[Ca^{2+}]_i$ oscillation. The inset shows the fluorescent image of two neurons expressing Y-GECO1 under 480 nm excitation. The color of the ratiometric signals correspond to the region highlighted by the same color in the inset. (B) Imaging of spontaneous $[Ca^{2+}]_i$ oscillation in the selected region of interest in the violet and

blue excitation channels. (C-F) Two-photon imaging of dissociated hippocampus neuron expressing Y-GECO1 (C) under 990 nm excitation and (D) 850 nm excitation. Scale bar: 30 μm. (E-F) Typical fluorescence traces recording spontaneous $[Ca^{2+}]_i$ oscillation (E) under 990 nm excitation and (F) 850 nm excitation. Note that C and D were not acquired in the same time.

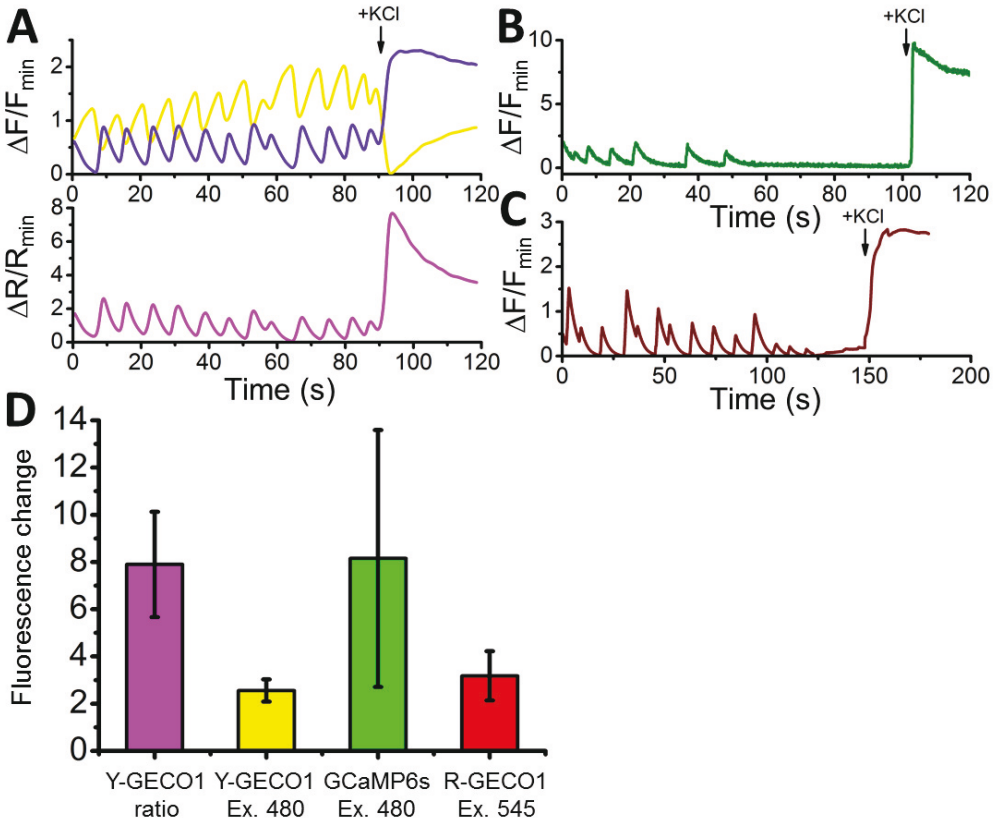

Figure 3.8 Performance of Y-GECO1 and select Ca^{2+} indicators in dissociated hippocampus neurons.

(A) Imaging of spontaneous $[Ca^{2+}]_i$ oscillation in neurons expressing Y-GECO1. The sampling frequency is 0.8 Hz. Exposure: 70 ms with 12.5 % neutral density filter applied. (A, upper) Fluorescent cell traces acquired under 480 nm (yellow line) and 440 nm (violet line) excitations. (A, lower) Excitation ratios, 440 to 480

nm. (B) Imaging of spontaneous $[Ca^{2+}]_i$ oscillation in neurons expressing GCaMP6s, recorded at excitation 480 nm. The sampling frequency is 20 Hz. Exposure: 50 ms with 25% neutral filter applied. (C) Imaging of spontaneous $[Ca^{2+}]_i$ oscillation in neurons expressing R-GECO1, recorded at excitation 545 nm and emission 590-650 nm. The sampling frequency is 25 Hz. Exposure: 40 ms without any neutral filter applied. (D) Comparison of fluorescence response of Y-GECO1, GCaMP6s and R-GECO1 in neurons upon KCl − induced depolarization in the presence of 50 mM KCl.

To determine if Y-GECO1 is suitable for use with multiphoton excitation, we imaged neurons expressing Y-GECO1 using a 2-photon excitation laser-scanning confocal microscope. Rhythmic decreases in fluorescence could be easily observed using 990 nm 2-photon excitation with 35 mW output power (Figure 3.7C and D), owing to the bright baseline fluorescence. The long Stokes shift fluorescence of Y-GECO1 could be detected using 850 nm 2-photon excitation (35 mW output power), however, it was much dimmer than the 990 nm excitation and the autofluorescence level was higher (Figure 3.7E and F). Accordingly, excitation around 990 nm is preferred. Y-GECO1 is potentially an excellent inverted intensiometric Ca^{2+} indicator for two-photon imaging *in vivo*, and the bright baseline fluorescence of Y-GECO1 facilitates easier identification of transfected cells compared to intensiometric Ca^{2+} indicators which are dim in the resting state, assuming similar expression levels.

We tested the performance of Y-GECO1 in hippocampal neurons in organotypic brain slices at room temperature (20 °C) using confocal microscopy. The Y-GECO1 plasmids with Synapsin I or CMV promoters were delivered by *ex*

vivo electroporation and expressed transiently in neural cells (Figure 3.9A, C and D). The bright baseline fluorescence of Y-GECO1 facilitated identification of transfected neurons. We used theophylline to excite the organotypic brain slices. Low millimolar doses of theophylline can evoke sustained rhythmic seizure-like activities in different neural networks including motor neurons and hippocampal neurons (*243-246*). Indeed, Y-GECO1 successfully detected evoked $[Ca^{2+}]_i$ transients and oscillations with large signal magnitude (Figure 3.9B and Movie S2) that mimic seizure-like discharge. Compared to cytoplasmic targeted Y-GECO1, processes could be satisfactorily visualized without saturation of the somata by tethering Y-GECO1 to the plasma membrane with the N-terminal peptide sequence of the *Src* kinase Lyn (*135*) (Figure 3.9C and D). Lyn-Y-GECO1 expressed in glial cells was able to detect Ca^{2+} waves in various subcellular locations and process terminals (Figure 3.9C). Although the FP body of Y-GECO1 belongs to *Anthozoa*-derived FPs, which are known to often form intracellular puncta in neurons (*247*), no bright intracellular puncta were found in neuronal cells expressing either cytoplasmic Y-GECO1 or membrane tethered Lyn-Y-GECO1. Our results suggest that Y-GECO1 can be a useful tool to study Ca^{2+} dynamic of neural cells *in vivo* with large signal magnitude.

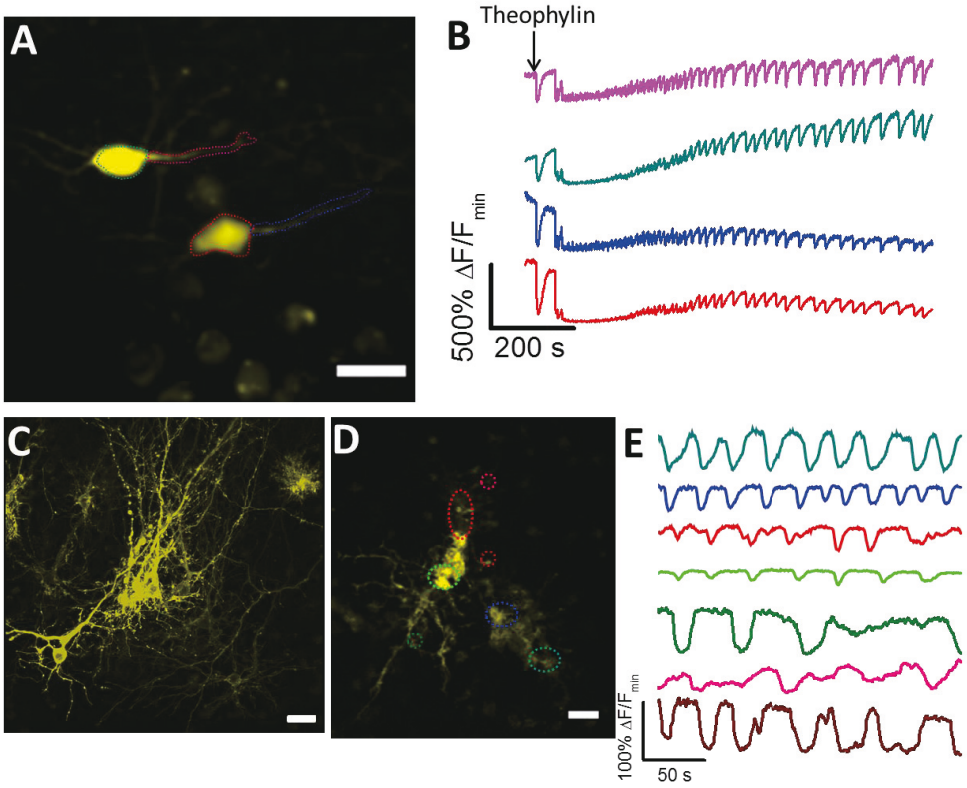

Figure 3.9 Confocal imaging of Y-GECO1 in organotypic slices.

(A) Confocal imaging of neurons expressing Y-GECO1 in a hippocampal slice cultured for 5-6 days. Scale bar: 40 μm. (B) 10 mM theophylline-induced $[Ca^{2+}]_i$ transient and oscillation in neurons was detected by Y-GECO1. The traces correspond to the regions in the image marked with the same color in (A). (C-D) Membrane targeted Lyn-Y-GECO1 in hippocampal slices. (C) 2D projection of a 3D image of neurons expressing Lyn-Y-GECO1 in a slice. Scale bar: 30 μm. (D) Glial cells expressing Lyn-Y-GECO1 with regions of interest indicated by colored dot circles. Three small circles indicate three different process terminals. Scale bar: 30 μm (E) Imaging of theophylline-induced $[Ca^{2+}]_i$ oscillation in glial cells expressing Lyn-Y-GECO1. The traces correspond to the regions of interest with the same color in (D).

3.5 Significance

We present a simple and low cost μFACS system with an integrated piezoelectric actuator for directed evolution of FP and FP-based indicators with throughput up to 300 cells/s. We developed a directed evolution approach that exploited μFACS for library enrichment, and ultimately led to improved variants of the single FP-based Ca^{2+} indicators Y-GECO. Three rounds of directed evolution of Y-GECO were done using both traditional and μFACS-aided approaches in parallel. Comparing the outcomes of these parallel experiments revealed that the use of μFACS improved screening results and saved considerable effort relative to the on-plate manual screening of colonies. Y-GECO1, the final product of directed evolution, possesses a novel yellow color that fills the 50 nm spectral gap between green fluorescent GCaMP and orange fluorescent O-GECO1 in the palette of genetically encoded Ca^{2+} indicators, and opens new opportunities for multicolor Ca^{2+} imaging. Y-GECO1 exhibits a large Ca^{2+} response and a moderate affinity to Ca^{2+} *in vitro*. We demonstrated that Y-GECO1 is a useful Ca^{2+} probe for Ca^{2+} imaging *in vitro* and *ex vivo*. Specifically, Y-GECO1 enables robust detection of Ca^{2+} oscillations in histamine-stimulated HeLa cells, spontaneous activity in untreated neuronal cell culture, and evoked Ca^{2+} transients in drug-treated functionally intact brain slices. Y-GECO1 is useful for both one-photon and two-photon imaging and, relative to typical direct response Ca^{2+} indicators, has a brighter baseline fluorescence that facilitates identification of transfected cells at resting Ca^{2+} concentrations.

3.6 Supplemental materials

Table 3.1 Properties of Y-GECO1 and other variants.

Protein	Ca^{2+}	λ_{abs} (nm) with ($mM^{-1}\cdot cm^{-1}$) in parenthesis	λ_{em} with Φ in parenthesis[1]	Brightness[2] ($mM^{-1}\cdot cm^{-1}$)	pK_a[3]	Dynamic range	K_d' for Ca^{2+} (nM)
GCaMP6f	-	496 (4)	513 (0.10)	0.4	8.7 ± 0.3	50x	405 ± 2 (2.3 ± 0.2)
	+	496 (58)	513 (0.59)	34	6.3 ± 0.1		
Y-GECO0.8	-	410 (25); 523 (31)	513 (0.003, 0.55)	0.08, 17	6.4 ± 0.1	67x	180 ± 10 (2.4 ± 0.2)
	+	411 (38); 522 (9)	513 (0.03, 0.39)	1.1, 3.5	8.1 ± 0.1		
Y-GECO1 ΔG8 (Y-GECO1f)	-	410 (21); 523 (40)	538 (ND[4])	ND	6.3 ± 0.1	80x	2500 ± 160 (2.7 ± 0.2)
	+	413 (41); 522 (10)	538 (ND)	ND	8.5 ± 0.2		
Y-GECO1	-	410 (21); 523 (39)	538 (0.003, 0.76)	0.06, 30	6.3 ± 0.1	200x	190 ± 8 (2.6 ± 0.2)
	+	413 (39); 522 (6)	538 (0.05, 0.18)	1.1, 2.0	8.9 ± 0.1		

Note: The excitation ratio for Y-GECOs is defined as (fluorescence intensity for excitation at 524 nm and emission at 560 nm)/ (fluorescence intensity for excitation at 413 nm and emission at 560 nm). [1]Quantum yield of Y-GECO in the Ca^{2+}-bound state was measured for excitation at both 413 nm and 524 nm. [2]Brightness is defined as the product of ε and Φ. The brightness of Y-GECO in the Ca^{2+}-bound state for excitation at both 413 nm and 522 nm is provided. [3]The pK_a of Y-GECO is defined as the pH at which the dynamic range is 50% of maximum. [4]Not determined.

Table 3.2 Characterization of the Ca^{2+}-dependent fluorescence of Ca^{2+} indicators in HeLa cells.

Cells were treated first with histamine (abb. His), then with Ca^{2+}/ionomycin (abb. Ca^{2+}), and finally with EGTA/ionomycin (abb. EGTA).

Protein (Excitation, nm)	n[1]	Maximum Ca^{2+} to minimum EGTA ratio	Maximum His to minimum His ratio	Maximum His to maximum Ca ratio
GCaMP6s (480)	39	20±7	11±3	0.9±0.3
Y-GECO1 (480)	57	6±1[2]	3.6±0.7[2]	0.6±0.1
Y-GECO1 (ratio[3])	57	13±3	9±2	0.6±0.3

[1]Number of individual transfected cells on which systematic calibration experiments were performed.

[2]The fluorescence change of Y-GECO1 is inverted when excited at 480 nm. The value is the reciprocal of the defined ratio in order to facilitate comparison.

[3]Excitation ratio: 440 nm to 480 nm.

Table 3.3 Oligonucleotides used in this work

Name	Sequence
RV_MluI_X_147mPapaya	GGCATGACGCGTRNVAGCTTCCCAATTAGTGGTCATTTTCTTCATTAC
FW_XhoI_X_148mPapaya	GCGATCCTCGAGBNYAGTACCGAGAAAATTGTGCCTGTTCCAAAGC
FW_XhoI_XX_148mPapaya	GCGATCCTCGAGBNYBNYAGTACCGAGAAAATTGTGCCTGTTCCAAAGC
FW_GGTGGS_mPapaya	GGAGGTACAGGCGGGAGTATGGTGAGCAAGGGCGAGGG
RV_GGTGGS_mPapaya	ACTCCCGCCTGTACCTCCCTTGTACAGCTCGTCCATGCCTGC
FW_XbaI_6His	GCGATGTCTAGAGGTTCTCATCATCATCATCATCATGGTATGGCTAGC
RV_CaM_stop_HindIII	GCGATGAAGCTTCTACTTCGCTGTCATCATTTGTACAAACTCTTCGTAGTTT
Fw_FCK_Gib_6His_YGECO	CTGGGGGCAGCGGGGGATCCACCATGGGTTCTCATCATCATCATCATGGTATGGC
RV_FCK_Gib_YGECO_stop	TCGATAAGCTTGATATCGAATTCTTACTTCGCTGTCATCATTTGTAC
Fw_del_13G	CGTAAGTGGAATAAGACACACGCAGTCAGAGCTATA
Fw_BamHI_Ly	TGGGGATCCACCATGGGATGTATAAAGAGTAAAAGAAAAGATAACTTAA

n	
Fw_Lyn_GECOs	ATGGGATGTATAAAGAGTAAAAGAAAAGATAACTTAAATGATGACGAAGATGATAAGGATCTCGCCACAATG
Fw_BamHI_Kozak_6His	AAACAGGAGGAATTAAGCTTGGGATCCACCATGGGTTCTCATCATCATCATCATCATGGTATGGC
RV_CaM_stop_EcoRI	CGCGAATTCCTACTTCGCTGTCATCATTTGTAC

3.7 References

34. M. Chattoraj, B. A. King, G. U. Bublitz, S. G. Boxer, Ultra-fast excited state dynamics in green fluorescent protein: multiple states and proton transfer. *Proceedings of the National Academy of Sciences of the United States of America* **93**, 8362 (1996).

36. T. Kogure, H. Kawano, Y. Abe, A. Miyawaki, Fluorescence imaging using a fluorescent protein with a large Stokes shift. *Methods* **45**, 223 (2008).

41. B. P. Cormack, R. H. Valdivia, S. Falkow, FACS-optimized mutants of the green fluorescent protein (GFP). *Gene* **173**, 33 (1996).

79. H. Hoi *et al.*, An Engineered Monomeric Zoanthus sp. Yellow Fluorescent Protein. *Chemistry & Biology* **20**, 1296 (2013).

86. J. J. Agresti *et al.*, Ultrahigh-throughput screening in drop-based microfluidics for directed evolution. *Proceedings of the National Academy of Sciences of the United States of America* **107**, 4004 (2010).

88. L. M. Davis, J. L. Lubbeck, K. M. Dean, A. E. Palmer, R. Jimenez, Microfluidic cell sorter for use in developing red fluorescent proteins with improved photostability. *Lab on a Chip* **13**, 2320 (2013).

92. T. Nagai, A. Sawano, E. S. Park, A. Miyawaki, Circularly permuted green fluorescent proteins engineered to sense Ca^{2+}. *Proceedings of the National Academy of Sciences of the United States of America* **98**, 3197 (2001).

95. J. Nakai, M. Ohkura, K. Imoto, A high signal-to-noise Ca^{2+} probe composed of a single green fluorescent protein. *Nature Biotechnology* **19**, 137 (2001).

108. Y. Zhao *et al.*, An Expanded Palette of Genetically Encoded Ca^{2+} Indicators. *Science* **333**, 1888 (2011).

119. O. Griesbeck, G. S. Baird, R. E. Campbell, D. A. Zacharias, R. Y. Tsien, Reducing the Environmental Sensitivity of Yellow Fluorescent Protein: MECHANISM AND APPLICATIONS. *Journal of Biological Chemistry* **276**, 29188 (2001).

133. T.-W. Chen *et al.*, Ultrasensitive fluorescent proteins for imaging neuronal activity. *Nature* **499**, 295 (2013).

135. J. Wu *et al.*, Improved Orange and Red Ca^{2+} Indicators and Photophysical Considerations for Optogenetic Applications. *ACS Chemical Neuroscience* **4**, 963 (2013).

137. M. J. Berridge, P. Lipp, M. D. Bootman, The versatility and universality of calcium signalling. *Nature Reviews Molecular Cell Biology* **1**, 11 (2000).

139. O. Garaschuk *et al.*, Optical monitoring of brain function *in vivo*: from neurons to networks. *Pflügers Archiv* **453**, 385 (2006).

148. K. Horikawa *et al.*, Spontaneous network activity visualized by ultrasensitive Ca^{2+} indicators, yellow Cameleon-Nano. *Nature Methods* **7**, 729 (2010).

153. L. Tian *et al.*, Imaging neural activity in worms, flies and mice with improved GCaMP calcium indicators. *Nature Methods* **6**, 875 (2009).

155. X. R. Sun *et al.*, Fast GCaMPs for improved tracking of neuronal activity. *Nature Communication* **4**, (2013).

170. J. Akerboom *et al.*, Optimization of a GCaMP Calcium Indicator for Neural Activity Imaging. *The Journal of Neuroscience* **32**, 13819 (2012).

210. J. Akerboom *et al.*, Genetically encoded calcium indicators for multi-color neural activity imaging and combination with optogenetics. *Frontiers in Molecular Neuroscience* **6**, (2013).

222. A. E. Palmer, R. Y. Tsien, Measuring calcium signaling using genetically targetable fluorescent indicators. *Nature Protocols* **1**, 1057 (2006).

227. M. J. Berridge, M. D. Bootman, H. L. Roderick, Calcium signalling: dynamics, homeostasis and remodelling. *Nature Reviews: Molecular Cell Biology* **4**, 517 (2003).

228. M. I. Kotlikoff, Genetically encoded Ca^{2+} indicators: using genetics and molecular design to understand complex physiology. *The Journal of Physiology* **578**, 55 (2007).

229. H. Hoi, T. Matsuda, T. Nagai, R. E. Campbell, Highlightable Ca^{2+} Indicators for Live Cell Imaging. *Journal of the American Chemical Society* **135**, 46 (2012).

230. C. Chen, S. H. Cho, F. Tsai, A. Erten, Y.-H. Lo, Microfluidic cell sorter with integrated piezoelectric actuator. *Biomedical Microdevices* **11**, 1223 (2009).

231. C. H. Chen *et al.*, Specific Sorting of Single Bacterial Cells with Microfabricated Fluorescence-Activated Cell Sorting and Tyramide Signal Amplification Fluorescence in Situ Hybridization. *Analytical Chemistry* **83**, 7269 (2011).

232. Y. Xia, G. M. Whitesides, Soft Lithography. *Annual Review of Materials Science* **28**, 153 (1998).

233. H. J. Carlson, R. E. Campbell, Circular permutated red fluorescent proteins and calcium ion indicators based on mCherry. *Protein Engineering Design and Selection* **26**, 763 (2013).

234. H.-w. Ai, K. L. Hazelwood, M. W. Davidson, R. E. Campbell, Fluorescent protein FRET pairs for ratiometric imaging of dual biosensors. *Nature Methods* **5**, 401 (2008).

235. C. Kantor *et al.*, in *Isolated Central Nervous System Circuits,* K. Ballanyi, Ed. (Humana Press, 2012), pp. 315-356.

236. A. Ruangkittisakul *et al.*, High sensitivity to neuromodulator-activated signaling pathways at physiological [K+] of confocally imaged respiratory center neurons in on-line-calibrated newborn rat brainstem slices. *The Journal of Neuroscience* **26**, 11870 (2006).

237. S. H. Cho, C. H. Chen, F. S. Tsai, J. M. Godin, Y.-H. Lo, Human mammalian cell sorting using a highly integrated micro-fabricated fluorescence-activated cell sorter ([small mu]FACS). *Lab on a Chip* **10**, 1567 (2010).

238. S. J. Remington *et al.*, zFP538, a Yellow-Fluorescent Protein from Zoanthus, Contains a Novel Three-Ring Chromophore. *Biochemistry* **44**, 202 (2004).

239. M. J. Higley, B. L. Sabatini, Calcium Signaling in Dendrites and Spines: Practical and Functional Considerations. *Neuron* **59**, 902 (2008).

240. R. Yuste, W. Denk, Dendritic spines as basic functional units of neuronal integration. *Nature* **375**, 682 (1995).

241. C. Grienberger, A. Konnerth, Imaging Calcium in Neurons. *Neuron* **73**, 862 (2012).

242. D. Smetters, A. Majewska, R. Yuste, Detecting Action Potentials in Neuronal Populations with Calcium Imaging. *Methods* **18**, 215 (1999).

243. J. M. Brundege, T. V. Dunwiddie, Modulation of excitatory synaptic transmission by adenosine released from single hippocampal pyramidal neurons. *The Journal of Neuroscience* **16**, 5603 (1996).

244. B. Panaitescu *et al.*, Methylxanthines do not affect rhythmogenic preBötC inspiratory network activity but impair bursting of preBötC-driven motoneurons. *Neuroscience* **255**, 158 (2013).

245. A. Klishin, T. Tsintsadze, N. Lozovaya, O. Krishtal, Latent N-methyl-D-aspartate receptors in the recurrent excitatory pathway between hippocampal CA1 pyramidal neurons: Ca ($^{2+}$)-dependent activation by blocking A1 adenosine receptors. *Proceedings of the National Academy of Sciences* **92**, 12431 (1995).

246. S. Thümmler, T. V. Dunwiddie, Adenosine Receptor Antagonists Induce Persistent Bursting in the Rat Hippocampal CA3 Region Via an NMDA

Receptor-Dependent Mechanism. *Journal of Neurophysiology* **83**, 1787 (2000).

247. D. Cai, K. B. Cohen, T. Luo, J. W. Lichtman, J. R. Sanes, Improved tools for the Brainbow toolbox. *Nature Methods* **10**, 540 (2013).

Chapter 4. All-optical electrophysiology in mammalian neurons using engineered microbial rhodopsins

4.1 Abstract

All-optical electrophysiology—spatially resolved simultaneous optical perturbation and measurement of membrane voltage—would open new vistas in neuroscience research. Here we present an "Optopatch" system for genetically targeted all-optical electrophysiology in mammalian neurons. We evolved two archaerhodopsin voltage indicators, QuasAr1 and QuasAr2, that show improved brightness, voltage sensitivity, and speed; and produce no photocurrent. We engineered a novel channelrhodopsin (ChR) actuator, CheRiff, that shows improved light sensitivity and kinetics. The reporters and actuator were designed so each can be optically excited without perturbing the other. Optical interrogation of neurons in brain slice clearly resolved single action potentials and subthreshold transients. The Optopatch platform enables neuronal electrophysiology with high throughput and high information content.

4.2 Introduction

Neural computations arise through electrical activity in networks of interacting neurons. Within each neuron, activity arises from membrane voltage dynamics in many electrically coupled compartments: synaptically induced voltages in dendritic spines (*248*), dendritic integration of synaptic inputs (*249*), action potential initiation in the axon, and propagation down the axon and back

A version of this chapter has been submitted for publication. I am a co-first author in the manuscript. I designed the screen strategy and engineered QuasAr, the key components of "Optopatch" system. I also contributed to the manuscript writing and QuasAr characterization. Additional result and discussion for directed evolution of Arch are included in this chapter.

into the dendrites (*250*). Thus to disentangle the complex interactions underlying neural dynamics, one would like to visualize membrane voltage across spatial scales, from single dendritic spines to large numbers of interacting neurons, while delivering spatially and temporally precise stimuli (*251, 252*). Optical methods for simultaneous perturbation and measurement of membrane potential could achieve this goal (*253*).

One would further like to target the stimulation and recording to genetically specified cells. Genetic targeting is particularly important in intact tissue where closely spaced cells often perform distinct functions. Genetic targeting is also valuable *in vitro*, for characterizing heterogeneous cultures that arise during stem cell differentiation to neurons (*254*), or while studying neurons co-cultured with other cell types.

Optical stimulation has been demonstrated with glutamate uncaging (*255*), photoactivated ion channel agonists (*256*), and microbial rhodopsin actuators (*257, 258*). Genetically encoded functional readouts include reporters of intracellular Ca^{2+} *(133)* and membrane voltage (*93, 129, 188, 259, 260*). Voltage-sensitive dyes offer good speed, sensitivity, and spectral tuning (*261, 262*), but cannot be delivered to a genetically specified subset of cells and often suffer from phototoxicity.

Simultaneous optical stimulation and readout of neural activity have been implemented via several combinations of the above techniques (*135, 263-265*). However, there is still a need for robust, sensitive, and fast tools for genetically targeted simultaneous optical stimulation and measurement of membrane voltage.

Here we introduce variants of an archaerhodopsin (Arch) voltage indicator and a channelrhodopsin actuator which individually show greatly improved performance relative to published optogenetic tools and which together constitute a tool for all-optical electrophysiology. First, we characterize the optical and electrophysiological properties of the indicator, the actuator, and the co-expressed pair (Optopatch). Second, we use Optopatch to probe neuronal excitation across a wide range of length scales, from single dendritic spines to fields containing dozens of neurons measured in parallel. Finally, we apply Optopatch in tissue. In organotypic brain slice, Optopatch initiates and reports action potentials and subthreshold dynamics with high SNRs.

4.3 Results

4.3.1 Directed evolution and engineering of an Arch-based voltage indicator

We previously showed that Arch functions as a fast and sensitive voltage indicator (*129*). However, the protein had undesirable attributes for a reporter: it was very dim, and the brightness was a nonlinear function of illumination intensity (*186*). Illumination for imaging generated a hyperpolarizing photocurrent, which partially suppressed neural firing. The mutant Arch (D95N) did not generate hyperpolarizing photocurrent, but its step response was dominated by a 41 ms time constant, too slow to resolve action potential (AP) waveforms.

We sought to repair these defects in engineered mutants of Arch. To accommodate the multiple selection criteria, we adopted a hierarchical approach to screening that prioritized brightness over multiple secondary selection criteria (Figure 4.1a). For the first round of screening, a library containing more than 10^4

mutants was generated by error prone PCR of the Arch D95N template and screened in *Escherichia coli*. Those colonies with the highest absolute brightness under excitation with low illumination intensity, relative to genetically fused mOrange2, were picked and the brightness improvements were confirmed by fluorescence measurements of overnight cultures in a microplate reader. A pool of plasmids encoding the brightest mutants was used as the template for the subsequent round of mutagenesis, DNA shuffling by StEP PCR (*266*), and screening. After five iterations of this protocol we arrived at a non-pumping variant of Arch with 5 mutations relative to wild-type (P60S, T80S, D95N, D106Y, and F161V) and significantly improved brightness under excitation with low illumination intensity. This variant, designated as Arch3.5, was used as the template for subsequent efforts to address the secondary selection criteria.

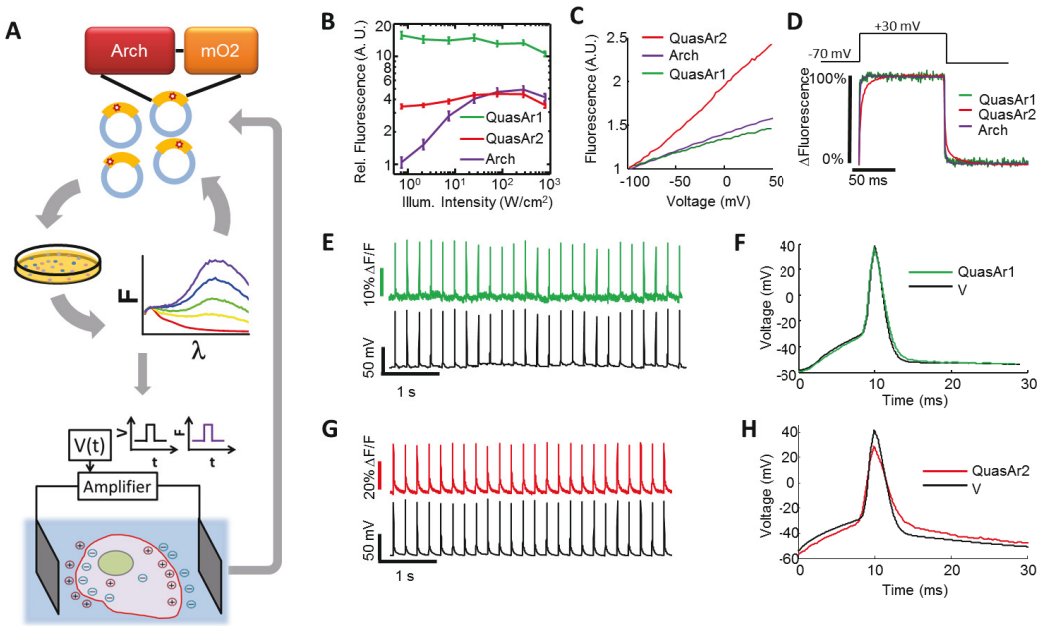

Figure 4.1 Non-pumping Arch-derived voltage indicators with improved speed, sensitivity, and brightness.

A) Hierarchical screen to select improved Arch mutants. Five rounds of random mutagenesis and screening for brightness were performed in *E. coli*. The brightest mutants were subjected to targeted mutagenesis and screening for speed and voltage sensitivity in HeLa cells via induced transient voltage. B) Fluorescence of Arch mutants fused to EGFP and expressed in HEK cells, as a function of illumination intensity. The plot shows Arch fluorescence (640 nm exc., 660 – 760 nm em.) normalized by illumination intensity (640 nm) and by EGFP fluorescence (488 nm exc., 525 – 575 nm em.) to control for cell-to-cell variations in expression. Typical fluorophores (*i.e.* brightness proportional to illumination intensity) would be a horizontal line. Error bars represent s.e.m. (n = 5 – 7 cells for each mutant). C) Fluorescence vs. membrane voltage for Arch, QuasAr1, and QuasAr2 expressed in HEK cells. D) Fluorescence responses to a step in membrane voltage from -70 to +30 mV. E) Simultaneous optical and electrical recording of APs in a rat hippocampal neuron expressing QuasAr1. Frame rate 1 kHz. F) Overlay of mean optically and electrically recorded AP waveforms. Frame rate 2 kHz. G, H) Same as E, F in neurons expressing QuasAr2.

With Arch3.5 in hand, we shifted our focus to tuning other properties of Arch including voltage sensitivity, response kinetics, and the undesirable dependence of brightness on illumination intensity. Positions Asp95 and Asp106 of Arch are structurally aligned with positions Asp85 and Asp96 of bacteriorhodopsin, and have been reported to play key roles in proton translocation during the photocycle (*267, 268*). As the voltage sensing mechanism of Arch is due to electric-field-dependent protonation of the retinal Schiff base (*269, 270*), we reasoned that perturbations of the proton translocation network around the Schiff

base could potentially affect the voltage sensitivity (*129*), response kinetics (*129*), or complex photophysics (*186*) of Arch variants. Accordingly, we constructed libraries in which each of these positions was randomized to a subset of all possible amino acid substitutions. For our first library we randomized position 95 using codon HVS (where H = A, C or T; V= A, C, or G; S = C or G), which encodes for all amino acids except Ala, Gly, Asp, Glu and Val. This library was screened by fluorescence imaging of *E. coli* colonies, and those variants that retained a high ratio of Arch to mOrange2 fluorescence were picked and expressed in HeLa cells. To assess and compare the response kinetics and voltage sensitivity, we used a pair of parallel platinum electrodes to apply a reproducible field potential across single cells and induce transient asymmetries in the membrane voltage (*271*) (Figure 4.2; Methods). This effort led to the identification of the Arch3.5 N95H variant (designated Arch3.7) that showed excellent brightness and fast response kinetics, but relatively poor voltage sensitivity (Table 4.1). Using Arch 3.7 as a template, we constructed a second library by randomizing position 106 to a subset of amino acids with polar or charged side chains (codon NRC, where N = A, C, G, or T; R = A or G). Screening of this library led to the identification of the Arch3.7 Y106H variant (designated QuasAr1) that had improved voltage sensitivity while retaining similar kinetics and brightness to Arch3.7.

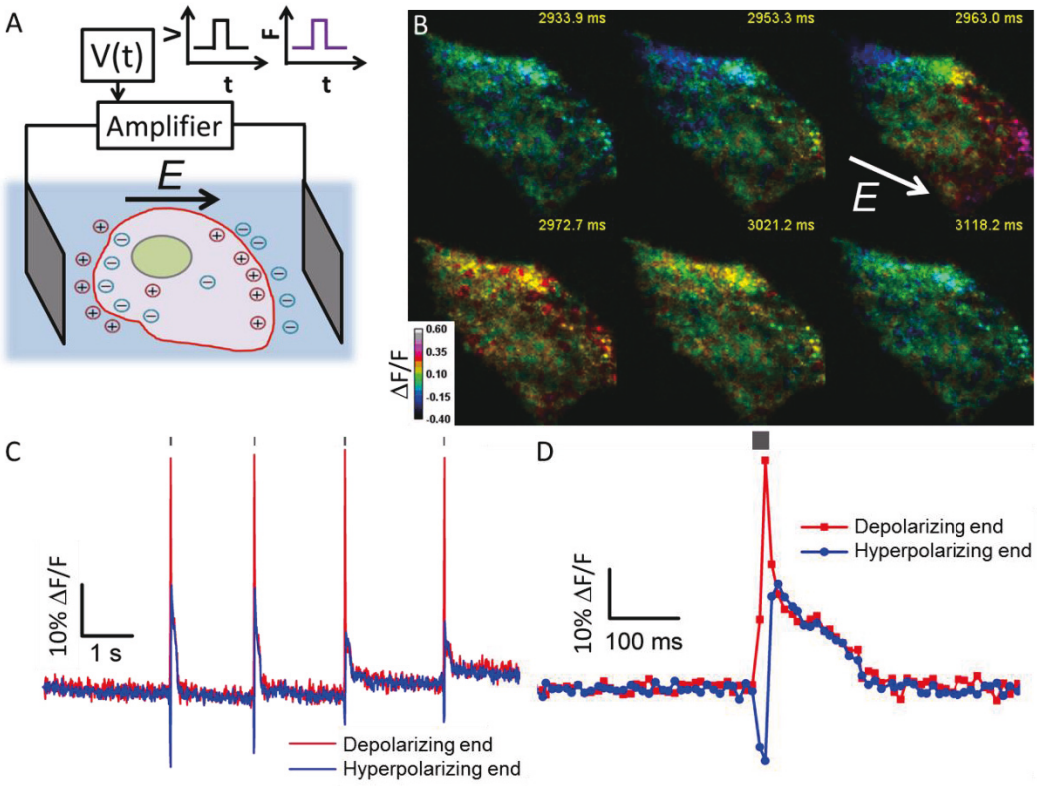

Figure 4.2 Induced transmembrane voltage (ITV) in Arch-expressing HeLa cells.

(A) Experimental setup, showing two platinum electrodes placed on either side of a transfected cell. V (t) represents the pulse generator and high-voltage amplifier. (B) Frames from a movie of a HeLa cell expressing QuasAr1. The cell was stimulated with an electrical pulse (20 ms, 50 V/cm). The images show the fluorescence response (ΔF/F). The arrow labeled 'E' indicates the direction of the electric field. (C) Fluorescence of the cell poles during the ITV experiment shown in (B). Gray marks above the fluorescence traces indicate timing and duration of the ITV pulses. (D) Zoomed in view of one fluorescence intensity peak from (C).

Table 4.1 Arch variants engineered in this work and their mutations that result in improved brightness, kinetic and voltage sensitivities.

Name	Mutations relative to Arch WT	Comments
Arch D95N	D95N	D95N diminished photocurrent but slower kinetics.
Arch variants engineered by directed evolution		
Arch3.2	P60S/D95N/D106Y/F161V/R237W	D106Y improved brightness; F161V improved protein folding.
Arch3.3	P60S/D95N/D106Y/F161V	Non-essential mutation R237W was removed during directed evolution.
Arch3.5	P60S/T80S/D95N/D106Y/F161V	T80S results in better folding/brightness.
Arch variants made by site-directed mutagenesis		
Arch3.7	P60S/T80S/D95H/D106Y/F161V	Combined with D106Y, D95H significantly increases the kinetic. The voltage sensitivity is poor.

Arch3.76	P60S/T80S/D95H/D106C/F161V	D106C results in better voltage sensitivity and membrane trafficking in mammalian cells.
QuasAr1	P60S/T80S/D95H/D106H/F161V	D106H results in further increased voltage sensitivity. Fast kinetic.
QuasAr 1.6	P60S/T80S/D95N/D106H/F161V	D95N/D106H results in better voltage sensitivity but a slow kinetic component.
QuasAr1.8	P60S/T80S/D95C/D106H/F161V	Similar to D95N/D106H, even better voltage sensitivity, irregular V vs. F correlation.
QuasAr2	P60S/T80S/D95Q/D106H/F161V	Excellent voltage sensitivity with fast kinetic; Dimmer than QuasAr1; Normal V vs. F correlation
QuasAr2 H106E	P60S/T80S/D95Q/D106E/F161V	Superb voltage sensitivity; Slow kinetic.

Examination of the modeled structure of QuasAr1 (Figure 4.3a) based on homologous protein Arch-2 (PDB: 2EI4, ref. (*272*)), reveals that mutations T80S and F161V are located in the periphery of the protein, while P60S is close to the Schiff base of the retinal chromophore. Given their location, we suspect that the T80S and F161V substitutions are unlikely to have a direct impact on the photophysical properties of the protein, and are more likely to have a role in improving the folding efficiency. In contrast, the close proximity of the P60S substitution to the Schiff base between K226 and the retinal chromophore suggests the substitution has a more direct role in influencing the photophysical properties of the protein. Specifically, this mutation is likely responsible for much of the observed improvements in brightness and voltage sensitivity. Introduction of individual substitutions (*i.e.*, T80S or F161V or P60S) in the context of Arch with D95H and D106H did not lead to comparable improvements in brightness as observed for QuasAr1. This result suggests that a synergetic effect between these three mutations plays an important role in the improved brightness of QuasAr1.

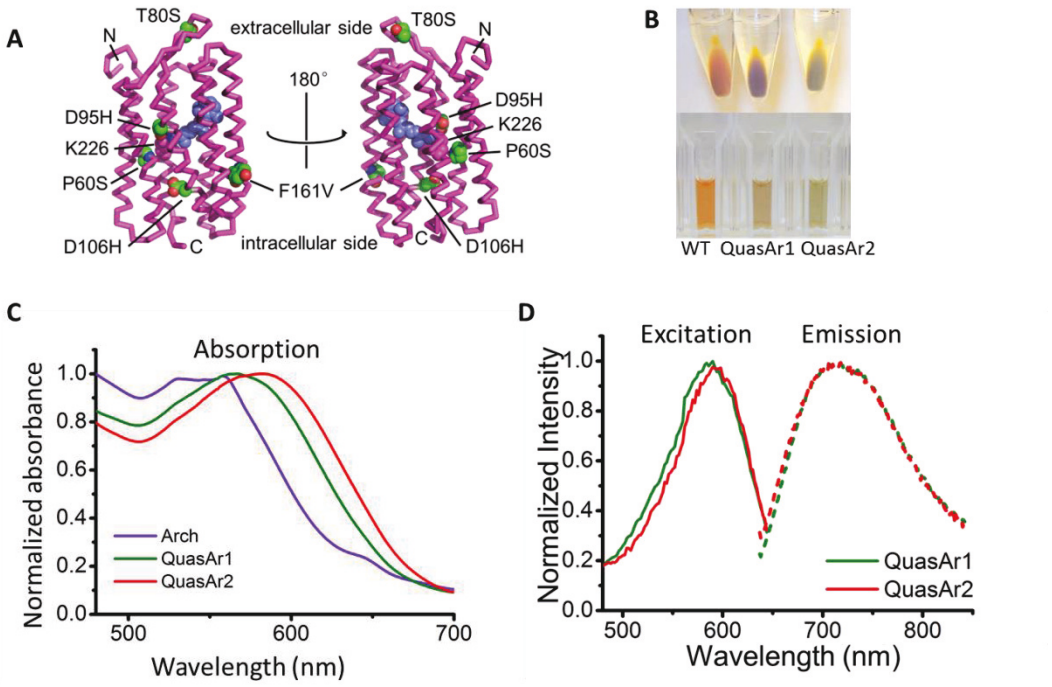

Figure 4.3 Structural and spectroscopic properties of QuasArs.

A) Locations of mutations in QuasAr1, modeled on the crystal structure of Arch-2 (PDB: 2EI4) (*272*). Arch-2 has 90% amino acid identity with Arch-3. The retinal chromophore is colored blue and mutations are colored green. B) Top: Images of *E. coli* pellets expressing Arch, QuasAr1, and QuasAr2. Bottom: Images of solubilized protein. C) Absorption spectra of Arch, QuasAr1 and QuasAr2, measured on solubilized protein. D) Excitation and emission spectra measured on QuasAr1 and QuasAr2. Arch was too dim to measure in the fluorometer. Emission spectra were recorded with λ_{exc} = 600 nm. Excitation spectra were measured with λ_{em} = 750 nm.

To enable more accurate electrophysiological characterization and low throughput screening in HEK cells and primary neuron cultures, we cloned QuasAr1 into a lentivirus vector with a CaMKII promoter and a 3' Woodchuck Hepatitis Virus Posttranscriptional Regulatory Element (WPRE). To improve membrane trafficking, we added an endoplasmic reticulum (ER) export motif and a trafficking signal (TS) sequence as previously described (*270*). Using this expression system, together with simultaneous patch clamp and fluorescence imaging, we examined a selection of QuasAr1 variants with mutations at position 95 (Asn, Cys, Gln, His and Tyr) and position 106 (Arg, Asp, Asn, Cys, Glu, His, Lys and Tyr). These experiments confirmed that histidine at position 106 provides the best combination of negligible photocurrent, improved voltage sensitivity, and fast kinetics. Furthermore, we found that QuasAr1 with either Gln, Cys, or Asn at position 95 exhibit better voltage sensitivity than QuasAr1 itself, while retaining reasonably fast kinetics. In particular, the H95Q variant of QuasAr1 (designated QuasAr2) exhibits better voltage sensitivity compared to the other two mutants. Notably, another improved Arch variant with substitutions D95Q and D106E has recently been reported (*273*). Introduction of the H106E substitutions into QuasAr2 resulted in a variant (QuasAr2 H106E) with excellent voltage sensitivity but slower fluorescent responses to voltage changes ($\tau > 3$ ms) (Table 4.1).

The two most promising mutants were named QuasAr1 and QuasAr2. Figure 4.3 shows absorption, fluorescence excitation, and emission spectra of the solubilized QuasAr proteins. The fluorescence quantum yields of solubilized QuasAr1 and 2 were 19- and 10-fold enhanced, respectively, relative to the non-pumping voltage indicator Arch (D95N) (Table 4.2). Due to the nonlinear dependence of fluorescence on illumination intensity in wild-type Arch (*186*),

comparisons to its fluorescence are only useful under illumination conditions used for fluorescence imaging.

Table 4.2 Quantum yields of Arch variants measured in solubilized protein.

Fluorescence emission spectra were recorded with excitation at 600 nm. Details of sample preparation and measurement procedures are given in Materials and Methods.

Protein Name	**Quantum yield**	**Quantum yield relative to Arch D95N**
Arch	N/A*	N/A*
Arch D95N	4×10^{-4}	1.0
QuasAr1	8×10^{-3}	19
QuasAr2	4×10^{-3}	10
Arch D95H/D106H	2×10^{-3}	4.2
Arch D95H/D106H/P60S	5×10^{-3}	12
Arch D95H/D106H/F161V	5×10^{-3}	13

* Due to the low light intensities used to determine QYs, fluorescence from Arch was not detected above baseline.

We compared the fluorescence, voltage sensitivity, and speed of the QuasArs to wild-type Arch in HEK cells, using epifluorescence microscopy and manual patch clamp. Under low intensity illumination (640 nm, 500 mW/cm^2), QuasAr1 was 15-fold brighter than wild-type Arch, and QuasAr2 was 3.3-fold brighter (Figure 4.1b; Methods). Neither mutant showed the optical nonlinearity seen in the wild-type protein. At high intensity (> 100 W/cm^2) QuasAr1 was 2.5-fold brighter than wild-type Arch, while the brightness of QuasAr2 and of wild-type Arch was comparable.

Fluorescence of Arch, QuasAr1, and QuasAr2 increased nearly linearly with membrane voltage between -100 mV and +50 mV (Figure 4.1c, Methods). Sensitivities were ($\Delta F/F$ per 100 mV): 95% for QuasAr2, 40% for Arch, and 33% for QuasAr1. The sensitivity of QuasAr2 is a significant improvement over both Arch and Arch (D95N) (previously reported to have $\Delta F/F \approx 60\%$ per 100 mV). Photon shot noise is less significant for brighter fluorophores, so the ability to resolve small steps in membrane voltage depends on absolute brightness, not just on fractional sensitivity, $\Delta F/F$. Thus the greater brightness of QuasAr1 relative to Arch overcame its slightly lower sensitivity from a signal-to-noise perspective.

Steps in membrane voltage (-70 mV to +30 mV) induced rapid fluorescence responses in both mutants and in wild-type Arch (Figure 4.1d). In QuasAr1 and Arch, the step response (0 to 90%) was faster than 0.5 ms, the temporal resolution of our measurement. In QuasAr2, the step response was bi-exponential. The dominant component (81% of the response) had a time constant of 1.0 ms; the remainder (19%) had a time constant of 16.5 ms. The step responses of all three proteins were symmetric between rising and falling edges.

In cultured rat hippocampal neurons, wild-type Arch generated photocurrents of 220 ± 30 pA (n = 6 cells; all statistics are mean ± s.e.m. unless specified) under red illumination often used for imaging (640 nm, 300 W/cm^2) and 140 ± 25 pA under blue light used for optogenetic stimulation (488 nm, 500 mW/cm^2) (Figure 4.4). These currents hyperpolarized cells by 25 ± 4 mV and 19 ± 3 mV, respectively. Neither QuasAr1 nor QuasAr2 generated detectable photocurrent in neurons under red light (tested up to 900 W/cm^2) or blue light (Figure 4.4).

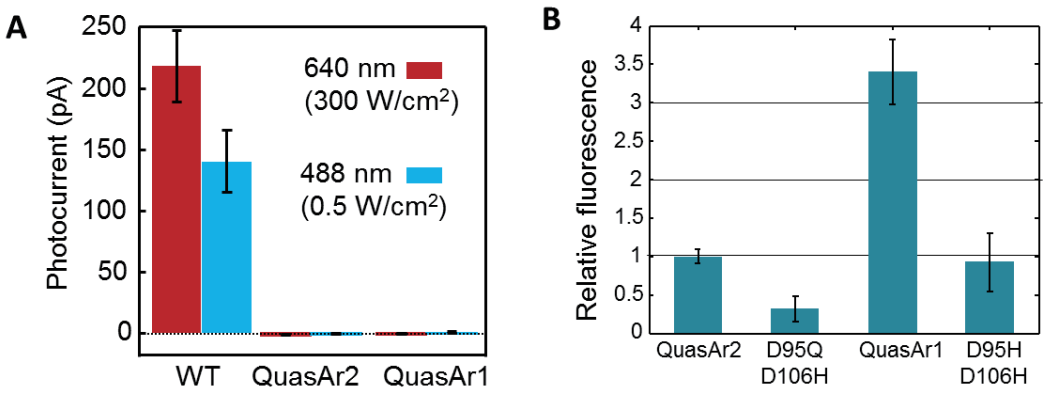

Figure 4.4 Photophysics of QuasArs in mammalian cells.

A) Wild-type Arch expressed in neurons generated substantial photocurrent under red (640 nm, 300 W/cm^2) or blue (488 nm, 500 mW/cm^2) illumination (n = 5 cells). Neither QuasAr1 (n = 9 cells) nor QuasAr2 (n = 7 cells) generated detectable photocurrents under either illumination condition, nor under red illumination at up to 900 W/cm^2. B) Comparison of fluorescence between QuasAr mutants and Arch double mutants, expressed as EGFP fusions in HEK cells. The double mutants had mutations at the locations of the proton acceptor (Asp95) and proton donor (Asp106) to the Schiff base. QuasAr1 has mutations D95H, D106H,

and QuasAr2 has mutations D95Q, D106H. The three additional backbone mutations in the QuasArs (P60S, T80S, F161V) increased brightness relative to the double mutants. Fluorescence of each Arch mutant was measured with excitation at 640 nm and emission from 660 – 760 nm. To control for variation in expression level, fluorescence was normalized by EGFP fluorescence (λ_{exc} = 488 nm, λ_{em} = 510 – 550 nm). Error bars represent s.e.m. for measurements on n = 5 to 10 cells.

Fluorescence of QuasAr1 and QuasAr2 reported APs in cultured neurons with high electrical and temporal precision (Figure 4.1e-h). When optically recorded APs (640 nm exc., 800 W/cm^2) were scaled to match the patch clamp recordings, the single-trial noise in the optical signal was equivalent to 3 to 3.5 mV (QuasAr1; Figure 4.1e), or to 1.2 to 2.5 mV (QuasAr2; Figure 4.1g), at a 1 kHz frame rate. These noise levels are specific to our optical setup and may differ for setups with different light sources, objectives, filters, or detectors (Methods).

To determine the temporal precision of the QuasAr indicators, we used the sub-frame interpolation algorithm of Refs. (*271, 274*) to infer the timing with which the fluorescence reached 70% of maximum at each AP, and compared to the high time-resolution patch clamp recording. Root-mean-square (r.m.s.) temporal jitter was 44 μs for QuasAr1 (n = 97 APs) and 61 μs for QuasAr2 (n = 99 APs). This jitter reflects the combined errors in timing intrinsic to the optical measurement (shot-noise and distortion of the waveform by the reporter) and errors introduced by temporal discretization of the camera frames and the

sub-frame interpolation. Thus optical recordings with QuasArs can determine spike timing with precision much greater than the camera exposure time.

QuasAr1 did not introduce detectable broadening in the optically recorded AP waveform, sampled at 2 kHz (Figure 4.1f). QuasAr2 broadened the optically recorded AP by 650 ± 150 μs relative to the simultaneously recorded electrical waveform at 70% maximum depolarization (n = 5 cells; mean ± s.d.) (Figure 4.1h).

The absence of a photocurrent and the improved brightness, sensitivity, and speed of the QuasAr reporters relative to the first-generation Arch-based indicators make the QuasArs attractive tools for voltage imaging (Table 4.3), either in isolation or in combination with other blue-shifted reporters or actuators.

Table 4.3 Spectroscopic and kinetic properties of Arch mutants.

Brightness, response speed, and sensitivity were measured in HEK293 cells. Photocurrent was measured in cultured rat hippocampal neurons under voltage-clamp at V_m = -65 mV.

Mutant	**Brightness (λ_{exc} = 640 nm)**		**Fluorescence response time to a voltage step (-70 mV to +30 mV)**			**Sensitivity (ΔF/F per 100 mV)**	**Photocurrent (pA) in neurons (300 W/cm^2, 640 nm)**
	0.7 W/cm^2	800 W/cm^2	τ_1 (ms)	τ_2 (ms)	% τ_1		
Arch (WT)	1	4.0	0.6	NA	NA	40%	220 ± 30
QuasAr1	15.2	10.3	<0.5	NA	NA	33%	0
QuasAr2	3.4	3.4	1.0	16.5	81%	95%	0

4.3.2 Optopatch constructs

The far-red excitation spectrum of the QuasAr reporters suggested that they could be paired with a blue light-activated channelrhodopsin to achieve all-optical electrophysiology. For spatially precise optical excitation, the channelrhodopsin should carry current densities sufficient to induce APs when only a subsection of a cell is excited. Existing optogenetic actuators have had only marginal success in achieving this goal (*275, 276*). Under typical neural culture conditions, rapid and robust initiation of precisely timed APs requires currents of approximately 1 nA for at least 2 ms (*277*). Furthermore, light used for imaging the reporter should not activate the actuator, and light used for activating the actuator should not confound the fluorescence signal of the reporter. Optical stimulation and readout can be spatially segregated, but doing so limits the scope of possible experiments, particularly in optically scattering tissues (*278*).

Here, we generate Optopatch constructs that can achieve optical stimulation and readout in the same cell. We chose CheRiff, an engineered version of a novel optogenetic actuator *Scherffelia dubia* ChR (sdChR) (*279*), as the optogenetic actuator in the Optopatch construct. Optopatch1 and Optopatch2 consisted of bicistronic vectors for co-expression of CheRiff-EGFP and QuasAr1- or QuasAr2-mOrange2, respectively (Figure 4.5). We also made Optopatch variants which contained non-fluorescent EGFP and mOrange2 mutants, freeing the spectrum for other uses (Methods). The QuasAr and CheRiff constructs could also be delivered separately, but the bicistronic vector maintained a more uniform ratio of actuator to reporter expression levels.

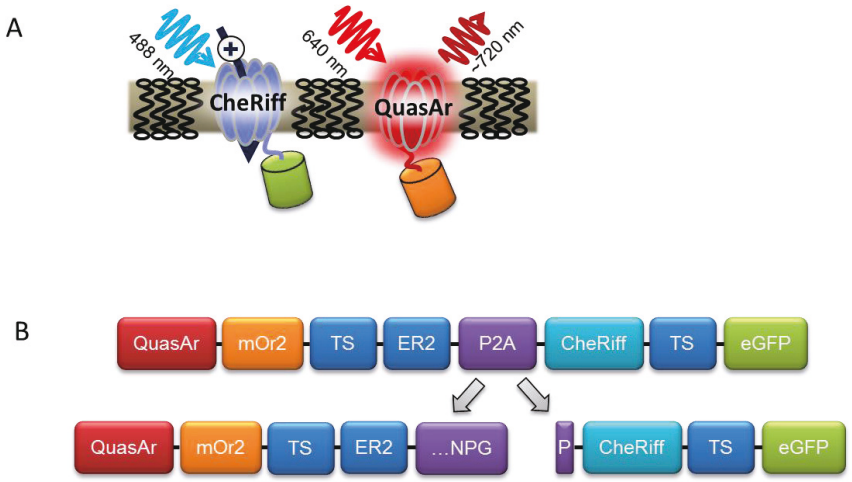

Figure 4.5 Optopatch construct.

A) The optopatch constructs lead to co-expression of CheRiff and QuasAr in the cell plasma membrane. The cell depolarizes when CheRiff is excited with blue light. Voltage fluctuations are recorded optically by exciting QuasAr with 640 nm light, and recording emission between 660 nm and 760 nm. B) The bicistronic vector consists of a QuasAr fused to mO2 with the TS and ER2 trafficking motifs followed by a porcine teschovirus-1 (P2A) sequence, and ending with CheRiff fused to EGFP. The P2A peptide causes a ribosomal skip, leading to approximately stoichiometric co-expression of the actuator and reporter.

We characterized Optopatch2 in detail. When expressed under a *CaMKIIα* promoter in cultured rat hippocampal neurons (Methods), Optopatch2 showed high expression and good membrane trafficking of both CheRiff and QuasAr2 (Figure 4.6a).

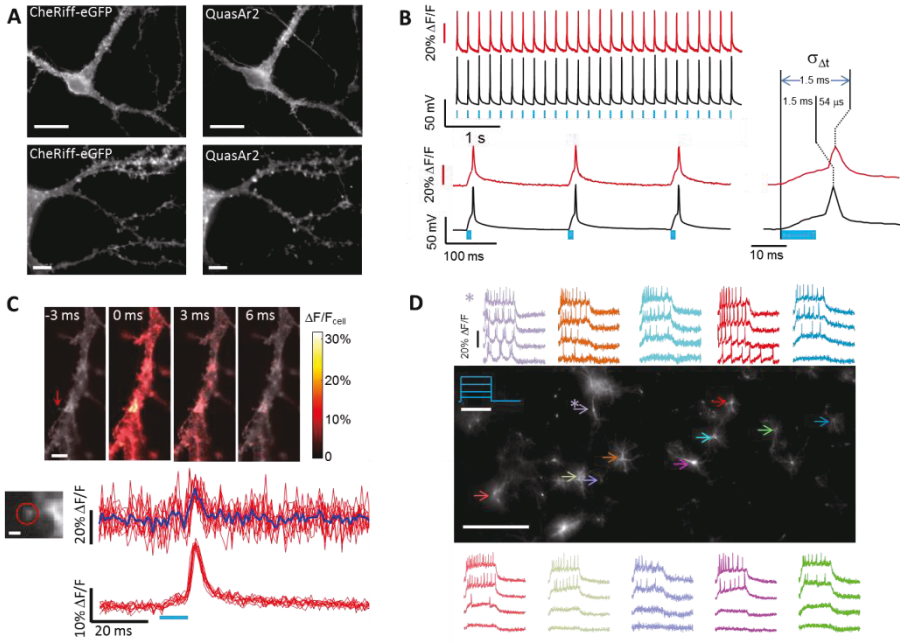

Figure 4.6 Optopatch2 enables high fidelity optical stimulation and recording in cultured neurons.

A) Trafficking of Optopatch components in cultured rat hippocampal neurons. Left: CheRiff-EGFP, measured via EGFP fluorescence. Right: QuasAr2, measured via retinal fluorescence. Scale bars: top 20 µm, bottom 5 µm. B) Temporally precise optical initiation and monitoring of single APs. Each blue bar represents a flash of whole-field illumination (488 nm, 25 mW/cm^2, 10 ms, repeated at 5 Hz). Red: Whole-cell single-trial fluorescence. Black: patch clamp recording. Trial-to-trial jitter in the relative timing is indicated in the right panel. C) Optical mapping of an optically induced AP. Stimulation at 488 nm, 95 mW/cm^2, 10 ms, repeated at 5 Hz, localized to the soma. Top: Filmstrip showing average of n = 20 temporally registered trials. Fluorescence is normalized to mean fluorescence of the dendrite. Images are composite of mean fluorescence (gray) and changes in fluorescence (heat map). Arrow indicates dendritic spine location.

Scale bar 5 μm. Bottom: Single-trial detection of back-propagating APs in a single dendritic spine, shown on the left. Scale bar 1 μm. Top traces: ten single-trial recordings from the spine (red) and their average (blue). Bottom traces: ten single-trial recordings from the parent dendrite. D) Parallel optical stimulation and recording. Stimulation waveforms shown on the top left (488 nm, 500 ms pulses, 0 to 10 mW/cm^2, repeated at 5 s intervals). Synaptic blockers were added to suppress network activity. Traces show simultaneously acquired single-trial fluorescence from 10 neurons, with correspondingly colored arrows indicating source cells. Asterisk indicates a cell that showed bursts of 3-4 APs under weak stimulation. Scale bar 500 μm. Image is of EGFP fluorescence.

A neuron expressing Optopatch2 was exposed to whole-field illumination with pulses of blue light (10 ms, 25 mW/cm^2) to stimulate CheRiff, and simultaneous constant illumination with red light (800 W/cm^2) to excite fluorescence of QuasAr2. We imaged fluorescence of QuasAr2 at a 1 kHz frame rate and calculated fluorescence from whole-cell average intensity, while simultaneously recording membrane voltage via a patch pipette. Figure 4.6b shows the close correspondence of the optical and electrical traces.

A key parameter is the temporal precision with which single spikes can be elicited and recorded. The r.m.s. jitter between onset of optical stimulation and peak of the electrically recorded AP was 1.5 ms (Figure 4.6b, right), similar to that found in other channelrhodopsins (*277*). Using sub-frame interpolation to infer optical spike timing (*271, 274*), we measured an r.m.s. jitter between optically and electrically recorded spikes of 54 μs (Figure 4.6b, right).

A second key parameter is the SNR in the fluorescence traces. In optically evoked APs monitored with whole-cell red illumination at 300 W/cm^2, the ratio of peak amplitude to baseline noise was 45 ± 5 (n = 8 cells), corresponding to an optical precision of ~2 mV on a 90 mV AP. Figure 4.6c shows a higher spatial resolution map of a back-propagating AP in a dendrite. Under high-intensity focused red illumination (2200 W/cm^2), the signal was detected in single dendritic spines on a single-trial basis, with a SNR of 2.5 in a 1 kHz bandwidth.

Due to the intense red light used to image QuasArs, photobleaching and phototoxicity are potential concerns. Thus a third key parameter is the long-term stability of the fluorescence signal. Neurons expressing Optopatch2 were exposed to whole-cell illumination for 30 minutes continuously at 640 nm, 300 W/cm^2. At 60 s intervals the response of the cells was probed with blue light to induce a burst of APs (5 pulses of 10 ms, 5 Hz, 20 mW/cm^2). The QuasAr2 fluorescence photobleached with a time constant of 17 min. However, the neurons continued to fire with 100% fidelity and the APs did not show a detectable change in width over a 30-minute recording (Figure 4.7).

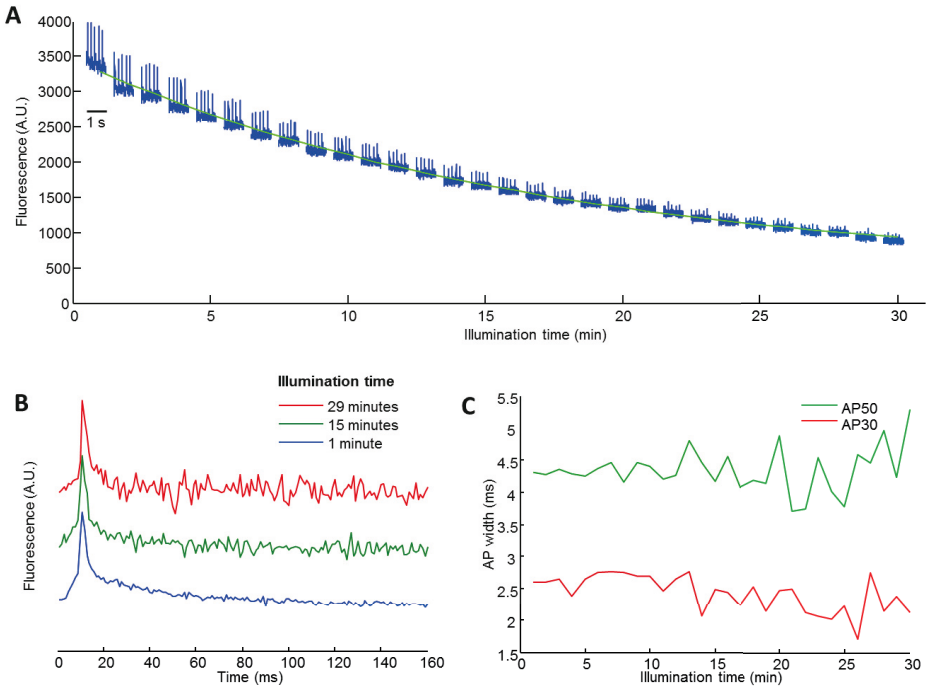

Figure 4.7 Photobleaching of QuasAr2 in Optopatch2.

A) Fluorescence traces from a neuron expressing Optopatch2. The cell was illuminated for 30 minutes continuously at 640 nm, 300 W/cm^2 and probed at 60 s intervals with blue light to induce a burst of APs (5 pulses of 10 ms, 5 Hz, 20 mW/cm^2). The cell fired APs with 100 % fidelity over the recording period, though the SNR decreased as the QuasAr2 fluorescence dropped. B) Fluorescence traces of APs at the beginning, middle, and end of the recording in (A). Each trace in (B) is an average of the 5 APs elicited during that time point. C) AP widths measured at 50% and 30% of the peak. APs did not show a detectable change in width over the 30-minute recording.

Optical electrophysiology holds the promise to facilitate rapid characterization of neuronal cultures. Based on the robust performance of

Optopatch2, we evaluated its utility in simultaneous measurements on large numbers of neurons. We constructed a low-magnification microscope which imaged a 1.2 × 3.3 mm field of view with 3 μm spatial resolution and 2 ms temporal resolution (Methods). This imaging system could record optically from up to 50 expressing cells in a single field of view, though we typically plated at a density of 15 – 25 expressing cells per field of view to facilitate image segmentation. Figure 4.8 shows an image of a neuronal culture acquired with this system

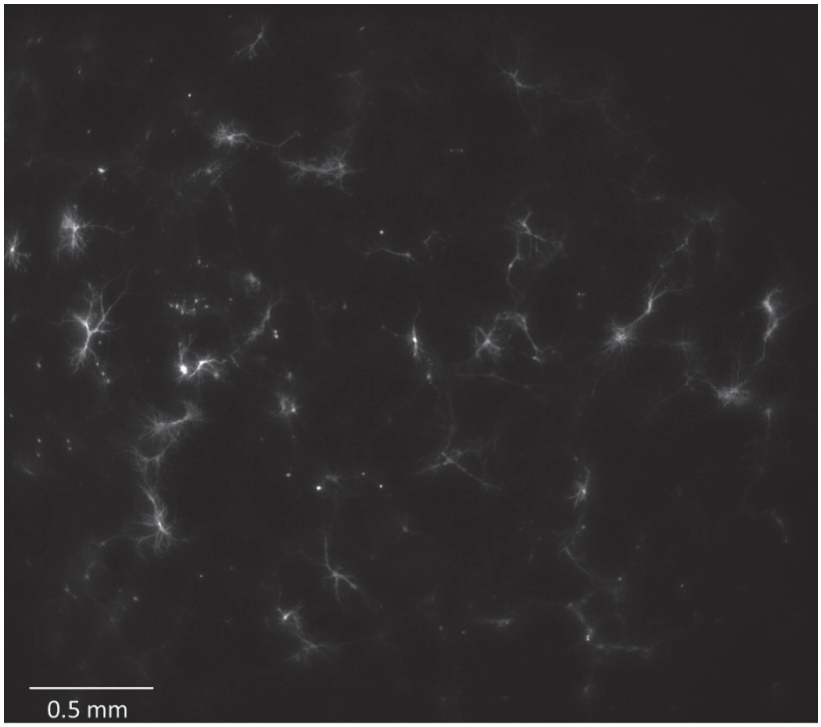

Figure 4.8 Low magnification optical system enables simultaneous imaging of many neurons.

Neurons expressing Optopatch2, imaged via EGFP fluorescence. More than 50 cells are visible in this field of view. Limitations on data-rate from the camera

required that the field of view be compressed in the vertical direction to 0.6 mm for optical recordings at 1 kHz, or to 1.2 mm for optical recordings at 500 Hz.

Using this low magnification system, we characterized the optically evoked firing patterns and AP waveforms in n = 169 neurons expressing Optopatch2, in the presence of synaptic blockers. Each field of view was exposed to whole-field pulses of blue light to evoke activity (0.5 s, repeated every 6 s, nine intensities increasing from 0 to 10 mW/cm^2). QuasAr2 fluorescence was simultaneously monitored with whole-field excitation at 640 nm, 100 W/cm^2 (Figure 4.6d). Several distinct firing patterns were observed, including fast-adapting and slow-adapting spike trains. Two neurons showed intermittent bursting (one of these is indicated by a star in Figure 4.6d). Optopatch measurements can therefore detect rare electrophysiological phenotypes that might be missed in a manual patch clamp measurement.

4.3.3 Imaging in organotypic slice culture

To explore applications of Arch-based reporters in tissue, we expressed Optopatch2 in organotypic mouse brain slice using biolistic gene delivery. Neurons that had taken up the gene were clearly visible via fluorescence of EGFP (indicating CheRiff) and QuasAr2 under wide-field epifluorescence imaging (20× N.A. 1.0 water immersion objective) (Figure 4.9). Upon illumination with pulses of blue light (10 ms, repeated at 5 Hz, 7.5 mW/cm^2), the fluorescence under red excitation (1,200 W/cm^2 nominal incident intensity, not corrected for light scatter) showed clearly resolved APs. Figure 4.9b shows a series of single-trial optical

recordings. These traces represent whole-cell fluorescence, without correction for photobleaching or background subtraction.

We performed Optopatch experiments on n = 7 separately prepared organotypic brain slices (Figure 4.9). AP amplitudes ranged from ΔF/F = 6.3 to 26.5% (calculated without subtraction of background autofluorescence). SNRs for single-trial detection of APs in a 1 kHz bandwidth ranged from 7.8 to 65.6. At lower red excitation intensity (400 W/cm^2 nominal incident intensity, not corrected for light scatter), SNRs for single-trial detection of APs ranged from 6.2 to 38.2. The jitter in timing between optical stimulus and optically resolved AP peak ranged from 0.4 to 1.1 ms.

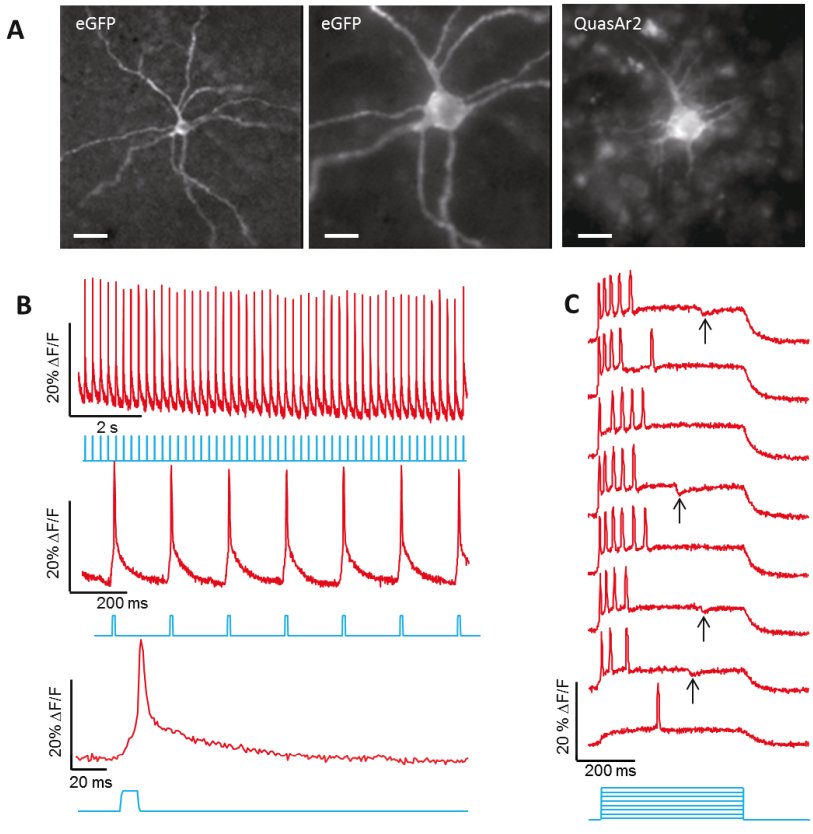

Figure 4.9 Optopatch2 in organotypic hippocampal slice culture.

A) Left and middle: EGFP fluorescence, indicating CheRiff distribution. Right: QuasAr2 fluorescence. Scale bars from left to right: 50 μm, 20 μm, 20 μm. B) Single-trial optical recordings of APs initiated by pulses of blue illumination (10 ms, 7.5 mW/cm^2). Signal represents whole-cell fluorescence without photobleaching correction or background subtraction. C) Bursts of APs triggered by steps of blue illumination (500 ms, 1-10 mW/cm^2). Inhibitory potentials (arrows) were sometimes observed during the stimulation intervals, but not during rest intervals, suggesting inhibitory feedback arising from optically induced network activity. For B) and C), red illumination was 1,200 W/cm^2 nominal incident intensity, not corrected for light scatter. Fluorescence collected at a frame rate of 1 kHz.

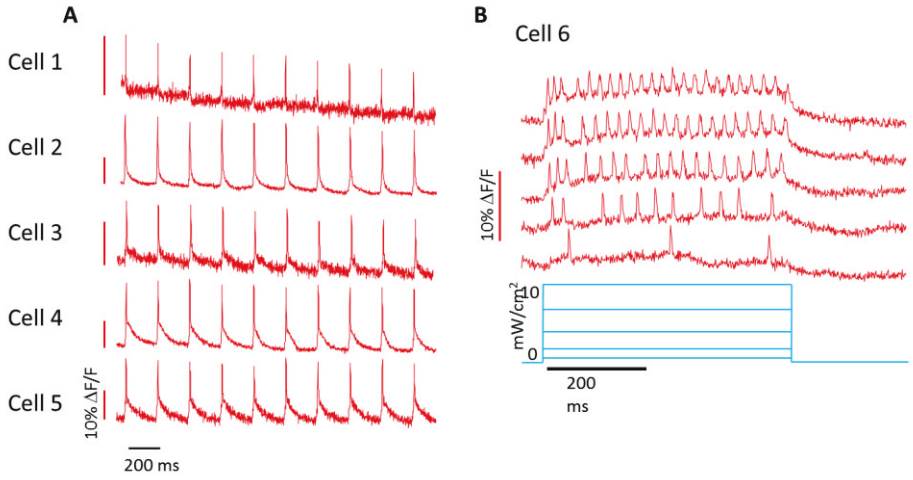

Figure 4.10 Optopatch measurements in organotypic slice culture.

A) Optical recordings of optically evoked action potentials in five separately prepared brain slices expressing QuasAr2. Differences in SNR reflect differences in cell depth and in expression level. Action potentials were induced with blue

light (10 ms, 7.5 mW/cm^2, repeated at 5 Hz). B) Sustained spiking in response to steps in blue light intensity (488 nm, 500 ms, increasing intensity from 1 to 10 mW/cm^2). QuasAr2 fluorescence was excited with illumination at 640 nm, 400 W/cm^2 incident on the sample, not corrected for scattering.

We further tested the response of neurons in tissue to extended pulses of blue illumination (0.5 s, 1 to 10 mW/cm^2). This stimulation elicited a variety of firing patterns, including single spikes, bursts (Figure 4.9C) and sustained activation (Figure 4.10). Optically induced spike trains were often interrupted by hyperpolarizing fluorescence transients, which we provisionally ascribe to inhibitory feedback in the local micro-circuit. We did not observe these inhibitory potentials in the absence of optical stimulation. These results demonstrate the feasibility of measuring single-cell, single-trial AP waveforms, excitability, and subthreshold dynamics in tissue.

4.4 Discussion

We have designed and implemented a bacterial colony-based screening approach for the identification of Arch-based voltage sensors with improved brightness. The major advantage of this approach is that it enables us to interrogate a very large number of randomly generated variants for improved fluorescent brightness, and thereby address the primary shortcoming of Arch as a voltage indicator. The alternative approach of solely relying on manual testing of each variant in mammalian cells (*183, 273*) has very low throughput and would be unlikely to lead to the discovery of mutants, particularly those at non-obvious

locations far from the chromophore, which provide substantial improvements in brightness. Of course, the danger of relying on a bacteria-based screen is that we pick up many variants that are bright but with diminished voltage sensitivity. Accordingly, we perform a secondary mammalian cell-based screen, with membrane depolarization by electric field stimulation, to assess the voltage sensing performance of the brightest variants and exclude those with low voltage sensitivity.

While library screening in the context of *E. coli* has proven very useful for the directed evolution of stand-alone FPs, FRET-based indicators, and single FP-based Ca^{2+} indicators (*108, 135*), at the outset of this work it was an open question whether this strategy would also prove useful for microbial opsin-based voltage indicators. To answer this question, several challenges need to be addressed. First of all, this strategy requires the voltage indicator to be expressed functionally in both bacteria and mammalian cells. In the case of FPs, a stand-alone FP or a FP-based indicator is a soluble protein that likely experiences an intracellular environment that is not too dissimilar from the cytoplasm of a mammalian cell. In contrast, microbial opsin-based voltage indicators are integral membrane proteins that would experience quite different molecular environments when expressed in bacteria and mammalian cells, given their distinct membrane compositions. Indeed, most microbial opsins can not be expressed functionally in both bacterial and eukaryotic cells (*280*). For example, PROPS can be functionally expressed in *E. coli* cells but fails to localize to the plasma membrane of mammalian cells even when assisted with membrane trafficking signal sequences (*185*). Fortunately, Cohen and coworkers found that Arch and its homologues can express well in both *E. coli* and mammalian cells, including

neurons (*129, 185*). This unique versatility of Arch with respect to functional expression in both bacteria and neurons provides a unique opportunity and led us to suspect that a bacteria-based screening strategy was worth pursuing.

The effectiveness of our screening approach was demonstrated by the fact that five rounds of directed evolution led to the identification of Arch variants with improved protein folding and brightness. An additional two rounds of screening libraries of Arch with randomized residues in position 95 and 106 led to the identification of QuasAr1 that is 15 times brighter than Arch WT in cell but retains comparable voltage sensitivity and speed. Based on the backbone of QuasAr1, manual test of several mutations on position 95 using patch clamp technique resulted in discovery of new variants QuasAr2, QuasAr1.8, and QuasAr1.6 with better voltage sensitivities than QuasAr1.

Our QuasAr series are still dim compared to FPs, but exhibit significant improvement for voltage imaging in cell cultures and tissue samples compared to Arch-3 WT and Arch-3 D95N. Despite the substantial progress we have made in improving the brightness of Arch, the quantum yield of QuasAr1 (the brightest variant) is only 4×10^{-3}, which is still one order of magnitude lower compared to the infrared FPs (*53*) that share a similar emission maximum and are regarded as being useful for live cell imaging applications. Fortunately, the QuasAr series of voltage sensors have excellent photostability that enables excitation using high power illumination. Unlike Arch-3 WT that generates a photocurrent under strong light illumination, there is essentially no photocurrent generated by the QuasAr series, and therefore our new voltage sensors do not perturb the membrane potential of targeted cells and permit the use of higher illumination intensities. Combined with the improved voltage sensitivity as well as a linear relationship

between brightness and illumination strength, the QuasAr series exhibits better performance in the voltage imaging of cell culture and intact tissues compared to Arch-3 WT and Arch-3 D95N. In fact, QuasAr1 and 3.77Q faithfully reported action potentials in single-trial basis with high SNR in cultured neurons. In addition, QuasAr2 clearly resolved spike trains in organotypic mouse brain slice, which was not possible using previous Arch-based voltage sensors (*281*).

We expect that further enhancement of Arch is possible, and that improved screening approaches and further exploration of large libraries of variants will ultimately lead to even brighter and better trafficking variants. For example, an engineered bacteria strain that is capable of producing retinal would enable a more efficient screen for brightness with higher throughput (*282*). Another possible improvement could be to use a fluorescence activated microfluidic cell sorter with integrated electrodes for field stimulation to screen and sort large libraries based on the overall performance of the voltage indicator. A mammalian cell-based screening approach such as this could also focus on identifying Arch variants with higher voltage sensitivities, which would also provide increased SNR even in the absence of further improvements in brightness. Yet another direction for Arch engineering is to optimize an Arch variant as a FRET acceptor from a FP donor with an emission spectra that overlaps with the absorbance spectrum of Arch (*273*). In this manner, the voltage response of Arch (which involves an increase in extinction coefficient) can be readout as either a ratiometric change in fluorescence (decrease in FP, increase in Arch), or as simply a decrease in the bright fluorescent signal of the FP donor.

Efforts to improve protein function often proceed along one of two lines: 1) mutagenesis of a single promising protein scaffold; or 2) exploration of

biodiversity for naturally evolved proteins. In this paper we apply both approaches: directed evolution for the QuasArs, and exploration of natural diversity for CheRiff. A *post hoc* justification of the appropriateness of the two strategies is as follows. Voltage-sensitive fluorescence plays no role in the natural function of any microbial rhodopsin, so this feature has experienced no selective pressure. Gradient ascent by directed evolution is thus likely to move toward a local optimum. This approach uncovered non-obvious mutations distant from the retinal chromophore which provided substantial improvements in brightness (Figure 4.3). In contrast, light-gated ion channel function is the primary natural role of channelrhodopsins. Due to varying ecological niches one might anticipate that different organisms have evolved channelrhodopsins with varied light sensitivities and kinetics, some of which may be fortuitously matched with the unnatural demands of optogenetic experiments.

The combination of improved reporter and improved actuator in the Optopatch constructs facilitates rapid, non-invasive characterization of genetically defined cells across spatial scales from microns to millimeters, and temporal scales from microseconds to days. Optopatch has not yet been implemented with real-time feedback on the illumination, so it is not suited for voltage-clamp experiments. Nonetheless, with the assistance of computational modeling, open-loop voltage measurements can probe ionic conductances and membrane electrical properties (*283, 284*).

We also demonstrated that Optopatch functions in intact mammalian tissue. With extension to multiple genetically specified cells, Optopatch measurements in tissue may provide a useful tool for functional circuit mapping (*252*). With improved optical sectioning capability, sub-cellular Optopatch measurements

could enable inference of electrophysiological parameters in multi-compartment neural models (*285*). Such models are the basis for studies of single-cell neuronal information processing. Applications *in vivo* will likely benefit from further improvements to the indicator, primarily increased brightness, and exploration of two-photon excitability or other contrast modalities.

4.5 Materials and Methods

4.5.1 Molecular biology procedures

Synthetic DNA oligonucleotides used for cloning and library construction were purchased from Integrated DNA Technologies. *Pfu* polymerase (Fermentas) or AccuPrime *Pfx* SuperMix (Invitrogen) were used for high fidelity non-mutagenic PCR amplifications in the buffer supplied by the respective manufacturer. *Taq* polymerase (New England Biolabs) in the presence of $MnCl_2$ (0.1 mM) was used for error-prone PCR. PCR products and products of restriction digests were routinely purified using preparative agarose gel electrophoresis followed by DNA isolation using the GeneJET gel extraction kit (Fermentas). Restriction endonucleases were purchased from Fermentas and used according to the manufacturer's recommended protocol. Ligations were performed using T4 ligase (Invitrogen) or Gibson Assembly (New England Biolabs). Small-scale isolation of plasmid DNA was performed by GeneJET miniprep kit (Fermentas). The cDNA sequences for all Arch variants and fusion constructs were confirmed by dye terminator cycle sequencing using the BigDye Terminator Cycle Sequencing kit (Applied Biosystems). Site-directed mutagenesis and randomization of targeted codons was performed with either the QuikChange Lightning Single or Multi kit (Agilent Technologies). The sequences of oligonucleotides used in directed evolution of QuasArs are shown in Table 4.4.

Table 4.4 Oligonucleotides used in directed evolution of QuasArs

Name	Sequence

Fw_XbaI_Arch	CGACTCTAGAATGGACCCCATCGCTCTG CAGGCTGGTTACGACCTGCTGGGTGAC GGC
RV_Arch	TGCTACTACCGGTCGGGGCTCGGGGGC CTC
FW_Arch_FP	GAGGCCCCCGAGCCCCGACCGGTAGTA GCAATGGTGAGCAAGGGCGAGGAG
RV_HindIII_FP	GATGAAGCTTTTACTT GTACAGCTCGTCCATGCCG
FW_Arch_95X	CTATTATGCCAGGTACGCCHVSTGGCTG TTTACCACCCCAC
FW_Arch_106X	CCCCACTTCTGCTGCTGNRCCTGGCCCT TCTCGCTAA
FW_Arch_95N	ATTATGCCAGGTACGCCAATTGGCTGTT TACCACC
FW_Arch_95C	CTA TTA TGC CAG GTA CGC CTGTTG GCT GTT TAC CAC CCC AC
FW_Arch_95Q	CTA TTA TGC CAG GTA CGC CCAGTG GCT GTT TAC CAC CCC AC
FW_Arch_106C	CCCCACTTCTGCTGCTGTGCCTGGCCCT TCTCGCTAA

Fw_Arch_106E	CCCCACTTCTGCTGCTGGAGCTGGCCCT TCTCGCTAA
Fw_BamHI_Kozak_Arch	CGACGGATCCACCATGGACCCCATCGC TCTGCAGGC
RV_FP_ERex_stp_XbaI	GATGTCTAGATTATTCATTCTCATAACA AAACTTGTACAGCTCGTCCATGCCG
FW_BamHI_Kozak_Arch_ValSer	TGGGATCCACCATGGTAAGTATCGCTCT GCAGGCTGGTTAC
RV_FP_TS	ATCCAGGGGGATGTACTCGCCTTCGCTT GTGATTCTACTCTTGTACAGCTCGTCCA TGCCG
RV_TS_ER export_ stop_EcoRI	GATGGAATTCTTATACTTCATTCTCATA ACAAAATCC ACCTACATTTATGTCTATTTGATCCAGG GGGATGTACTCGCC

4.5.2 Construction of Arch mutant libraries

A library of > 10^4 mutants was generated by error-prone PCR of the gene encoding Arch D95N. These variants were then joined with the gene encoding mOrange2 by a two-part overlap extension PCR. The 5' piece used in the overlap extension was prepared by error-prone PCR of Arch D95N as template with a mixture of the forward primer (Fw_XbaI_Arch) and reverse primer (RV_Arch).

Primer Fw_XbaI_Arch contains an *XbaI* site and primer RV_Arch contains an overlap region with primer FW_Arch_FP. The 3' piece for use in the overlap extension was prepared by high fidelity PCR amplification of mOrange2 using a forward primer (FW_Arch_FP) and a reverse primer (RV_HindIII_FP). Primer RV_HindIII_FP contains a stop codon and a *HindIII* site. The full-length Arch-mOrange2 gene library was assembled by overlap extension PCR using an equimolar mixture of primers Fw_XbaI_Arch and RV_HindIII_FP together with a mixture of the 5' and 3' PCR fragments described above (50 ng each) as the template. In later rounds of directed evolution, error-prone PCR and StEP PCR DNA shuffling [25] were both used for construction of Arch-mOrange2 gene libraries.

The full-length PCR product (approximately 1,500 b.p.) was purified by agarose gel electrophoresis, doubly digested, and ligated between the *XbaI* and *HindIII* sites of a modified pBAD vector which was generated by deleting the ETorA tag between the *NcoI* and *XbaI* sites of the pTorPE vector [62] using Quikchange Lightning kit.

Following ligation, electrocompetent *E. coli* strain DH10B was transformed with the library of gene variants and cultured overnight at 37 °C on 10-cm Petri dishes of LB-agar supplemented with 100 μL of 4 mM retinal (Sigma-Aldrich), 100 μg/mL ampicillin (Sigma), and up to 0.0020% (wt/vol) L-arabinose (Alfa Aesar). The retinal solution was added on the surface of LB-agar plates evenly and air-dried prior to plating the cell suspension. At concentrations of L-arabinose higher than 0.0020% (wt/vol) we observed abnormal colony morphologies and reduced fluorescent brightness, presumably due to cytotoxicity caused by overexpression.

4.5.3 Screening of Arch mutants in *E. coli*

The imaging system used for library screening has previously been described in detail (*108*). We screened 10,000–20,000 colonies (10–20 plates of bacterial colonies) per round of random mutagenesis. For libraries generated by randomization of one or more codons, we screened approximately 3-fold more colonies than the expected library diversity (e.g. 3,000 colonies for a 1,000-member library).

We acquired two images of colonies using filter sets for mOrange2 (exc. 540 - 580 nm, em. 600 - 660 nm) and Arch (exc. 604-640 nm and em. 660 - 700 nm). An image of the ratio of Arch: mOrange2 fluorescence was calculated, and the colonies with the top 0.01% to 0.1% highest ratios were manually picked. Picked clones were individually cultured in 2 mL liquid LB medium (200 μg/mL ampicillin) shaken (250 rpm) overnight at 37 °C.

Protein expression was induced by adding 2 mL of liquid LB medium containing 120 μM retinal, 200 μg/mL ampicillin and 0.2% L-arabinose to the overnight culture, followed by incubation at 37 °C for 3 hours. The cell pellets were collected by centrifugation, washed and resuspended in buffered M9 salt solution containing 7 g/L Na_2HPO_4, 3 g/L KH_2PO_4, 0.5 g/L NaCl and 1 g/L NH_4Cl. The suspension was then diluted 5-fold prior to acquisition of its fluorescence spectrum in a Safire 2 fluorescence microplate reader (Tecan).

The emission profiles of each variant under excitation at 525 nm and 600 nm were acquired and normalized by the absorbance at 600 nm. The cell pellets of the three variants with the highest ratios of Arch to mOrange2 and the two variants

with the brightest absolute Arch fluorescence were treated for plasmid DNA extraction, and the pooled genes were used as templates for construction of gene libraries in the next round of directed evolution.

After five iterations we arrived at a non-pumping variant of Arch with five mutations relative to wild-type (P60S, T80S, D95N, D106Y, and F161V) and significantly improved brightness under excitation with low illumination intensity. This variant, designated Arch 3.5, was used as the template for subsequent efforts to address the secondary selection criteria.

4.5.4 Random mutagenesis at positions Asp95 and Asp106

We next focused on tuning other properties of Arch including voltage sensitivity, response kinetics, membrane trafficking and the undesirable dependence of brightness on illumination intensity. Positions Asp95 and Asp106 of Arch are structurally aligned with positions Asp85 and Asp96 of bacteriorhodopsin, and have been reported to play key roles in proton translocation during the photocycle [26,27]. The voltage sensing mechanism of Arch is likely due to electric-field-dependent protonation of the retinal Schiff base [13,64], so we reasoned that perturbations of the proton translocation network around the Schiff base could potentially affect the voltage sensitivity, response kinetics, or complex photophysics[24].

We constructed libraries in which Asp95 and Asp106 were randomized to a subset of all possible amino acid substitutions. First, we randomized position 95 using codon HVS (where H = A, C or T; V= A, C, or G; S = C or G), which encodes for all amino acids except Ala, Gly, Asp, Glu and Val. This library was

screened by fluorescence imaging of *E. coli* colonies. Variants that retained a high ratio of Arch to mOrange2 fluorescence were picked and expressed in HeLa cells for screening via induced transmembrane voltage (see below).

The mutation N95H emerged as the best from the first round of screening in HeLa cells. We then constructed a second library by randomizing position 106 to a subset of amino acids with polar or charged side chains (codon NRC, where N = A, C, G, or T; R = A or G), and screened these in HeLa cells. The variant with histidine at position 106 proved most promising and was designated QuasAr1.

4.5.5 Solubilization and spectroscopic characterization of QuasAr1 and QuasAr2.

E. coli expressing QuasAr1 and QuasAr2 were grown in 12 mL liquid LB medium with 200 μg/ml ampicillin overnight. The next day, 12 mL of liquid LB medium containing 50 μM retinal, 200 μg/ml ampicillin and 0.1% arabinose was added into the overnight culture, followed by additional incubation at 37 °C for 4 hours. The cell pellets were collected by centrifugation and lysed by suspension in B-PER solution (Pierce). The cytoplasmic fraction was discarded after centrifugation and the colored insoluble fraction was resuspended in phosphate buffered saline (PBS) containing 1.5% n-dodecyl-β-D-maltopyranoside (Affymetrix, Inc.). The suspension was homogenized by an ultrasonic homogenizer and centrifuged (17,000 g for 15 mins, 4 °C). The solubilized protein in the supernatant was used for *in vitro* spectroscopic characterization.

Absorption spectra were recorded on a DU-800 UV-visible spectrophotometer (Beckman) and fluorescence spectra were recorded on a

Safire2 plate reader (Tecan). Cy5 carboxylic acid (Cyandye) was used as the reference for quantum yield measurement. Quantum yield measurements were performed on a series of dilutions of each protein solution and standard, with absorbance values ranging from 0.01 to 0.05 at 600 nm. The fluorescence emission spectra of each dilution were recorded with excitation at 600 nm and the total fluorescence intensities obtained by integration. Integrated fluorescence intensity vs. absorbance was plotted for each protein and each standard. Quantum yields, Φ, were determined from the slopes (*S*) of each line using the equation: $\Phi_{protein} = \Phi_{standard} \times (S_{protein}/S_{standard})$.

4.5.6 Expression vectors for HeLa cells

To express Arch-mOrange2 variants in HeLa cells, the gene in the pBAD vector was first amplified by PCR using primers Fw_BamHI_Kozak_Arch and RV_FP_ERex_stp_XbaI. This reverse primer encodes the endoplasmic reticulum (ER) export sequence from the inward-rectifier potassium channel Kir2.1 (FCYENE) [65], which has been reported to be effective for improving the membrane trafficking of Arch in mammalian cells[29].

The purified DNA was digested with BamHI and XbaI restriction enzymes and ligated into a purified pcDNA3.1 plasmid that had been digested with the same two enzymes. The ligation reaction was used for transformation of electrocompetent *E. coli* strain DH10B cells. Cells were plated on LB/agar supplemented with ampicillin and individual colonies were picked into 4 mL of LB/ampicillin following overnight incubation at 37 °C. Liquid cultures were shaken at 250 rpm and 37 °C for 12-15 h and then a small scale isolation of plasmid DNA was performed. Each gene in pcDNA3.1 was fully sequenced using

T7_FW, and BGH_RV primers. Plasmids were then used for cell transfection as described below.

4.5.7 Induced transmembrane voltage (ITV) in HeLa cells

We co-expressed prospective Arch variants in HeLa cells with the inward rectifier potassium channel, Kir2.1. Expression of Kir2.1 lowered the resting potential to approximately -60 mV, close to the resting potential of neurons [66,67]. We reasoned that this effect would center the ITV close to the physiologically relevant range.

HeLa cells were grown to 40-60% confluence on home-made 35 mm glass bottom dishes or 24-well glass bottom plates. Cells were transfected with 1 μg of plasmid DNA comprising a 1:1 mixture of Arch variant and Kir2.1, using either 2 μL Turbofect (Thermo Scientific) or 2 μL Lipofectamine 2000 (Invitrogen) according to the manufacturer's instructions. After 3 h incubation, the medium was exchanged to DMEM with 10% fetal bovine serum. Cells were incubated for an additional 24 h at 37 °C in a CO_2 incubator. Immediately prior to imaging, cells were washed twice with Hanks balanced salt solution (HBSS) and then 1 mL of 20 mM HEPES buffered HBSS was added.

Cell imaging was performed with an inverted Eclipse Ti-E (Nikon) equipped with a Photometrics QuantEM 512SC camera, a 150 W mercury-xenon lamp (Hamamatsu), and a 10 mW 638 nm semiconductor diode laser (56ICS/S2669, Melles Griot CleanBeam) aligned just above the angle for total internal reflection. The filters were: 590-650 nm (excitation), 668-738 nm (emission), and 666 nm (dichroic). Movies were acquired at 10 ms/frame. The NIS-Elements Advanced

Research software (Nikon) was used for microscope and camera control and data acquisition. A schematic of the setup is shown in Figure 4.2.

To probe the response kinetics and voltage sensitivity, we used a pair of parallel platinum electrodes to apply a reproducible electric field across the cell culture and induce transient asymmetries in the membrane voltage [28]. Platinum electrodes with a gap of 0.5 cm were mounted in a custom plastic support. The electrode pair was placed in the imaging dish or well, and voltage pulses from a 6824A 40V/25A DC Power Supply (HP) were applied using waveforms generated by a pulse generator PG 58A (Gould Advance Ltd). The typical waveform had square-wave pulses lasting 20 ms, and pulse amplitudes from 25 – 35 V. Fluorescence was imaged at 100 Hz frame rate in 4×4 binning mode for 10 seconds. During each voltage pulse, opposite sides of the cell showed opposite fluorescence transients. Typical fluorescence traces are shown in Figure 4.2.

Raw fluorescence traces were corrected for background autofluorescence and photobleaching. The average voltage sensitivity ($\Delta F/F_{min}$) and SNR of each Arch variant were compared to the best variant of the previous generation, and only the variants with equal or improved performance were chosen as templates for the next round of screening.

4.5.8 Expression vectors for HEK cells and neurons

To enable more accurate electrophysiological characterization via patch clamp in HEK cells and primary neuron cultures, we cloned QuasAr1 into the BamHI/EcoRI sites of lentivirus vector FCK-Arch-GFP (Addgene: 22217). This vector contains a *CaMKII*α promoter and a WPRE after the 3' end of the open

reading frame. The Arch cDNA was generated by PCR using forward primer FW_BamHI_Kozak_Arch_ValSer and overlapping reverse primers RV_FP_TS and RV_TS_ERex_ stp_EcoRI. These reverse primers introduce a TS motif and ER export signal peptide sequence at the C-terminus of the protein.

4.5.9 Simultaneous electrophysiology and fluorescence in HEK cells

HEK cells were cultured and transfected following standard protocols [13]. Briefly, HEK-293 cells were grown at 37 ^{o}C, 5% CO_2, in DMEM supplemented with 10% FBS and penicillin-streptomycin. Plasmids were transfected using Transit 293T (Mirus) following the manufacturer's instructions, and assayed 48 hours later. The day before recording, cells were re-plated onto glass-bottom dishes (MatTek) at a density of ~10,000 cells/cm^2.

Cells were supplemented with retinal by diluting stock retinal solutions (40 mM, DMSO) in growth medium to a final concentration of 5 μM, and then returning the cells to the incubator for 0.5 - 1 hour. All imaging and electrophysiology were performed in Tyrode buffer (containing, in mM: 125 NaCl, 2.5 KCl, 3 $CaCl_2$, 1 $MgCl_2$, 10 HEPES, 30 glucose pH 7.3, and adjusted to 305-310 mOsm with sucrose). A gap junction blocker, 2-aminoethoxydiphenyl borate (50 μM, Sigma), was added to eliminate electrical coupling between cells.

Filamented glass micropipettes (WPI) were pulled to a tip resistance of 5–10 MΩ, and filled with internal solution containing 125 mM potassium gluconate, 8 mM NaCl, 0.6 mM MgCl2, 0.1 mM CaCl2, 1 mM EGTA, 10 mM HEPES, 4 mM Mg-ATP, 0.4 mM Na-GTP (pH 7.3); adjusted to 295 mOsm with sucrose. Pipettes were positioned with a Sutter MP285 manipulator. Whole-cell, voltage

and current clamp recordings were acquired using an Axopatch 700B amplifier (Molecular Devices), filtered at 2 kHz with the internal Bessel filter and digitized with a National Instruments PCIE-6323 acquisition board at 5-10 kHz. Data was only acquired from HEK cells having reversal potentials between -10 and -40 mV, access resistance < 25 MΩ and membrane resistance > 0.5 GΩ.

Simultaneous whole-cell patch clamp recordings and fluorescence recordings were acquired on a home-built, inverted epifluorescence microscope, described previously[13] and described below in the section "Optopatch Apparatus". We examined variants of QuasAr1 with mutations at position 95 (Asn, Cys, Gln, His and Tyr) and position 106 (Arg, Asp, Asn, Cys, Glu, His, Lys and Tyr). These experiments confirmed that histidine at position 106 provided undetectable photocurrent, and the best combination of improved voltage sensitivity, and fast kinetics. Mutants with Gln, Cys, or Asn at position 95 exhibited better voltage sensitivity compared to QuasAr1, while retaining fast kinetics. We designated the H95Q mutant QuasAr2.

4.5.10 Electrophysiology in neurons

Measurements were performed on primary cultures at 13 - 15 DIV. Experiments were conducted in Tyrode's solution containing 125 mM NaCl, 2.5 mM KCl, 3 mM $CaCl_2$, 1 mM $MgCl_2$, 10 mM HEPES, 30 mM glucose (pH 7.3) and adjusted to 305–310 mOsm with sucrose. Prior to imaging, neurons were incubated with 5 μM all-*trans* retinal for 30 minutes and then washed with Tyrode's solution.

Synaptic blockers were added to the imaging medium for measurements of single-cell electrophysiology (Arch photocurrents, and single-cell excitability). The blockers comprised NBQX (10 μM, Tocris), D (−)-2-amino-5-phosphonovaleric acid (AP5; 25 μM, Tocris), and gabazine (SR-95531, 20 μM, Tocris). For measurements of channelrhodopsin photocurrents in neurons, TTX (1 μM, Tocris) was included along with the synaptic blockers to prevent recruitment of voltage gated sodium channels.

During experiments with rapid stimulation (> 1 Hz), the red illumination was maintained continuously. Experiments were performed at 23 ºC under ambient atmosphere.

4.5.11 Organotypic brain slice culture.

Organotypic hippocampal slices cultures were prepared from postnatal day 6-8 Sprague-Dawley rats as described previously (*286*). The brain was taken out and immediately placed in chilled dissection media. Transverse hippocampal slices were cut with 400 μm thickness and 4 to 6 slices were placed in a sterile culture plate insert (Millicell-CM, Millipore) in 6-well plates containing prewarmed media. Slices were biolistically transfected with a Helios Gene Gun (BioRad) at 2 days *in vitro* (DIV 2). Bullets were prepared using 12.5 μg of 1.6 μm gold particles and 80 – 100 μg of plasmid DNA. Slices were maintained until imaging at DIV 12-16.

Immediately prior to imaging, slices were affixed to a nylon mesh weight and mounted upside down in a delta T brainslice adapter for inverted microscope

imaging (Bioptechs). Artificial cerebrospinal fluid (ACSF) was bubbled with carbogen (95% O_2, 5% CO_2) and flowed over the slice at 1 mL/min at 23 °C.

4.6 References

53. D. M. Shcherbakova, V. V. Verkhusha, Near-infrared fluorescent proteins for multicolor *in vivo* imaging. *Nature Methods* **10**, 751 (2013).

93. M. S. Siegel, E. Y. Isacoff, A Genetically Encoded Optical Probe of Membrane Voltage. *Neuron* **19**, 735 (1997).

108. Y. Zhao *et al.*, An Expanded Palette of Genetically Encoded Ca^{2+} Indicators. *Science* **333**, 1888 (2011).

129. J. M. Kralj, A. D. Douglass, D. R. Hochbaum, D. Maclaurin, A. E. Cohen, Optical recording of action potentials in mammalian neurons using a microbial rhodopsin. *Nature Methods* **9**, 90 (2012).

133. T.-W. Chen *et al.*, Ultrasensitive fluorescent proteins for imaging neuronal activity. *Nature* **499**, 295 (2013).

135. J. Wu *et al.*, Improved Orange and Red Ca^{2+} Indicators and Photophysical Considerations for Optogenetic Applications. *ACS Chemical Neuroscience* **4**, 963 (2013).

183. L. Jin *et al.*, Single Action Potentials and Subthreshold Electrical Events Imaged in Neurons with a Fluorescent Protein Voltage Probe. *Neuron* **75**, 779 (2012).

185. J. M. Kralj, D. R. Hochbaum, A. D. Douglass, A. E. Cohen, Electrical Spiking in Escherichia coli Probed with a Fluorescent Voltage-Indicating Protein. *Science* **333**, 345 (2011).

186. D. Maclaurin, V. Venkatachalam, H. Lee, A. E. Cohen, Mechanism of voltage-sensitive fluorescence in a microbial rhodopsin. *Proceedings of the National Academy of Sciences of the United States of America* **110**, 5939 (2013).

188. G. Cao *et al.*, Genetically Targeted Optical Electrophysiology in Intact Neural Circuits. *Cell* **154**, 904 (2013).

248. R. Yuste, Electrical Compartmentalization in Dendritic Spines. *Annual Review of Neuroscience* **36**, 429 (2013).

249. T. Branco, B. A. Clark, M. Häusser, Dendritic Discrimination of Temporal Input Sequences in Cortical Neurons. *Science* **329**, 1671 (2010).

250. W. Hu *et al.*, Distinct contributions of Nav1.6 and Nav1.2 in action potential initiation and backpropagation. *Nature Neuroscience* **12**, 996 (2009).

251. S. Peron, K. Svoboda, From cudgel to scalpel: toward precise neural control with optogenetics. *Nature Methods* **8**, 30 (2011).

252. L. Petreanu, T. Mao, S. M. Sternson, K. Svoboda, The subcellular organization of neocortical excitatory connections. *Nature* **457**, 1142 (2009).

253. M. Scanziani, M. Hausser, Electrophysiology in the age of light. *Nature* **461**, 930 (2009).

254. G. L. Boulting *et al.*, A functionally characterized test set of human induced pluripotent stem cells. *Nature Biotechnology* **29**, 279 (2011).

255. T. Furuta *et al.*, Brominated 7-hydroxycoumarin-4-ylmethyls: Photolabile protecting groups with biologically useful cross-sections for two photon

photolysis. *Proceedings of the National Academy of Sciences* **96**, 1193 (1999).

256. R. H. Kramer, D. L. Fortin, D. Trauner, New photochemical tools for controlling neuronal activity. *Current Opinion in Neurobiology* **19**, 544 (2009).

257. E. S. Boyden, F. Zhang, E. Bamberg, G. Nagel, K. Deisseroth, Millisecond-timescale, genetically targeted optical control of neural activity. *Nature Neuroscience* **8**, 1263 (2005).

258. J. G. Bernstein, P. A. Garrity, E. S. Boyden, Optogenetics and thermogenetics: technologies for controlling the activity of targeted cells within intact neural circuits. *Current Opinion in Neurobiology* **22**, 61 (2012).

259. A. J. Lam *et al.*, Improving FRET dynamic range with bright green and red fluorescent proteins. *Nature Methods* **9**, 1005 (2012).

260. W. Akemann *et al.*, Two-photon voltage imaging using a genetically encoded voltage indicator. *Scientific Reports* **3**, (2013).

261. E. W. Miller *et al.*, Optically monitoring voltage in neurons by photo-induced electron transfer through molecular wires. *Proceedings of the National Academy of Sciences of the United States of America*, (2012).

262. P. Yan *et al.*, Palette of fluorinated voltage-sensitive hemicyanine dyes. *Proceedings of the National Academy of Sciences of the United States of America*, (2012).

263. K. E. Vogt, S. Gerharz, J. Graham, M. Canepari, Combining Membrane Potential Imaging with l-Glutamate or GABA Photorelease. *PLoS ONE* **6**, e24911 (2011).

264. M. Canepari, D. Zecevic, K. E. Vogt, D. Ogden, M. De Waard, Combining Calcium Imaging with Other Optical Techniques. *Cold Spring Harbor Protocols* **2013**, pdb.top066167 (2013).

265. S. Tsuda *et al.*, Probing the function of neuronal populations: Combining micromirror-based optogenetic photostimulation with voltage-sensitive dye imaging. *Neuroscience Research* **75**, 76 (2013).

266. H. Zhao, L. Giver, Z. Shao, J. A. Affholter, F. H. Arnold, Molecular evolution by staggered extension process (StEP) *in vitro* recombination. *Nature Biotechnology* **16**, 258 (1998).

267. J. Lanyi, Proton transfer and energy coupling in the bacteriorhodopsin photocycle. *Journal of Bioenergetics and Biomembranes* **24**, 169 (1992).

268. J. K. Lanyi, Bacteriorhodopsin. *Annual Review of Physiology* **66**, 665 (2004).

269. G. Pucihar, T. Kotnik, D. Miklavcic, Measuring the induced membrane voltage with Di-8-ANEPPS. *Journal of visualized experiments : JoVE*, 12671 (2009).

270. V. Gradinaru *et al.*, Molecular and Cellular Approaches for Diversifying and Extending Optogenetics. *Cell* **141**, 154 (2010).

271. A. Foust, M. Popovic, D. Zecevic, D. A. McCormick, Action Potentials Initiate in the Axon Initial Segment and Propagate through Axon Collaterals Reliably in Cerebellar Purkinje Neurons. *The Journal of Neuroscience* **30**, 6891 (2010).

272. N. Enami *et al.*, Crystal Structures of Archaerhodopsin-1 and -2: Common Structural Motif in Archaeal Light-driven Proton Pumps. *Journal of Molecular Biology* **358**, 675 (2006).

273. Y. Gong, J. Z. Li, M. J. Schnitzer, Enhanced Archaerhodopsin Fluorescent Protein Voltage Indicators. *PLoS ONE* **8**, e66959 (2013).

274. M. A. Popovic, A. J. Foust, D. A. McCormick, D. Zecevic, The spatio-temporal characteristics of action potential initiation in layer 5 pyramidal neurons: a voltage imaging study. *The Journal of Physiology* **589**, 4167 (2011).

275. P. Schoenenberger, Å. Grunditz, T. Rose, T. Oertner, Optimizing the spatial resolution of Channelrhodopsin-2 activation. *Brain Cell Biology* **36**, 119 (2008).

276. J. Wang, M. T. Hasan, H. S. Seung, Laser-evoked synaptic transmission in cultured hippocampal neurons expressing channelrhodopsin-2 delivered by adeno-associated virus. *Journal of Neuroscience Methods* **183**, 165 (2009).

277. J. Mattis *et al.*, Principles for applying optogenetic tools derived from direct comparative analysis of microbial opsins. *Nature Methods* **9**, 159 (2012).

278. Z. V. Guo, A. C. Hart, S. Ramanathan, Optical interrogation of neural circuits in Caenorhabditis elegans. *Nature Methods* **6**, 891 (2009).

279. N. C. Klapoetke *et al.*, Independent optical excitation of distinct neural populations. *Nature Methods* **11**, 338 (2014).

280. B. Y. Chow *et al.*, High-performance genetically targetable optical neural silencing by light-driven proton pumps. *Nature* **463**, 98 (2010).

281. H. Mutoh, W. Akemann, T. Knöpfel, Genetically Engineered Fluorescent Voltage Reporters. *ACS Chemical Neuroscience* **3**, 585 (2012).

282. H.-J. Jang *et al.*, Retinoid production using metabolically engineered Escherichia coli with a two-phase culture system. *Microbial Cell Factories* **10**, 59 (2011).

283. Q. J. M. Huys, M. B. Ahrens, L. Paninski, Efficient Estimation of Detailed Single-Neuron Models. *Journal of Neurophysiology* **96**, 872 (2006).

284. J. C. Williams *et al.*, Computational Optogenetics: Empirically-Derived Voltage- and Light-Sensitive Channelrhodopsin-2 Model. *PLoS Computational Biology* **9**, e1003220 (2013).

285. J. Huggins, L. Paninski, Optimal experimental design for sampling voltage on dendritic trees in the low-SNR regime. *Journal of Computational Neuroscience* **32**, 347 (2012).

286. L. Stoppini, P. A. Buchs, D. Muller, A simple method for organotypic cultures of nervous tissue. *Journal of Neuroscience Methods* **37**, 173 (1991).

Chapter 5. Conclusions and future directions.

Cell biology is in the era of light. Since the discovery, cloning and development of FPs (*1, 4, 287*), optical imaging has greatly enhanced our knowledge and understanding of complex biological system. Although FPs are still mainly used as a fluorescent tag for revealing expression and localization of targeted cellular proteins, genetically encoded fluorescent indicators based on FP now generate much more excitement within the research community. After decades of development, genetically encoded fluorescent indicators have started showing their promise in reporting biochemical and physiological information in targeted cell populations and subcellular organelles for long period of time. However, protein engineering of improved genetically encoded fluorescent indicators still remains challenging, due to our poor understanding about structure-function relation of proteins.

In this thesis, I explored a powerful protein engineering algorithm called directed evolution, which mimics the process of natural selection of proteins, producing improved properties of interest related to genetically encoded fluorescent indicators. Depending on the targeted properties screened for, I designed various screening strategies that can estimate the probe function of variants and select superior variants in high-throughput. All my screening strategies share a common feature: a novel primary screen in high throughput and a secondary functional screen with high precision. The iterative rounds of screening lead to genetically encoded fluorescent indicators with improved and even new properties. This general screening scheme has been proven successful for evolving Ca^{2+} indicators and microbial opsin-based voltage indicators. In the

following sections, I summarize the work described in previous chapters, and discussed possible future directions for development of protein indicators and the potential methodologies.

5.1 Summary and future directions

A decade after the introduction of single FP-based GECIs and a number of improvements in the series of GCaMP variants, there remained only one color of indicator (i.e., green fluorescent) available. This lack of color diversity meant that Ca^{2+} imaging was essentially a monochromic endeavor, which limits the range of signaling that can be studied. The complex mechanism of GCaMP revealed by structural analysis (*121, 122*) suggested that it would likely be difficult to engineer different colors of GCaMP based on different FP scaffolds using rational approaches.

To address the engineering challenge for improved GECIs, I developed a high throughput colony-based screening method for directed evolution of single FP-based GECIs described in Chapter 2. The key concept of this screening method is to target mutants into the periplasmic space of *E. coli*, where periplasmic Ca^{2+} concentration can be manipulated by changing the Ca^{2+} concentration in the environment. This approach enables rapid estimation of Ca^{2+} responses of mutants and facilitates high throughput screening. The work resulted in expansion of the palette of single FP-based GECIs from blue to red and a new type of emission ratiometric indicator with novel Ca^{2+}-sensing mechanism and unprecedented large dynamic range (11,000% change in emission ratio) (*108*). This new palette of GECIs is called GECOs (genetically encoded calcium indicator for optical imaging), and has opened the door to multicolor Ca^{2+}

imaging. In addition, introduction of the red fluorescent GECI (RFP-based GECI), R-GECO, enables deeper Ca^{2+} imaging in tissue, due to less scattering effect and lower autofluorescence when using red-shifted excitation and emission wavelengths. Improved versions of R-GECO and other types of single RFP-based GECIs were soon developed (*135, 210, 288*). In principle, R-GECO can combine the use of optogenetic actuators with blue-shift actuation wavelengths to enable simultaneous optical detection and control of Ca^{2+} dynamics in the same cell. However, studies found that R-GECO and descendants exhibit complex photoisomerization and the red emission intensity can artificially increase under strong blue light illumination (*135, 210*), which limit their optogenetic applications. Another type of red GECIs utilizing a cp version of mRuby as the fluorescent reporter, termed RCaMP, does not exhibit complex photoisomerization and is suitable for optogenetic experiments, but the dynamic range is smaller than R-GECO variants (*210*).

Although we developed an effective colony-based screening method for improving GECIs, this method is a time consuming and laborious process. To accelerate the development of genetically encoded Ca^{2+} indicators, I designed and built a μFACS for screening GECIs with improved properties, which is described in Chapter 3. The results indicate that a μFACS aided directed evolution approach can identify superior variants with less effort, compared to the traditional manual on-plate screening approach (*108*). In addition, I engineered a novel yellow FP-based Ca^{2+} indicator based on mPapaya (*79*), termed Y-GECO. Using the μFACS aided directed evolution approach, I successfully evolved the brightness as well as the Ca^{2+} response of Y-GECO. The final product, Y-GECO1, is bright

at resting intracellular Ca^{2+} concentration, and exhibits excellent fluorescence response to Ca^{2+} transients in mammalian cell lines.

In Chapter 4, I switched my research focus from GECIs to GEVIs. Despite a lot of recent advancements in the field of GEVIs, the performance of currently available GEVIs is still not comparable to GECIs in terms of fluorescence response and brightness. The new class of GEVIs based on microbial opsins is promising due to the excellent voltage sensitivity and response kinetics (*129, 185*). However, illumination of the wild-type Arch generated photocurrent. The mutant Arch D95N had a substantial slow component, albeit no photocurrent. In addition, both Arch and Arch D95N were dim, with complex photophysics (*186*). In this Chapter, to overcome multiple critical issues of Arch-based voltage indicators, I developed a hierarchic screening approach and successfully evolved two Archaerhodopsin-based voltage indicators (QuasAr1 and QuasAr2) with improved brightness, voltage sensitivities and speed. Our collaborators combined the QuasAr series with a novel channelrhodopsin actuator and engineered co-expression constructs, Optopatch, that enable genetically targeted all optical electrophysiology in dissociated neuron culture, human stem cell-derived neurons as well as intact brain slice tissues.

Development of genetically encoded indicators for improved performance in imaging is a challenging problem of protein engineering, due to limited information on dynamic structural conformation changes as well as intramolecular interactions at the atomic level. In my thesis, I explored several different directed evolution approaches for improving the properties of genetically encoded Ca^{2+} and voltage indicators. The results indicate the power of directed evolution for evolving FP-based indicators in cases where rational design would be difficult if

not impossible. A successful directed evolution approach requires a proper experimental design to measure the targeted fluorescent properties of indicator mutants in a high-throughput manner, which requires innovative thinking. For example, in the case of Ca^{2+} indicators, one can target them to the periplasm, which facilitates the selection of variants with large Ca^{2+} response by controlling periplasmic Ca^{2+} concentrations of hundreds of thousands of colonies. Alternatively, millions of variants expressed in bacterial cells could be screened by a high-throughput microfluidic cell sorter in a couple of hours.

5.2 Perspective

Despite of the rapid development of genetically encoded indicators, there is still a large gap between genetically encoded indicators and synthetic organic dye in terms of performance. To make them practical and routine tools for optical imaging in tissue samples, significant engineering is required to improve the properties of genetically encoded indicators, including brightness, response kinetics and magnitude, photostability and selectivity. Engineering of indicators with near-infrared emission should be a priority due to the longer penetration path of near infrared fluorescence in scattering tissue samples and reduced phototoxicity (*205*).

Directed evolution is perhaps one of the most effective approaches currently for improving indicator properties, as there is not enough structural information on indicators of interest for rational design. It is critical and challenging to design effective screening strategies to identify and select superior variants efficiently from libraries with enormous amounts of mutants. In the future, a microfluidic system might be one of the most promising high-throughput platform

technologies for directed evolution of protein indicators, as it is cost-effective and amenable to customization. The recent advances in microfluidic technologies, such as droplet microfluidics (*86*), may enable fabrication of complicated microfluidic devices that are capable of measuring fluorescence properties of hundreds of thousands of protein variants and select improved ones in a short time period. Such high-throughput screening systems will enable broader coverage of the sequence landscape, which increases the odds of identification of superior variants, and significantly save labor, cost and time for directed evolution experiments.

Performance of genetically encoded fluorescent indicators may also be different in a cellular environment compared to *in vitro*, owing to the complicated matrix effect and high background fluorescence signal inside the cells *in vivo*. Directed evolution of protein indicators in an environment that approximates the environment of real-world applications may be the best approach to account for various experimental factors in the practical situation. For instance, despite the relatively low throughput, neuron-based screening has been demonstrated to be capable of selecting GCaMP variants that exhibit superior performance for neuroimaging (*133*) compared to its predecessor, GCaMP5 (*170*), which performs better than GCaMP6 *in vitro*. Another way to circumvent the matrix effect may be to engineer a pair of CaM/M13 proteins that do not cross-react with other endogenous components in the cell (*289*).

In addition to high throughput screening systems, computational design is a very attractive complementary technique (*289-294*). Protein sequence space is so vast that one optimal mutant might never be found by random mutagenesis and recombination even with the most powerful high throughput screen.

Structure-based computational design of protein variants can search the protein sequence space more completely than real-world screen in laboratory, and optimize the composition of sequences in a library. Recently, Structure-based computational design of protein libraries for improving fluorescent proteins has achieved moderate success (*294, 295*), which in principle could also applied to screen genetically encoded fluorescent indicators for improved properties. In the future, provided that computational designed library can be synthesized for a reasonable cost, screening a computational designed library using high throughput screening approach may have higher probability to discover the optimal sequence, compared to screening a library generated by random mutagenesis and recombination.

5.3 References

1. O. Shimomura, F. H. Johnson, Y. Saiga, Extraction, Purification and Properties of Aequorin, a Bioluminescent Protein from the Luminous Hydromedusan, Aequorea. *Journal of Cellular and Comparative Physiology* **59**, 223 (1962).

4. M. Chalfie, Y. Tu, G. Euskirchen, W. W. Ward, D. C. Prasher, Green Fluorescent Protein as a Marker for Gene-Expression. *Science* **263**, 802 (1994).

79. H. Hoi *et al.*, An Engineered Monomeric Zoanthus sp. Yellow Fluorescent Protein. *Chemistry & Biology* **20**, 1296 (2013).

86. J. J. Agresti *et al.*, Ultrahigh-throughput screening in drop-based microfluidics for directed evolution. *Proceedings of the National Academy of Sciences of the United States of America* **107**, 4004 (2010).

108. Y. Zhao *et al.*, An Expanded Palette of Genetically Encoded Ca^{2+} Indicators. *Science* **333**, 1888 (2011).

121. Q. Wang, B. Shui, M. I. Kotlikoff, H. Sondermann, Structural Basis for Calcium Sensing by GCaMP2. *Structure* **16**, 1817 (2008).

122. J. Akerboom *et al.*, Crystal Structures of the GCaMP Calcium Sensor Reveal the Mechanism of Fluorescence Signal Change and Aid Rational Design. *Journal of Biological Chemistry* **284**, 6455 (2009).

129. J. M. Kralj, A. D. Douglass, D. R. Hochbaum, D. Maclaurin, A. E. Cohen, Optical recording of action potentials in mammalian neurons using a microbial rhodopsin. *Nature Methods* **9**, 90 (2012).

133. T.-W. Chen *et al.*, Ultrasensitive fluorescent proteins for imaging neuronal activity. *Nature* **499**, 295 (2013).

135. J. Wu *et al.*, Improved Orange and Red Ca^{2+} Indicators and Photophysical Considerations for Optogenetic Applications. *ACS Chemical Neuroscience* **4**, 963 (2013).

170. J. Akerboom *et al.*, Optimization of a GCaMP Calcium Indicator for Neural Activity Imaging. *The Journal of Neuroscience* **32**, 13819 (2012).

185. J. M. Kralj, D. R. Hochbaum, A. D. Douglass, A. E. Cohen, Electrical Spiking in Escherichia coli Probed with a Fluorescent Voltage-Indicating Protein. *Science* **333**, 345 (2011).

186. D. Maclaurin, V. Venkatachalam, H. Lee, A. E. Cohen, Mechanism of voltage-sensitive fluorescence in a microbial rhodopsin. *Proceedings of the National Academy of Sciences of the United States of America* **110**, 5939 (2013).

205. A. H. Marblestone* *et al.*, Physical Principles for Scalable Neural Recording. *Frontiers in Computational Neuroscience* **7**, (2013).

210. J. Akerboom *et al.*, Genetically encoded calcium indicators for multi-color neural activity imaging and combination with optogenetics. *Frontiers in Molecular Neuroscience* **6**, (2013).

287. D. C. Prasher, V. K. Eckenrode, W. W. Ward, F. G. Prendergast, M. J. Cormier, Primary structure of the Aequorea victoria green-fluorescent protein. *Gene* **111**, 229 (1992).

288. M. Ohkura, T. Sasaki, C. Kobayashi, Y. Ikegaya, J. Nakai, An Improved Genetically Encoded Red Fluorescent Ca^{2+} Indicator for Detecting Optically Evoked Action Potentials. *PLoS ONE* **7**, e39933 (2012).

289. A. E. Palmer *et al.*, Ca^{2+} Indicators Based on Computationally Redesigned Calmodulin-Peptide Pairs. *Chemistry & Biology* **13**, 521 (2006).

290. M. A. Dwyer, L. L. Looger, H. W. Hellinga, Computational design of a biologically active enzyme. *Science* **304**, 1967 (2004).

291. D. B. Gordon, S. A. Marshall, S. L. Mayot, Energy functions for protein design. *Current Opinion in Structural Biology* **9**, 509 (1999).

292. B. Kuhlman *et al.*, Design of a novel globular protein fold with atomic-level accuracy. *Science* **302**, 1364 (2003).

293. C. A. Voigt, S. L. Mayo, F. H. Arnold, Z.-G. Wang, Computational method to reduce the search space for directed protein evolution. *Proceedings of the National Academy of Sciences of the United States of America* **98**, 3778 (2001).

294. T. P. Treynor, C. L. Vizcarra, D. Nedelcu, S. L. Mayo, Computationally designed libraries of fluorescent proteins evaluated by preservation and

diversity of function. *Proceedings of the National Academy of Sciences of the United States of America* **104**, 48 (2007).

295. R. A. Chica, M. M. Moore, B. D. Allen, S. L. Mayo, Generation of longer emission wavelength red fluorescent proteins using computationally designed libraries. *Proceedings of the National Academy of Sciences* **107**, 20257 (2010).

Bibliography

1. O. Shimomura, F. H. Johnson, Y. Saiga, Extraction, Purification and Properties of Aequorin, a Bioluminescent Protein from the Luminous Hydromedusan, Aequorea. *Journal of Cellular and Comparative Physiology* **59**, 223 (1962).
2. M. Ormö *et al.*, Crystal structure of the Aequorea victoria green fluorescent protein. *Science* **273**, 1392 (1996).
3. R. Y. Tsien, The green fluorescent protein. *Annual Review of Biochemistry* **67**, 509 (1998).
4. M. Chalfie, Y. Tu, G. Euskirchen, W. W. Ward, D. C. Prasher, Green Fluorescent Protein as a Marker for Gene-Expression. *Science* **263**, 802 (1994).
5. S. Inouye, F. I. Tsuji, Aequorea green fluorescent protein: Expression of the gene and fluorescence characteristics of the recombinant protein. *FEBS Letters* **341**, 277 (1994).
6. O. Shimomura, Structure of the chromophore of Aequorea green fluorescent protein. *FEBS Letters* **104**, 220 (1979).
7. N. P. Lemay *et al.*, The Role of the Tight-Turn, Broken Hydrogen Bonding, Glu222 and Arg96 in the Post-translational Green Fluorescent Protein Chromophore Formation. *Chemical physics* **348**, 152 (2008).
8. R. Heim, D. C. Prasher, R. Y. Tsien, Wavelength mutations and posttranslational autoxidation of green fluorescent protein. *Proceedings of the National Academy of Sciences of the United States of America* **91**, 12501 (1994).

9. A. B. Cubitt *et al.*, Understanding, improving and using green fluorescent proteins. *Trends in Biochemical Sciences* **20**, 448 (1995).

10. R. M. Wachter, J. L. Watkins, H. Kim, Mechanistic Diversity of Red Fluorescence Acquisition by GFP-like Proteins. *Biochemistry* **49**, 7417 (2010).

11. B. G. Reid, G. C. Flynn, Chromophore Formation in Green Fluorescent Protein. *Biochemistry* **36**, 6786 (1997).

12. D. P. Barondeau, C. D. Putnam, C. J. Kassmann, J. A. Tainer, E. D. Getzoff, Mechanism and energetics of green fluorescent protein chromophore synthesis revealed by trapped intermediate structures. *Proceedings of the National Academy of Sciences of the United States of America* **100**, 12111 (2003).

13. M. A. Rosenow, H. A. Huffman, M. E. Phail, R. M. Wachter, The Crystal Structure of the Y66L Variant of Green Fluorescent Protein Supports a Cyclization−Oxidation−Dehydration Mechanism for Chromophore Maturation. *Biochemistry* **43**, 4464 (2004).

14. J. Petersen *et al.*, The 2.0-Å Crystal Structure of eqFP611, a Far Red Fluorescent Protein from the Sea Anemone Entacmaea quadricolor. *Journal of Biological Chemistry* **278**, 44626 (2003).

15. F. V. Subach, V. V. Verkhusha, Chromophore Transformations in Red Fluorescent Proteins. *Chemical Reviews* **112**, 4308 (2012).

16. A. Miyawaki, D. M. Shcherbakova, V. V. Verkhusha, Red fluorescent proteins: chromophore formation and cellular applications. *Current Opinion in Structural Biology* **22**, 679 (2012).

17. V. V. Verkhusha, D. M. Chudakov, N. G. Gurskaya, S. Lukyanov, K. A. Lukyanov, Common Pathway for the Red Chromophore Formation in Fluorescent Proteins and Chromoproteins. *Chemistry & Biology* **11**, 845 (2004).

18. R. L. Strack, D. E. Strongin, L. Mets, B. S. Glick, R. J. Keenan, Chromophore Formation in DsRed Occurs by a Branched Pathway. *Journal of the American Chemical Society* **132**, 8496 (2010).

19. S. Pletnev, F. V. Subach, Z. Dauter, A. Wlodawer, V. V. Verkhusha, Understanding Blue-to-Red Conversion in Monomeric Fluorescent Timers and Hydrolytic Degradation of Their Chromophores. *Journal of the American Chemical Society* **132**, 2243 (2010).

20. L. A. Gross, G. S. Baird, R. C. Hoffman, K. K. Baldridge, R. Y. Tsien, The structure of the chromophore within DsRed, a red fluorescent protein from coral. *Proceedings of the National Academy of Sciences of the United States of America* **97**, 11990 (2000).

21. O. M. Subach, P. J. Cranfill, M. W. Davidson, V. V. Verkhusha, An Enhanced Monomeric Blue Fluorescent Protein with the High Chemical Stability of the Chromophore. *PLoS ONE* **6**, e28674 (2011).

22. M. Cotlet *et al.*, Identification of different emitting species in the red fluorescent protein DsRed by means of ensemble and single-molecule spectroscopy. *Proceedings of the National Academy of Sciences of the United States of America* **98**, 14398 (2001).

23. P. Dedecker, F. C. De Schryver, J. Hofkens, Fluorescent Proteins: Shine on, You Crazy Diamond. *Journal of the American Chemical Society* **135**, 2387 (2013).

24. S. H. Bokman, W. W. Ward, Renaturation of Aequorea green-fluorescent protein. *Biochemical and Biophysical Research Communications* **101**, 1372 (1981).

25. S. R. Meech, Excited state reactions in fluorescent proteins. *Chemical Society Reviews* **38**, 2922 (2009).

26. L. M. Tolbert, A. Baldridge, J. Kowalik, K. M. Solntsev, Collapse and Recovery of Green Fluorescent Protein Chromophore Emission through Topological Effects. *Accounts of Chemical Research* **45**, 171 (2011).

27. H. Niwa *et al.*, Chemical nature of the light emitter of the Aequorea green fluorescent protein. *Proceedings of the National Academy of Sciences of the United States of America* **93**, 13617 (1996).

28. K. L. Litvinenko, N. M. Webber, S. R. Meech, An ultrafast polarisation spectroscopy study of internal conversion and orientational relaxation of the chromophore of the green fluorescent protein. *Chemical Physics Letters* **346**, 47 (2001).

29. N. M. Webber, K. L. Litvinenko, S. R. Meech, Radiationless Relaxation in a Synthetic Analogue of the Green Fluorescent Protein Chromophore. *The Journal of Physical Chemistry B* **105**, 8036 (2001).

30. M. Vengris *et al.*, Ultrafast Excited and Ground-State Dynamics of the Green Fluorescent Protein Chromophore in Solution. *The Journal of Physical Chemistry A* **108**, 4587 (2004).

31. S. S. Stavrov, K. M. Solntsev, L. M. Tolbert, D. Huppert, Probing the Decay Coordinate of the Green Fluorescent Protein: Arrest of Cis−Trans Isomerization by the Protein Significantly Narrows the Fluorescence Spectra. *Journal of the American Chemical Society* **128**, 1540 (2006).

32. W. W. Ward, H. J. Prentice, A. F. Roth, C. W. Cody, S. C. Reeves, Spectral perturbations of the aequorea green-fluorescent protein. *Photochemistry and Photobiology* **35**, 803 (1982).

33. H.-w. Ai, N. C. Shaner, Z. Cheng, R. Y. Tsien, R. E. Campbell, Exploration of New Chromophore Structures Leads to the Identification of Improved Blue Fluorescent Proteins. *Biochemistry* **46**, 5904 (2007).

34. M. Chattoraj, B. A. King, G. U. Bublitz, S. G. Boxer, Ultra-fast excited state dynamics in green fluorescent protein: multiple states and proton transfer. *Proceedings of the National Academy of Sciences of the United States of America* **93**, 8362 (1996).

35. K. Brejc *et al.*, Structural basis for dual excitation and photoisomerization of the Aequorea victoria green fluorescent protein. *Proceedings of the National Academy of Sciences of the United States of America* **94**, 2306 (1997).

36. T. Kogure, H. Kawano, Y. Abe, A. Miyawaki, Fluorescence imaging using a fluorescent protein with a large Stokes shift. *Methods* **45**, 223 (2008).

37. K. D. Piatkevich *et al.*, Monomeric red fluorescent proteins with a large Stokes shift. *Proceedings of the National Academy of Sciences of the United States of America* **107**, 5369 (2010).

38. D. M. Shcherbakova, M. A. Hink, L. Joosen, T. W. J. Gadella, V. V. Verkhusha, An Orange Fluorescent Protein with a Large Stokes Shift for Single-Excitation Multicolor FCCS and FRET Imaging. *Journal of the American Chemical Society* **134**, 7913 (2012).

39. S. F. Field, M. V. Matz, Retracing evolution of red fluorescence in GFP-like proteins from Faviina corals. *Molecular Biology and Evolution* **27**, 225 (2010).

40. H. Mizuno *et al.*, Light-dependent regulation of structural flexibility in a photochromic fluorescent protein. *Proceedings of the National Academy of Sciences of the United States of America* **105**, 9227 (2008).

41. B. P. Cormack, R. H. Valdivia, S. Falkow, FACS-optimized mutants of the green fluorescent protein (GFP). *Gene* **173**, 33 (1996).

42. A. Crameri, E. A. Whitehorn, E. Tate, W. P. C. Stemmer, Improved Green Fluorescent Protein by Molecular Evolution Using DNA Shuffling. *Nature Biotechnology* **14**, 315 (1996).

43. R. Heim, A. B. Cubitt, R. Y. Tsien, Improved green fluorescence. *Nature* **373**, 663 (1995).

44. A. S. Mishin *et al.*, The First Mutant of the Aequorea victoria Green Fluorescent Protein That Forms a Red Chromophore†. *Biochemistry* **47**, 4666 (2008).

45. M. V. Matz *et al.*, Fluorescent proteins from nonbioluminescent Anthozoa species. *Nature Biotechnology* **17**, 969 (1999).

46. J. Wiedenmann *et al.*, A far-red fluorescent protein with fast maturation and reduced oligomerization tendency from Entacmaea quadricolor (Anthozoa, Actinaria). *Proceedings of the National Academy of Sciences of the United States of America* **99**, 11646 (2002).

47. N. C. Deliolanis *et al.*, Performance of the red-shifted fluorescent proteins in deep-tissue molecular imaging applications. *Journal of Biomedical Optics* **13**, 044008 (2008).

48. R. Weissleder, A clearer vision for *in vivo* imaging. *Nature Biotechnology* **19**, 316 (2001).

49. V. Ntziachristos, Fluorescence Molecular Imaging. *Annual Review of Biomedical Engineering* **8**, 1 (2006).

50. M. W. Davidson, R. E. Campbell, Engineered fluorescent proteins: innovations and applications. *Nature Methods* **6**, 713 (2009).

51. D. M. Shcherbakova, O. M. Subach, V. V. Verkhusha, Red Fluorescent Proteins: Advanced Imaging Applications and Future Design. *Angewandte Chemie International Edition* **51**, 10724 (2012).

52. D. Shcherbo *et al.*, Near-infrared fluorescent proteins. *Nature Methods* **7**, 827 (2010).

53. D. M. Shcherbakova, V. V. Verkhusha, Near-infrared fluorescent proteins for multicolor *in vivo* imaging. *Nature Methods* **10**, 751 (2013).

54. M. Drobizhev, N. S. Makarov, S. E. Tillo, T. E. Hughes, A. Rebane, Two-photon absorption properties of fluorescent proteins. *Nature Methods* **8**, 393 (2011).

55. P. T. C. So, C. Y. Dong, B. R. Masters, K. M. Berland, Two-photon excitation fluorescence microscopy. *Annual Review of Biomedical Engineering* **2**, 399 (2000).

56. D. A. Shagin *et al.*, GFP-like proteins as ubiquitous metazoan superfamily: evolution of functional features and structural complexity. *Molecular biology and evolution* **21**, 841 (2004).

57. M. V. Matz *et al.*, Fluorescent proteins from nonbioluminescent Anthozoa species. *Nature biotechnology* **17**, 969 (1999).

58. D. Yarbrough, R. M. Wachter, K. Kallio, M. V. Matz, S. J. Remington, Refined crystal structure of DsRed, a red fluorescent protein from coral, at 2.0-angstrom resolution. *Proceedings of the National Academy of Sciences of the United States of America* **98**, 462 (2001).

59. U. Lauf, P. Lopez, M. M. Falk, Expression of fluorescently tagged connexins: a novel approach to rescue function of oligomeric DsRed-tagged proteins. *FEBS letters* **498**, 11 (2001).

60. P. Gavin, R. J. Devenish, M. Prescott, An approach for reducing unwanted oligomerisation of DsRed fusion proteins. *Biochemical and biophysical research communications* **298**, 707 (2002).

61. A. Soling, A. Simm, N. Rainov, Intracellular localization of Herpes simplex virus type 1 thymidine kinase fused to different fluorescent proteins depends on choice of fluorescent tag. *FEBS letters* **527**, 153 (2002).

62. Y. G. Yanushevich *et al.*, A strategy for the generation of non-aggregating mutants of Anthozoa fluorescent proteins. *FEBS Letters* **511**, 11 (2002).

63. R. E. Campbell *et al.*, A monomeric red fluorescent protein. *Proceedings of the National Academy of Sciences of the United States of America* **99**, 7877 (2002).

64. H. W. Ai, J. N. Henderson, S. J. Remington, R. E. Campbell, Directed evolution of a monomeric, bright and photostable version of Clavularia cyan fluorescent protein: structural characterization and applications in fluorescence imaging. *The Biochemical journal* **400**, 531 (2006).

65. G. H. Patterson, J. Lippincott-Schwartz, A photoactivatable GFP for selective photolabeling of proteins and cells. *Science* **297**, 1873 (2002).

66. N. C. Shaner *et al.* Evaluating and improving the photostability of fluorescent proteins, *Proceedings of the SPIE* (2009), vol. 7191, pp. 719105-719105-11.

67. N. C. Shaner *et al.*, Improving the photostability of bright monomeric orange and red fluorescent proteins. *Nature Methods* **5**, 545 (2008).

68. N. C. Shaner, G. H. Patterson, M. W. Davidson, Advances in fluorescent protein technology. *Journal of Cell Science* **120**, 4247 (2007).

69. N. C. Shaner *et al.*, Improved monomeric red, orange and yellow fluorescent proteins derived from Discosoma sp. red fluorescent protein. *Nature Biotechnology* **22**, 1567 (2004).

70. J. L. Lubbeck, K. M. Dean, H. Ma, A. E. Palmer, R. Jimenez, Microfluidic flow cytometer for quantifying photobleaching of fluorescent proteins in cells. *Analytical Chemistry* **84**, 3929 (2012).

71. D. Shcherbo *et al.*, Far-red fluorescent tags for protein imaging in living tissues. *Biochem. J* **418**, 567 (2009).

72. R. Ando, H. Mizuno, A. Miyawaki, Regulated fast nucleocytoplasmic shuttling observed by reversible protein highlighting. *Science* **306**, 1370 (2004).

73. C. C. David *et al.*, Spectroscopic characterization of Venus at the single molecule level. *Photochemical & Photobiological Sciences* **11**, 358 (2012).

74. J. S. Marchant, G. E. Stutzmann, M. A. Leissring, F. M. LaFerla, I. Parker, Multiphoton-evoked color change of DsRed as an optical highlighter for cellular and subcellular labeling. *Nature Biotechnology* **19**, 645 (2001).

75. A. M. Bogdanov *et al.*, Green fluorescent proteins are light-induced electron donors. *Nature Chemical Biology* **5**, 459 (2009).

76. H. Hoi *et al.*, A monomeric photoconvertible fluorescent protein for imaging of dynamic protein localization. *Journal of Molecular Biology* **401**, 776 (2010).

77. G.-J. Kremers, K. L. Hazelwood, C. S. Murphy, M. W. Davidson, D. W. Piston, Photoconversion in orange and red fluorescent proteins. *Nature Methods* **6**, 355 (2009).

78. F. V. Subach, K. D. Piatkevich, V. V. Verkhusha, Directed molecular evolution to design advanced red fluorescent proteins. *Nature Methods* **8**, 1019 (2011).

79. H. Hoi *et al.*, An Engineered Monomeric Zoanthus sp. Yellow Fluorescent Protein. *Chemistry & Biology* **20**, 1296 (2013).

80. H.-w. Ai, S. Olenych, P. Wong, M. Davidson, R. Campbell, Hue-shifted monomeric variants of Clavularia cyan fluorescent protein: identification of the molecular determinants of color and applications in fluorescence imaging. *BMC Biology* **6**, 13 (2008).

81. J.-D. Pédelacq, S. Cabantous, T. Tran, T. C. Terwilliger, G. S. Waldo, Engineering and characterization of a superfolder green fluorescent protein. *Nature Biotechnology* **24**, 79 (2005).

82. J. Goedhart *et al.*, Bright cyan fluorescent protein variants identified by fluorescence lifetime screening. *Nature Methods* **7**, 137 (2010).

83. T. Grotjohann *et al.*, Diffraction-unlimited all-optical imaging and writing with a photochromic GFP. *Nature* **478**, 204 (2011).

84. H. Hoi *et al.*, An Engineered Monomeric Zoanthus sp. Yellow Fluorescent Protein. *Chemistry and Biology*.

85. K. M. Esvelt, J. C. Carlson, D. R. Liu, A system for the continuous directed evolution of biomolecules. *Nature* **472**, 499 (2011).

86. J. J. Agresti *et al.*, Ultrahigh-throughput screening in drop-based microfluidics for directed evolution. *Proceedings of the National Academy of Sciences of the United States of America* **107**, 4004 (2010).

87. J. L. Lubbeck, K. M. Dean, L. M. Davis, A. E. Palmer, R. Jimenez, A Microfluidic Cell Sorter for Directed Evolution of Fluorescent Proteins Based on Dark-State Conversion and Photobleaching. *Biophysical Journal* **100**, 175a (2011).

88. L. M. Davis, J. L. Lubbeck, K. M. Dean, A. E. Palmer, R. Jimenez, Microfluidic cell sorter for use in developing red fluorescent proteins with improved photostability. *Lab on a Chip* **13**, 2320 (2013).

89. S. C. Alford, J. Wu, Y. Zhao, R. E. Campbell, T. Knöpfel, Optogenetic reporters. *Biology of the Cell* **105**, 14 (2013).

90. T. K. Kerppola, Bimolecular fluorescence complementation (BiFC) analysis as a probe of protein interactions in living cells. *Annual review of biophysics* **37**, 465 (2008).

91. I. Ghosh, A. D. Hamilton, L. Regan, Antiparallel leucine zipper-directed protein reassembly: application to the green fluorescent protein. *Journal of the American Chemical Society* **122**, 5658 (2000).

92. T. Nagai, A. Sawano, E. S. Park, A. Miyawaki, Circularly permuted green fluorescent proteins engineered to sense Ca^{2+}. *Proceedings of the National Academy of Sciences of the United States of America* **98**, 3197 (2001).

93. M. S. Siegel, E. Y. Isacoff, A Genetically Encoded Optical Probe of Membrane Voltage. *Neuron* **19**, 735 (1997).

94. G. S. Baird, D. A. Zacharias, R. Y. Tsien, Circular permutation and receptor insertion within green fluorescent proteins. *Proceedings of the National Academy of Sciences of the United States of America* **96**, 11241 (1999).

95. J. Nakai, M. Ohkura, K. Imoto, A high signal-to-noise Ca^{2+} probe composed of a single green fluorescent protein. *Nature Biotechnology* **19**, 137 (2001).

96. K. Saito *et al.*, Luminescent proteins for high-speed single-cell and whole-body imaging. *Nature Communication* **3**, 1262 (2012).

97. Spencer C. Alford, Ahmed S. Abdelfattah, Y. Ding, Robert E. Campbell, A Fluorogenic Red Fluorescent Protein Heterodimer. *Chemistry & Biology* **19**, 353 (2012).

98. S. C. Alford, Y. Ding, T. Simmen, R. E. Campbell, Dimerization-Dependent Green and Yellow Fluorescent Proteins. *ACS Synthetic Biology* **1**, 569 (2012).

99. G. Grynkiewicz, M. Poenie, R. Y. Tsien, A new generation of Ca^{2+} indicators with greatly improved fluorescence properties. *Journal of Biological Chemistry* **260**, 3440 (1985).

100. C. Wu *et al.*, *In vivo* far-red luminescence imaging of a biomarker based on BRET from Cypridina bioluminescence to an organic dye. *Proceedings of the National Academy of Sciences of the United States of America* **106**, 15599 (2009).

101. T. K. Kerppola, Bimolecular fluorescence complementation (BiFC) analysis as a probe of protein interactions in living cells. *Annual review of biophysics* **37**, 465 (2008).

102. J. Chu *et al.*, A novel far-red bimolecular fluorescence complementation system that allows for efficient visualization of protein interactions under physiological conditions. *Biosensors and Bioelectronics* **25**, 234 (2009).

103. J.-Y. Fan *et al.*, Split mCherry as a new red bimolecular fluorescence complementation system for visualizing protein–protein interactions in living cells. *Biochemical and Biophysical Research Communications* **367**, 47 (2008).

104. G. Jach, M. Pesch, K. Richter, S. Frings, J. F. Uhrig, An improved mRFP1 adds red to bimolecular fluorescence complementation. *Nature Methods* **3**, 597 (2006).

105. K. Ohashi, T. Kiuchi, K. Shoji, K. Sampei, K. Mizuno, Visualization of cofilin-actin and Ras-Raf interactions by bimolecular fluorescence complementation assays using a new pair of split Venus fragments. *BioTechniques* **52**, 45 (2012).

106. Y. J. Shyu, H. Liu, X. Deng, C. Hu, Identification of new fluorescent protein fragments for biomolecular fluorescence complementation analysis under physiological conditions. *BioTechniques* **40**, 61 (2006).

107. C.-D. Hu, Y. Chinenov, T. K. Kerppola, Visualization of Interactions among bZIP and Rel Family Proteins in Living Cells Using Bimolecular Fluorescence Complementation. *Molecular Cell* **9**, 789 (2002).

108. Y. Zhao *et al.*, An Expanded Palette of Genetically Encoded Ca^{2+} Indicators. *Science* **333**, 1888 (2011).

109. G. Miesenbock, D. A. De Angelis, J. E. Rothman, Visualizing secretion and synaptic transmission with pH-sensitive green fluorescent proteins. *Nature* **394**, 192 (1998).

110. T. Kuner, G. J. Augustine, A Genetically Encoded Ratiometric Indicator for Chloride: Capturing Chloride Transients in Cultured Hippocampal Neurons. *Neuron* **27**, 447 (2000).

111. P. Eli, A. Chakrabartty, Variants of DsRed fluorescent protein: Development of a copper sensor. *Protein Science* **15**, 2442 (2006).

112. G. T. Hanson *et al.*, Investigating mitochondrial redox potential with redox-sensitive green fluorescent protein indicators. *Journal of Biological Chemistry* **279**, 13044 (2004).

113. C. T. Dooley *et al.*, Imaging dynamic redox changes in mammalian cells with green fluorescent protein indicators. *Journal of Biological Chemistry* **279**, 22284 (2004).

114. H. Østergaard, A. Henriksen, F. G. Hansen, J. R. Winther, Shedding light on disulfide bond formation: engineering a redox switch in green fluorescent protein. *The EMBO Journal* **20**, 5853 (2001).

115. S. Tang *et al.*, Design and application of a class of sensors to monitor Ca^{2+} dynamics in high Ca^{2+} concentration cellular compartments. *Proceedings of the National Academy of Sciences of the United States of America* **108**, 16265 (2011).

116. S. Chen, Z.-j. Chen, W. Ren, H.-w. Ai, Reaction-Based Genetically Encoded Fluorescent Hydrogen Sulfide Sensors. *Journal of the American Chemical Society* **134**, 9589 (2012).

117. Z.-j. Chen, W. Ren, Q. E. Wright, H.-w. Ai, Genetically Encoded Fluorescent Probe for the Selective Detection of Peroxynitrite. *Journal of the American Chemical Society* **135**, 14940 (2013).

118. S. Topell, J. Hennecke, R. Glockshuber, Circularly permuted variants of the green fluorescent protein. *FEBS Letters* **457**, 283 (1999).

119. O. Griesbeck, G. S. Baird, R. E. Campbell, D. A. Zacharias, R. Y. Tsien, Reducing the Environmental Sensitivity of Yellow Fluorescent Protein: MECHANISM AND APPLICATIONS. *Journal of Biological Chemistry* **276**, 29188 (2001).

120. J. Nakai, M. Ohkura, K. Imoto, A high signal-to-noise Ca^{2+} probe composed of a single green fluorescent protein. *Nat Biotech* **19**, 137 (2001).

121. Q. Wang, B. Shui, M. I. Kotlikoff, H. Sondermann, Structural Basis for Calcium Sensing by GCaMP2. *Structure* **16**, 1817 (2008).

122. J. Akerboom *et al.*, Crystal Structures of the GCaMP Calcium Sensor Reveal the Mechanism of Fluorescence Signal Change and Aid Rational Design. *Journal of Biological Chemistry* **284**, 6455 (2009).

123. F. Helmchen, W. Denk, Deep tissue two-photon microscopy. *Nature Methods* **2**, 932 (2005).

124. G. Miesenböck, I. G. Kevrekidis, Optical imaging and control of genetically designated neurons in functioning circuits. *Annual Review of Neuroscience* **28**, 533 (2005).

125. K. Svoboda, R. Yasuda, Principles of Two-Photon Excitation Microscopy and Its Applications to Neuroscience. *Neuron* **50**, 823 (2006).

126. P. Marcaggi, H. Mutoh, D. Dimitrov, M. Beato, T. Knöpfel, Optical measurement of mGluR1 conformational changes reveals fast activation, slow deactivation, and sensitization. *Proceedings of the National Academy of Sciences* **106**, 11388 (2009).

127. T. Bozza, J. P. McGann, P. Mombaerts, M. Wachowiak, *In vivo* Imaging of Neuronal Activity by Targeted Expression of a Genetically Encoded Probe in the Mouse. *Neuron* **42**, 9 (2004).

128. S. A. Hires, Y. Zhu, R. Y. Tsien, Optical measurement of synaptic glutamate spillover and reuptake by linker optimized glutamate-sensitive fluorescent reporters. *Proceedings of the National Academy of Sciences* **105**, 4411 (2008).

129. J. M. Kralj, A. D. Douglass, D. R. Hochbaum, D. Maclaurin, A. E. Cohen, Optical recording of action potentials in mammalian neurons using a microbial rhodopsin. *Nature Methods* **9**, 90 (2012).

130. D. Dimitrov *et al.*, Engineering and Characterization of an Enhanced Fluorescent Protein Voltage Sensor. *PLoS ONE* **2**, e440 (2007).

131. H. Tsutsui, S. Karasawa, Y. Okamura, A. Miyawaki, Improving membrane voltage measurements using FRET with new fluorescent proteins. *Nat Meth* **5**, 683 (2008).

132. W. Akemann, H. Mutoh, A. Perron, J. Rossier, T. Knopfel, Imaging brain electric signals with genetically targeted voltage-sensitive fluorescent proteins. *Nature Methods* **7**, 643 (2010).

133. T.-W. Chen *et al.*, Ultrasensitive fluorescent proteins for imaging neuronal activity. *Nature* **499**, 295 (2013).

134. T. Thestrup *et al.*, Optimized ratiometric calcium sensors for functional *in vivo* imaging of neurons and T lymphocytes. *Nature Methods* **advance online publication**, (2014).

135. J. Wu *et al.*, Improved Orange and Red Ca^{2+} Indicators and Photophysical Considerations for Optogenetic Applications. *ACS Chemical Neuroscience* **4**, 963 (2013).

136. M. J. Berridge, Neuronal calcium signaling. *Neuron* **21**, 13 (1998).

137. M. J. Berridge, P. Lipp, M. D. Bootman, The versatility and universality of calcium signalling. *Nature Reviews Molecular Cell Biology* **1**, 11 (2000).

138. R. Kerr *et al.*, Optical Imaging of Calcium Transients in Neurons and Pharyngeal Muscle of C. elegans. *Neuron* **26**, 583 (2000).

139. O. Garaschuk *et al.*, Optical monitoring of brain function *in vivo*: from neurons to networks. *Pflügers Archiv* **453**, 385 (2006).

140. W. Göbel, F. Helmchen, *In vivo* calcium imaging of neural network function. *Physiology* **22**, 358 (2007).

141. M. Mank, O. Griesbeck, Genetically Encoded Calcium Indicators. *Chemical Reviews* **108**, 1550 (2008).

142. D. W. Domaille, E. L. Que, C. J. Chang, Synthetic fluorescent sensors for studying the cell biology of metals. *Nature Chemical Biology* **4**, 168 (2008).

143. A. Miyawaki *et al.*, Fluorescent indicators for Ca^{2+} based on green fluorescent proteins and calmodulin. *Nature* **388**, 882 (1997).

144. V. A. Romoser, P. M. Hinkle, A. Persechini, Detection in living cells of ca^{2+}-dependent changes in the fluorescence emission of an indicator

composed of two green fluorescent protein variants linked by a calmodulin-binding sequence: a new class of fluorescence indicators. *Journal of Biological Chemistry* **272**, 13270 (1997).

145. M. Mank *et al.*, A genetically encoded calcium indicator for chronic *in vivo* two-photon imaging. *Nature Methods* **5**, 805 (2008).

146. A. Miyawaki, O. Griesbeck, R. Heim, R. Y. Tsien, Dynamic and quantitative Ca^{2+} measurements using improved cameleons. *Proceedings of the National Academy of Sciences of the United States of America* **96**, 2135 (1999).

147. T. Nagai, S. Yamada, T. Tominaga, M. Ichikawa, A. Miyawaki, Expanded dynamic range of fluorescent indicators for Ca^{2+} by circularly permuted yellow fluorescent proteins. *Proceedings of the National Academy of Sciences of the United States of America* **101**, 10554 (2004).

148. K. Horikawa *et al.*, Spontaneous network activity visualized by ultrasensitive Ca^{2+} indicators, yellow Cameleon-Nano. *Nature Methods* **7**, 729 (2010).

149. N. Heim, O. Griesbeck, Genetically Encoded Indicators of Cellular Calcium Dynamics Based on Troponin C and Green Fluorescent Protein. *Journal of Biological Chemistry* **279**, 14280 (2004).

150. M. Mank *et al.*, A FRET-Based Calcium Biosensor with Fast Signal Kinetics and High Fluorescence Change. *Biophysical Journal* **90**, 1790 (2006).

151. D. F. Reiff *et al.*, *In vivo* Performance of Genetically Encoded Indicators of Neural Activity in Flies. *The Journal of Neuroscience* **25**, 4766 (2005).

152. J. Díez-García *et al.*, Activation of cerebellar parallel fibers monitored in transgenic mice expressing a fluorescent Ca^{2+} indicator protein. *European Journal of Neuroscience* **22**, 627 (2005).

153. L. Tian *et al.*, Imaging neural activity in worms, flies and mice with improved GCaMP calcium indicators. *Nature Methods* **6**, 875 (2009).

154. K. R. Gee *et al.*, Chemical and physiological characterization of fluo-4 Ca^{2+}-indicator dyes. *Cell Calcium* **27**, 97 (2000).

155. X. R. Sun *et al.*, Fast GCaMPs for improved tracking of neuronal activity. *Nature Communication* **4**, (2013).

156. A. Fiala *et al.*, Genetically Expressed Cameleon in Drosophila melanogaster Is Used to Visualize Olfactory Information in Projection Neurons. *Current Biology* **12**, 1877 (2002).

157. D. Yu, G. S. Baird, R. Y. Tsien, R. L. Davis, Detection of Calcium Transients in DrosophilaMushroom Body Neurons with Camgaroo Reporters. *The Journal of Neuroscience* **23**, 64 (2003).

158. J. W. Wang, A. M. Wong, J. Flores, L. B. Vosshall, R. Axel, Two-Photon Calcium Imaging Reveals an Odor-Evoked Map of Activity in the Fly Brain. *Cell* **112**, 271 (2003).

159. L. Liu, O. Yermolaieva, W. A. Johnson, F. M. Abboud, M. J. Welsh, Identification and function of thermosensory neurons in Drosophila larvae. *Nature Neuroscience* **6**, 267 (2003).

160. S.-i. Higashijima, M. A. Masino, G. Mandel, J. R. Fetcho, Imaging Neuronal Activity During Zebrafish Behavior With a Genetically Encoded Calcium Indicator. *Journal of Neurophysiology* **90**, 3986 (2003).

161. M. T. Hasan *et al.*, Functional Fluorescent Ca^{2+} Indicator Proteins in Transgenic Mice under TET Control. *PLoS Biology* **2**, e163 (2004).

162. J. Díez-García, W. Akemann, T. Knöpfel, *In vivo* calcium imaging from genetically specified target cells in mouse cerebellum. *NeuroImage* **34**, 859 (2007).

163. D.-l. Qiu, T. Knöpfel, An NMDA Receptor/Nitric Oxide Cascade in Presynaptic Parallel Fiber–Purkinje Neuron Long-Term Potentiation. *The Journal of Neuroscience* **27**, 3408 (2007).

164. D.-l. Qiu, T. Knöpfel, Presynaptically expressed long-term depression at cerebellar parallel fiber synapses. *Pflügers Archiv - European Journal of Physiology* **457**, 865 (2009).

165. E. Warp *et al.*, Emergence of Patterned Activity in the Developing Zebrafish Spinal Cord. *Current Biology* **22**, 93 (2012).

166. M. L. Fletcher *et al.*, Optical Imaging of Postsynaptic Odor Representation in the Glomerular Layer of the Mouse Olfactory Bulb. *Journal of Neurophysiology* **102**, 817 (2009).

167. M. L. Fletcher, Analytical Processing of Binary Mixture Information by Olfactory Bulb Glomeruli. *PLoS ONE* **6**, e29360 (2011).

168. C. D. Harvey, P. Coen, D. W. Tank, Choice-specific sequences in parietal cortex during a virtual-navigation decision task. *Nature* **484**, 62 (2012).

169. M. B. Ahrens, M. B. Orger, D. N. Robson, J. M. Li, P. J. Keller, Whole-brain functional imaging at cellular resolution using light-sheet microscopy. *Nature Methods* **10**, 413 (2013).

170. J. Akerboom *et al.*, Optimization of a GCaMP Calcium Indicator for Neural Activity Imaging. *The Journal of Neuroscience* **32**, 13819 (2012).

171. M. L. Andermann, A. M. Kerlin, C. Reid, Chronic cellular imaging of mouse visual cortex during operant behavior and passive viewing. *Frontiers in Cellular Neuroscience* **4**, (2010).

172. M. Minderer *et al.*, Chronic imaging of cortical sensory map dynamics using a genetically encoded calcium indicator. *The Journal of Physiology* **590**, 99 (2012).

173. D. A. Dombeck, C. D. Harvey, L. Tian, L. L. Looger, D. W. Tank, Functional imaging of hippocampal place cells at cellular resolution during virtual navigation. *Nature Neuroscience* **13**, 1433 (2010).

174. D. Huber *et al.*, Multiple dynamic representations in the motor cortex during sensorimotor learning. *Nature* **484**, 473 (2012).

175. K. Ataka, V. A. Pieribone, A Genetically Targetable Fluorescent Probe of Channel Gating with Rapid Kinetics. *Biophysical Journal* **82**, 509 (2002).

176. R. Sakai, V. Repunte-Canonigo, C. D. Raj, T. Knöpfel, Design and characterization of a DNA-encoded, voltage-sensitive fluorescent protein. *European Journal of Neuroscience* **13**, 2314 (2001).

177. G. Guerrero, M. S. Siegel, B. Roska, E. Loots, E. Y. Isacoff, Tuning FlaSh: Redesign of the Dynamics, Voltage Range, and Color of the Genetically Encoded Optical Sensor of Membrane Potential. *Biophysical Journal* **83**, 3607 (2002).

178. B. J. Baker *et al.*, Three fluorescent protein voltage sensors exhibit low plasma membrane expression in mammalian cells. *Journal of Neuroscience Methods* **161**, 32 (2007).

179. A. Lundby, H. Mutoh, D. Dimitrov, W. Akemann, T. Knöpfel, Engineering of a Genetically Encodable Fluorescent Voltage Sensor

Exploiting Fast Ci-VSP Voltage-Sensing Movements. *PLoS ONE* **3**, e2514 (2008).

180. L. Jin *et al.*, Random insertion of split-cans of the fluorescent protein venus into Shaker channels yields voltage sensitive probes with improved membrane localization in mammalian cells. *Journal of Neuroscience Methods* **199**, 1 (2011).

181. L. Barnett, J. Platisa, M. Popovic, V. A. Pieribone, T. Hughes, A Fluorescent, Genetically-Encoded Voltage Probe Capable of Resolving Action Potentials. *PLoS ONE* **7**, e43454 (2012).

182. W. Akemann *et al.*, Imaging neural circuit dynamics with a voltage-sensitive fluorescent protein. *Journal of Neurophysiology* **108**, 2323 (2012).

183. L. Jin *et al.*, Single Action Potentials and Subthreshold Electrical Events Imaged in Neurons with a Fluorescent Protein Voltage Probe. *Neuron* **75**, 779 (2012).

184. B. Chanda *et al.*, A hybrid approach to measuring electrical activity in genetically specified neurons. *Nature Neuroscience* **8**, 1619 (2005).

185. J. M. Kralj, D. R. Hochbaum, A. D. Douglass, A. E. Cohen, Electrical Spiking in Escherichia coli Probed with a Fluorescent Voltage-Indicating Protein. *Science* **333**, 345 (2011).

186. D. Maclaurin, V. Venkatachalam, H. Lee, A. E. Cohen, Mechanism of voltage-sensitive fluorescence in a microbial rhodopsin. *Proceedings of the National Academy of Sciences of the United States of America* **110**, 5939 (2013).

187. E. Pastrana, Light-based electrophysiology. *Nature Methods* **9**, 38 (2011).

188. G. Cao *et al.*, Genetically Targeted Optical Electrophysiology in Intact Neural Circuits. *Cell* **154**, 904 (2013).

189. M. A. LYNCH, Long-Term Potentiation and Memory. *Physiological Reviews* **84**, 87 (2004).

190. S. H. Snyder, R. B. Innis, Peptide Neurotransmitters. *Annual Review of Biochemistry* **48**, 755 (1979).

191. C. W. Cotman, D. T. Monaghan, in *Excitatory Amino Acids and Epilepsy,* R. Schwarcz, Y. Ben-Ari, Eds. (Springer US, 1986), vol. 203, pp. 237-252.

192. S. Okumoto *et al.*, Detection of glutamate release from neurons by genetically encoded surface-displayed FRET nanosensors. *Proceedings of the National Academy of Sciences of the United States of America* **102**, 8740 (2005).

193. R. Y. Tsien, Building and breeding molecules to spy on cells and tumors. *FEBS Letters* **579**, 927 (2005).

194. J. S. Marvin *et al.*, An optimized fluorescent probe for visualizing glutamate neurotransmission. *Nature Methods* **10**, 162 (2013).

195. Q.-T. Nguyen *et al.*, An *in vivo* biosensor for neurotransmitter release and in situ receptor activity. *Nature Neuroscience* **13**, 127 (2010).

196. J. G. Yamauchi *et al.*, Characterizing Ligand-Gated Ion Channel Receptors with Genetically Encoded Ca^{2+} Sensors. *PLoS ONE* **6**, e16519 (2011).

197. T. C. Sudhof, The synaptic vesicle cycle: a cascade of protein–protein interactions. *Nature* **375**, 645 (1995).

198. M. Ng *et al.*, Transmission of Olfactory Information between Three Populations of Neurons in the Antennal Lobe of the Fly. *Neuron* **36**, 463 (2002).

199. Y. Li, R. W. Tsien, pHTomato, a red, genetically encoded indicator that enables multiplex interrogation of synaptic activity. *Nature Neuroscience* **15**, 1047 (2012).

200. K. Berglund *et al.*, Imaging synaptic inhibition in transgenic mice expressing the chloride indicator, Clomeleon. *Brain Cell Biology* **35**, 207 (2006).

201. J. S. Grimley *et al.*, Visualization of Synaptic Inhibition with an Optogenetic Sensor Developed by Cell-Free Protein Engineering Automation. *The Journal of Neuroscience* **33**, 16297 (2013).

202. P. J. Keller, A. D. Schmidt, J. Wittbrodt, E. H. Stelzer, Reconstruction of zebrafish early embryonic development by scanned light sheet microscopy. *Science* **322**, 1065 (2008).

203. S. Abrahamsson *et al.*, Fast multicolor 3D imaging using aberration-corrected multifocus microscopy. *Nature Methods* **10**, 60 (2012).

204. S. Quirin, D. S. Peterka, R. Yuste, Instantaneous three-dimensional sensing using spatial light modulator illumination with extended depth of field imaging. *Optics Exp* **21**, 16007 (2013).

205. A. H. Marblestone *et al.*, Physical Principles for Scalable Neural Recording. *Frontiers in Computational Neuroscience* **7**, (2013).

206. A. M. Caravaca-Aguirre, E. Niv, D. B. Conkey, R. Piestun, Real-time resilient focusing through a bending multimode fiber. *Optics Express* **21**, 12881 (2013).

207. A. N. Zorzos, E. S. Boyden, C. G. Fonstad, Multiwaveguide implantable probe for light delivery to sets of distributed brain targets. *Optics Letters* **35**, 4133 (2010).

208. A. N. Zorzos, J. Scholvin, E. S. Boyden, C. G. Fonstad, Three-dimensional multiwaveguide probe array for light delivery to distributed brain circuits. *Optics Letters* **37**, 4841 (2012).

209. D. B. Conkey, A. M. Caravaca-Aguirre, R. Piestun, High-speed scattering medium characterization with application to focusing light through turbid media. *Optics express* **20**, 1733 (2012).

210. J. Akerboom *et al.*, Genetically encoded calcium indicators for multi-color neural activity imaging and combination with optogenetics. *Frontiers in Molecular Neuroscience* **6**, (2013).

211. R. Y. Tsien, *Monitoring cell calcium*. Calcium as a cellular regulator (Oxford University Press, Oxford, UK, New York, 1999), pp. 28-54.

212. Single-letter abbreviations for amino acid residues are: A, Ala; C, Cys; D, Asp; E, Glu; F, Phe; G, Gly; H, His; I, Ile; K, Lys; L, Leu; M, Met; N, Asn; P, Pro; Q, Gln; R, Arg; S, Ser; T, Thr; V, Val; W, Trp; and Y, Tyr.

213. Y. N. Tallini *et al.*, Imaging cellular signals in the heart *in vivo*: Cardiac expression of the high-signal Ca^{2+} indicator GCaMP2. *Proceedings of the National Academy of Sciences of the United States of America* **103**, 4753 (2006).

214. Materials and methods are available as supporting material at *Science* Online.

215. C. M. Barrett, N. Ray, J. D. Thomas, C. Robinson, A. Bolhuis, Quantitative export of a reporter protein, GFP, by the twin-arginine translocation pathway in *Escherichia coli*. *Biochemical and Biophysical Research Communications* **304**, 279 (2003).

216. H. Zhao, W. Zha, *In vitro*'sexual'evolution through the PCR-based staggered extension process (StEP). *Nature Protocols* **1**, 1865 (2006).

217. Y. Shinkai *et al.*, Behavioral choice between conflicting alternatives is regulated by a receptor guanylyl cyclase, GCY-28, and a receptor tyrosine kinase, SCD-2, in AIA interneurons of Caenorhabditis elegans. *The Journal of Neuroscience* **31**, 3007 (2011).

218. H. Imamura *et al.*, Visualization of ATP levels inside single living cells with fluorescence resonance energy transfer-based genetically encoded indicators. *Proceedings of the National Academy of Sciences of the United States of America* **106**, 15651 (2009).

219. M. Nakano, H. Imamura, T. Nagai, H. Noji, Ca^{2+} regulation of mitochondrial ATP synthesis visualized at the single cell level. *ACS Chemical Biology* **6**, 709 (2011).

220. F. Zhang *et al.*, Optogenetic interrogation of neural circuits: technology for probing mammalian brain structures. *Nature Protocols* **5**, 439 (2010).

221. Z. Cheng, R. E. Campbell, Assessing the Structural Stability of Designed β - Hairpin Peptides in the Cytoplasm of Live Cells. *ChemBioChem* **7**, 1147 (2006).

222. A. E. Palmer, R. Y. Tsien, Measuring calcium signaling using genetically targetable fluorescent indicators. *Nature Protocols* **1**, 1057 (2006).

223. R. Das, D. Baker, Macromolecular modeling with rosetta. *Annual Review of Biochemistry* **77**, 363 (2008).

224. D. J. Mandell, E. A. Coutsias, T. Kortemme, Sub-angstrom accuracy in protein loop reconstruction by robotics-inspired conformational sampling. *Nature Methods* **6**, 551 (2009).

225. P. Gangola, B. Rosen, Maintenance of intracellular calcium in Escherichia coli. *Journal of Biological Chemistry* **262**, 12570 (1987).

226. A. W. Karzai, E. D. Roche, R. T. Sauer, The SsrA–SmpB system for protein tagging, directed degradation and ribosome rescue. *Nature Structural & Molecular Biology* **7**, 449 (2000).

227. M. J. Berridge, M. D. Bootman, H. L. Roderick, Calcium signalling: dynamics, homeostasis and remodelling. *Nature Reviews: Molecular Cell Biology* **4**, 517 (2003).

228. M. I. Kotlikoff, Genetically encoded Ca^{2+} indicators: using genetics and molecular design to understand complex physiology. *The Journal of Physiology* **578**, 55 (2007).

229. H. Hoi, T. Matsuda, T. Nagai, R. E. Campbell, Highlightable Ca^{2+} Indicators for Live Cell Imaging. *Journal of the American Chemical Society* **135**, 46 (2012).

230. C. Chen, S. H. Cho, F. Tsai, A. Erten, Y.-H. Lo, Microfluidic cell sorter with integrated piezoelectric actuator. *Biomedical Microdevices* **11**, 1223 (2009).

231. C. H. Chen *et al.*, Specific Sorting of Single Bacterial Cells with Microfabricated Fluorescence-Activated Cell Sorting and Tyramide Signal Amplification Fluorescence in Situ Hybridization. *Analytical Chemistry* **83**, 7269 (2011).

232. Y. Xia, G. M. Whitesides, Soft Lithography. *Annual Review of Materials Science* **28**, 153 (1998).

233. H. J. Carlson, R. E. Campbell, Circular permutated red fluorescent proteins and calcium ion indicators based on mCherry. *Protein Engineering Design and Selection* **26**, 763 (2013).

234. H.-w. Ai, K. L. Hazelwood, M. W. Davidson, R. E. Campbell, Fluorescent protein FRET pairs for ratiometric imaging of dual biosensors. *Nature Methods* **5**, 401 (2008).

235. C. Kantor *et al.*, in *Isolated Central Nervous System Circuits,* K. Ballanyi, Ed. (Humana Press, 2012), pp. 315-356.

236. A. Ruangkittisakul *et al.*, High sensitivity to neuromodulator-activated signaling pathways at physiological [K^+] of confocally imaged respiratory center neurons in on-line-calibrated newborn rat brainstem slices. *The Journal of Neuroscience* **26**, 11870 (2006).

237. S. H. Cho, C. H. Chen, F. S. Tsai, J. M. Godin, Y.-H. Lo, Human mammalian cell sorting using a highly integrated micro-fabricated fluorescence-activated cell sorter (μFACS). *Lab on a Chip* **10**, 1567 (2010).

238. S. J. Remington *et al.*, zFP538, a Yellow-Fluorescent Protein from Zoanthus, Contains a Novel Three-Ring Chromophore. *Biochemistry* **44**, 202 (2004).

239. M. J. Higley, B. L. Sabatini, Calcium Signaling in Dendrites and Spines: Practical and Functional Considerations. *Neuron* **59**, 902 (2008).

240. R. Yuste, W. Denk, Dendritic spines as basic functional units of neuronal integration. *Nature* **375**, 682 (1995).

241. C. Grienberger, A. Konnerth, Imaging Calcium in Neurons. *Neuron* **73**, 862 (2012).

242. D. Smetters, A. Majewska, R. Yuste, Detecting Action Potentials in Neuronal Populations with Calcium Imaging. *Methods* **18**, 215 (1999).

243. J. M. Brundege, T. V. Dunwiddie, Modulation of excitatory synaptic transmission by adenosine released from single hippocampal pyramidal neurons. *The Journal of Neuroscience* **16**, 5603 (1996).

244. B. Panaitescu *et al.*, Methylxanthines do not affect rhythmogenic preBötC inspiratory network activity but impair bursting of preBötC-driven motoneurons. *Neuroscience* **255**, 158 (2013).

245. A. Klishin, T. Tsintsadze, N. Lozovaya, O. Krishtal, Latent N-methyl-D-aspartate receptors in the recurrent excitatory pathway between hippocampal CA1 pyramidal neurons: Ca^{2+}-dependent activation by blocking A1 adenosine receptors. *Proceedings of the National Academy of Sciences* **92**, 12431 (1995).

246. S. Thümmler, T. V. Dunwiddie, Adenosine Receptor Antagonists Induce Persistent Bursting in the Rat Hippocampal CA3 Region Via an NMDA Receptor-Dependent Mechanism. *Journal of Neurophysiology* **83**, 1787 (2000).

247. D. Cai, K. B. Cohen, T. Luo, J. W. Lichtman, J. R. Sanes, Improved tools for the Brainbow toolbox. *Nature Methods* **10**, 540 (2013).

248. R. Yuste, Electrical Compartmentalization in Dendritic Spines. *Annual Review of Neuroscience* **36**, 429 (2013).

249. T. Branco, B. A. Clark, M. Häusser, Dendritic Discrimination of Temporal Input Sequences in Cortical Neurons. *Science* **329**, 1671 (2010).

250. W. Hu *et al.*, Distinct contributions of Nav1.6 and Nav1.2 in action potential initiation and backpropagation. *Nature Neuroscience* **12**, 996 (2009).

251. S. Peron, K. Svoboda, From cudgel to scalpel: toward precise neural control with optogenetics. *Nature Methods* **8**, 30 (2011).

252. L. Petreanu, T. Mao, S. M. Sternson, K. Svoboda, The subcellular organization of neocortical excitatory connections. *Nature* **457**, 1142 (2009).

253. M. Scanziani, M. Hausser, Electrophysiology in the age of light. *Nature* **461**, 930 (2009).

254. G. L. Boulting *et al.*, A functionally characterized test set of human induced pluripotent stem cells. *Nature Biotechnology* **29**, 279 (2011).

255. T. Furuta *et al.*, Brominated 7-hydroxycoumarin-4-ylmethyls: Photolabile protecting groups with biologically useful cross-sections for two photon photolysis. *Proceedings of the National Academy of Sciences* **96**, 1193 (1999).

256. R. H. Kramer, D. L. Fortin, D. Trauner, New photochemical tools for controlling neuronal activity. *Current Opinion in Neurobiology* **19**, 544 (2009).

257. E. S. Boyden, F. Zhang, E. Bamberg, G. Nagel, K. Deisseroth, Millisecond-timescale, genetically targeted optical control of neural activity. *Nature Neuroscience* **8**, 1263 (2005).

258. J. G. Bernstein, P. A. Garrity, E. S. Boyden, Optogenetics and thermogenetics: technologies for controlling the activity of targeted cells within intact neural circuits. *Current Opinion in Neurobiology* **22**, 61 (2012).

259. A. J. Lam *et al.*, Improving FRET dynamic range with bright green and red fluorescent proteins. *Nature Methods* **9**, 1005 (2012).

260. W. Akemann *et al.*, Two-photon voltage imaging using a genetically encoded voltage indicator. *Scientific Reports* **3**, (2013).

261. E. W. Miller *et al.*, Optically monitoring voltage in neurons by photo-induced electron transfer through molecular wires. *Proceedings of the National Academy of Sciences of the United States of America*, (2012).

262. P. Yan *et al.*, Palette of fluorinated voltage-sensitive hemicyanine dyes. *Proceedings of the National Academy of Sciences of the United States of America*, (2012).

263. K. E. Vogt, S. Gerharz, J. Graham, M. Canepari, Combining Membrane Potential Imaging with l-Glutamate or GABA Photorelease. *PLoS ONE* **6**, e24911 (2011).

264. M. Canepari, D. Zecevic, K. E. Vogt, D. Ogden, M. De Waard, Combining Calcium Imaging with Other Optical Techniques. *Cold Spring Harbor Protocols* **2013**, pdb.top066167 (2013).

265. S. Tsuda *et al.*, Probing the function of neuronal populations: Combining micromirror-based optogenetic photostimulation with voltage-sensitive dye imaging. *Neuroscience Research* **75**, 76 (2013).

266. H. Zhao, L. Giver, Z. Shao, J. A. Affholter, F. H. Arnold, Molecular evolution by staggered extension process (StEP) *in vitro* recombination. *Nature Biotechnology* **16**, 258 (1998).

267. J. Lanyi, Proton transfer and energy coupling in the bacteriorhodopsin photocycle. *Journal of Bioenergetics and Biomembranes* **24**, 169 (1992).

268. J. K. Lanyi, Bacteriorhodopsin. *Annual Review of Physiology* **66**, 665 (2004).

269. G. Pucihar, T. Kotnik, D. Miklavcic, Measuring the induced membrane voltage with Di-8-ANEPPS. *Journal of visualized experiments : JoVE*, 12671 (2009).

270. V. Gradinaru *et al.*, Molecular and Cellular Approaches for Diversifying and Extending Optogenetics. *Cell* **141**, 154 (2010).

271. A. Foust, M. Popovic, D. Zecevic, D. A. McCormick, Action Potentials Initiate in the Axon Initial Segment and Propagate through Axon Collaterals Reliably in Cerebellar Purkinje Neurons. *The Journal of Neuroscience* **30**, 6891 (2010).

272. N. Enami *et al.*, Crystal Structures of Archaerhodopsin-1 and -2: Common Structural Motif in Archaeal Light-driven Proton Pumps. *Journal of Molecular Biology* **358**, 675 (2006).

273. Y. Gong, J. Z. Li, M. J. Schnitzer, Enhanced Archaerhodopsin Fluorescent Protein Voltage Indicators. *PLoS ONE* **8**, e66959 (2013).

274. M. A. Popovic, A. J. Foust, D. A. McCormick, D. Zecevic, The spatio-temporal characteristics of action potential initiation in layer 5 pyramidal neurons: a voltage imaging study. *The Journal of Physiology* **589**, 4167 (2011).

275. P. Schoenenberger, Å. Grunditz, T. Rose, T. Oertner, Optimizing the spatial resolution of Channelrhodopsin-2 activation. *Brain Cell Biology* **36**, 119 (2008).

276. J. Wang, M. T. Hasan, H. S. Seung, Laser-evoked synaptic transmission in cultured hippocampal neurons expressing channelrhodopsin-2 delivered by adeno-associated virus. *Journal of Neuroscience Methods* **183**, 165 (2009).

277. J. Mattis *et al.*, Principles for applying optogenetic tools derived from direct comparative analysis of microbial opsins. *Nature Methods* **9**, 159 (2012).

278. Z. V. Guo, A. C. Hart, S. Ramanathan, Optical interrogation of neural circuits in Caenorhabditis elegans. *Nature Methods* **6**, 891 (2009).

279. N. C. Klapoetke *et al.*, Independent optical excitation of distinct neural populations. *Nature Methods* **11**, 338 (2014).

280. B. Y. Chow *et al.*, High-performance genetically targetable optical neural silencing by light-driven proton pumps. *Nature* **463**, 98 (2010).

281. H. Mutoh, W. Akemann, T. Knöpfel, Genetically Engineered Fluorescent Voltage Reporters. *ACS Chemical Neuroscience* **3**, 585 (2012).

282. H.-J. Jang *et al.*, Retinoid production using metabolically engineered Escherichia coli with a two-phase culture system. *Microbial Cell Factories* **10**, 59 (2011).

283. Q. J. M. Huys, M. B. Ahrens, L. Paninski, Efficient Estimation of Detailed Single-Neuron Models. *Journal of Neurophysiology* **96**, 872 (2006).

284. J. C. Williams *et al.*, Computational Optogenetics: Empirically-Derived Voltage- and Light-Sensitive Channelrhodopsin-2 Model. *PLoS Computational Biology* **9**, e1003220 (2013).

285. J. Huggins, L. Paninski, Optimal experimental design for sampling voltage on dendritic trees in the low-SNR regime. *Journal of Computational Neuroscience* **32**, 347 (2012).

286. L. Stoppini, P. A. Buchs, D. Muller, A simple method for organotypic cultures of nervous tissue. *Journal of Neuroscience Methods* **37**, 173 (1991).

287. D. C. Prasher, V. K. Eckenrode, W. W. Ward, F. G. Prendergast, M. J. Cormier, Primary structure of the Aequorea victoria green-fluorescent protein. *Gene* **111**, 229 (1992).

288. M. Ohkura, T. Sasaki, C. Kobayashi, Y. Ikegaya, J. Nakai, An Improved Genetically Encoded Red Fluorescent Ca^{2+} Indicator for Detecting Optically Evoked Action Potentials. *PLoS ONE* **7**, e39933 (2012).

289. A. E. Palmer *et al.*, Ca^{2+} Indicators Based on Computationally Redesigned Calmodulin-Peptide Pairs. *Chemistry & Biology* **13**, 521 (2006).

290. M. A. Dwyer, L. L. Looger, H. W. Hellinga, Computational design of a biologically active enzyme. *Science* **304**, 1967 (2004).

291. D. B. Gordon, S. A. Marshall, S. L. Mayot, Energy functions for protein design. *Current Opinion in Structural Biology* **9**, 509 (1999).

292. B. Kuhlman *et al.*, Design of a novel globular protein fold with atomic-level accuracy. *Science* **302**, 1364 (2003).

293. C. A. Voigt, S. L. Mayo, F. H. Arnold, Z.-G. Wang, Computational method to reduce the search space for directed protein evolution. *Proceedings of the National Academy of Sciences of the United States of America* **98**, 3778 (2001).

294. T. P. Treynor, C. L. Vizcarra, D. Nedelcu, S. L. Mayo, Computationally designed libraries of fluorescent proteins evaluated by preservation and diversity of function. *Proceedings of the National Academy of Sciences of the United States of America* **104**, 48 (2007).

295. R. A. Chica, M. M. Moore, B. D. Allen, S. L. Mayo, Generation of longer emission wavelength red fluorescent proteins using computationally designed libraries. *Proceedings of the National Academy of Sciences of the United States of America* **107**, 20257 (2010).